Impact-Related Processes on Mercury and the Moon

by

Lillian Rose Ostrach

A Dissertation Presented in Partial Fulfillment
of the Requirements for the Degree
Doctor of Philosophy

Approved October 2013 by the
Graduate Supervisory Committee:

Mark S. Robinson, Chair
James F. Bell III
Philip R. Christensen
Amanda B. Clarke
Edward J. Garnero

ARIZONA STATE UNIVERSITY

December 2013

ABSTRACT

Impact craters are ubiquitous throughout the Solar System, formed by one of the principal processes responsible for surface modification of terrestrial planets and solid bodies (i.e., asteroids, icy moons). The impact cratering process is well studied, particularly on the Moon and Mercury, where the results remain uncomplicated by atmospheric effects, plate tectonics, or interactions with water and ices. Crater measurements, used to determine relative and absolute ages for geologic units by relating the cumulative crater frequency per unit area to radiometrically-determined ages from returned samples, are sensitive to the solar incidence angle of images used for counts. Earlier work is quantitatively improved by investigating this important effect and showing that absolute model ages are most accurately determined using images with incidence angles between 65° and 80°, and equilibrium crater diameter estimates are most accurate at ~80° incidence angle.

A statistical method is developed using crater size-frequencies to distinguish lunar mare age units in the absence of spectral differences. Applied to the Moon, the resulting areal crater densities confidently identify expansive units with >300–500 my age differences, distinguish non-obvious secondaries, and determine that an area $>1\times10^4$ km^2 provides statistically robust crater measurements. This areal crater density method is also applied to the spectrally-homogeneous volcanic northern smooth plains (NSP) on Mercury. Although crater counts and observations of embayed craters indicate that the NSP experienced at least two resurfacing episodes, no observable age units are observed using areal crater density measurements, so smooth plains emplacement occurred over a relatively short timescale (<500 my).

For the first time, the distribution of impact melt on Mercury and the Moon are compared at high resolution. Mercurian craters with diameters ≥30 km have a greater areal extent of interior melt deposits than similarly sized lunar craters, a result consistent with melt-generation model predictions.

The effects of shaking on compositional sorting within a granular regolith are experimentally tested, demonstrating the possibility of mechanical segregation of particles in the lunar regolith. These results provide at least one explanation toward understanding the inconsistencies between lunar remote sensing datasets and are important for future spacecraft sample return missions.

DEDICATION

Grandpa, you may be the rocket scientist, but I am the rock scientist.

– and –

To my parents, who very rarely said no, and never when it truly mattered.
Mom, today is my day and I'll move mountains. Because you always said I could.

Papa, you taught me to reach. And when I couldn't quite grasp, you've always given me an extra boost.

– and –

Jack:
It's been great, worth the wait!
Can you believe that this is really year eight?

ACKNOWLEDGMENTS

Although the physical writing of this dissertation was a primarily singular task, during which time I camped at my cubicle desk at LROC, spread my papers across my very tiny dining room table, and embraced the silence in ISTB-IV Room 631, the motivation, composition, and ultimately the completion of my research was a group effort. There is no way I would have successfully concluded this body of work alone.

I would like to thank Mark Robinson, my primary advisor, for taking a chance on a martian and providing me with constant challenges to promote the growth of my scientific skills. He very quickly taught me that the Moon is incredibly complex and yet really simple (often both at the same time). Also that new observational evidence sometimes contradicts decades of accepted understanding and theories, which happens often with Mercury. The opportunities to work with brand-new datasets from LROC and MESSENGER, forge collaborations with members of the science teams, and contribute meaningful results using these new data fundamentally changed my perspective as a budding planetary scientist.

My dissertation advisory committee, Phil Christensen, Amanda Clarke, Ed Garnero, and Jim Bell provided me with insight and new ideas on how to interpret my findings. With their help, I have tried to see the bigger picture and implications of my highly focused research, for which I thank them. I would also like to recognize an absent advisory committee member, Ron Greeley, because he challenged me to become a better scientist. With a wicked grin and a twinkle in his eye, Ron forced me to admit my limits while pushing me to recognize the depth of knowledge I possessed. His course field trips

expanded my field experience and helped me to grasp the importance of field studies in relation to planetary science interpretation.

I would also like to thank the wonderful professors and mentors at Brown University. In particular I thank Jan Tullis, who welcomed me into the Geology Department and provided unceasing academic support and motivation, and Jim Head, who helped me to begin this particular journey into planetary geoscience.

I give thanks also to my fellow graduate students, postdocs, and office-mates, residing at ASU and elsewhere. Drew Enns and Sarah Braden: Team Cerberus! Working with you two was awesome and I will miss our cubicle conversations; late research nights will never be the same. Without the guidance of Sam Lawrence, Julie Stopar, Brett Denevi, and Emerson Speyerer, I have no doubt that I would have read fewer publications, stayed farther away from Matlab, and questioned less rigorously than I do now. LROCers, working with you was fabulous–every single minute–and I am going to miss your enthusiasm, dedication, and shenanigans. To my Brown University family, especially Ailish Kress, Angela Stickle, Laura Kerber, Jenny Whitten, Leah Cheek, Mark Salvatore, Carolyn Ernst, Rachel Klima, Jay Dickson, and Caleb Fassett, you are fantastic. We talk science, we do science, we talk life, we cheerlead; I am so grateful for everything you've taught me and suggested I ponder. Paul Byrne and Christian Klimczak, it has been a pleasure collaborating with you on MESSENGER science and I look forward to continuing scientific discussion with you both.

As with many ventures there are people behind the scenes, the support staff who make so many tasks easier. Pattie Dodson seemingly effortlessly passed required paperwork and reimbursements through the ASU pipeline, always with a smile. The

SESE HQ Administrative Staff, particularly Becky Polley and Becca Dial, answered all my questions related to SESE and ASU policies/deadlines to ensure that I didn't overlook any requirement, however small. Many thanks to Chris Skiba and the ASU Machine Shop for helping me plan, construct, and manufacture experimental containers, as well as Peter Gougen, Laboratory Manager for the Engineering Department, who set me up with a quiet laboratory space and provided me the use of equipment from his department including the large vertical shaker.

I have immeasurable gratitude to the staff at ASU Health Services, who kept me as well-tuned as possible, and so I thank in particular Patty Sherman, Elena Chrisman, Alexa Paredes, and Dr. Stefanie Schroeder for managing to keep me functioning despite my work-ethic's best intentions.

There's nothing quite like meeting dear friends around 5:30am almost every day while waiting for the campus gym to open. Barb, Rachelle, Jay, Katie, Carsten, and Joe, your expectation (shall I say "requirement"?) of my presence daily certainly kept me a bit saner. I'm so grateful that you bullied me, texted me, and cared enough to keep encouraging me not only in my academics but also in my pursuit of fitness. To my ASU yoga kula, I also give thanks; with your community guidance, I found balance on and off the mat.

I would like to thank my family. In particular, my parents, for unwavering support, telephone calls full of love and patience, and the occasional card or care package that always contained my dear friend Andrew (Jackson) to take out to dinner. My other parents, the Dread Pirates Aunt Omi and Uncle Jeff, who anchored me in treacherous waters with our twice-weekly phone calls deserve a hearty "Yo-ho!". My adopted

siblings, Kaydi, Caleb, Kiawa, and Sara B., who constantly checked-in and were there. Also, thanks to my dearest Sister the Younger, Sarah, who has, for the past five years, continued to motivate me with hilarious quips and cheerleading. I doubt that anyone else has had a younger sister proclaim to the world via social media that "...my sister is cooler than your sister. She's a planetary geologist. WHAT. Bet your sister can't count craters. BAM!" Sarah, you've been in China for most of the crunch time having your Grand Adventure, so I'm not sure that I was able to sufficiently repay the favor of having you edit my dissertation as I approached the finish line. Maybe someday you'll read this tome without falling asleep.

Last, but very importantly, I must acknowledge my other half, Jack. We've been separated by nearly 2300 miles for more than five years now, and I'm not quite sure how we've managed. I suppose I have his patience and perseverance to thank, in addition to (relatively) low airfares with Southwest Airlines. Also, free cell phone minutes and texts. I know that I've driven him crazy quite a few times over the years (probably more times recently…) but even so, he never complained (at least not to me). Without you, Jack, I am less. To the Moon, sweetheart!

TABLE OF CONTENTS

Page

CHAPTER Page

CHAPTER Page

CHAPTER Page

APPENDIX Page

LIST OF TABLES

LIST OF FIGURES

Figure Page

Figure Page

Figure Page

Figure Page

CHAPTER 1

INTRODUCTION

Impact cratering is one of four dominant geologic surface processes that occurs throughout the Solar System (including volcanism, tectonism, and gradation, Figure 1.1; Greeley, 1994). Airless terrestrial objects such as the Moon and Mercury (Figure 1.2) provide excellent test sites to investigate the surface modification and products resulting from the impact cratering process. Unlike craters on Earth, impact craters on the Moon and Mercury are not affected by plate tectonics (although tectonic activity may modify the final crater form, Figure 1.3), interactions with water (either during impact or subsequent crater modification), or aeolian erosion (which also strongly affects crater morphologies on Mars). Thus, investigating the morphology and characteristics of lunar and mercurian impact craters provides unique insight into the impact cratering process. Learning about the geologic processes and history of one planet enables increased understanding and comparison to other planets, and comparative planetology focused on impact cratering provides a means to address key science questions related to terrestrial planetary evolution. The Moon and Mercury are two of the most accessible planets for impact cratering investigations, because new high-resolution data allow specific observations to be made to test existing hypotheses and to make significant progress toward answering basic questions related to the evolution of the terrestrial planets over geologic time.

Requested by NASA, scientifically important concepts and questions pertaining to planetary geoscience are presented in documents prepared by the Space Studies Board of the National Research Council (NRC). These documents are intended to serve as

roadmaps for future scientific research and exploration, relying on input from the planetary science community who are best prepared to discuss and identify outstanding hypotheses related to the workings of the Solar System and planetary processes through time. *The Scientific Context for Exploration of the Moon* (SCEM) (2007; hereafter "NRC, 2007") lists fundamental concepts related to lunar science in addition to testable science hypotheses to support the Vision for Space Exploration (NASA, 2004). The work presented in this dissertation addresses key aspects of the SCEM Science Goals identified for the following SCEM Science Concepts: (1) The Moon reveals the inner Solar System bombardment history (Science Concept 1), (2) The Moon is ideal for investigating the impact process at the planetary scale (Science Concept 6), and (3) The Moon is ideal for investigations of regolith processes (Science Concept 7) (NRC, 2007). Similarly, the recent Planetary Decadal Survey (2011; hereafter "NRC, 2011") provides recommendations to NASA that address crucial science objectives for the 2013–2022 decade, and a crosscutting theme focuses on the workings of solar systems, specifically "revealing planetary processes through time" (NRC, 2011, p. 69). An important question identified is: "What are the major surface features and modification processes on each of the inner planets?" (NRC, 2011, p. 117). The significance of better understanding the planetary impact record and impact fluxes is also emphasized as essential science to pursue in the next decade, because examining the impact history of the terrestrial planets and icy satellites is dependent on the lunar chronology (NRC, 2011). The research presented here contributes to questions raised in the Planetary Decadal Survey (2011) by using measured crater frequencies to better understand the lunar and mercurian impact records and observations of impact cratering products (i.e., impact melt) to gain insight

into the impact cratering process. I also investigate the history of volcanic emplacement using crater size-frequency measurements for specific regions on the Moon and Mercury to address the question: “What are the distribution and timescale of volcanism on the inner planets?” (NRC, 2011, p. 117).

In **Chapter 2** of this dissertation I examine the effects of different illumination conditions on crater identification and provide a description of the techniques used to analyze measured crater frequencies and derive absolute model ages. Previous studies (Soderblom, 1972; Young, 1975; Wilcox et al., 2005) determined that consistent identification of craters is affected by incidence angle and fewer craters are visible in images with smaller incidence angles. Therefore, identification of craters in images taken at small incidence angles may affect identification of the small crater population (<1 km in diameter) and subsequent crater size-frequency analyses. Accurate small crater measurements are crucial to investigations pertaining to determination of recent lunar cratering rates and determination of absolute model ages (e.g., Neukum et al., 1975; Schultz et al., 1977; Neukum, 1983; Hiesinger et al., 2012) as well as estimations of regolith depths (Quaide and Oberbeck, 1968; Shoemaker et al., 1969; Wilcox et al., 2005). Utilizing Apollo Metric and Lunar Reconnaissance Orbiter Narrow Angle Camera (LROC NAC) images taken at different incidence angles, I estimate the equilibrium crater diameter for a region in Mare Imbrium and at the Apollo 11 Landing Site and derive absolute model ages that are consistent with published ages (Hiesinger et al., 2000; Hiesinger et al., 2003). Absolute model ages derived from crater counts (>700 m diameter) on LROC Wide Angle Camera (WAC) mosaics for western Mare Serenitatis confirm that more craters are identified at larger incidence angles. This chapter furthers

the SCEM Science Goal 1c, “Establish a precise absolute chronology” (NRC, 2007), by determining an optimal incidence angle range of ~65°–80° to use when completing crater counts for relative and absolute age dating. SCEM Science Goal 1d, “Assess the recent impact flux” (NRC, 2007), is also addressed by confirming that Mare Imbrium, Mare Tranquillitatis, and Mare Serenitatis are too old (~3.5–3.6 Ga) to use to investigate the <3 Ga impact flux.

In **Chapter 3 and Chapter 4**, areal crater density (ACD) analysis is used as a novel approach to identify resurfacing boundaries in lunar and mercurian volcanic smooth plains. ACD analysis provides a reliable technique to distinguish relative ages among geologic units when spectral information is not available or units do not exhibit spectral contrasts. These chapters address questions posed in the Planetary Decadal Survey (2011) related to the impact record and timing of volcanic emplacement for the Moon and Mercury.

In **Chapter 3**, the ACD methodology is developed and tested in Mare Imbrium using crater counts on LROC WAC mosaics, where previously reported age units defined with multispectral data (Hiesinger et al., 2000; Bugiolacchi and Guest, 2008) are distinguished for age contrasts >300–500 million years and spatial extents $>1 \times 10^4$ km^2. Non-obvious secondary craters are identified in ACD maps with diameters between 500 m and ~850 m and comprise a significant portion of the crater population, further supporting the use of craters ≥1 km in diameter for absolute model age determination in agreement with e.g., Neukum et al., 1975a; Neukum, 1983; McEwen and Bierhaus, 2006 and in support of Science Goal 1c (NRC, 2007). ACD measurements in Mare Imbrium

enable discussion of SCEM Science Goal 1e, “Study the role of secondary impact craters on crater counts” (NRC, 2007).

In **Chapter 4**, I test hypotheses concerning the timing of smooth plains emplacement for the northern smooth plains (NSP) on Mercury with measured crater frequencies and ACD measurements. Using newly acquired orbital image data from the MErcury Surface, Space ENvironment, GEochemistry, and Ranging (MESSENGER) spacecraft, I define the local stratigraphy for the northern polar region of Mercury, complementing previous studies for other regions (e.g., Trask, 1975; Strom, 1977; Spudis and Guest, 1988; Strom and Neukum, 1988; Strom et al., 2008, 2011; Fassett et al., 2009; Denevi et al., 2013a), to provide insight into the global stratigraphic record and the relative ages of key geologic units on Mercury. Crater size-frequency and ACD analyses reveal evidence for multiple resurfacing of the NSP over a short geologic timescale, and stratigraphic relations among buried craters demonstrate that at least two periods of volcanic modification occurred prior to the formation of the post-plains crater population. From buried crater rim height estimates, the minimum regional NSP volume is between 4.08×10^6 km^3 and 9.84×10^6 km^3. The results presented add to the understanding of the volcanic history of Mercury by comparing the relative ages of the NSP to the volcanic smooth plains located elsewhere (Spudis and Guest, 1988; Strom and Neukum, 1988; Strom et al., 2008; Fassett et al., 2009; Denevi et al., 2013a). Thus, this chapter provides new information related to the impact record and volcanic history of Mercury (NRC, 2011).

Chapter 5 diverges from observations of natural impact processes to investigate the mechanical sorting of an analog lunar regolith that results from seismic shaking in a

controlled laboratory setting. Seismic shaking induced by nearby impacts, ejecta emplacement, or shallow moonquakes may explain discrepancies between remotely sensed compositional datasets. Ilmenite is a titanium-rich mineral abundant in some returned lunar samples (e.g., Heiken, 1975; Papike et al., 1982), and titanium abundance estimates derived from Clementine UV-VIS spectral reflectance (CSR) and Lunar Prospector Gamma Ray Spectrometer (LP GRS) orbital measurements for the nearside maria do not match everywhere (e.g., Prettyman et al., 2006). Using an experimental bimodal mixture of different bulk densities to simulate a physical regolith subjected to vertical and horizontal shaking vibrations, I find that denser ilmenite particles sink into a less-dense matrix regardless of the size contrast between ilmenite and the matrix particles. These results imply that mechanical sorting due to seismic shaking is a possible explanation for some regions on the Moon where titanium abundance estimates differ between CSR and LP GRS. These findings further support SCEM Science Concept 7 (NRC, 2007), which focuses on better understanding regolith processes and the lunar environment, in addition to exploring a potential modification process to the lunar surface (Schultz and Gault, 1975; NRC, 2011).

Using new global datasets obtained by LROC and MESSENGER, **Chapter 6** investigates the occurrence and distribution of impact melt within lunar and mercurian impact craters. For Mercury (11.6×10^6 km^2 area) and the Moon (8.8×10^6 km^2 area), I identified craters ≥8 km in diameter with ponded impact melt deposits, mapped the extent of those interior deposits, and calculated melt pond area to use as an approximation for melt pond volume. Both the Moon and Mercury show the expected increase in melt deposit area with increasing crater diameter. For craters ≥30 km in diameter, mercurian

craters contain larger areal extents of interior ponded impact melt than their lunar counterparts, which is consistent with models that predict more impact melt in mercurian craters than similarly-sized lunar craters (e.g., Gault et al., 1975; Grieve and Cintala, 1997; Pierazzo et al., 1997; Cintala and Grieve, 1998a; 1998b). My results improve understanding of the impact process (NRC, 2011) through comparative planetology, in addition to indirectly relating to SCEM Science Goal 6c, "Quantify the effects of planetary characteristics…on crater formation and morphology" (NRC, 2007).

Chapter 7 summarizes the results of this dissertation and presents possible opportunities for future work.

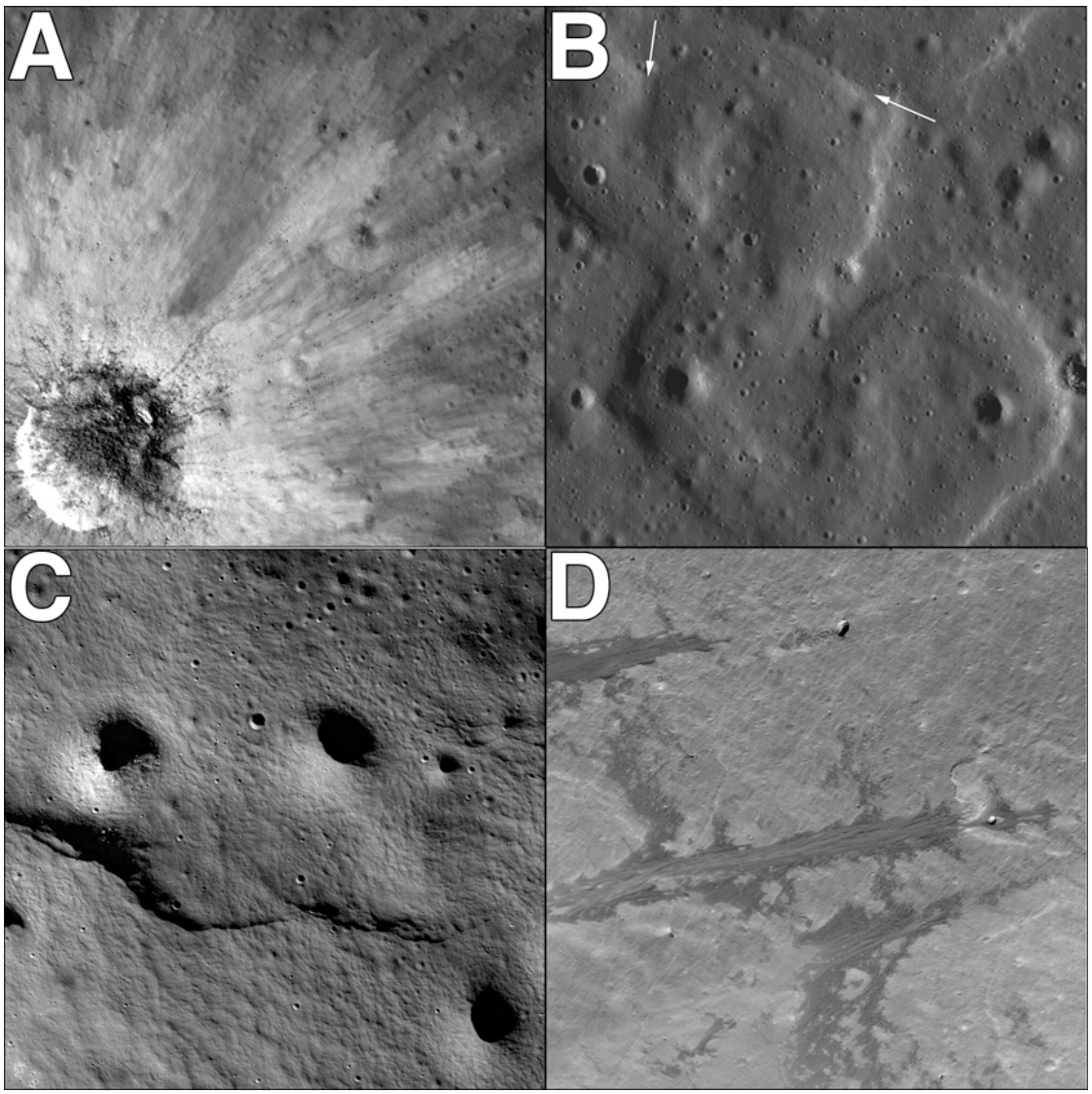

Figure 1.1. Lunar examples of the four primary geologic surface processes occurring on terrestrial planets. (A) Impact cratering; ~270 m diameter crater on the farside (25.88°S, 136.08°E), LROC NAC M159059694R, image width 855 m. (B) Volcanism; a sinuous rille located on the floor of Ulugh Beigh A crater exhibits oxbow bends (white arrows; 33.85°N, 81.05°E), LROC NAC M102672335L, image width 1.56 km. (C) Tectonism; a lobate scarp (thrust fault) formed in the wall material of Schrödinger basin (79.30°S, 126.50°E), LROC NAC M159099396R, image width 1.1 km. (D) Gradation; a granular debris flow on the wall of Stevinus A crater (8 km diameter, 31.75°S, 51.55°E, downhill to the right), LROC NAC M154893929R, image is 500 m across. Images courtesy of NASA/GSFC/Arizona State University and used in LROC Featured Images (www.lroc.sese.asu.edu) written by the author (Appendix A).

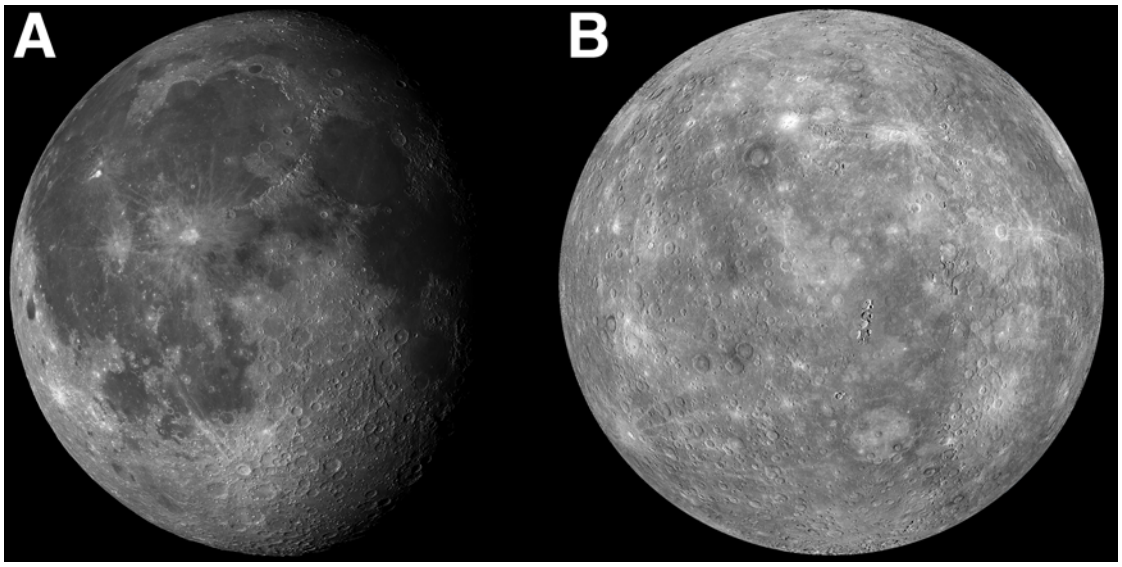

Figure 1.2. (A) Nearside LROC WAC 643 nm normalized reflectance map of the Moon (centered 0°N, 0°E), with natural shading added using the WAC Digital Terrain Model; lunar radius ~1737 km. Image credit: NASA/GSFC/Arizona State University.
(B) Hemispherical monochrome mosaic (749 nm) of Mercury imaged by MESSENGER (centered 0°N, 75°E, Rembrandt basin in lower right and Caloris basin at upper right on the eastern limb); mercurian radius ~2440 km. Image credit: NASA/Johns Hopkins University Applied Physics Laboratory/Carnegie Institute of Washington.

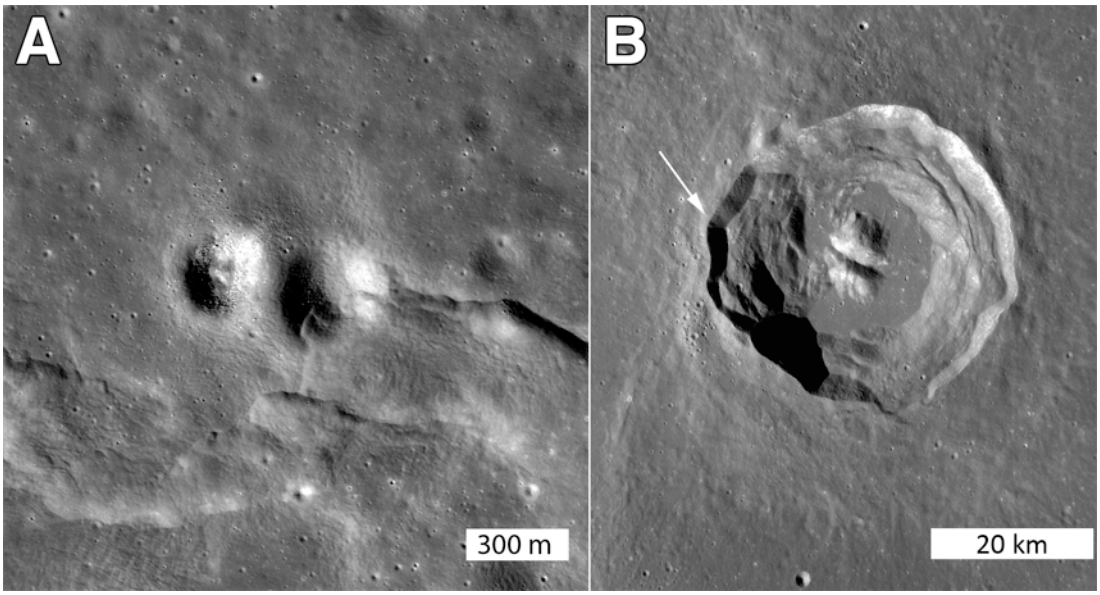

Figure 1.3. Tectonic modifications to craters. (A) A wrinkle ridge cross-cuts and deforms an ~330 m diameter impact crater in Mare Imbrium (44.41°N, 357.19°E), LROC NAC M104540211R, image width is 1.7 km. (B) Bürg crater (41 km diameter, located at 45.07°N, 28.21°E) is a complex crater with terraced walls that formed post-impact as a result of fracturing and faulting of the target rock, LROC WAC monochrome mosaic. Image credit: NASA/GSFC/Arizona State University; images used in LROC Featured Images written by the author (Appendix A).

CHAPTER 2

EFFECTS OF INCIDENCE ANGLE ON RELATIVE AND ABSOLUTE AGE DATING

2.1. Introduction

Solar incidence angle (measured from the surface normal, noontime is 0°; Figure 2.1) affects consistent identification and measurement of craters on a planetary surface (Moore, 1972; Soderblom, 1972; Young, 1975; Wilcox et al., 2005). In smaller incidence angle images morphologic details are diminished and thus craters are difficult to identify and measure, particularly for smaller (<1 km diameter) craters and even more so for degraded craters with shallower slopes (Wilcox et al., 2005). At larger incidence angles, subtle topography is enhanced and shadowing of the surface can remove small craters from the observed distribution (Moore, 1972; Soderblom, 1972; Wilcox et al., 2005). Accurate small crater population statistics are necessary in determination of relative and absolute model ages (AMAs) of younger units (e.g., Neukum et al., 1975a; Schultz et al., 1977; Neukum, 1983; Hiesinger et al., 2012) as well as estimations of regolith depths (Quaide and Oberbeck, 1968; Shoemaker et al., 1969; Wilcox et al., 2005).

Determining the equilibrium crater diameter is also useful for estimating the depth of the lunar regolith; crater density should relate to regolith thickness. The equilibrium diameter represents the steady-state between the formation of new craters and the removal of older craters (Shoemaker et al., 1969; Gault, 1970; Soderblom, 1970), and the maximum average regolith thickness for an area is equal to the initial depth of the equilibrium crater diameter minus the rim height (e.g., Shoemaker et al., 1969). Using higher resolution image data, Wilcox et al. (2005) investigated previous hypotheses that

the number of craters identified in an image is dependent on the incidence angle and that more craters would be detected at larger incidence (Soderblom, 1972; Young, 1975). Using scanned Lunar Orbiter and Apollo Metric images for three different mare regions (AMAs agreed within uncertainty) imaged at different incidence angles, Wilcox et al. (2005) showed that fewer craters were visible at smaller incidence angles and proposed that illumination influences equilibrium diameter estimates of the counted crater population. Oberbeck (2008) disputed this finding, that an equilibrium crater population was observed by Wilcox et al. (2005), and suggested that a sharp kink, as opposed to a gradual rollover, in the cumulative size-frequency distribution (SFD) is necessary to define the equilibrium crater population.

The Lunar Reconnaissance Orbiter Narrow Angle Camera (LROC NAC) and Wide Angle Camera (WAC) images, in addition to scanned Apollo Metric images, provide the necessary data to follow up on these earlier studies and more accurately examine the effects of incidence angle on crater measurements. Using Apollo Metric images of the same area taken at different incidence angles, crater SFDs for a region in Mare Imbrium are measured to identify the equilibrium crater population and estimate equilibrium crater diameter (if equilibrium is observed). LROC NAC images of the Apollo 11 Landing Site taken at different incidence angles are also used to measure crater SFDs, which extend to diameters smaller than those measured in Apollo Metric images. Furthermore, crater SFDs are measured in Mare Serenitatis using LROC WAC mosaics to characterize differences in crater distribution resulting from illumination at larger diameters (>500 m to several km).

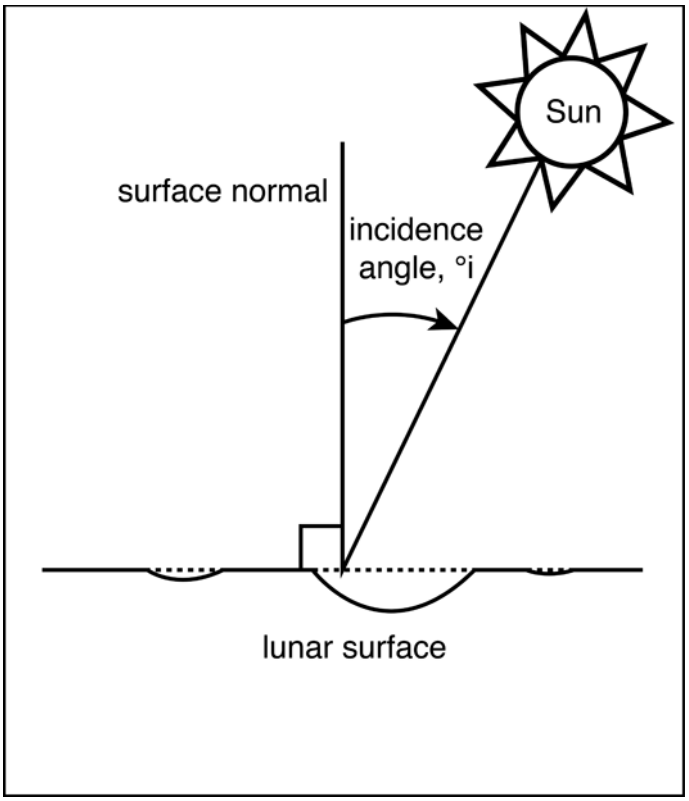

Figure 2.1. Cartoon sketch illustrating the measurement of solar incidence angle as defined in this work. Incidence angle is measured from the surface normal of the spheroid, where noontime is 0° incidence.

2.2. Background

Determining relative and absolute model ages for planetary surfaces relies on observed superposition relationships (to define geologic units) and on measurements of crater SFDs. Superposition relationships observed around the Copernicus crater region were used to derive a global stratigraphic time scale for the Moon (Shoemaker, 1962; Shoemaker and Hackman, 1962), and subsequent mapping using this time scale indicated that the mare materials were formed during the Imbrian and Eratosthenian systems (e.g., Wilhelms, 1987 and references therein). Therefore, SFD analysis is the primary technique used to distinguish relative ages for different mare units (frequently determined on the

basis of multispectral differences, e.g., Schaber, 1973; Charette et al., 1974; Johnson et al., 1977; Pieters, 1978; Hiesinger et al., 2000; 2003; 2010), and the measured crater frequencies are then translated into absolute age estimates (Section 2.3.3).

Discussions of crater diameter measurements involve terminology that is sometimes ambiguous because different terms have been adopted to explain similar aspects of crater SFDs. Hartmann et al. (1981) and Melosh (1989) provide in-depth discussions of vocabulary often used by planetary scientists, and to limit confusion the following terms used throughout this chapter are defined:

- *Primary impact crater:* A crater formed by impact of a meteoroid on the planetary surface. Also referred to as a "primary crater" or "primary".
- *Secondary impact crater:* A crater formed from the impact of ejected material resulting from a primary impact. Referred to as "secondary crater" or "secondaries". Secondary craters usually are categorized as "obvious" or "non-obvious", and obvious secondaries form in connected crater chains, herringbone patterns, or overlapping clusters of craters, and these morphologies may help determine the parent primary crater (e.g., Shoemaker, 1962; Oberbeck and Morrison, 1973). Non-obvious secondaries are not easily distinguished from the primary crater population and frequently form many kilometers from their parent primary (e.g., Wilhelms, 1976a; Wilhelms et al., 1978; McEwen and Bierhaus, 2006).
- *Production function:* The theoretical crater SFD resulting from all primary impacts over time in the absence of erosion (e.g., volcanic embayment, ejecta emplacement). Measured (real) crater SFDs will reflect the effects of erosion on the production population for a planetary surface. The production function is used to determine absolute model ages of a surface (Section 2.3.3). In the cumulative SFD

plot (Section 2.3.2), the production function slope can range between -1.8 to -4 depending on the diameter range (e.g., Baldwin, 1964; Trask, 1966; Baldwin, 1969; Shoemaker et al., 1969; Soderblom, 1970; Baldwin, 1971; Neukum et al., 1975a) but is usually between -3.3 and -4.0 for diameters <1 km (Soderblom, 1970).

- *Equilibrium or equilibrium distribution:* The crater density reflecting the maximum number of craters possible on the surface such that for each new crater formed, an older crater is destroyed (e.g., Trask, 1966; Gault, 1970). Equilibrium conditions reflect between 1% and 10% of the theoretical saturation conditions (Gault, 1970), and are mathematically represented by the discrete equation

$$N(D)=10^{-1.1}D^{-2} \qquad \text{(Equation 2.1)}$$

  where N(D) is the cumulative number of craters greater than or equal to a given diameter per km^2 and *D* is the diameter in km (Trask, 1966). In the cumulative SFD plot (Section 2.3.2), the equilibrium slope is usually -2 for diameters <300–500 m (e.g., Trask, 1966; Soderblom, 1970). AMAs cannot be determined from an equilibrium distribution. Also referred to as "steady-state" or "equilibrium function".
- *Saturation:* Theoretical maximum number of craters that can be hexagonally packed, so that the surface area covered by craters is 90.5% of the total area studied (Gault, 1970). Alternative terms such as "geometric saturation", "cookie-cutter saturation", and "empirical saturation" (e.g., Woronow, 1977; Hartmann et al., 1981; Hartmann, 1984; Melosh, 1989; Richardson, 2009) reflect adaptations to Gault's (1970) original definition and are not used here.
- *Equilibrium crater diameter (D_{eq}):* The diameter at which the cumulative SFD transitions from production to equilibrium for a surface (Gault, 1970; Soderblom, 1970; Schultz et al., 1977). For smaller craters (<1 km diameter), the cumulative SFD deviates from a slope of about -3.4 (production) to -2 (equilibrium) (Trask, 1966;

Soderblom, 1970), and for the maria, D_{eq} is ~150–250 m (e.g., Shoemaker et al., 1969; Soderblom, 1970; Soderblom and Lebofsky, 1972; Young, 1975; Schultz et al., 1977; Wilcox et al., 2005). Equilibrium crater diameter estimates can be employed to determine regolith depth (Shoemaker et al., 1969; Gault, 1970; Soderblom, 1970; Wilcox et al., 2005).

A key principle of crater SFD analysis is that impact cratering is a random process and that the accumulation of craters over time for a given surface reflects the age of that surface (e.g., Neukum et al., 1975a; McGill, 1977; Hartmann et al., 1981; Neukum, 1983; Neukum and Ivanov, 1994). However, relative and absolute model ages derived from crater SFDs are sensitive to several factors. The region in question should be comprised of an area of uniform age, which is assumed to consist of one geologic unit (e.g., Neukum et al., 1975a; 1975b; McGill, 1977; Hartmann et al., 1981; Neukum, 1983; Neukum and Ivanov, 1994). Only primary impact craters should be considered for the measurement region; volcanically embayed or partially flooded craters, in addition to obvious secondary craters and volcanic craters, should be ignored and removed from the measurement region and crater statistics when possible (e.g., Neukum et al., 1975a; Hartmann et al., 1981; Neukum, 1983). However, isolated secondaries occurring at great distances from their parent primary are difficult (if not impossible) to discern from primary craters (e.g., McEwen et al., 2005; McEwen and Bierhaus, 2006; Dundas and McEwen, 2007; also discussed in **Chapter 3**), but their presence in crater counts is argued to have a negligible effect on the SFD measurements (Neukum et al., 1975a; Werner et al., 2009). In an attempt to reduce uncertainty in measuring crater diameters, particularly between different individuals, a set of crater counting techniques were

codified by Greeley and Gault (1970), Neukum et al. (1975a), König (1977), Hartmann et al. (1981), Neukum (1983), and Neukum and Ivanov (1994) (Section 2.3.1). Furthermore, for the study areas in Mare Imbrium, Mare Serenitatis, and Mare Tranquillitatis, potential uncertainties in measurements of crater size due to target differences (e.g., Schultz et al., 1977; van der Bogert et al., 2010) are unlikely because only lunar basalts were studied, and it is reasonable to assume that the study regions have similar physical properties (e.g., well-developed regolith lacking the competency of bedrock or recent impact melts).

There is continuing debate whether equilibrium conditions are observed on planetary surfaces, particularly for the old, heavily cratered terrains (e.g., Marcus, 1970; Woronow, 1977; Hartmann, 1984; Chapman and McKinnon, 1986; Neukum and Ivanov, 1994; Richardson, 2009). For studies of the maria, which focus primarily on craters ≤4 km in diameter, there is agreement among workers that the small craters reach equilibrium near diameters of 100–300 m (e.g., Trask, 1966; Gault, 1970; Marcus, 1970; Soderblom, 1970; 1972; Young, 1975; Schultz et al., 1977; Hartmann, 1984; Wilcox et al., 2005; Richardson, 2009). Theoretical and schematic cumulative SFD plots that frequently illustrate the transition from production to equilibrium as a distinct inflection point or kink (Figure 11 in Gault, 1970; Figure 10.5 in Melosh, 1989) in the cumulative SFD slope, where the kink equals the equilibrium crater diameter. Nonetheless, in practice the transition to equilibrium is not necessarily described by a sharp kink and instead is sometimes observed as a gradual rolling over of the cumulative SFD as the production function transitions to the equilibrium (e.g., Trask, 1966; Shoemaker et al., 1969; Gault, 1970; Young, 1975; Melosh, 1989; Wilcox et al., 2005).

Wilcox et al. (2005) observed a gradual rollover in cumulative SFDs measured on Lunar Orbiter and Apollo Metric images (resolutions ranging from 6.4–9 meter pixel scale), results that were called into question by Oberbeck (2008). Oberbeck (2008) argued that Wilcox et al. (2005) did not demonstrate the presence of an equilibrium population and thus that the equilibrium crater diameter estimates were not valid, referencing Melosh's (1989) explanation for determining the presence of an equilibrium distribution and the equilibrium crater diameter. However, Oberbeck's assertion is based on a misinterpretation of Melosh's explanation, which states: "The inflection point between these two curves is at diameter $D_e(1)$ where the production curve crosses the equilibrium line" (Melosh, 1989, p.194), and the description that follows refers to idealized illustrations (Figure 10.5, Melosh, 1989) in which a kink or inflection point is emphasized. Subsequently, Melosh (1989) refers to a cumulative SFD where measured crater data are plotted (adapted from Gault, 1970), and while there is a noticeable change in slope indicating the equilibrium crater diameter, the inflection is less of a kink and more of a gradual rollover similar to that observed by Wilcox et al. (2005). Therefore, Oberbeck (2008) may not have grounds to assert that the equilibrium population and related equilibrium crater diameter estimates identified by Wilcox et al. (2005) are incorrect.

Oberbeck (2008) attributes the gradual rollover in the cumulative SFDs to factors other than equilibrium, such as crater loss due to shadowing, effects of image resolution, missed craters during counting, or "certain types of geologic processes". Wilcox et al. (2005) discussed the effects of shadowing on crater identification, emphasizing that the large incidence angle image would promote hiding of smaller craters in shadow, but that

such a result would promote flattening of the cumulative SFD slope at the smallest diameters, first described by Soderblom (1972). Slope flattening at small diameters is observed in the cumulative SFDs only for those bins below a reasonable resolution threshold (5–7 pixels); slope fits are not computed for diameters <65 m, which is equal to the 7 pixel threshold multiplied by the coarsest resolution image (9 meter pixel scale) (Wilcox et al., 2005). Moreover, the individual performing the counts was trained in the technique of crater SFD measurements (Denevi, 2010, personal communication), so while it is possible that craters were missed during counting, it is unlikely that the number of craters missed comprised a statistically significant portion of the craters counted. Lastly, geological processes, such as ejecta emplacement and volcanic flooding, can affect the measured SFD (Neukum et al., 1975a). Resurfacing events may result in kinks observed in the cumulative SFD (e.g., Neukum and Horn, 1976), but such resurfacing effects are unlikely for this case because of the youth of the mare in which the study areas were selected (Hiesinger et al., 2003; Wilcox et al., 2005) as well as the location of the measurement area away from recent craters with ejecta blankets (Denevi, 2010, personal communication). Therefore, although Oberbeck (2008) presents valid alternative explanations to the gradual rollover in the cumulative SFD, crater loss due to these factors in the Wilcox et al. (2005) work will be minimal.

Finally, Oberbeck (2008) criticizes the method by which Wilcox et al. (2005) completed slope fits to the cumulative SFDs, declaring that the least squares fit method used to determine the break from a -3.4 to a -2 slope was invalid. This criticism is rooted in the argument that he interprets there is no equilibrium distribution present due to the gradual rollover in the cumulative SFD, in addition to the use of “as few as three data

points" used to determine the slope fits (Oberbeck, 2008). Since it is well established that the inflection between production and equilibrium can be poorly defined (e.g., Trask, 1966; Shoemaker et al., 1969; Gault, 1970; Young, 1975; Melosh, 1989; Wilcox et al., 2005) and the slope fitting procedure employed by Wilcox et al. (2005) is similar to the simple application of the cumulative SFD equilibrium function, Equation 2.1 (Trask, 1966), Oberbeck's (2008) argument is not substantiated.

The statement criticizing the use of few data points is valid; the method of binning data affects the presentation in the cumulative SFD and may influence subsequent analyses. Standard plotting techniques were suggested in 1978–1979 (Crater Analysis Techniques Working Group, 1979), when it became clear that the different methods of data binning and plotting were so varied that comparisons between published data were at times impossible (Trask, 1966; Gault, 1970; Greeley and Gault, 1970; Young, 1975; Neukum et al., 1975a; Hartmann et al., 1981 all use different binning methods). However, Wilcox et al. (2005) used the suggested standardized presentation method (cumulative SFD, root-2 binning with ±one standard deviation uncertainty), which limits the number of data points available for slope fits. By considering a larger count area to improve the statistics of the smallest craters (i.e., those with slopes that tend to flatten as a result of shadowing), further tests of the validity of these fits could be completed. Consequently, Oberbeck's (2008) invalidation of Wilcox et al.'s (2005) results is not well founded.

Here, I continue the investigation of the effects of incidence angle on crater identification and determination of equilibrium crater diameter (c.f., Young, 1975; Wilcox et al., 2005) by using Apollo Metric, LROC NAC, and LROC WAC images.

2.3. Technique

2.3.1. Crater Counts

Initially, crater rims were digitized in each image using an interactive monitor-cursor program written in IDL (http://www.exelisvis.com/ProductsServices/IDL.aspx) named “Circle” (P.C. Thomas and M.S. Robinson, unpublished). Circle fits a circle to three analyst-defined points on a crater rim, recording the crater center in pixel space (lines, samples) and calculating the crater radius, which are later converted to the appropriate geo-referenced center latitude, longitude, and crater diameter. Later, crater measurements for the Apollo 11 Landing Site in LROC NAC images were made using the CraterTools extension (Kneissl et al., 2011) for the ESRI ArcMap 10 geographical information system (GIS) program. The CraterTools program computes a best-fit circle to three analyst-defined points on a crater rim and records the center latitude, longitude, and diameter to a project database. Obvious secondary craters, identified by their occurrence in chains, herringbone patterns, or clustered groups, were excluded from the measurements and the areas containing obvious secondaries were excluded from the final count area.

Three individuals (A, L–the author, and S) were trained to complete crater counts and at least two individuals digitized each Apollo Metric image (over 17,500 craters total). Only one individual (L) digitized craters in the LROC NAC and WAC images (over 10,500 craters total). To limit false identification of craters and maintain consistency between individuals, all analysts were trained on the same portion of Apollo Metric image AS15-M-1010 (not the area used in this investigation), and count statistics are expected to vary by up to a factor of two between trained individuals (Greeley and

Gault, 1970; Robbins et al., 2013a; 2013b). A 7 pixel identification threshold was selected because craters 7 pixels and larger were confidently and consistently identified in images by all individuals. Only craters ≥7 pixels in diameter were used to derive crater statistics (e.g., cumulative SFD slopes, AMAs; Appendix B), but all craters identified are plotted to emphasize the differences in crater identification between individuals as the pixel threshold was approached. Individuals were not required to digitize the images in a particular manner beyond appropriate primary crater identification (e.g., circular depression versus circular positive-relief feature) and marking of the crater rim; that is, a systematic digitizing approach whereby the images were digitized along the length or width of the image was recommended but not required.

From these crater counts, crater frequencies are plotted in cumulative SFD plots (Crater Analysis Techniques Working Group, 1979; Section 2.3.2). Absolute model ages were derived using the CraterStats software (Michael and Neukum, 2010) by employing the Neukum et al. (2001a) chronology function to the data (Section 2.3.3). Crater equilibrium diameters were estimated by determining the diameter at which the production function and the equilibrium with a -2 slope intersect (method after Wilcox et al., 2005). To determine the production function, a least squares fitting routine was applied to the cumulative SFDs to determine the slope of the steeply sloped portion of the cumulative SFD (~-3.0 to -4.0; e.g., Trask, 1966; Shoemaker et al., 1969; Soderblom, 1970), usually for diameter bins between 100 m to 1 km. However, cumulative SFDs for smaller incidence angle images began to roll over at diameters <150 m in the Apollo Metric images and the LROC NAC images of the Apollo 11 Landing Site rolled over at diameters <170 m. To determine the equilibrium function, a least squares fitting routine

with a constant -2 slope (Trask, 1966) was applied to the less steeply sloped portion of the SFD; in some cases, the best fit was the standard equilibrium function (Trask, 1966; Gault, 1970).

Simple craters, <15–20 km in diameter, generally are bowl-shaped (e.g., Melosh, 1989), and relationships between crater depth and diameter were derived from Lunar Orbiter shadow-length measurements and topographic maps created from Apollo Metric images (e.g., Pike, 1974; 1976; 1977). In this investigation, maximum regolith depth was estimated using the depth to diameter ratio for simple craters, where maximum crater depth is 20% of the measured crater diameter (Pike, 1974). This estimate includes excavation and compression, so an approximation of average crater depth that incorporates crater shallowing and removal of rim height (above the original surface) was also made. For an idealized bowl-shaped crater with a depth/diameter ratio of 0.2, the average crater depth is 14% of the diameter (e.g., Pike, 1974; 1976; Wilcox et al., 2005).

2.3.2. Crater Data Presentation

Two methods are commonly used to present crater data; the cumulative SFD plot and the relative SFD plot (R-plot) (Crater Analysis Techniques Working Group, 1979). All of the measured crater data presented here are plotted as cumulative SFDs because AMAs and measures of production and equilibrium slopes are traditionally determined from the cumulative distribution (e.g., Trask, 1966; Gault, 1970; Greeley and Gault, 1970; Neukum et al., 1975a; 1975b; Neukum and König, 1976; Neukum and Ivanov, 1994; Hiesinger et al., 2000; Neukum et al., 2001a; Hiesinger et al., 2003; 2011). Derivation of the R-plot is presented in **Chapter 4**, where R-plots are used in analyses of the crater populations of the north polar region of Mercury. Both plots use double

logarithmic axes with the same scale and consistent units, and uncertainties estimating ±one standard deviation are calculated from the square root of the number of craters for a given bin (Crater Analysis Techniques Working Group, 1979). Crater counts are frequently binned, often using root-2 binning (e.g., Crater Analysis Techniques Working Group, 1979; Hartmann et al., 1981) or "pseudo-log" binning, where 18 bins per diameter decade are designated (e.g., for 1 km ≤ D ≤ 10 km, the bin steps are 1.0, 1.1, 1.2, 1.3, 1.4, 1.5, 1.7, 2.0, 2.5, 3.0, 3.5, 4.0, 4.5, 5.0, 6.0, 7.0, 8.0, 9.0, 10.0; e.g., Neukum et al., 1975a; König, 1977; Neukum, 1983; Hiesinger et al., 2000; Neukum et al., 2001a; Hiesinger et al., 2012). The small steps in pseudo-log binning reflect the observations that for a count region, there are significantly more small craters than large ones (e.g., Neukum et al., 1975a; Neukum, 1983; Neukum and Ivanov, 1994). A limitation to the cumulative SFD plot is that the cumulative number of craters at a given diameter depends on the number of craters at all larger diameters. Once the data are binned, the crater frequencies are plotted.

The cumulative SFD plot represents the cumulative distribution of the measured crater frequencies (Crater Analysis Techniques Working Group, 1979), reflecting the number of craters larger than or equal to a given diameter per measured area, usually 1 km^2 or 10^6 km^2. Measured crater frequencies between 4–100 km in diameter for a variety of locations including different mare regions, Apollo landing sites, ejecta blankets for young, large craters (e.g., Greeley and Gault, 1970; Neukum et al., 1975a; König, 1977; Neukum, 1983) and for diameters ≤1 km (e.g., Shoemaker, 1971) indicate that the cumulative distribution of craters approximates a power law function dependent on crater diameter,

$$N(D) \text{ or } N_{cum} = cD^{b} \qquad \text{(Equation 2.2)}$$

where N_{cum} (or N(D)) is the cumulative number of craters greater than or equal to a given diameter per unit area (usually 1 km^2), *D* is the diameter in km, *c* is a coefficient that varies depending on surface age, and *b*, sometimes called the slope index (Crater Analysis Techniques Working Group, 1979), is the slope of the crater diameter distribution (e.g., Neukum et al., 1975a; 1975b; Hartmann et al., 1981; Melosh, 1989). Least square fits to measured crater data indicate that at D <300 m, the crater population is approximated using *b* = -2; for 300 m < D < 4 km, the crater population is best fit with *b* = -3.4; and for D > 4 km, the crater population is approximated with *b* = -1.8 (Figure 2.2; e.g., Shoemaker et al., 1970; Shoemaker, 1971; Baldwin, 1971; Neukum et al., 1975a; Hartmann et al., 1981).

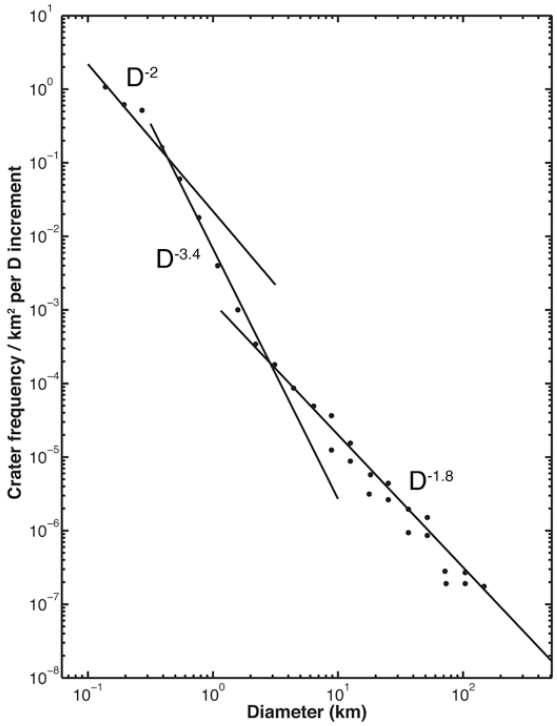

Figure 2.2. Cumulative SFD plot for average lunar mare. Three curves are fitted to the crater counts on the basis of observed trends over specific diameters and serve as the basis for the cumulative SFD power law (data from Hartmann et al., 1981, page 1114, plot 11; calculated uncertainties not plotted).

2.3.3. The Lunar Chronology Function

Analyses of crater frequencies are the primary means of determining time-stratigraphic relationships. Interpretation of geology is aided by an understanding of the relative ages of surface units derived from crater statistics, which can then be converted into absolute age estimates by application of a chronology function. From measured crater frequencies of maria and Apollo landing sites (e.g., Greeley and Gault, 1970; Shoemaker et al., 1970; Shoemaker, 1971; Neukum et al., 1975a; König, 1977) it was determined that one general cumulative SFD describes all crater populations (Neukum et al., 1975a; 1975b; Neukum and Ivanov, 1994). This complex continuous curve is called the lunar production function (e.g., Neukum, 1983; Neukum and Ivanov, 1994; Neukum et al., 2001a) and is represented by an 11^{th} order polynomial

$$\log(N(D)) = a_0 + \sum_{k=1}^{11} a_k (\log(D))^k \qquad \text{(Equation 2.3)}$$

where a_0 is the time that the unit has been exposed to meteorite bombardment (Neukum et al., 1975b; Neukum, 1983; Neukum and Ivanov, 1994; Neukum et al., 2001a). The work by Neukum et al. (2001a) provides the coefficients for the lunar production function, which is valid for crater diameters between 10 m and 100 km, and Neukum and Ivanov (1994) present a discussion of how the coefficients have changed through analyses of new crater measurements. The standard lunar production function thus allows comparisons of crater frequencies for different crater populations over different diameter ranges, providing a means to determine the relative ages of these geologic units. The relative age of a geologic unit is determined for a given reference diameter (usually 1 km, 10 km, or 20 km) and the cumulative crater density for a geologic unit is related to the exposure of the unit to meteorite bombardment. The measure of relative age is often

referred to as the "crater retention age" (Neukum, 1983), and older geologic units will have greater cumulative crater densities (greater crater retention ages) than younger ones.

For the Moon, samples of known provenance from the Apollo and Luna landing sites provide the ability to correlate the radiometric ages measured from returned samples to measured crater frequencies (e.g., Hartmann et al., 1981; Neukum, 1983; Neukum and Ivanov, 1994; Neukum et al., 2001a; Stöffler and Ryder, 2001). The empirical relationship of the correlation between radiometrically dated samples and crater frequencies at the landing sites allows the derivation of a lunar chronology function that estimates the crater production rate as a function of absolute age (Figure 2.3; e.g., Hartmann et al., 1981; Neukum, 1983). A least squares fit to the crater frequencies and radiometric ages is mathematically expressed as

$$N(D \geq 1\text{ km}) = 5.44 \times 10^{-14}\left[\exp(6.93 \times t) - 1\right] + 8.38 \times 10^{-4} t \qquad \text{(Equation 2.4)}$$

where $N(D \geq 1\text{ km})$ is the cumulative crater frequency for diameters ≥1 km per km^2 and t is the age, with units of 10^9 years (Neukum, 1983; Neukum and Ivanov, 1994; Neukum et al., 2001a). This mathematical fit assumes that the impactor population retained a constant size distribution, which may not be accurate (e.g., Neukum and Ivanov, 1994; Neukum et al., 2001; Marchi et al., 2009; Le Feuvre and Wieczorek, 2011). Nevertheless, by using Equation 2.4 and solving for t it is possible to derive absolute ages for any geologic unit on the lunar surface once the crater SFD is measured.

The lunar chronology represents an estimated distribution and, consequently, any absolute ages derived for measured crater distributions represent absolute *model* ages, and these AMAs assume that the cratering chronology does not include inherent uncertainty. For example, the range of radiometric ages exhibited by the returned samples

from each landing site (e.g., Hartmann et al., 1981; Stöffler and Ryder, 2001 and references therein) complicates the correlation of crater frequencies to radiometric ages. Neukum and coworkers (e.g., Neukum et al., 1975b; Neukum, 1983; Neukum and Ivanov, 1994; Neukum et al., 2001a) adopted the practice of correlating the crater SFDs with radiometric ages by using the mode of the radiometric age dates, arguing that the most frequently measured radiometric age probably reflects the major event responsible for "resetting" the radiometric clocks of the samples (discussed at length by Neukum and Ivanov, 1994). However, the nature of the chronology derivation is dependent on the current calibration (crater SFDs for the landing sites) and data (radiometric ages); the accuracy of absolute model ages determined for measured crater frequencies may be improved with subsequent iterations of the chronology (e.g., Marchi et al., 2009; Le Feuvre and Wieczorek, 2011; Robbins, 2013). While the lunar chronology (Neukum et al., 2001a) is well-defined for units >3 Ga (although Stöffler and Ryder (2001) recommend a new calibration for the ~4 to 3 Ga age range based on reexamination of the radiometric ages of returned samples), the chronology is less well-constrained for ages younger than 3 Ga due to the limited number of young units (<1 Ga) that were sampled and uncertainty in some cases of the provenance of the sample (i.e., Copernicus ejecta, sampled at the Apollo 12 landing site; e.g., Neukum, 1983; Stöffler and Ryder, 2001). The <1 Ga time frame is of particular interest because the absolute ages of the four young craters (Copernicus, Tycho, North Ray, and Cone) used as calibration points in the lunar chronology are critical in the derivation of AMAs for young unsampled materials across the whole Moon.

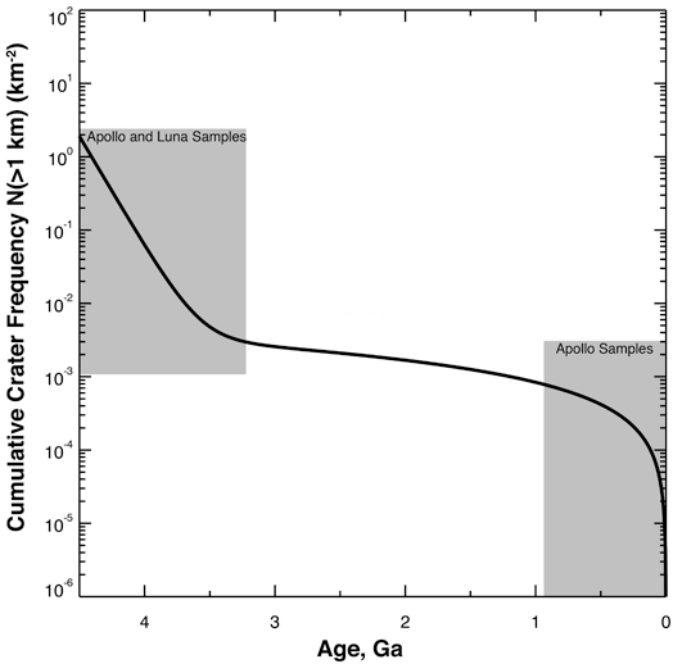

Figure 2.3. Graphical display of the lunar chronology curve for 4.5 Ga to the present. For ages older than ~3.2 Ga, multiple Apollo and Luna rock and regolith samples constrain the chronology. For ages younger than 3 Ga, but especially 1 Ga, the assigned ages are less well-constrained by samples.

2.4. Data

Tabulated cumulative crater SFD measurements for all regions and analysts are provided in Appendix B.

2.4.1. Mare Imbrium

Four Apollo Metric images of the same 100 km^2 study area with different incidence angles allow a detailed characterization of the effect of incidence angle on cumulative SFDs (Table 2.1). The study region was centered at 27.3°N, 341.8°E in Mare Imbrium east of Lambert crater (Figure 2.4), and images acquired at 87° (AS15-M-1010), 82° (AS15-M-1152), 71° (AS15-M-1835), and 50° (AS15-M-2461) incidence angles (Figure 2.5) were chosen for crater measurements. Lambert crater (25.77°N, 339.01E, ~30 km in diameter), located among young flows in southern Mare Imbrium (e.g.,

Schaber, 1973; Boyce and Dial, 1975; Hiesinger et al., 2000), provides a location to measure crater frequencies that is not contaminated by secondary craters. Pixel scales of the scanned Apollo Metric images varied between 6.6 and 7.6 meters, and the images were resampled to 10 meter pixel scale for the counts. A resolution threshold of 7 pixels, equivalent to 70 meters, was selected as the minimum crater diameter confidently measured in the Apollo Metric images.

To test if a gradual rollover in the cumulative SFDs is due to resolution effects or to the observation of the equilibrium crater population, craters were counted on a higher resolution LROC NAC image (56° incidence angle) covering a portion of the Apollo Metric count area (M104633604L, Figure 2.6). The NAC image was resampled to 2 meter pixel scale and an area 4 km^2 was selected for crater measurements. For the NAC image, the 7 pixel resolution threshold is equivalent to 14 meters.

Table 2.1. Image Data Used for Crater Size-Frequency Distribution Measurements.

Image	**Location**	**Pixel Scale (m)**	**Area (km^2)**	**Incidence Angle**
Apollo Metric				
AS15-M-1010	M. Imbrium	10	1E+02	87°
AS15-M-1152	M. Imbrium	10	1E+02	82°
AS15-M-1835	M. Imbrium	10	1E+02	71°
AS15-M-2461	M. Imbrium	10	1E+02	50°
LROC NAC				
M104633604L	M. Imbrium	2	2.00E+0	56°
M116161085R	Apollo 11	0.7	2.09E+0	82°
M150368601R	Apollo 11	0.7	2.17E+0	64°
LROC WAC Mosaics				
Boxes 1–3	M. Serenitatis	100	4.00E+02	66°
Boxes 1–3	M. Serenitatis	100	4.00E+02	46°
Western Region	M. Serenitatis	100	3.90E+04	66°
Western Region	M. Serenitatis	100	3.90E+04	46°

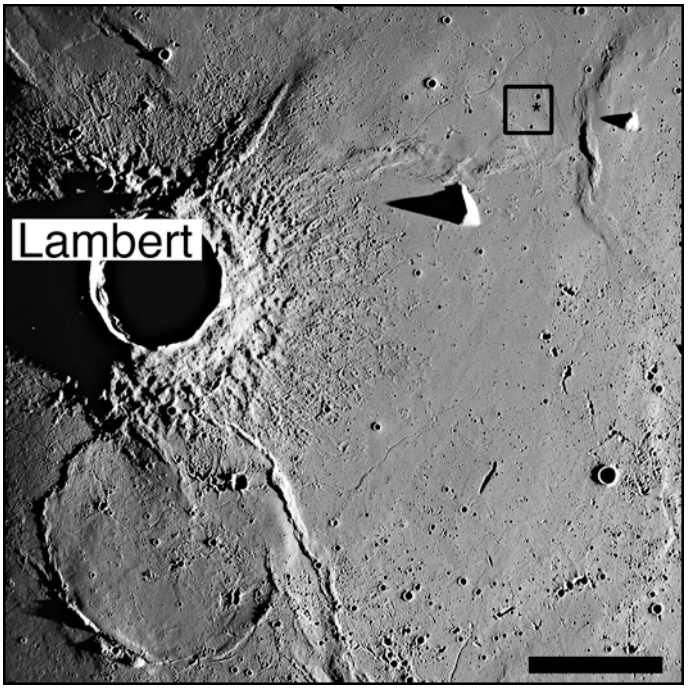

Figure 2.4. Context image for the Mare Imbrium count area. The black box contains the Apollo Metric count area, which is 100 km^2 and centered at 27.30°N, 341.80°E. The LROC NAC count area (asterisk, Figure 2.6) is also shown. Scale bar is 30 km; Apollo Image AS15-M-1010, 87° incidence angle. North is up and illumination is from the right.

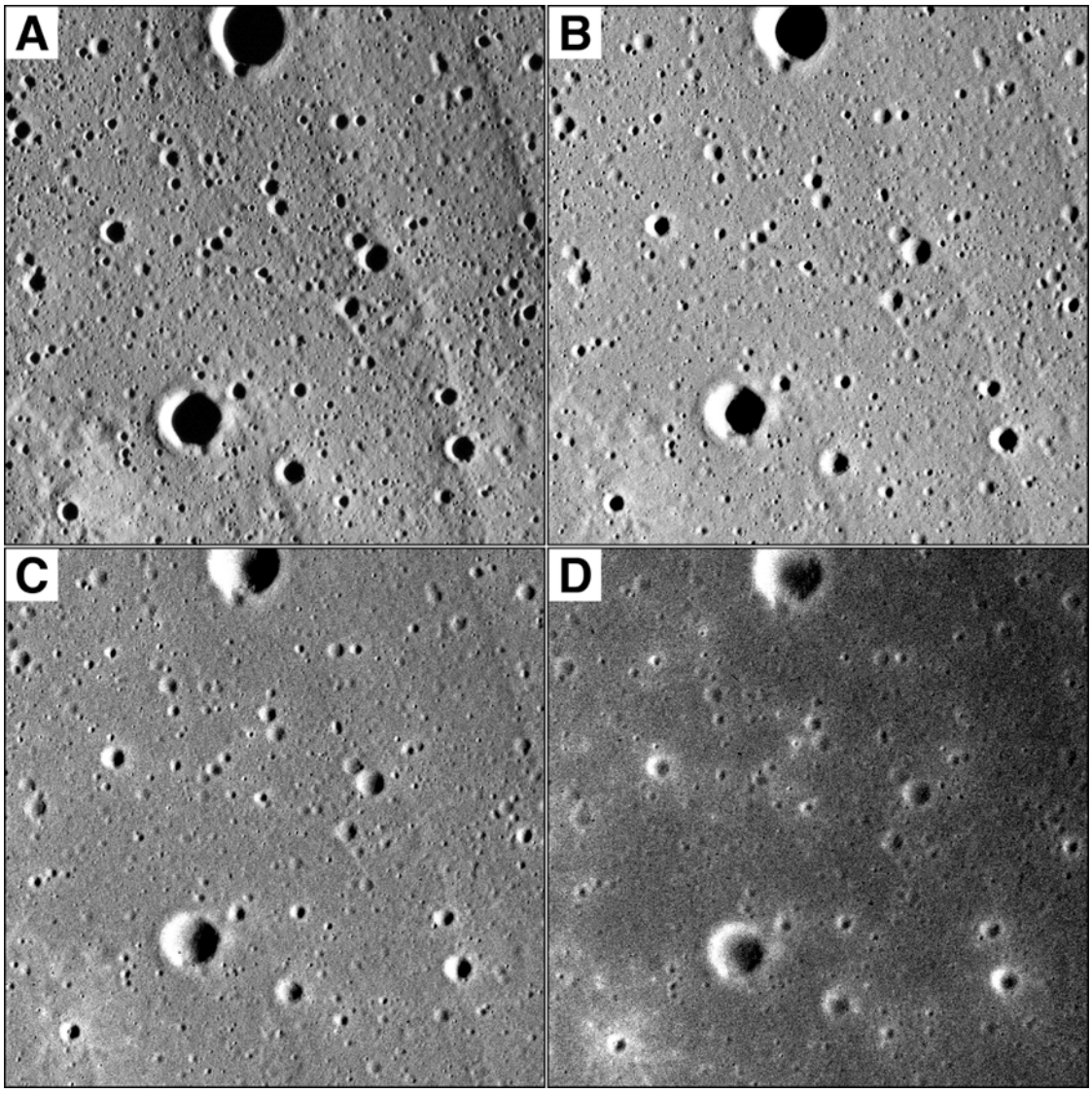

Figure 2.5. Views of the Mare Imbrium study area shown in Figure 2.4 at four different incidence angles. Width of each frame is 10 km^2. (A) Apollo Image AS15-M-1010, taken at 87° incidence angle, (B) Apollo Image AS15-M-1152, taken at 82° incidence angle, (C) Apollo Image AS15-M-1835, taken at 71° incidence angle, and (D) Apollo Image AS15-M-2461, taken at 50° incidence angle.

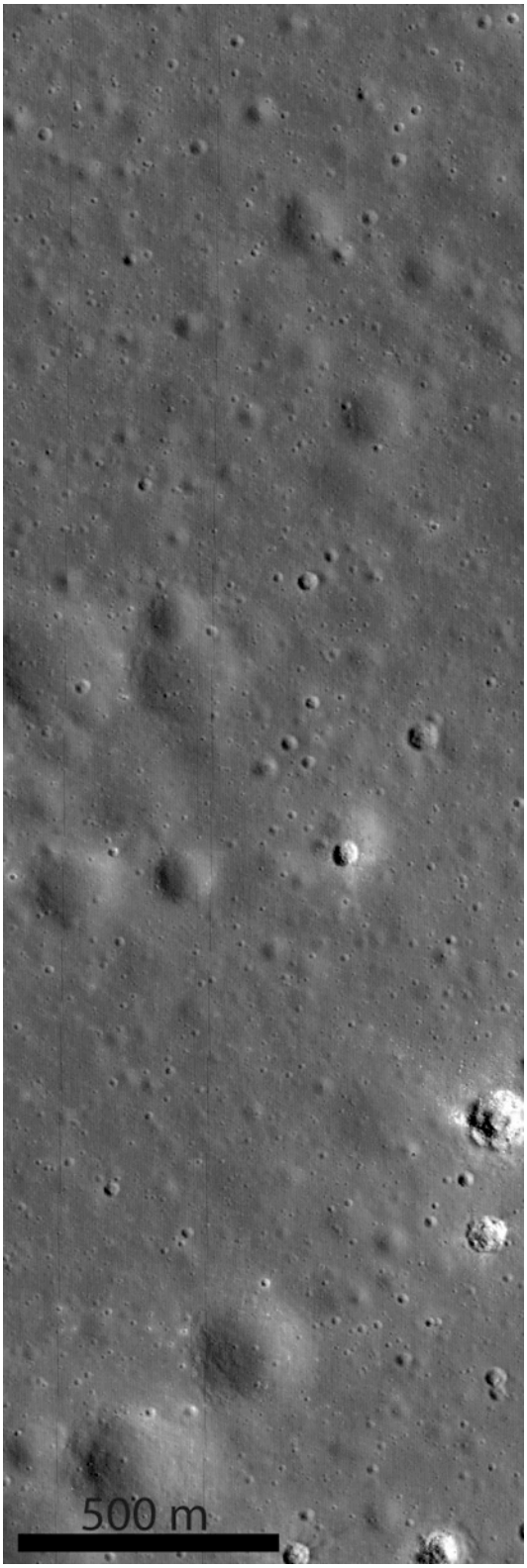

Figure 2.6. Subsection of LROC NAC M104633604L (centered at 27.32°N, 342.01°E), resampled to 2 meter pixel scale, for a 4 km^2 area within the original region studied in Apollo Metric Images (Figure 2.4). Incidence angle is 56°.

2.4.2. Apollo 11 Landing Site

The Apollo 11 Landing Site in Mare Tranquillitatis (0.67°N, 23.47°E) has repeat LROC NAC coverage at different illuminations (Table 2.1) allowing another test of the validity of the rollover observed by Wilcox et al. (2005). NAC images taken at 82° incidence angle (M116161085R) and 64° incidence angle (M150368601R) were selected and resampled to 0.7 meter pixel scale (Figure 2.7). A count area ~2 km^2 centered on the Lunar Module descent stage was selected for crater frequency measurements. The 7 pixel resolution threshold limits crater measurements to diameters ≥4.9 meters.

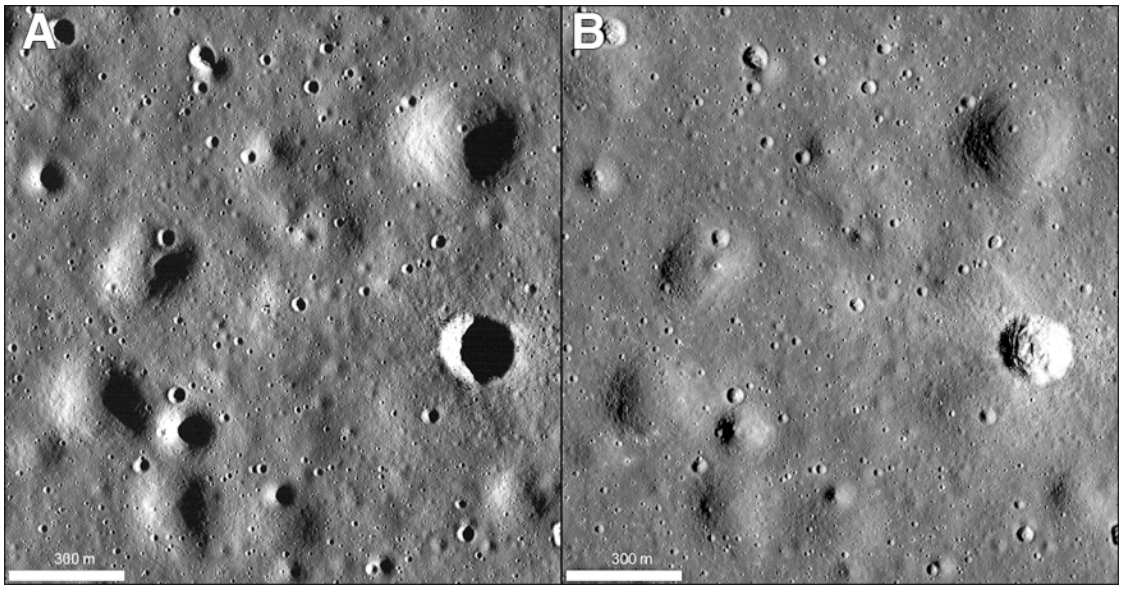

Figure 2.7. LROC NAC images of the Apollo 11 Landing Site, centered on the Lunar Module descent stage (0.67°N, 23.47°E), and resampled to 0.7 meter pixel scale. Fresh crater in the middle right is West crater (0.67°N, 23.49°E, 190 m diameter). (A) LROC NAC M116161085R, 82° incidence angle with illumination from the right. Shadowed regions inside the largest craters were removed from the count area. (B) LROC NAC M150368601R, 64° incidence angle with illumination from the left.

2.4.3. Mare Serenitatis

Regions in Mare Serenitatis were selected in 100 meter pixel scale LROC WAC normalized reflectance mosaics (Speyerer et al., 2011) with average incidence angles of 66° and 46° (Figure 2.8, Table 2.1) to characterize differences in crater distribution

resulting from illumination for larger diameter craters (>500 m to several km). Initially, three 400 km^2 areas of "average" mare (i.e., no large craters nearby, no obvious secondaries, visually similar in appearance) were chosen within western Mare Serenitatis on which to perform crater counts. Later, an area ~4×10^4 km^2 was selected that contained the three smaller count regions. Areas with obvious secondary craters were excluded from the measurements. The 7 pixel threshold limits crater identification in the LROC WAC mosaics to 700 meters.

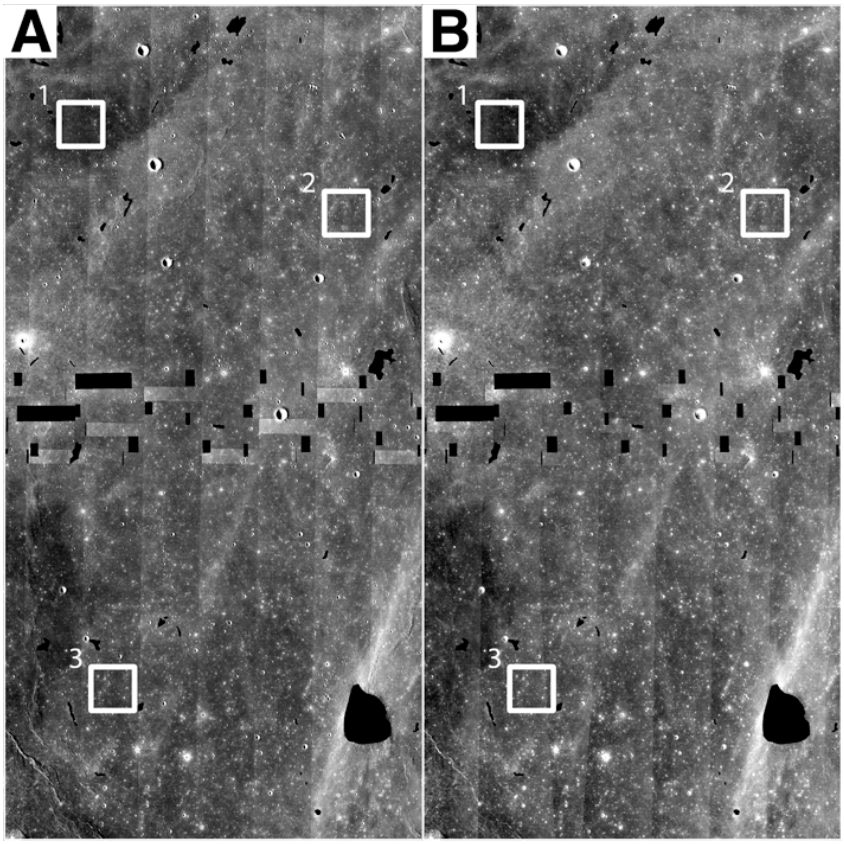

Figure 2.8. LROC WAC monochrome normalized reflectance mosaics of the western portion of Mare Serenitatis (centered at 27.21°N, 15.49°E), northwest of Bessel crater (masked by irregular black polygon in lower right corner) at 100 meter pixel scale. (A) LROC WAC mosaic with an average incidence angle of 66°, and (B) LROC WAC mosaic with an average incidence angle of 46°. Irregular polygons scattered throughout the mosaic are masked secondary craters, and their associated areas were removed from the total count area of ~4.0×10^4 km^2. White boxes labeled 1–3 are 20 km in width. Black rectangles in the center of (A) and (B) are gores in the LROC WAC mosaic from incomplete coverage.

2.5. Results

2.5.1. Mare Imbrium

A minimum of two individuals counted craters for the selected region in each Apollo Metric image. At 87° incidence angle (AS15-M-1010, Figure 2.5A) subtle changes in topography are visible, thus enhancing the shallow slopes and eroded rims of degraded craters. An example of the count area marked with digitized craters is shown in Figure 2.9. The cumulative SFDs between A and L are statistically inseparable at large diameters but deviate at diameters <~200 m (Figure 2.10A). Both SFDs cross the standard equilibrium line (10% saturation, Gault, 1970), and the equilibrium crater diameter estimates are ~190 m (analyst A), ~175 m (analyst L). Regolith depth estimates are 27–38 m (analyst A) and 24–35 (analyst L) (Table 2.2). AMA fits are 3.51 +0.03/-0.04 Ga for analyst A and 3.50 ±0.04 Ga for analyst L (Figure 2.11).

The 82° incidence angle cumulative SFD is similar between individuals A and L (Figure 2.10B). The SFDs are statistically indistinguishable at the larger diameters but separate around 100 m diameter. Overall, the cumulative crater frequencies are lower than in the 82° incidence angle image. An apparent equilibrium crater diameter of ~160 m (analyst A) and ~175 m (analyst L) is observed, and regolith depth estimates have a range of 22–32 m (analyst A) and 25–35 m (analyst L) (Table 2.2). The AMA fit is 3.48 +0.04/-0.05 Ga for analyst A and 3.53 +0.03/-0.04 Ga for analyst L (Figure 2.12).

The surface detail in the 71° incidence angle image is less than the 87° incidence and many of the shallowest craters are not readily visible (Figure 2.5C). Three individuals (A, L, and S) counted on the 71° incidence image. As before, the SFDs (Figure 2.10C) are statistically indistinguishable at the larger diameters (>~200 m), but

the counts for analysts A and L follow the standard equilibrium slope while the count by analyst S begins to gradually roll over around ~150 m diameter, separating from the trends exhibited by the SFDs measured by analysts A and L around 100–120 m in diameter. The overall cumulative crater frequencies measured are less for the 71° incidence angle image than for either the 82° or 87° incidence angle image. Estimates of apparent equilibrium diameters are ~150 m for analyst A, ~150 m for analyst L, and ~180 m for analyst S. Corresponding regolith depth estimates have ranges 21–29 m for analyst A, 21–30 m for analyst L, and 25–36 m for analyst S (Table 2.2). AMAs determined from the SFDs are 3.48 ±0.03 Ga for analyst A, 3.52 +0.03/-0.04 Ga for analyst L, and 3.41 +0.04/-0.05 for analyst S (Figure 2.13). Figure 2.14 shows the difference in number of craters digitized by analysts A and L for the 87° incidence angle image (AS15-M-1010) and the 71° incidence angle image (AS15-M-1835), and at smaller crater diameters, the difference in number of craters digitized for a given diameter is greater than at larger crater diameters.

Only the larger, freshest craters are visible in the 50° incidence angle image (Figure 2.5D). Counting and interpreting this image is more difficult because of the grainy quality of the original film (poor signal to noise ratio, SNR). Individuals L and S digitized this image, and the overall cumulative crater frequency of measured craters is lower than the other three incidence angles. The SFDs (Figure 2.10D) are statistically inseparable above ~150 m diameter, but both exhibit a gradual rollover beginning around 170 m. Neither SFD intersects the standard equilibrium line, but the deviation at ~170 m diameter is fit by a -2 slope corresponding to an equilibrium crater diameter of 200 m (analyst L) and 230 m (analyst S). Regolith estimates are 28–40 m for analyst L and

32–46 m for analyst S (Table 2.2). AMAs determined for these SFDs are 3.51 ±0.04 Ga and 3.39 +0.06/-0.09 Ga for the measurements by analyst L and analyst S, respectively (Figure 2.15).

Similar to AS15-M-2461 (50° incidence angle), the freshest and largest craters are the most visible in the LROC NAC image (56° incidence angle, Figure 2.6), and the cumulative SFD for the 4 km^2 count area plots below those of the Apollo Metric images but has a similar slope (Figure 2.16). The largest diameter bins in the NAC cumulative SFD overlap the smallest diameter bins for the Apollo Metric cumulative SFDs, providing a means of comparison between counts at these diameters. The upper uncertainties in the NAC counts approach the 56° incidence angle Apollo Metric SFD. The NAC SFD extends to substantially smaller diameters than the Apollo Metrics (down to ~5 m) due to the higher spatial resolution of the NAC. The largest diameter bins in the NAC SFD have a slope similar to the smaller diameter bins in the Apollo Metric SFD even with the large uncertainties, and the NAC SFD follows an equilibrium slope of -2, which cannot be properly dated with an AMA fit (Figure 2.17).

Table 2.2. Equilibrium Crater Diameter and Regolith Depth Estimates.

Image	Analyst	b[a]	D_{eq} (m)	Regolith Depth (m)	
				Maximum	Average
AS15-M-1010	A	-3.8	190	38	27
AS15-M-1010	L	-3.5	175	35	24
AS15-M-1152	A	-3.5	160	32	22
AS15-M-1152	L	-3.5	175	35	25
AS15-M-1835	A	-3.1	150	29	21
AS15-M-1835	L	-3.3	150	30	21
AS15-M-1835	S	-3.7	180	36	25
AS15-M-2461	L	-3.1	200	40	28
AS15-M-2461	S	-3.9	230	46	32
M104633604L	L	–[*]	–	–	–
M116161085R	L	-4.4	230	46	32
M150368601R	L	-4.7	180	36	25

[a]Slope index for the least squares fit to the production function of the measured crater distribution.

[*]Only the equilibrium population was measured (see text for details).

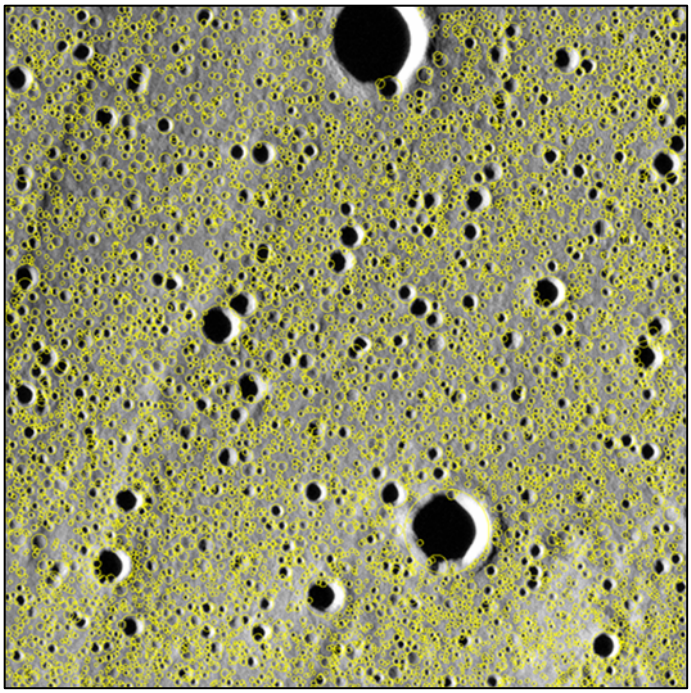

Figure 2.9. Example of a marked crater count in Circle for AS15-M-1010 (87° incidence angle). Craters digitized with diameters <70 m (equivalent to 7 pixels) were not included in the tabulated data (Appendix B). Image width is 10 km.

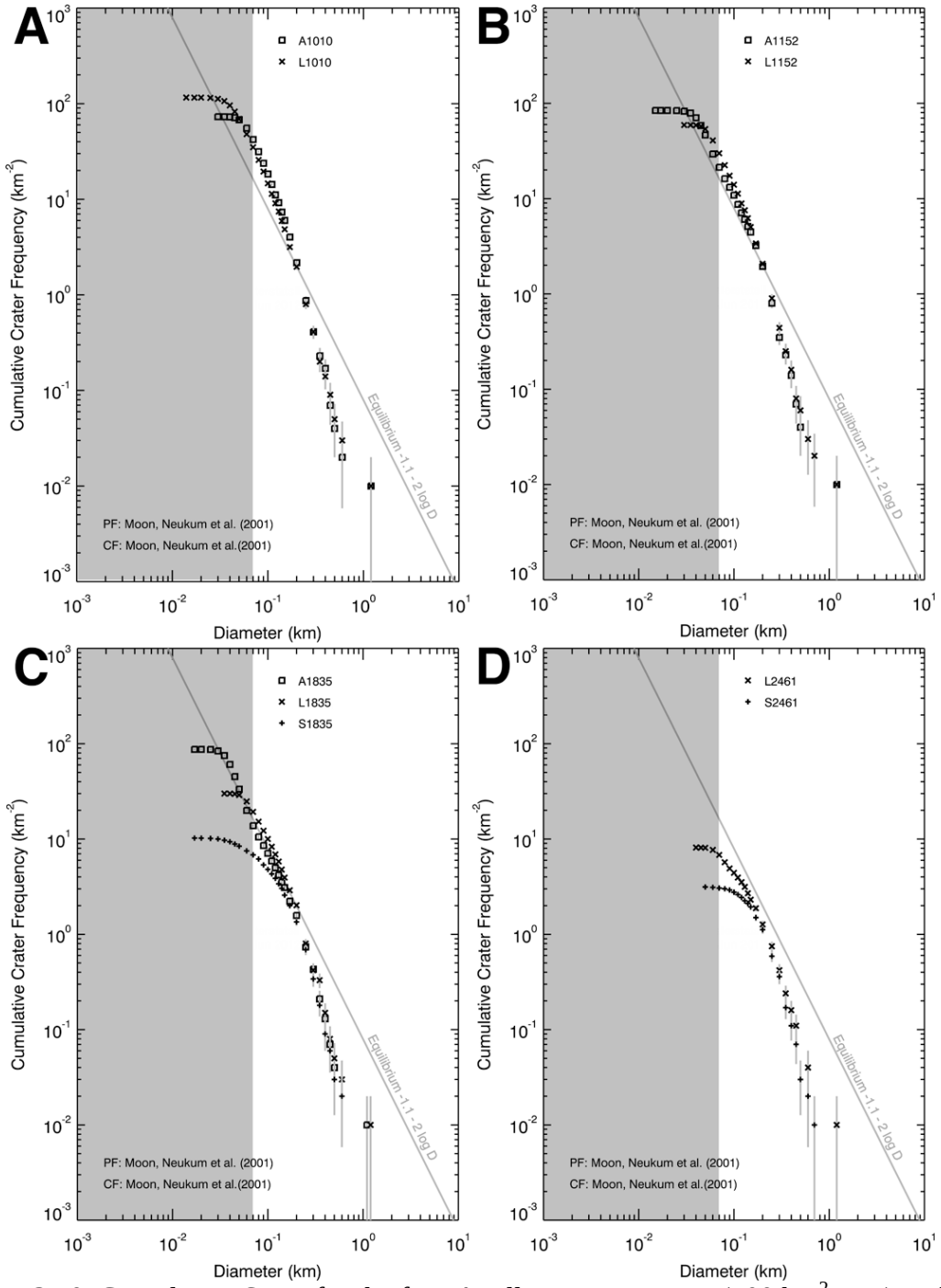

Figure 2.10. Cumulative SFDs for the four Apollo Metric images (100 km^2 area) with pseudo-log binning. (A) AS15-M-1010 at 87° incidence angle, (B) AS15-M-1152 at 82° incidence angle, (C) AS15-M-1835 at 71° incidence angle, and (D) AS15-M-2461 at 50° incidence angle. The gray region represents the identification threshold (7 pixels), and craters with diameters less than 70 m were not included in statistical analyses. A minimum of two individuals performed crater counts on each Apollo Metric image, noted by the letters A, L (the author), and S. The standard equilibrium curve (Trask, 1966; Gault, 1970) is plotted as a gray line.

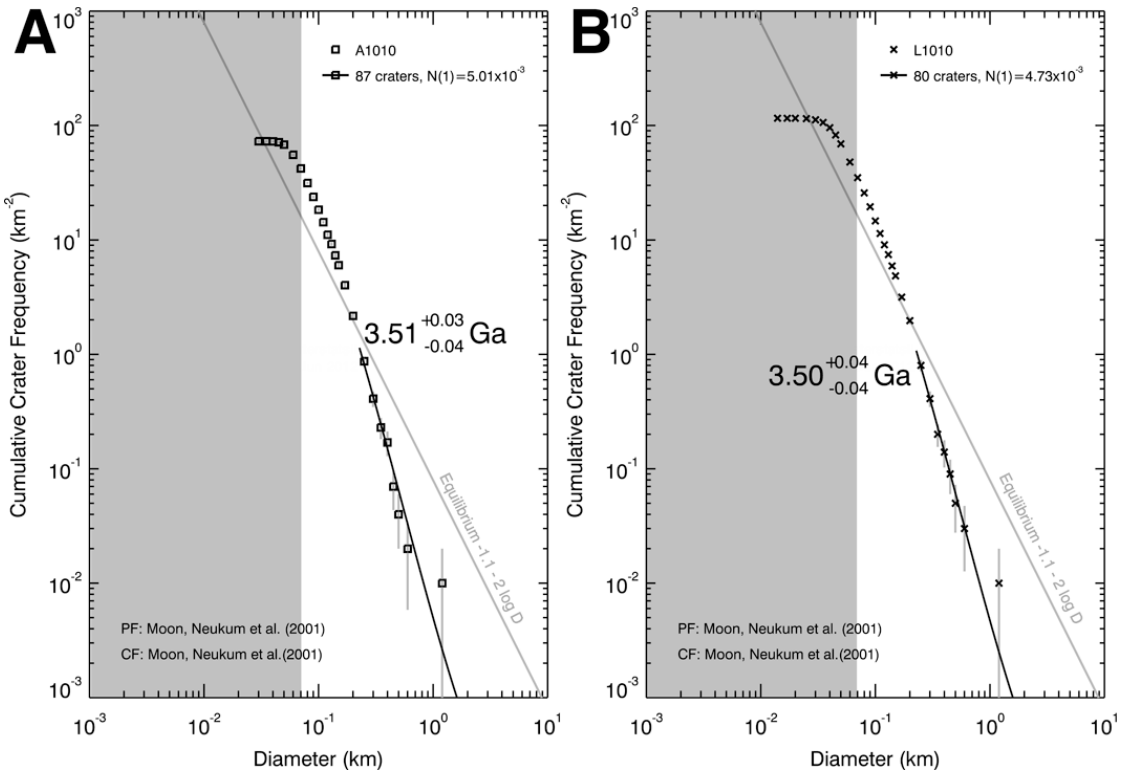

Figure 2.11. AMAs determined for AS15-M-1010 taken at 87° incidence angle (Figure 2.5A) for analysts (A) A and (B) L. Identification threshold is grayed below 70 m diameter.

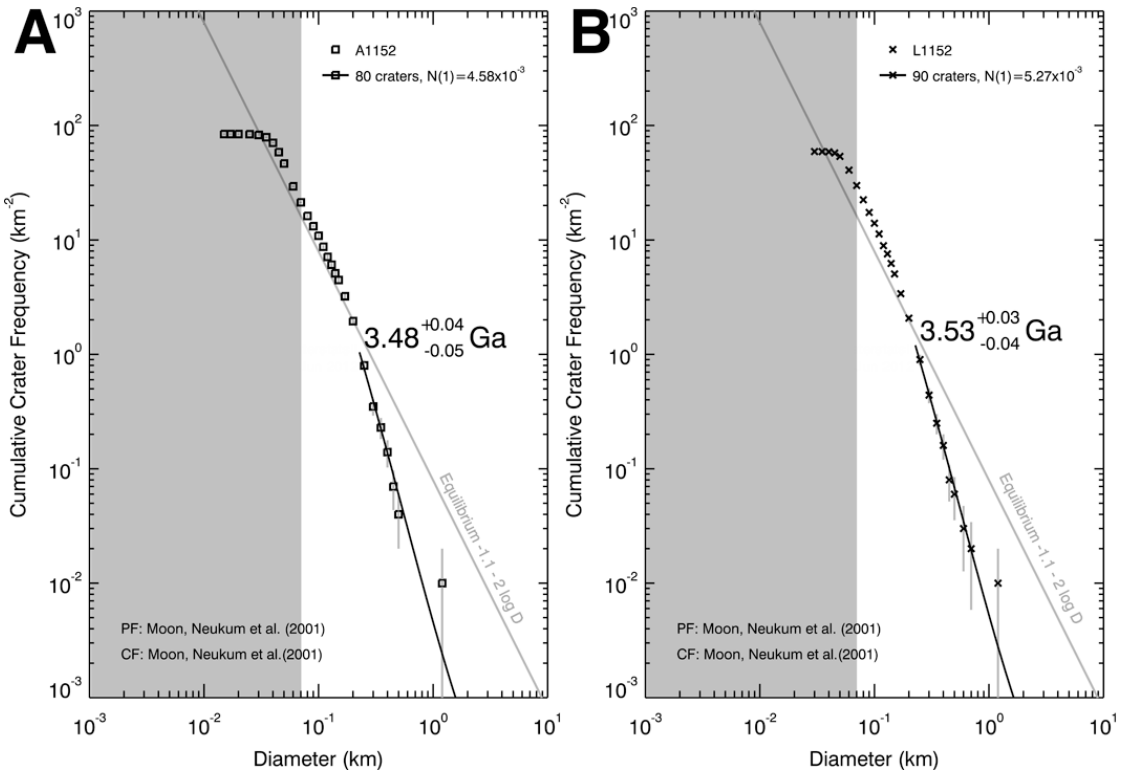

Figure 2.12. AMAs determined for AS15-M-1152 taken at 82° incidence angle (Figure 2.5B) for analysts (A) A and (B) L. Identification threshold is grayed below 70 m diameter.

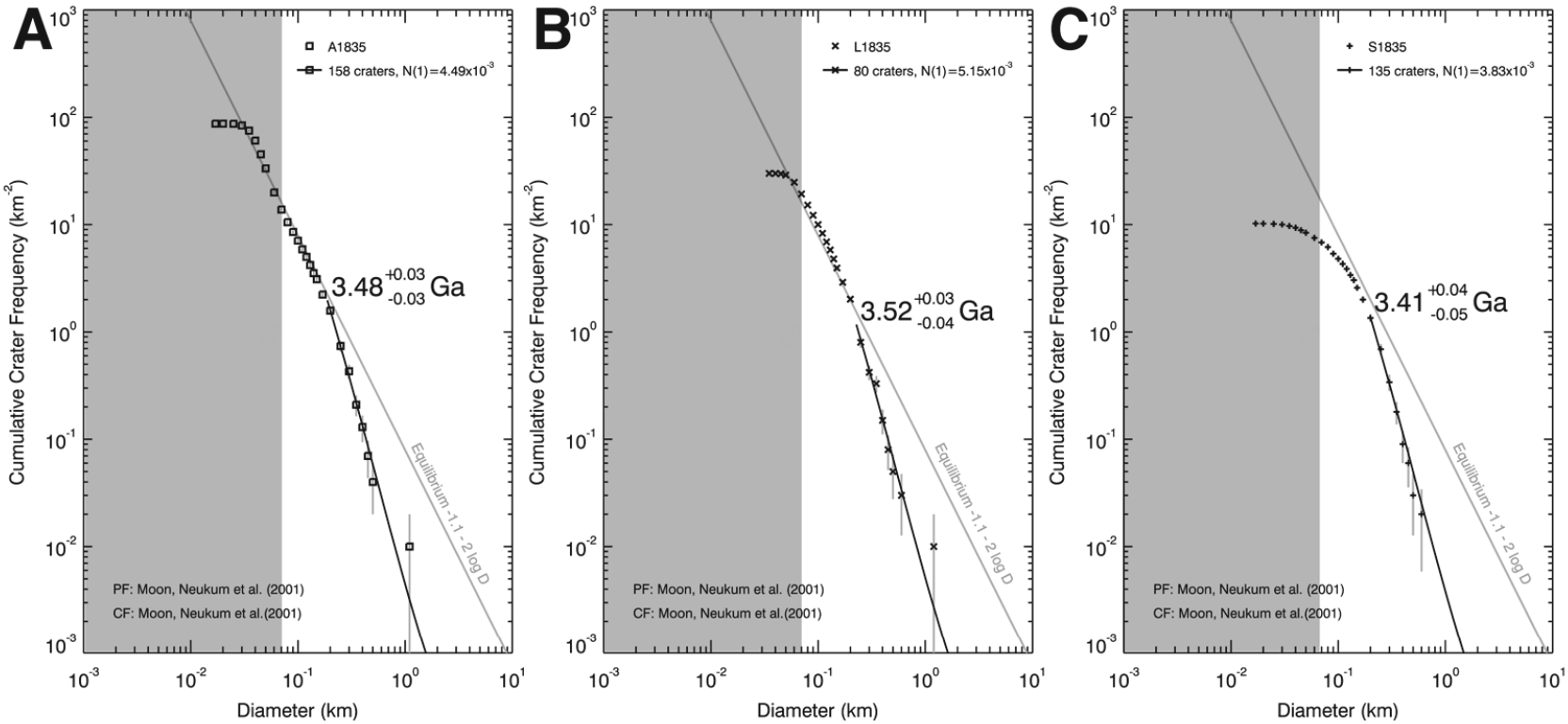

Figure 2.13. AMAs determined for AS15-M-1835 taken at 71° incidence angle (Figure 2.5C) for analysts (A) A, (B) L, and (C) S. Identification threshold is grayed below 70 m diameter.

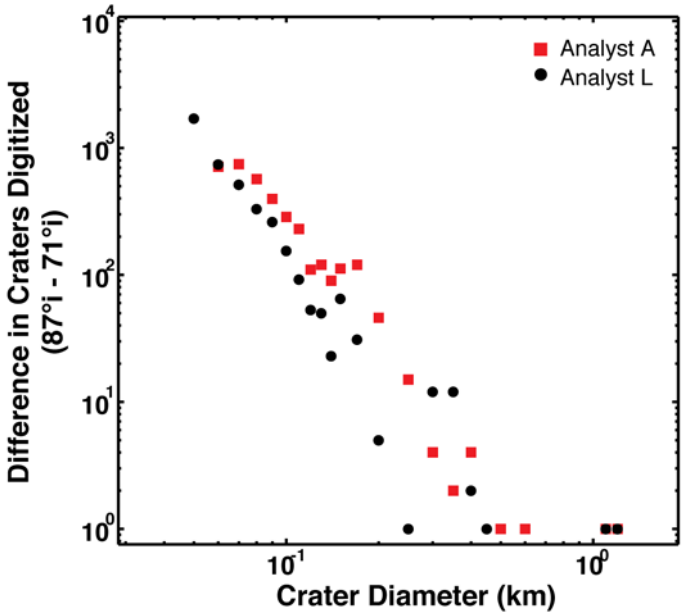

Figure 2.14. Difference in number of craters digitized on the Apollo Metric images AS15-M-1010 and AS15-M-1835 (incidence angles of 87° and 71°; Figure 2.5A, 2.5C) for analysts A and L.

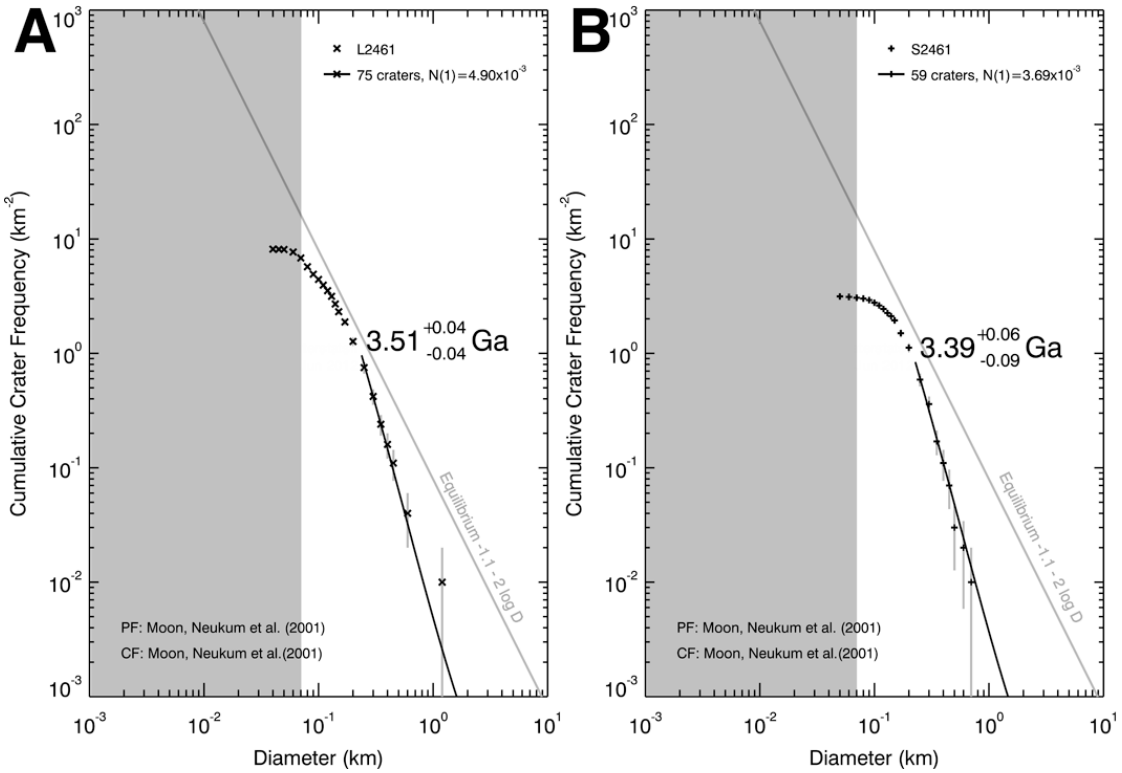

Figure 2.15. AMAs determined for AS15-M-2461 taken at 50° incidence angle (Figure 2.5D) for analysts (A) L and (B) S. Identification threshold is grayed below 70 m diameter.

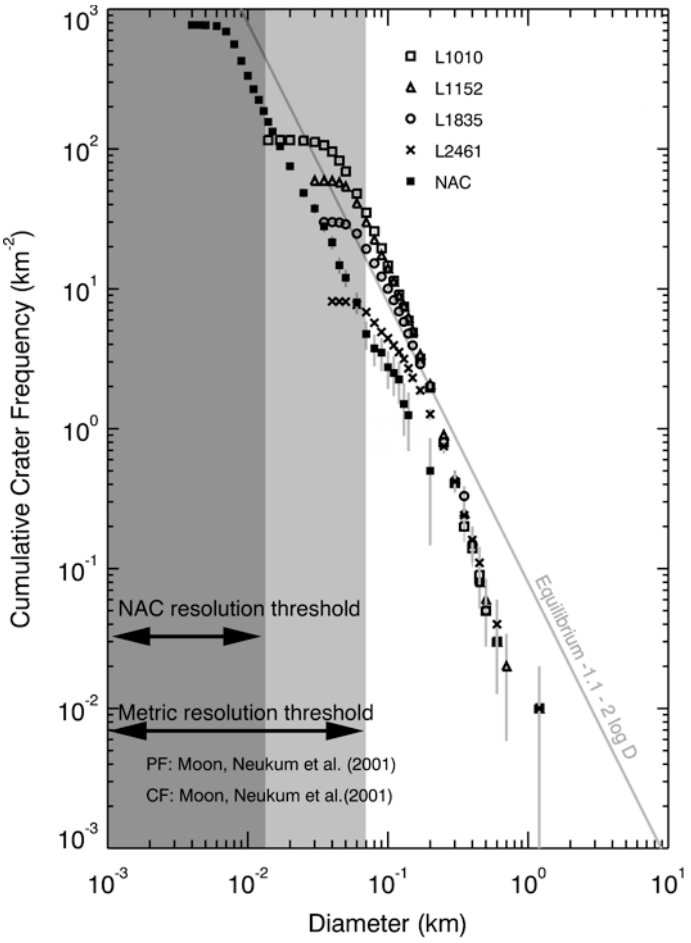

Figure 2.16. Cumulative SFDs measured by analyst L for all four subsections of the Apollo Metric images (AS15-M-1010, 87° incidence angle; AS15-M-1152, 82° incidence angle; AS15-M-1835, 71° incidence angle; AS15-M-2461, 50° incidence angle; Figure 2.5) with a 100 km^2 count area and the cumulative SFD for a 4 km^2 count area within LROC NAC image M106633604L (56° incidence angle; Figure 2.6) that overlaps part of the Apollo Metric count area. Identification threshold is grayed below 70 m diameter for the Apollo Metric SFDs and below 14 m diameter for the NAC SFD.

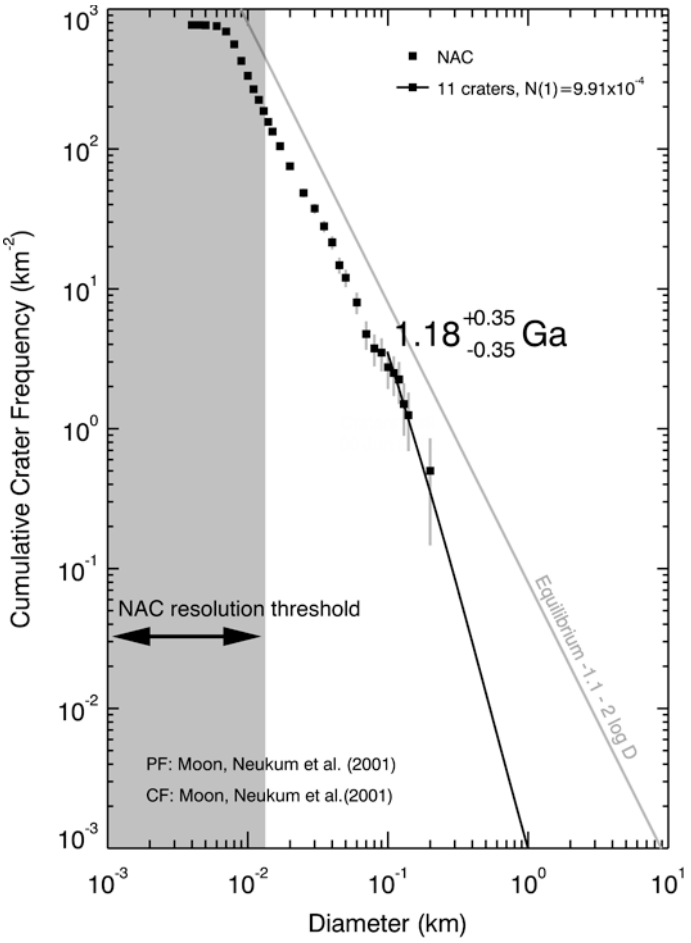

Figure 2.17. AMA derived for the NAC count on M106633604L (56° incidence angle; Figure 2.6), which is in equilibrium (-2 slope; Trask, 1966). Identification threshold grayed below 14 m diameter.

2.5.2. Apollo 11 Landing Site

For the ~2 km^2 area centered on the Apollo 11 Lunar Module descent stage (Figure 2.9), cumulative SFDs (analyst L) for measurements on 82° and 64° incidence angle images show that while more craters are identified with larger diameters at larger incidence angles (Figure 2.18, Appendix B Table B11, B12), the SFDs are statistically inseparable for most diameters and the counts deviate significantly between 5–10 m in diameter. The two largest bins in the SFDs represent the smallest craters present in the production population and have steep slopes (-4.4 for 82° incidence angle and -4.7 for

64° incidence angle). These largest diameters observed in the NAC count area are used to derive AMAs. At 82° incidence, an AMA of 3.56 +0.13/-1.50 Ga is estimated and at 64° incidence an AMA of 3.48 +0.12/-0.73 Ga is estimated; both ages are in agreement with published AMAs (Hiesinger et al., 2000) and Apollo 11 rock samples (e.g., Stöffler and Ryder, 2001 and references therein). Equilibrium crater diameter is estimated to be ~230 m at 82° incidence angle and ~180 m at 64° incidence angle, with corresponding regolith depth estimates of 32–46 m and 25–36 m, respectively (Table 2.2). Both SFDs deflect below the standard equilibrium line around ~50–90 m diameter, beginning to re-approach equilibrium as the SFD approaches the resolution threshold (Figure 2.18).

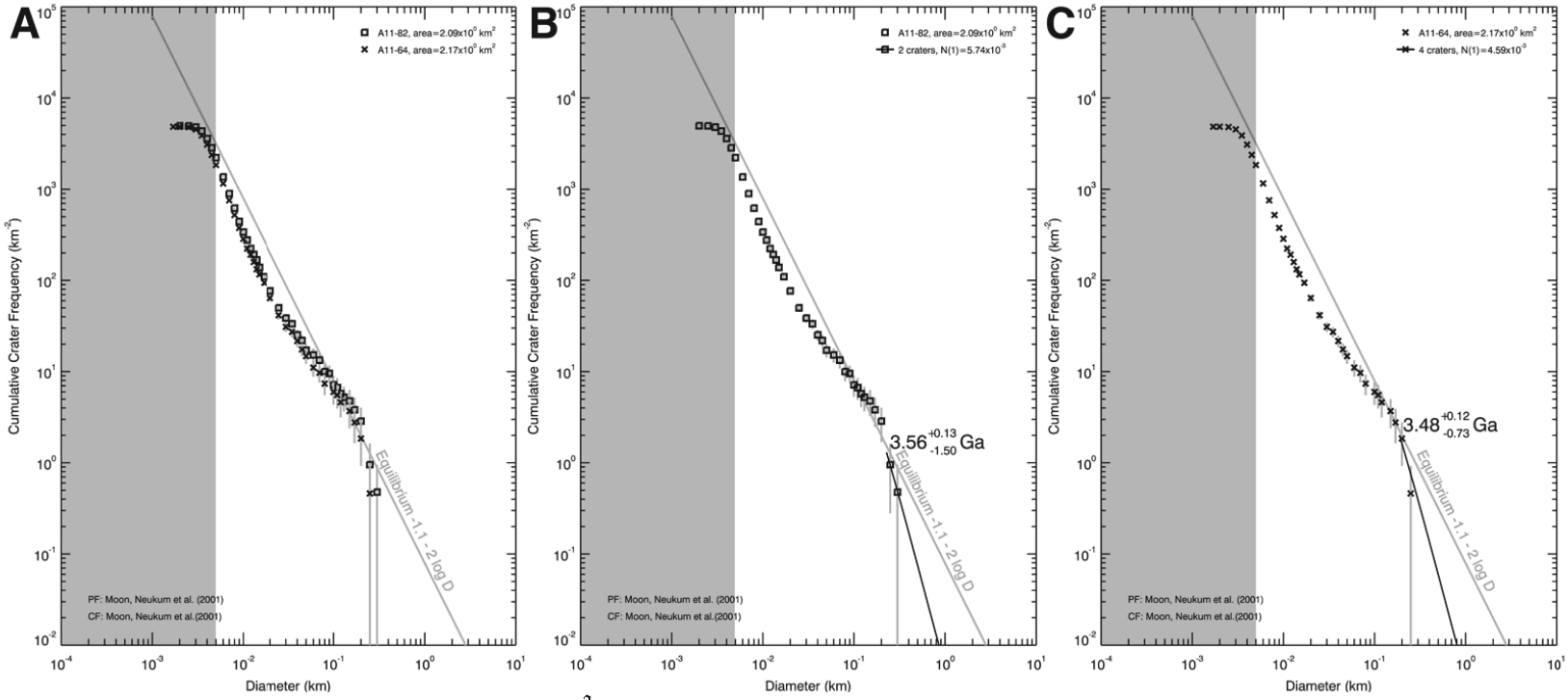

Figure 2.18. (A) Cumulative SFDs for an ~2 km^2 region centered on the Apollo 11 Lunar Module descent stage (Figure 2.7). (B) AMA fit to the 82° incidence angle SFD, measured for an area 2.09 km^2. (C) AMA fit to the 64° incidence angle SFD, measured for an area 2.17 km^2. LROC NAC M116161085R with 82° incidence angle and NAC M1050368601R with 64° incidence angle were resampled to 0.7 meter pixel scale. Identification threshold is grayed below 5 m diameter.

2.5.3. Mare Serenitatis

Initially, three 400 km^2 areas in Mare Serenitatis were selected in normalized reflectance WAC mosaics with average incidence angles of 66° and 46° (Figure 2.8). Figure 2.19 and 2.20 show digitized craters marked on the WAC mosaics. Cumulative SFDs for these measurements are statistically indistinguishable but have large uncertainties (Figure 2.21). Example isochron fits to the 66° and 46° incidence angle SFDs indicate that the 66° incidence angle SFD is best fit by a 3.5 Ga AMA while the 46° incidence angle SFD could be fit either by a 3.4 Ga or 3.0 Ga AMA (Figure 2.21), and the difference in AMA for the 46° incidence angle SFD reflects the poor count statistics arising from a small area. To obtain better crater statistics (larger count area allowing more counted craters), the measurement area was expanded to ~4×10^4 km^2 (Figure 2.8). Similar to the Apollo Metric and NAC SFDs, the WAC SFDs are statistically indistinguishable for craters ≥2 km in diameter, and for craters ≤2 km in diameter, the 66° incidence angle cumulative SFD measurements are greater than those at 46° incidence angle (Figure 2.22, Appendix B Table B19, B20). AMA determinations give an age of 3.47 ±0.01 Ga for the 66° incidence angle image and an age of 3.41 ±0.02 Ga for the 46° incidence angle image; these AMAs are consistent with previously published estimates (Hiesinger et al., 2000). Figure 2.23 shows the difference in number of craters digitized at 66° and 46° incidence angle versus crater diameter. Similar to the Apollo Metric observations, there is a smaller difference in number of craters digitized for larger diameters. Measurements of crater diameter in the WAC mosaics indicate that the observed SFD is in production and determination of an equilibrium crater diameter is not possible.

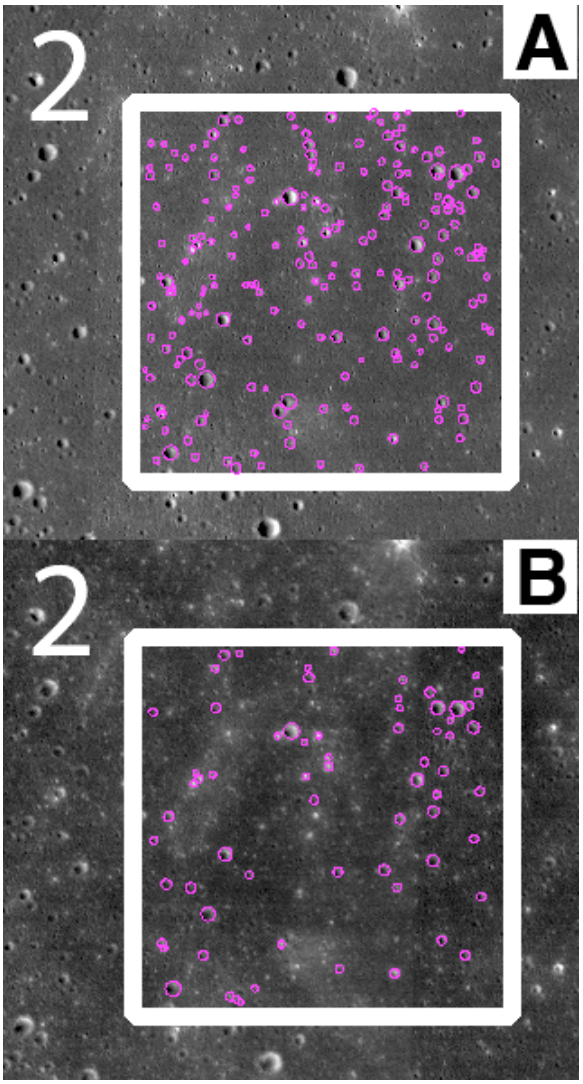

Figure 2.19. LROC WAC close-up in Circle of Box 2 in Mare Serenitatis (Figure 2.8) at (A) 66° incidence angle and (B) 46° incidence angle. Box width is 20 km, and any craters less than 7 pixels in diameter (corresponding to 700 m) were removed from SFD analysis.

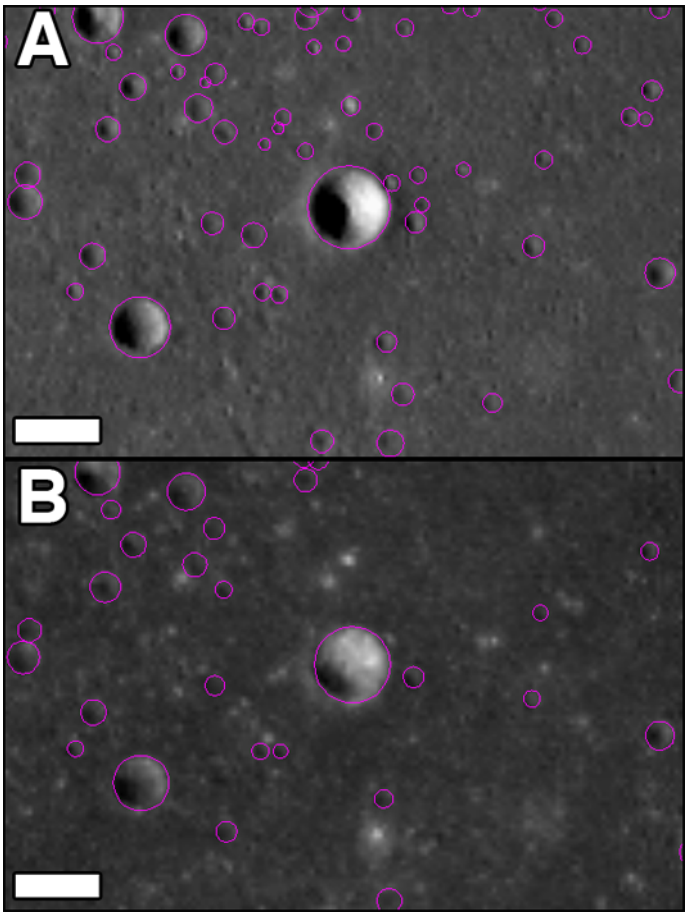

Figure 2.20. 4× zoom in Circle on the LROC WAC mosaics; purple circles are marked craters. Not all craters marked are larger than the 700 m identification threshold. (A) 66° incidence angle mosaic, with the center crater measured at 1.8 km in diameter, and (B) 46° incidence angle mosaic, with the center crater measured at 1.6 km in diameter. Scale bar is 2 km.

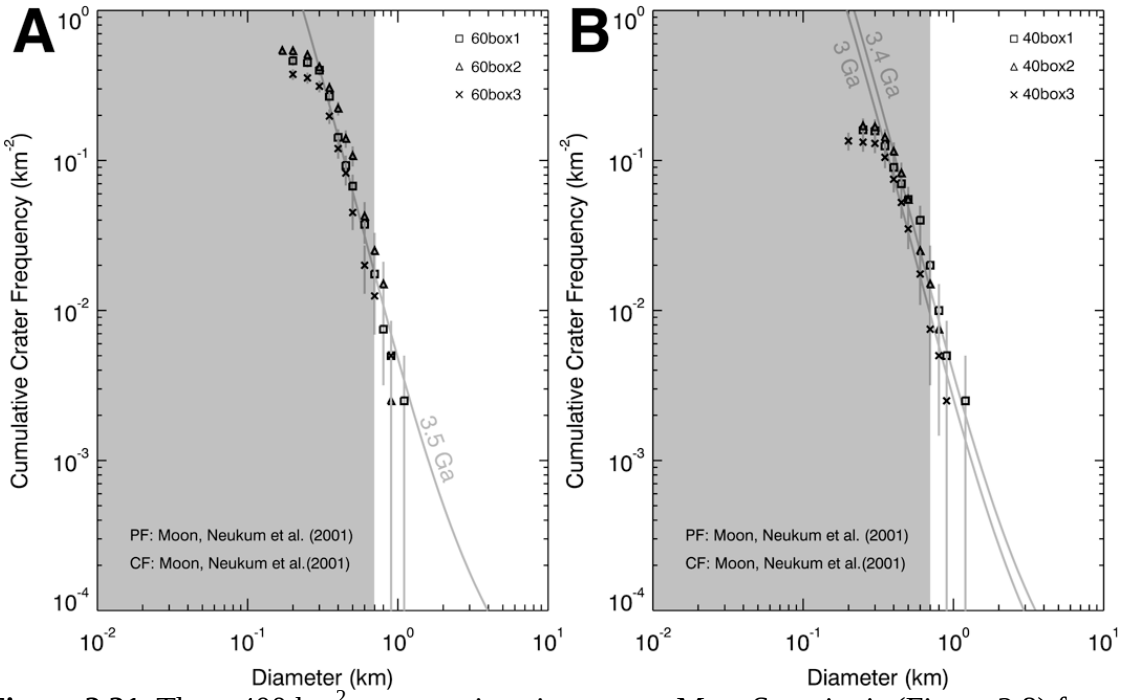

Figure 2.21. Three 400 km^2 count regions in western Mare Serenitatis (Figure 2.8) for (A) 66° incidence angle and the (B) 46° incidence angle LROC WAC mosaics. (A) SFDs for Box 1–3 at 66° incidence angle. (B) SFDs for Box 1–3 at 46° incidence angle. In both (A) and (B) the uncertainties are large at larger diameters, reflecting the small numbers of craters counted. Identification threshold is grayed below 700 m diameter.

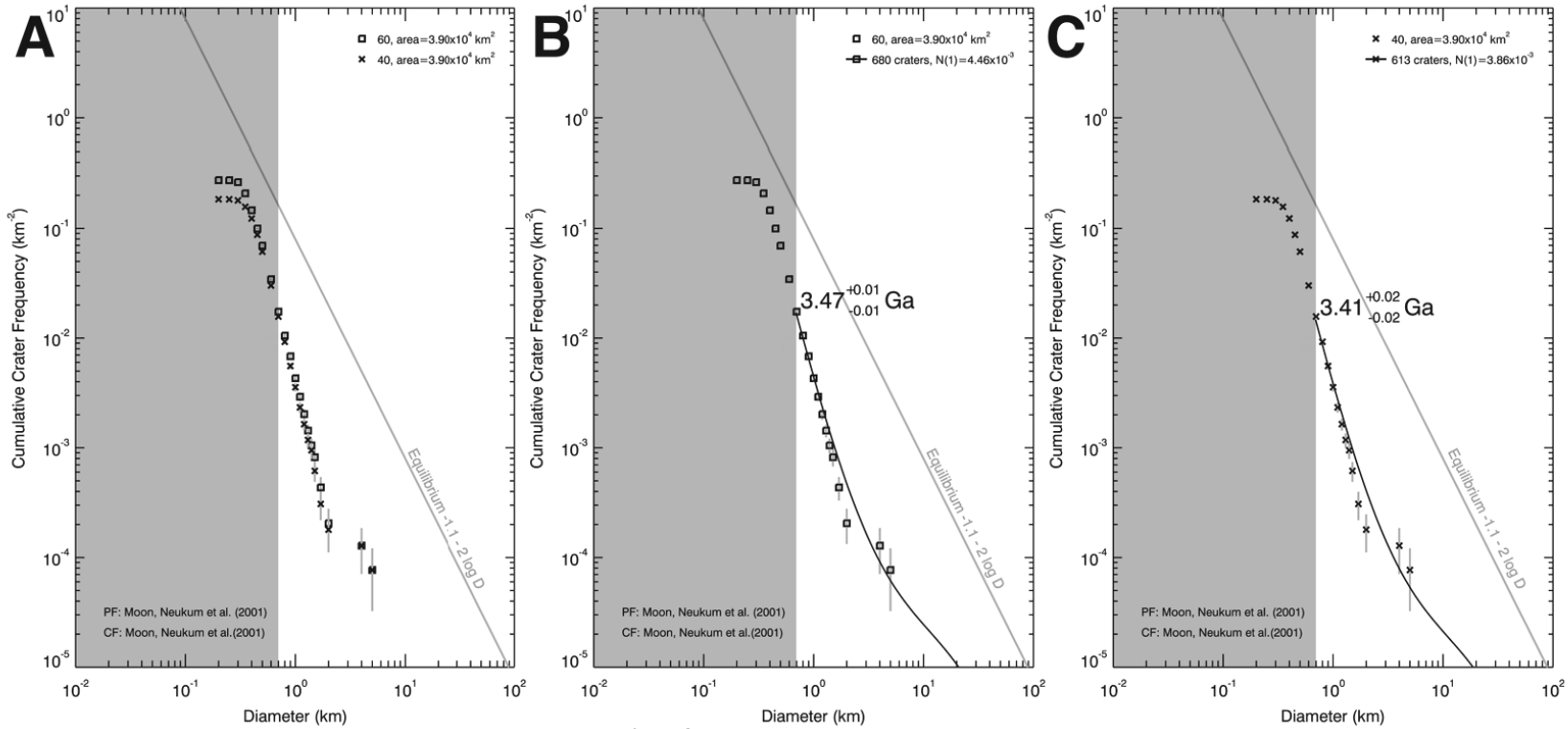

Figure 2.22. (A) Cumulative SFDs for the ~4.0 × 10^4 km^2 count region in Mare Serenitatis (Figure 2.8), measured on LROC WAC mosaics with average incidence angles of 66° and 46°. (B) AMA fit to the 66° incidence angle SFD. (C) AMA fit to the 46° incidence angle SFD. Identification threshold is grayed below 700 m diameter.

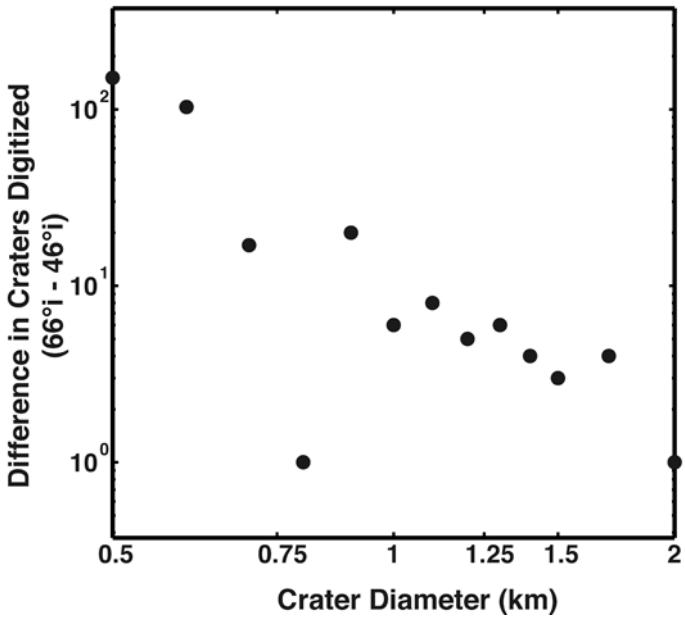

Figure 2.23. Difference in number of craters digitized at 66° and 46° incidence angles on LROC WAC mosaics for western Mare Serenitatis (Figure 2.8).

2.6. Discussion

2.6.1. Count Variation Between Individuals

This work primarily focuses on testing the hypothesis that incidence angle affects an analyst's ability to both detect craters and accurately measure their diameters. In this investigation, three individuals collected crater measurements of the same region from images with different incidence angles. Crater counts collected by a single individual are exposed to measurement errors based on their counting technique, experience, and the inherent statistical uncertainties, whereas the data collected by multiple individuals is affected by the errors and uncertainties associated with each separate measurement. The results from this investigation are consistent with previous investigations that employed multiple analysts for crater counting (e.g., Gault, 1970; Greeley and Gault, 1970; Robbins et al., 2013a; 2013b), but unlike some investigations (e.g., Gault, 1970; Greeley and

Gault, 1970; Young, 1975) the crater frequencies were not averaged for final analysis. Differences between the results of trained individuals are expected, with an estimated variation of ±20% when ≥50 craters are counted per size class (Gault, 1970; Greeley and Gault, 1970). When only 3–5 craters are counted per class, the crater frequency results generally agree to within a factor of two (Greeley and Gault, 1970). For this investigation, the three individuals were trained using the largest incidence angle Apollo Metric image (AS15-M-1010, 87° incidence angle) and the IDL-based Circle program. Although all individuals had similar amounts of training prior to commencing measurements, there are differences in the final counts reflecting that individuals perceive images in different ways and measure craters differently (i.e., click differently). The analysts were instructed to identify and record only those craters for which they were certain, so crater measurements may be prone to subjective interpretation. Moreover, all three analysts had little to no crater counting experience at the beginning of this investigation, but as the investigation progressed through the different phases, analyst L (primary author) gained more experience by counting craters on all the images and as a result, it may be that additional technical expertise affected later crater measurements. Another possibility influencing the count differences for individuals is the effect of time spent crater counting, coupled with the time of day crater counting was completed. Greeley and Gault (1970) limited the amount of time an analyst spent crater counting based on analyses of analyst fatigue; here, formal measurements to test fatigue were not employed. Analysts were not instructed to limit their counting time per session, although suggestions to take frequent breaks were recommended. Consequently, the analysts spent variable time counting during each session, ranging from one hour to multiple hours

depending on their availability (all were students) and enthusiasm. Likewise, individuals made crater measurements during different times of the day depending on their schedules, and it is possible that alertness and subjectivity varied among analysts depending on the time of day (e.g., beginning versus conclusion of the work day; before or after attending class; before or after coffee, mealtime). For example, a combination of some of these factors may explain why the SFDs for the 87° and 82° incidence angle images completed by analyst L do not show a decrease in estimated crater equilibrium diameter (Table 2.3), even though a decrease is observed in the SFDs measured by analyst A. For analyst L, the cumulative SFDs are statistically indistinguishable (Figure 2.16) but number of craters measured per bin is different (Table 2.3). For differences between bins that are <10 craters, the difference likely reflects the change in detection owing to the smaller incidence angle in addition to a 1–2 pixel maximum uncertainty in measurement. The Circle program operated using a context view of the image and craters were marked on a 4× zoom window, and it is possible that small errors were made during crater rim determination, especially as incidence angle decreased and less pristine crater rims became more difficult to discern. A notable difference is observed for the measured cumulative SFDs of the 71° incidence angle Apollo Metric image (Figure 2.10C), where two of the individuals (A and L) measured statistically inseparable crater populations to provide an equilibrium crater diameter estimate of ~150 m while the third individual (S) measured an SFD with an equilibrium crater diameter estimated at ~180 m. The cause of this discrepancy is unclear, but a similar difference is observed between analysts L and S for the 50° incidence angle image, where the equilibrium diameter estimate again differs between individuals by 30 m. One explanation is that analysts L and S used different

strategies during counting: analyst L methodically moved the zoom window from left to right, moving down almost one zoom window height after completing a counting "row", to simulate a grid, whereas analyst S preferred to mark the craters by moving about the context view window in a less-patterned or less-regular fashion.

2.6.2. Effects of Incidence Angle on Crater Identification and Measurement

2.6.2.1. Small Crater Population

The cumulative SFDs for the four Apollo Metric frames exhibit the effects of different incidence angles on crater counts (Figure 2.10, 2.16); the overall cumulative frequency of measured craters decreases with decreasing incidence angle. The largest craters were repeatedly identified in each image whereas the smaller craters were not (e.g., Figure 2.10, Appendix B Table B1–B9), indicating that consistent identification of craters on a mare surface is influenced by solar incidence angle, findings in agreement with previous studies (Young, 1975; Wilcox et al., 2005). Table 2.3 presents the difference in number of craters per bin in the four Apollo Metric images counted by analyst L, and the number of craters identified generally decreases with decreasing incidence angle. The largest bin (1.2 km) has one crater identified in all images, but at 400 m, five craters are identified in the 87° and 50° incidence angle images and seven and eight craters are identified in the 82° and 71° incidence angle images, respectively. In these cases, where difference in number of craters identified does not exceed 10, the difference is attributed primarily to the difficulty in accurately determining rim locations (and thus estimating diameter). None of the larger craters in the study area have fresh and distinct rim crests, and although the contrast between the mare surface and the crater interior is sharp, determining the break in ground surface slope representative of the

crater rim is difficult. Thus, measurement uncertainty of a few pixels in marking of the crater rim results in the crater moving to a larger or smaller diameter bin. Further work examining measurement differences for the same large craters, which are among the best preserved, most visible, and most consistently recorded in the images, may aid in determination of maximum measurement uncertainty for each individual, as well as statistically correlating the size variation for the same crater marked at different incidence angles (Figure 3 in Young, 1975).

At the largest diameters (~≥200–300 m), the cumulative SFDs at each illumination are similar (Figure 2.10, 2.16); all have a steep production function slope ranging from -3.1 to -3.9, and the different observers counted the same, or very similar, cumulative numbers of craters in each diameter bin (Appendix B Table B1–B9). The difference in number of craters digitized at 87° incidence angle and 71° incidence angle versus diameter for Apollo Metric data collected by two individuals (Figure 2.14) suggests that at larger incidence angles, more craters are identified and recorded with larger diameters, but the largest craters are consistently identified at different illuminations. These findings are consistent with Young (1975), who found that more craters were visible at larger incidence angles. For an older region in Mare Imbrium, almost all craters identified in the 86° incidence angle image were also identified at 38° incidence, but at the larger incidence angles the crater diameters were measured to be larger (Young, 1975).

Results from Apollo Metric crater counts for the 50° incidence angle image are the least consistent between two observers, perhaps owing to counting techniques (Figure 2.10), while the SFDs for the 71° incidence angle image are most consistent between

observers. The small crater equilibrium and the production function are observed in all images, and some of the deviation between production and equilibrium may be attributed to the effects of incidence angle on crater detection. The similarity and consistency in observations between individuals and the resulting AMA agreements (~3.5 Ga for analysts A and L in both images) for the SFDs measured on the 82° and 71° incidence angle images suggests that, based on the Apollo Metric counts, ~70° to ~80° is an optimal incidence angle range for investigations pertaining to age determination.

The small crater trends (~≤200 m diameter) vary significantly between and among observers at different illuminations (Figure 2.10, 2.16). The small crater population for all but one SFD (analyst S) in the 71° incidence angle image and the 50° incidence angle SFD are fit well with a -2 slope (>3 data points, R^2>0.95–0.98) and the variation between numbers of craters identified in different diameter bins is large (Table 2.3). These observations reflect the change in visibility of the smallest craters. The smallest craters on a mare surface form in regolith and are the biggest contributors to regolith mixing and overturn (e.g., Soderblom, 1970), and because the regolith is mostly unconsolidated (at least at the scales necessary to form craters hundreds of meters in diameter), small craters are affected more strongly by impact erosion (e.g., Soderblom, 1970; 1972; Soderblom and Lebofsky, 1972; Schultz et al., 1977) and the effects of seismic modification due to larger impacts (Schultz and Gault, 1975). As a result, small craters degrade faster than large craters (Soderblom, 1970; Soderblom and Lebofsky, 1972) and will be more difficult to discern in small incidence angle illumination conditions than at larger incidence angles, when the subtle topography surrounding the craters is pronounced (Soderblom, 1972; Young, 1975). The crater equilibrium diameter is estimated to be

175 m (analyst L) for the 87° incidence angle image and 200 m (analyst L) for the 50° incidence angle image, and the increase in equilibrium crater diameter estimate between the larger and smaller incidence angles does not follow the trend observed for the other images. The equilibrium diameter estimates decrease with decreasing incidence angle for the 87°, 82°, and 71° incidence angle images, findings consistent with observations by Young (1975) and Wilcox et al. (2005), suggesting that crater measurements made on larger incidence angle images result in the most accurate estimate of crater diameter. Therefore, because the quality of the 50° incidence angle image has poor SNR (discussed in Section 2.4.1), the estimated equilibrium diameter is unreliable.

The results of the LROC NAC count of a subsection of the Apollo Metric count area (Figure 2.4, 2.6) further suggests the 50° incidence angle Apollo Metric image counts are unreliable. The NAC subscene cumulative SFD has a -2 equilibrium slope, indicating that the equilibrium population is being sampled, but the NAC SFD plots lower than the Apollo Metric counts (Figure 2.16). Because the NAC SFD is measured from a subsection of the Apollo Metric count area, however, the NAC count should reflect the distribution of craters measured in the Apollo Metric images in this investigation (Figure 2.16). Instead, the lower cumulative crater frequencies for the NAC area are attributed to the small count area (4 km^2) that contributes to poor crater statistics: two craters were identified in the largest NAC bin (200 m), while 52 craters were identified in the same bin for AS15-M-2461. Similarly, 111 craters were identified for the 70 m bin in AS15-M-2461 while only four craters were identified in the same bin in the NAC area. Furthermore, the NAC count measured only the equilibrium population and cannot be used to assess the anomalous equilibrium crater diameter derived from the 50°

incidence angle Apollo metric image. Therefore, the next steps to resolve this unanticipated result can follow one of two paths (or both). First, search for and identify another Apollo Metric image in the 50°–70° incidence angle range (ideally closer to 50° than 70°, with a more favorable SNR) for the study area, recreate the count area boundaries, and measure the crater population. This option is ideal because the new crater SFD may be directly compared to the other Apollo Metric SFDs, but an image in the desired incidence angle range may not be available. Second, the NAC subscene can be expanded to a larger area (at least 10–15 km^2) and focus on measuring craters ≥100 m in diameter (≥50 pixels at 2 meter pixel scale) to attempt to identify the production function and improve the crater statistics.

LROC NAC images (0.5–2 meter pixel scales; Robinson et al., 2010), allow crater measurements to extend to diameters <10 m, providing an opportunity to examine the current cratering chronology and provide revisions to the chronology using new counts at the calibration sites (i.e., Apollo and Luna landing sites; e.g., Hiesinger et al., 2012; Robbins, 2013). Crater frequencies down to 10 m in diameter allow crater populations of young features with spatially limited extents, such as impact melt, to be assigned relative and absolute model ages (10 m is currently the smallest diameter to which the Neukum et al. (2001a) chronology may be fit). Equilibrium crater diameter estimates from NAC images with differing incidence angles (Figure 2.18) follow the trend observed by Wilcox et al. (2005) and those in the Apollo Metric SFDs of this investigation (Figure 2.10). In the two NAC images of Apollo 11, the equilibrium crater diameter decreases from 230 m at 82° incidence to 180 m at 64° incidence (Figure 2.18), and more craters are identified in the larger incidence angle image (4600 versus 4000 craters total). The largest craters

(with the exception of West crater) at the Apollo 11 Landing Site are heavily degraded, with shallowly sloping walls and poorly defined rims. The absence of well-defined rims on these craters leads to greater measurement uncertainty when determining the apparent crater diameter. At 82° incidence angle, many of the degraded craters appear bowl-shaped; part of the crater cavity is in shadow and the remainder is illuminated so that a break in slope between the mare surface and the crater cavity is pronounced (Figure 2.7). In contrast, at 64° incidence angle (Figure 2.7), very little of the crater cavity is in shadow or strongly illuminated and the inflection between rim summit and the drop off to the interior is harder to discern. Typically, the analyst will follow what s/he interprets as a break in slope when marking the rim, and for smaller incidence angle images, perhaps the diameter is systematically underestimated by a small amount relative to that measured for a crater using a larger incidence angle image.

2.6.2.2. Larger Diameter Craters

Measurements of larger crater diameters (≥700 m) on the LROC WAC mosaics also exhibit a greater number of craters identified in the larger incidence angle image, but only the production function is observed. The cumulative SFDs for the WAC counts at 66° and 46° incidence angles for three 400 km^2 regions are not statistically separable (Figure 2.21), and the large uncertainties in the cumulative SFD indicate that 400 km^2 is too small an area to derive robust crater count statistics at the WAC 100 meter pixel scale, an observation furthered by results presented in **Chapter 3**. Increasing the measurement area to ~4×10^4 km^2 improves the count statistics and decreases uncertainties for all but the largest diameters measured (<10 craters total for diameters ≥2 km). For the larger count area, the resulting difference in number of craters digitized

at 66° and 46° incidence angle versus crater diameter (Figure 2.23) is consistent with the observations from Apollo Metric and NAC images (e.g., Figure 2.14) that more craters are consistently identified in larger incidence angle images.

2.6.3. Identifying the Equilibrium Diameter

An important question to consider is whether the equilibrium crater population is truly reflected in the small crater slope (diameters <300 m, including the gradual rollover) observed in the Apollo Metric and LROC NAC cumulative SFDs (Figure 2.10, 2.16, 2.18). A sharp kink in the SFD is not observed for either of these cases, but a least squares fit to the data indicate a break in slope (Appendix B Figure B1–B6). Is Oberbeck's (2008) hypothesis valid, and is the gradual rollover observed in the cumulative SFDs due to factors such as resolution limits of the images or insufficient count area?

Resolution limits are an unlikely cause for the observed gradual rollover in the measured SFDs. The effects of resolution on accurately measuring crater diameters are mitigated by designating a threshold diameter of 7 pixels, which exceeds the diameter range where pronounced flattening of the slope of the SFD occurs (Figure 2.10, 2.16, 2.18). Thus, the cumulative SFDs and the transition from production to equilibrium (Figure 2.10, 2.18) do not reflect resolution limits.

Inadequate areal extents of the count areas may lead to imprecise identification of the equilibrium diameter. However insufficient count area size is also unlikely for the Apollo Metric SFDs, based on the number of craters counted (>17,700 craters total, with a maximum of 4200 craters counted in a single image) and by comparison to an LROC NAC subscene (>600 craters total). The LROC NAC crater measurements in Mare

Imbrium (Figure 2.6, 2.16, 2.17) extend to craters 14 m in diameter, allowing observations well below the onset diameter of the small crater equilibrium population (between ~150 m and 300 m, e.g., Young, 1975; Schultz et al., 1977; Wilcox et al., 2005). Between 70 m and ~150 m in diameter, the cumulative SFD bins of the 56° incidence angle NAC and 50° incidence angle Apollo Metric counts overlap (Figure 2.16). This overlap provides a means of comparison at these diameters, where the NAC SFD slope at these diameters is -2 (small crater equilibrium) and is parallel to the equilibrium slope observed in the Apollo Metric images taken at 71°, 82°, and 87° incidence angles (Figure 2.16). For the NAC SFD (56° incidence angle) and AS15-M-2461 (50° incidence angle Apollo Metric), equilibrium conditions are met below the 10% geometric saturation limit, which is a common occurrence (Gault, 1970; Richardson, 2009).

The results presented here do not support Oberbeck's (2008) hypothesis that a sharp kink is required in the cumulative SFD to indicate the transition from production to equilibrium. Therefore, a gradual rollover in the cumulative SFD that reflects a change in slope from production (~-3.0 to -4.0; e.g., Soderblom, 1970) to equilibrium (-2; Trask, 1966) may be considered to be the SFD inflection point indicative of equilibrium. Thus, equilibrium crater diameter estimates derived from the intersection of the production and equilibrium functions determined by a least squares fit to the measured crater frequencies are valid. For the Mare Imbrium region investigated in Apollo Metric images, the equilibrium crater diameter decreases from an average (analysts A and L) of 182 m to 167 m to 150 m with decreasing incidence angles of 87° to 82° to 71°, respectively, as a direct result of the decrease in detectable craters. This trend is consistent with

observations by Wilcox et al. (2005). The equilibrium crater diameter estimate also decreases from 230 m to 180 m for the LROC NAC images of the Apollo 11 Landing Site, where incidence angle decreases from 82° to 64°.

2.6.4. Regolith Depth Estimates

Using the equilibrium diameter is one method by which regolith depths may be inferred (Wilcox et al., 2005). The inferred regolith depths are directly correlated to the equilibrium crater diameter by depth to diameter relationships (Pike, 1974), so the ability to accurately estimate equilibrium crater diameter is necessary for estimating regolith depth. Using the equilibrium crater diameters estimated from the Apollo Metric images in Mare Imbrium, the average regolith depth is between 21 m and 26 m (corresponding to 150 m and 182 m equilibrium diameters). From estimates of equilibrium crater diameter from the NAC images of the Apollo 11 Landing Site, the average regolith depth ranges from 25 m to 32 m (corresponding to 180 m and 230 m equilibrium diameters). These estimates suggest that the Mare Tranquillitatis location (Apollo 11) is older than the Mare Imbrium location, agreeing with AMAs (Figure 2.11–2.13, 2.15, 2.18; Hiesinger et al., 2000). Equilibrium conditions are not the same for surfaces of different ages (Young, 1975), and older surfaces will have larger equilibrium crater diameters (Trask, 1966). In this case, crater measurements were made at the same incidence angle (82°, so no correction factor is necessary to compare relative surface ages, c.f., Young, 1975), and the larger equilibrium diameter at Apollo 11 (230 m versus 182 m) is indicative of an older surface age. Moreover, older surfaces should have a thicker regolith (e.g., Shoemaker et al., 1969), and the average regolith depth estimate for Apollo 11 is 32 m compared to 26 m in Mare Imbrium.

2.6.5. Implications for AMAs

Accurate equilibrium crater diameter estimates provides relative age information for a surface, but absolute model age dating relies on the production population of the measured cumulative SFD. Consequently, a sufficient distribution of craters in production must be measured to determine AMAs. For the mare, a sufficient number of craters with diameters ≥250–300 m is needed (ideally >30; e.g., Silverman, 1986; Davis, 2002) based on the equilibrium diameter estimates presented here and previously (e.g., Trask, 1966; Shoemaker et al., 1969; Gault, 1970; Greeley and Gault, 1970; Young, 1975; Neukum et al., 1975a; Schultz et al., 1977; Wilcox et al., 2005). Crater measurements for the production population (<50 craters with diameters ≥250–300 m) on Apollo Metric images used in this investigation produce different AMAs that agree within the statistical uncertainty (~3.5 Ga; Figure 2.11–2.13, 2.15). However, only 2–4 craters ≥250–300 m in diameter were measured on the NAC images of the Apollo 11 Landing Site, primarily because of the small count area. An AMA of ~3.5–3.6 Ga is fit to the two diameter bins, and although this AMA agrees with previous age determinations (Hiesinger et al., 2000), the result could be statistically improved by increasing the count area. By increasing the NAC count area, more craters with diameters ≥250 m would be measured, improving the statistical robustness of the AMA fit. Incorporating crater counts made on LROC WAC mosaics would further improve count statistics by including craters ≥500–700 m in diameter. Ideally areas large enough to include significant numbers of diameters ≥1 km are measured because the lunar chronology is tied to the 1 km reference diameter and the larger diameter bins are crucial to determining a statistically robust AMA. Thus, utilizing counts from NAC and WAC mosaics for age

determination of mare surfaces estimated to be ≥3.0 Ga (i.e., most maria with the exception of some regions in Oceanus Procellarum; Hiesinger et al., 2003) enables measurement of the equilibrium (to derive regolith depth estimates) and the production population (to derive AMAs). Of course, for age measurements of very young features (e.g., impact melt, Copernican-aged craters) and spatially limited areas (e.g., highland ponds; Robinson et al., 2011), using only NAC images is necessary because the small crater population (10 m to ~500 m in diameter) is critical to age determination, and measurements on WAC images will not resolve craters ≤500 m in diameter.

Table 2.3. Number of Craters Identified for Specific Bins, Individual L.*

D (km)	AS15-M-1010	AS15-M-1152	AS15-M-1835	AS15-M-2461
0.07	921	751	407	111
0.08	629	503	298	80
0.09	484	339	223	49
0.1	326	272	171	48
0.11	232	237	140	41
0.12	162	136	109	38
0.13	153	132	103	45
0.14	107	119	84	39
0.15	169	165	104	43
0.17	119	132	88	61
0.2	117	117	122	52
0.25	39	46	38	33
0.3	21	19	9	18
0.35	6	9	18	8
0.4	5	8	7	5
0.45	4	2	3	7
0.5	2	3	2	0
0.6	2	1	2	3
0.7	0	1	0	0
1.2	1	1	1	1

*Not cumulative.

2.7. Conclusions: Optimal Incidence Angle

Previous studies investigating crater frequencies utilized images with incidence angles ranging from ~60° to 80° based on available image data (e.g., Shoemaker et al., 1969; Gault, 1970; Greeley and Gault, 1970; Soderblom, 1970; Baldwin, 1971; Soderblom, 1972; Soderblom and Lebofsky, 1972; Boyce and Dial, 1975; Young, 1975; Neukum et al., 1975a; Boyce, 1976; König, 1977; Schultz et al., 1977; Baldwin, 1985; Hiesinger et al., 2000; 2003). However, using the same (or similar) incidence angle images for all measurements was not always possible (e.g., Neukum et al., 1975a; Neukum and König, 1976; König, 1977; Hiesinger et al., 2000). Over a 30° incidence angle range, Young (1975) found a 25% change in apparent measured diameter for 100 m craters, suggesting that crater measurements made on multiple images with different incidence angles could provide significantly different derived ages. The global LROC WAC observations (Robinson et al., 2010; Speyerer et al., 2011) provide an opportunity to complete crater measurements at a constant average incidence angle for large areas and for diameters ≥700 m (e.g., **Chapter 3**). Similarly, spatially limited features visible in LROC NAC images are often located within a single image or image pair, where incidence angle is nearly constant.

The results presented here, that incidence angle (50°–87°) affects the number of craters counted and the sizes measured, have significant implications for different aspects of crater measurement analyses and improve upon previous findings (e.g., Soderblom, 1972; Young, 1975; Schultz et al., 1977; Wilcox et al., 2005). The four Apollo Metric images (Figure 2.5, 2.11–2.13, 2.15) return AMAs of ~3.5 Ga for the Mare Imbrium study area, while estimates of the equilibrium crater diameter decrease significantly with

decreasing incidence angle. The SFDs at the Apollo 11 Landing Site measured on NAC images (64° and 82° incidence angle) are statistically inseparable, but the derived AMAs differ as a result of the small number of craters counted in the largest bins. Measured crater frequencies in Mare Serenitatis using 46° and 66° incidence angle WAC mosaics return AMAs of ~3.4 and ~3.5 Ga, respectively, and the AMA for the 46° incidence angle image reflects the underestimation of crater diameters. In this work, the difference in estimated equilibrium crater diameter exceeds 30 m for images taken at incidence angles over a range of ~20°. The range in crater equilibrium diameter in turn directly affects estimates of average regolith depth.

Selecting images with an appropriate incidence angle range is dependent on the measurement objective (e.g., estimates of AMAs, equilibrium crater diameter, regolith depth). Crater frequencies measured on images acquired over incidence angles ranging between ~65° and 80° do have differences (Figure 2.10, 2.14, 2.16, 2.18, 2.22, 2.23). AMAs derived for the different regions (Mare Imbrium, Mare Tranquillitatis, and Mare Serenitatis) produce different ages, even though the majority of AMAs agree within the statistical uncertainties for each study area. Thus, AMAs for a unit or between units will be most consistent when SFDs are measured on images with the same or similar incidence angles (i.e., within a few degrees). An optimal incidence angle range for relative and absolute age dating studies is between ~65° and 80°. Small incidence angle images (<60°) are not as useful for AMA derivation because the smaller incidence angle promotes measurements that underestimate crater diameter and the resulting AMAs. Conversely, equilibrium crater diameter estimates and subsequent inferred regolith depths are significantly influenced by changes in incidence angle over the ~65°–87° range,

confirming earlier hypotheses (Soderblom, 1972; Young, 1975; Wilcox et al., 2005). Measurements made on smaller incidence angle (64° and 71°) images underestimate crater diameters relative to those made on images at larger incidence angles, leading to equilibrium crater diameter estimates that are too small. Instead, measurements at larger incidence angles (82° and 87°) suggest that the emphasis of the break in slope at the perceived crater rim (due to shadowing) allow a more accurate determination of crater diameter and thus equilibrium crater diameter, a result consistent with previous work (Wilcox et al., 2005). Although more craters are detected on the surface at 87° than at 71° incidence angle in the Apollo Metric images, the enhancement of subtle topography and pronounced shadows in the 87° incidence angle image hides nearby smaller craters in the shadows of larger craters (e.g., Moore, 1972; Soderblom, 1972; Wilcox et al., 2005). Consequently, crater counts on images taken at ~80° incidence angle should provide the most accurate equilibrium crater diameter and regolith depth estimates by detecting more craters than measurements made at 71° incidence angle while mitigating the effects of enhanced shadows observed at 87° incidence angle.

CHAPTER 3

AREAL CRATER DENSITY ANALYSIS OF VOLCANIC SMOOTH PLAINS: A NEW APPROACH TO DISTINGUISHING AGE UNITS

3.1. Introduction

Unraveling relative and absolute model ages for defined geologic units on planetary surfaces relies on observed superposition relationships and measurements of crater size-frequency distributions (SFD). Of the two methods, SFD analysis is the primary technique used to distinguish relative ages for mare smooth plains units, which can then be translated into absolute age estimates. Absolute age chronologies rely on crater counts calibrated to radiometric ages of returned samples (e.g., Hartmann et al., 1981; Neukum, 1983), and with the exception of the Moon, samples of known surface provenance from other bodies do not exist.

The lunar maria were emplaced over an extended period of time (>2 Ga; e.g., Hartmann et al., 1981; Stöffler et al., 2006; Hiesinger et al., 2011), and mare units exhibit marked color differences in multispectral data that are interpreted to correlate with distinct mineralogical units and ages (e.g., Pieters, 1978; Hiesinger et al., 2000; Staid and Pieters, 2001; Hiesinger et al., 2011; Staid et al., 2011). Efforts using crater counts to date color units identified within Mare Imbrium (e.g., Schaber et al., 1975; Hiesinger et al., 2000; Bugiolacchi and Guest, 2008; Hiesinger et al., 2011), measures of crater morphology and degradation (e.g., Schaber, 1973; Boyce et al., 1974; Boyce and Dial, 1975; Boyce, 1976), and geologic mapping (Carr, 1965; Moore, 1965; Hackman, 1966; Schaber, 1969; Page, 1970; M'Gonigle and Schleicher, 1972) provide a relative and absolute timeline of lunar mare emplacement in this region. From these studies, most

agree that volcanic filling of the Imbrium basin occurred in three primary phases. The older basalts are interpreted to be Imbrian in age (e.g., Schaber, 1969) and are exposed mostly in the east, while the younger basalts are Eratosthenian and late Imbrian in age (e.g., Page, 1970) and are found in the western portion of the Imbrium basin. Multispectral classification was used to distinguish geologic units prior to commencing crater counts and deriving absolute model ages (e.g., Schaber et al., 1975; Pieters, 1978; Hiesinger et al., 2000; Staid and Pieters, 2001; Bugiolacchi and Guest, 2008; Staid et al., 2011), but not all planetary bodies exhibit multispectral differences within volcanic units (age and composition), as is the case on Mercury (e.g., Robinson et al., 2008; Denevi et al., 2009; 2013a).

Here, areal crater density (ACD) analysis is used as a novel approach to identify resurfacing boundaries within Mare Imbrium (Figure 3.1), as a test case for mercurian studies. ACD as a measurement tool was successfully employed to investigate variations in crater retention age across the lunar surface (Head et al., 2010), and to compare lunar and mercurian crater populations (Fassett et al., 2011). After developing a refined methodology, ACD measurements within Mare Imbrium show a regional boundary at the contact between two spectrally distinct regions. The geologic contact is confidently observed in ACD maps derived for a study region of ~1×10^4 km^2, which should be considered a minimum area size to use for crater counting in the mare. In addition, I identify far-flung, non-obvious secondary craters with the ACD measurement technique, which comprise a significant portion of the crater population with diameters between 500 m and ~850 m and indicate that absolute model dating of the mare should be limited to craters ≥1 km in diameter (in agreement with e.g., Neukum et al., 1975a; Neukum,

1983; McEwen and Bierhaus, 2006). Geologic units dated as older (3.2–3.6 Ga from Hiesinger et al., 2000; 3.0–3.3 Ga from Bugiolacchi and Guest, 2008) exhibit higher ACD (>35652 craters with diameters ≥500 m per 10^6 km^2) and younger units (2.0–3.0 Ga from Hiesinger et al., 2000; 2.2 Ga from Bugiolacchi and Guest, 2008) have lower ACD (<25974 craters with diameters ≥500 m per 10^6 km^2), and the ACD results are in agreement with other dating studies of this region (e.g., Schaber, 1973; Boyce and Dial, 1975; Schaber et al., 1975). Furthermore, spectral units with modeled absolute age differences of several hundred million years (Hiesinger et al., 2000) are not observed in the ACD map created here, suggesting that while the reported ages are statistically different, the ages may not be geologically meaningful. Thus, ACD measurements provide a reliable technique to distinguish relative ages among geologic units when spectral information is not available or units do not exhibit spectral contrasts, as well as provide a means to explore the statistical significance of published absolute model ages.

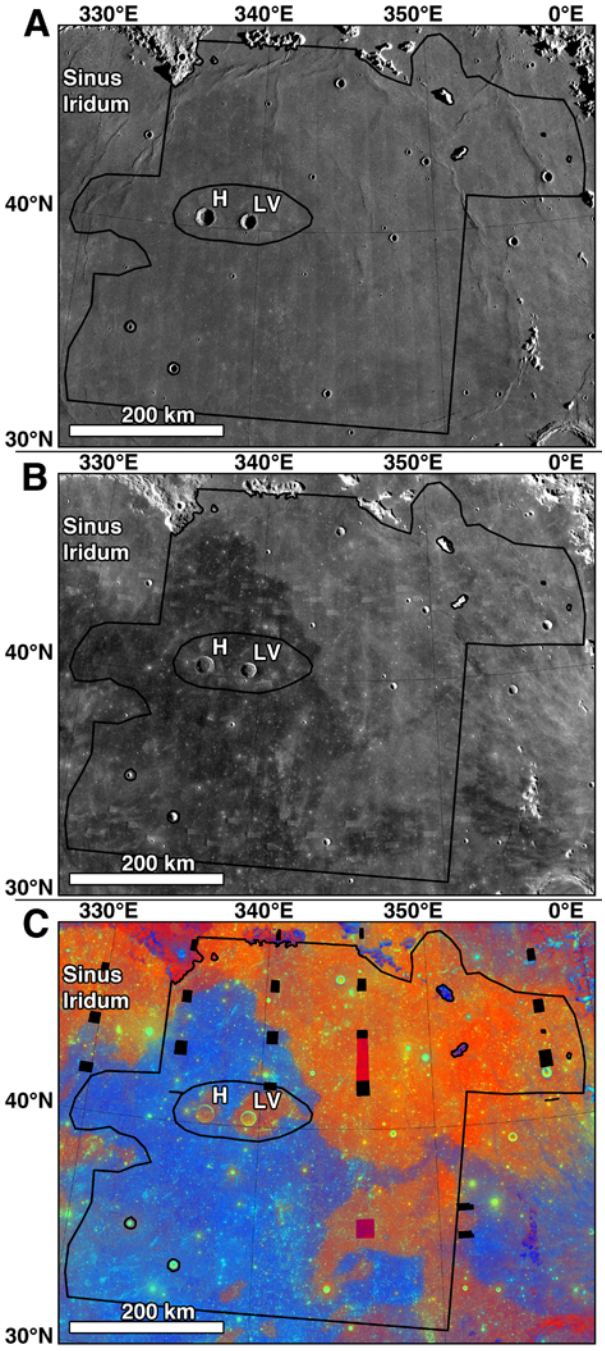

Figure 3.1. Mare Imbrium study area outlined in black, covering a total area of 2.27×10^5 km^2, shown in equal area projection. Sinus Iridum, Helicon crater (H, 40.42°N, 336.89°E, diameter ~24 km) and Le Verrier crater (LV, 40.33°N, 339.39°E, diameter ~21 km) identified in (A). (A) LROC WAC monochrome normalized reflectance mosaic with an average incidence angle of 75°, (B) LROC WAC normalized reflectance mosaic with an average incidence angle of 57°, and (C) Clementine multispectral ratio mosaic (R=750/415, G=750/950, B=415/750).

3.2. Methods and Data

3.2.1. Data and Study Region

The Lunar Reconnaissance Orbiter Camera Wide Angle Camera (LROC WAC) 100 meter pixel scale monochrome mosaics (Robinson et al., 2010; Speyerer et al., 2011) at large (75°) and small (57°) solar incidence angles (measured from the surface normal, noontime is 0°) in an equal-area map projection were used to identify an area within Mare Imbrium (~1145 km diameter, centered at 33°N, 345°E). In addition, a ratio composite mosaic was derived using Clementine UV-VIS multispectral 100 meter pixel scale images (Nozette et al., 1994; McEwen and Robinson, 1997). From the 415–750–950 nm Clementine UV-VIS filters, RGB colors were mapped to red = 750/415 nm, green = 750/950 nm, and blue = 415/750 to enhance color variations representative of mineralogical variability and normalize differences in albedo (Belton et al., 1992). A region centered at 39.77°N, 342.99°E and encompassing 2.27×10^5 km^2 (Figure 3.1) was selected that contained strong spectral contrasts in the Clementine multispectral data and also large published model age differences (Hiesinger et al., 2000; Bugiolacchi and Guest, 2008). The spectral boundary was approximately centered within the count area to promote comparable sampling areas for density analysis.

Within the study area, there are two spatially expansive spectral units: red and blue, characterized primarily by differences in spectral reflectance in the visible to near-infrared (415 nm to 1000 nm). The spectral units correspond with variations in composition and age of emplacement (e.g., Schaber, 1973; Boyce and Dial, 1975; Schaber et al., 1975; Pieters, 1978; Hiesinger et al., 2000; Staid and Pieters, 2001; Bugiolacchi and Guest, 2008; Staid et al., 2011). The blue unit, covering the western

portion of Mare Imbrium (1.08×10^5 km^2), contains ~18–20 wt% FeO and ~8–10 wt% TiO_2, estimated from Clementine multispectral reflectance (Lucey et al., 2000). Comparatively, the red unit, covering eastern Mare Imbrium (1.20×10^5 km^2), contains ~15–18 wt% FeO and ~1–3 wt% TiO_2 derived from Clementine spectral measurements (Lucey et al., 2000). Previous work by Hiesinger et al. (2000) and more recent work by Bugiolacchi and Guest (2008) subdivided the two sizeable spectral units into several smaller units based on subtle spectral variations that were subsequently dated using crater counts. However, here only a single red unit (average model age 3.5 Ga from Hiesinger et al., 2000; 3.3 Ga from Bugiolacchi and Guest, 2008) and a single blue unit (average model age 3.0 Ga from Hiesinger et al., 2000; 2.2 Ga from Bugiolacchi and Guest, 2008) are considered because the primary focus is to use ACD measurements to test if crater density contrasts can independently discriminate two units with significant age differences.

3.2.2. Crater Counting

Interpretation of crater counts assume that cratering is a random process and that accumulation of craters over time for a given surface reflects the age of that surface (e.g., Neukum et al., 1975a; McGill, 1977; Hartmann et al., 1981; Neukum, 1983). For crater counting results to be valid (e.g., used to derive absolute model ages), only primary craters should be considered and the region in question should be comprised of an area of uniform age, assumed to consist of one geologic unit (e.g., Neukum et al., 1975a; 1975b; McGill, 1977; Hartmann et al., 1981; Neukum, 1983). Since older surfaces have accumulated more primary craters than younger surfaces, a measure of ACD should

reflect spatial variations in crater retention across volcanic plains, indicating differential regions of resurfacing, and thus age units.

I utilized the CraterTools extension (Kneissl et al., 2011) to ESRI ArcMap Desktop 10 geographic information systems (GIS) software to count all approximately circular, non-overlapping craters with diameter, D ≥500 m using the LROC WAC mosaics. Obvious secondary craters forming crater chains, herringbone patterns, and overlapping clustered groupings of craters were excluded from the measurements, and the areas containing obvious secondaries were excluded from the final count area.

From these crater counts, I derived absolute model ages using the CraterStats software (Michael and Neukum, 2010) by employing the Neukum et al. (2001) chronology function to the data and displayed the results in the cumulative crater size-frequency plot (Crater Analysis Techniques Working Group, 1979). Additionally, I determined the crater retention age, which is the number of craters of a given diameter, D, normalized to 10^6 km^2 and written as N(D). N(D) uncertainties are approximated by ±one standard deviation, calculated as the square root of the number of craters (Crater Analysis Techniques Working Group, 1979). N(0.5) and N(1) values for the study area provide a means to assess relative ages of geologic units independent of isochron model age fits of the data to the lunar chronology function.

3.2.3. Measuring Areal Crater Density

3.2.3.1. Display

The ACD maps may be displayed in numerous ways (e.g., grayscale, color scale, color classified, discrete values, etc.), and here the ACD is displayed in a three-color classification scheme. Classification simplifies the presentation of the ACD map to

emphasize statistically significant density variation (resulting from age differences). The three classes are determined from Poisson probabilities, the calculation of which provided statistical support for appropriate neighborhood radius size selection (Section 3.2.3.2). The Poisson probabilities calculated for the 10^{th} percentile of the observed crater population within the study region (Section 3.2.3.2) provide statistically meaningful bounds on which to base the color classification, and 80% of the observed population should be contained within the calculated range (52–70 craters per average neighborhood, corresponding to N(0.5) = ~25975–35651).

3.2.3.2. Output Cell Size and Neighborhood Radius

ACD is determined from a point density calculation and the center of each crater is represented as a point; geologic application of point density for spatial analyses are discussed in detail by Davis (2002). The point density calculation in ArcMap 10 employs a moving neighborhood approach, where no weighting factor is assigned to crater center points on the basis of crater diameter, and the output cell size and the neighborhood radius are user-defined. Output cell size is the measurement unit used during the density calculation ("pixel size" of resulting raster), and varying output cell size affects the density plot appearance. Figure 3.2A-C illustrates the effects of changing output cell size on the density calculation. With a neighborhood radius of 25 km, an output cell size of 1 km produces a density map with fine details (Figure 3.2A). However, increasing output cell size to larger sizes, such as 5 km (Figure 3.2B) and 10 km (Figure 3.2C), produces a visibly pixelated density map without small-scale detailed structure while retaining regional density trends.

In contrast, varying neighborhood radius alters the spatial structure observed in the resulting density map such that smaller neighborhood sizes emphasize statistical variations and larger neighborhood sizes smooth real variation. Figure 3.2D-F demonstrate the effects of different neighborhood radii. Using an output cell size of 1 km, small neighborhood sizes emphasize local (small area) variations, as is the case with a 10 km radius (Figure 3.2D). For a 10 km radius, the number of craters with D ≥500 m per average neighborhood, *n*, is 10. There is a 13% chance that the neighborhood will contain ≤6 craters and a 14% chance that the neighborhood will contain ≥14 craters, indicating that most of the density variation is statistical in nature and that the neighborhood area is too small. Selecting a neighborhood radius of 25 km (Figure 3.2E) provides robust sampling across the study area (>30 craters per average neighborhood; e.g., Silverman, 1986; Davis, 2002) that emphasizes regional density variations (distinct "high" and "low" density areas) while also displaying smaller local variations in density (Figure 3.3A). For a 25 km neighborhood radius, $n = 61$, and the standard deviation (estimated as $n^{0.5}$ for n craters) is 7.8, so the calculated density map is robust at the ~13% level against the crater count statistics for terrain of "average" age (i.e., representative of average neighborhoods). There is an 11% chance that a neighborhood will contain ≤51 craters and ≥71 craters. There is only a 2% chance that a neighborhood will contain ≤45 craters or ≥78 craters, demonstrating that most of the variation in crater density is real as opposed to statistical noise. Large neighborhood sizes smooth both local and regional variation, as is the case with a 50 km radius (Figure 3.2F), where $n = 245$. There is an 11% chance that the neighborhood will contain ≤225 craters or ≥265 craters. Therefore, while variation in the density map will reflect real variations in crater frequency at the regional scale,

determining the influence of statistical noise will be difficult. Regional boundaries, if present, will be greatly smoothed, and local, small area variations that reflect surface geology (erasure due to ejecta emplacement, formation of non-obvious secondaries) will be lost, suggesting that a 50 km radius is too large for the crater population and study area in Mare Imbrium (Figure 3.3B).

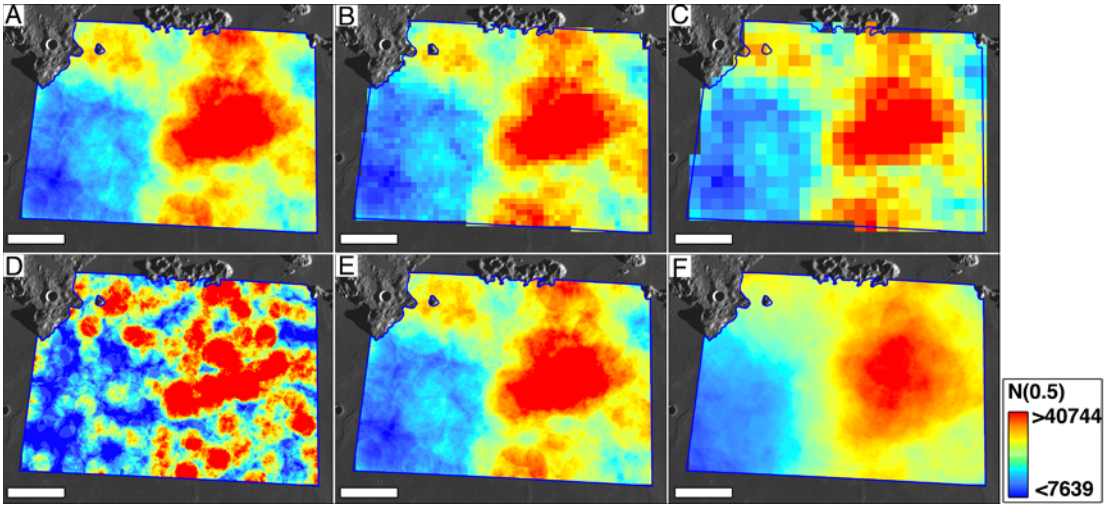

Figure 3.2. Effects of variation on output cell size and neighborhood radius on the resulting ACD measurements. Scale bar is 50 km. Neighborhood radius of 25 km: (A) output cell size of 1 km, (B) 5 km and (C) 10 km. Output cell size of 1 km: (D) 10 km radius, (E) 25 km radius, and (F) 50 km radius. Refer to text for detailed discussion; rainbow color ramp used to help clarify changes resulting from output cell and neighborhood radius differences.

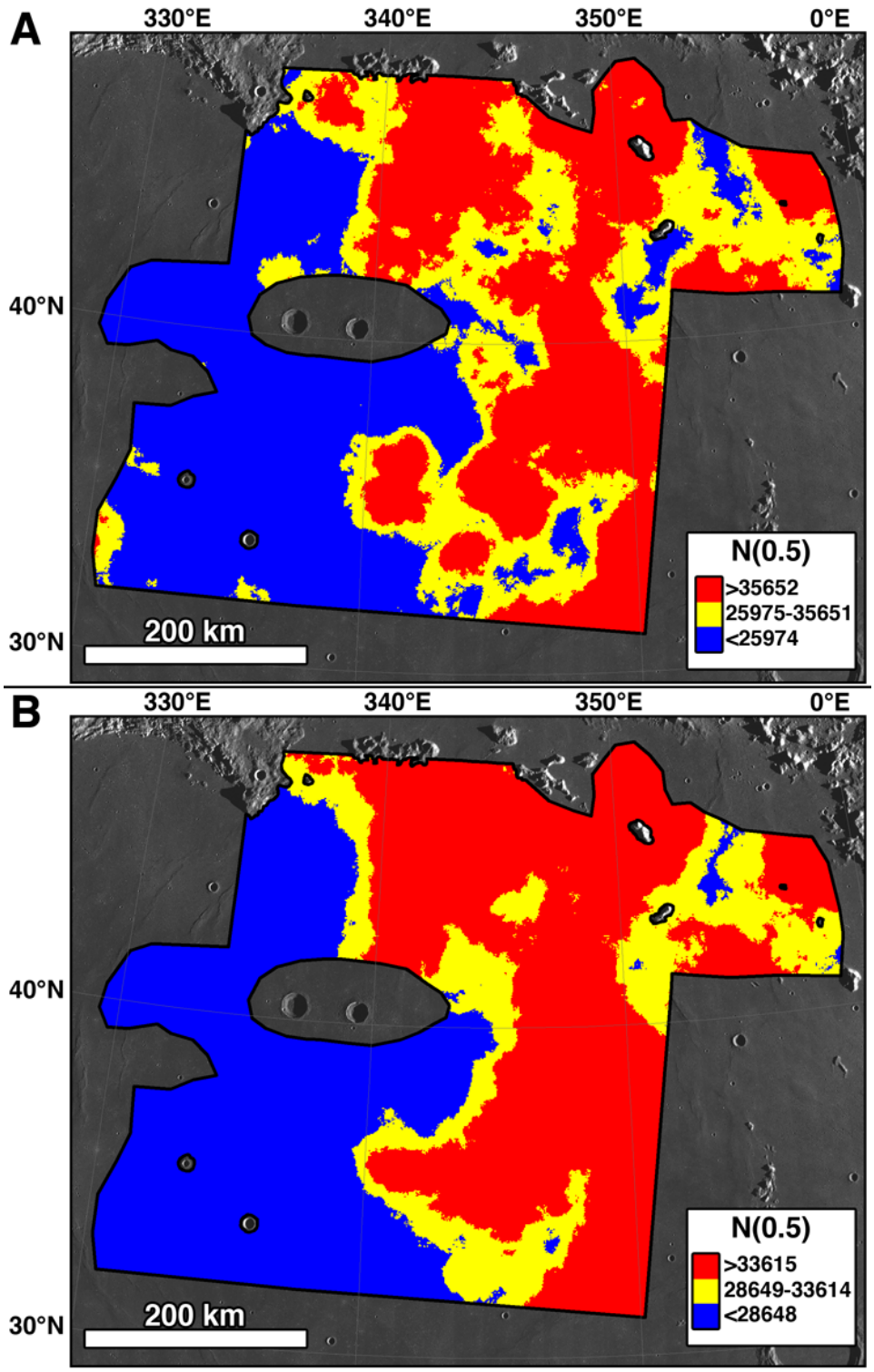

Figure 3.3. ACD maps centered at 39.77°N, 342.99°E in Mare Imbrium. Output cell size is 1 km and neighborhood radius is 25 km (A) and 50 km (B). Both maps exhibit a northwest to southeast regional boundary; for the larger neighborhood radius, local crater density variations are smoothed. Color classification boundaries reflect the 10th percentile for the measured crater populations. Table 3.4 provides regional ACD values for (A).

3.2.3.3. Edge Correction

The point density measurement in ArcMap 10 does not natively correct for edge effects resulting from calculations within neighborhoods near the data collection boundary. Within ArcMap 10, I investigated two methods to minimize edge effects on the final ACD. First, and easiest to employ, is a buffered approach whereby the boundary of the ACD map is buffered to a distance of one neighborhood radius. Thus, for a density map derived using a neighborhood radius of 25 km, creating a boundary by subtracting 25 km from all edges will guarantee that the resulting ACD magnitudes include only neighborhoods that are within the region of data collection. While this method effectively removes all edge effects, it by nature reduces the size of the study area.

To minimize data loss, I employed a second approach to correct for edge effects, which I call “point correction”. The point correction is a weighted edge correction method (e.g., Silverman, 1986; Haase, 1995; Goreaud and Pélissier, 1999; Pommerening and Stoyan, 2006) that determines the proportion of neighborhood area included within the study region (Figure 3.4; Appendix C details the procedure). When the point correction is applied to the measured areal point crater density, the corrected ACD map reflects the proportion of the study area contained within each neighborhood at each output cell location (Figure 3.4, 3.5). Hereafter, any term referring to density measurements considers the corrected areal crater point density unless otherwise specified.

I assessed the effectiveness of the point correction method by comparing the computed corrected ACD maps for overlapping subareas of increasing size within the study region (Figure 3.6). Density differences, limited to within 25 km of the boundary

(one neighborhood radius), reflect the inclusion of data beyond the boundary and do not represent edge artifacts. To illustrate, a black circle with a 25 km radius was placed near the boundary of the subarea within the area exhibiting subarea and entire study region density differences (Figure 3.7; Table 3.1). The uncorrected subarea density (Figure 3.7A) exhibits a large and small region of high magnitude (red, N(0.5) ≥35652), surrounded by an area of moderate magnitude (yellow, N(0.5) = 25975–35651), which is in turn surrounded by low magnitude (blue, N(0.5) ≤25974). The high and moderate uncorrected densities have rounded boundaries that do not extend to the edge of the subarea (Figure 3.7A). However, when the point correction (Figure 3.7B, Figure 3.8) is applied, the spatial extent of the low density region decreases (Figure 3.7C).

The ACD measurement is derived from crater data contained within the defined study region, and therefore, expanding the study area may cause a change in the crater density magnitudes near the original, unexpanded boundary area. When the ACD for the entire study area within Mare Imbrium is compared to that of the subarea, one marked change between the measurements is the decrease in size of the low density region in the southeast corner (Figure 3.6C, 3.7B, 3.7C), and difference maps scaled to one percent and five percent (Figure 3.9) reveal the effect of additional data on the ACD measurement. A difference of <0.99 or <0.95 in the one percent and five percent difference maps, respectively, indicates that the subarea density values exceed the entire region density values, and the extent of the difference corresponds to the low density area surrounded by intermediate values in the subarea density map. When new data are included that extend beyond the subarea boundary, there is a greater measured crater frequency beyond the boundary and this increase in measured crater frequency influences

the density calculation because those data are now used for density calculations for neighborhoods located within 25 km of the subarea boundary. Likewise, differences >1.01 and >1.05 in the one percent and five percent maps (Figure 3.9) reflect a decrease in measured crater frequency for the area extending beyond the subarea boundary.

This concept is further emphasized when a 30 km buffer is applied to the subarea to create a second, smaller region (2.16×10^4 km^2, comprising ~50% of the original subarea, Figure 3.10). Differences are only observed between the smaller region and the original subarea within 25 km of the boundary (Figure 3.10C, 3.10D), reflecting the inclusion of data in the density calculation for the original subarea as opposed to errors related to improper application of the point correction. Furthermore, the smaller region may be considered to be a minimum area size upon which to apply the ACD measurement technique (Figure 3.10B) because the density values match between the original subarea and smaller region in the central portion of the difference map. This area, which is ~8800 km^2 in size, exhibits the regional boundary between spectral units interpreted to represent two distinct crater populations. However, the large proportion of area contained within 25 km to the boundary in this small region suggests that larger measurement sizes are preferable when available, a finding further emphasized by the results from successive increases in study area size (discussed above).

Table 3.1. Density Differences at Boundary, within Example Neighborhood[a].

Dataset	Minimum N(0.5)	Maximum N(0.5)	Average N(0.5)[b]	N(0.5) Neighborhood Center
Subarea_uncor[c]	17825	46855	32877 ± 181	28011
Subarea	32859	49439	39290 ± 198	35903
Entire Area	28011	46855	37973 ± 195	37179

[a]Neighborhood centered at 44.949°N, 345.450°E.
[b]Uncertainty estimates were calculated from the square root of the number of average craters.
[c]Subarea_uncor = uncorrected ACD for subarea.

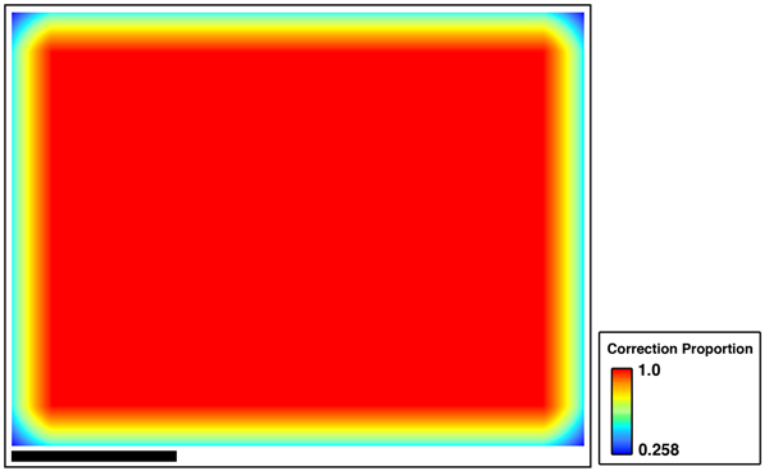

Figure 3.4. Point correction example for a rectangular measurement area, grid spacing is 100 m. The map illustrates that output cells within the central region of measurement do not require a correction, whereas output cells located proximal to the edge will cause neighborhoods to contain a proportion of valid data. Scale bar is 100 km.

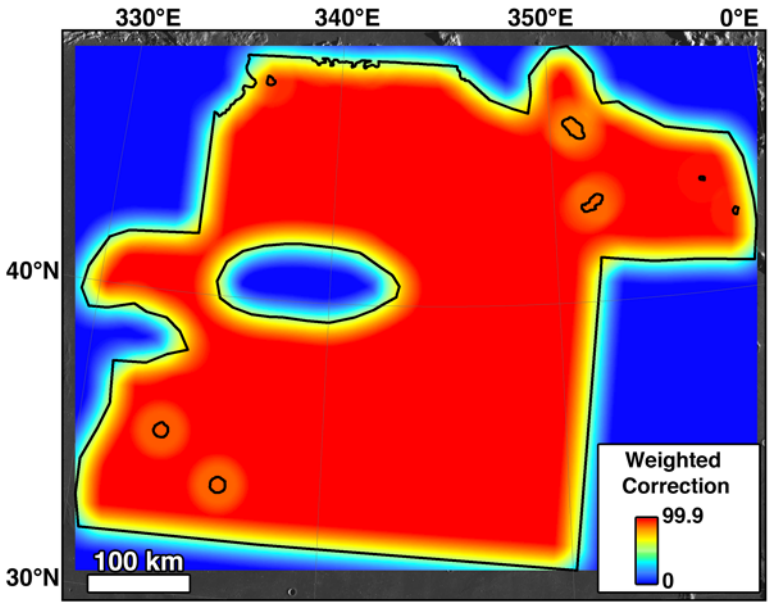

Figure 3.5. Point density for the 100 m spaced point correction applied to the observed ACD for the entire study region. The point correction is derived by dividing each point density value by the maximum value (99.9) to calculate the proportion of valid data within the neighborhood area.

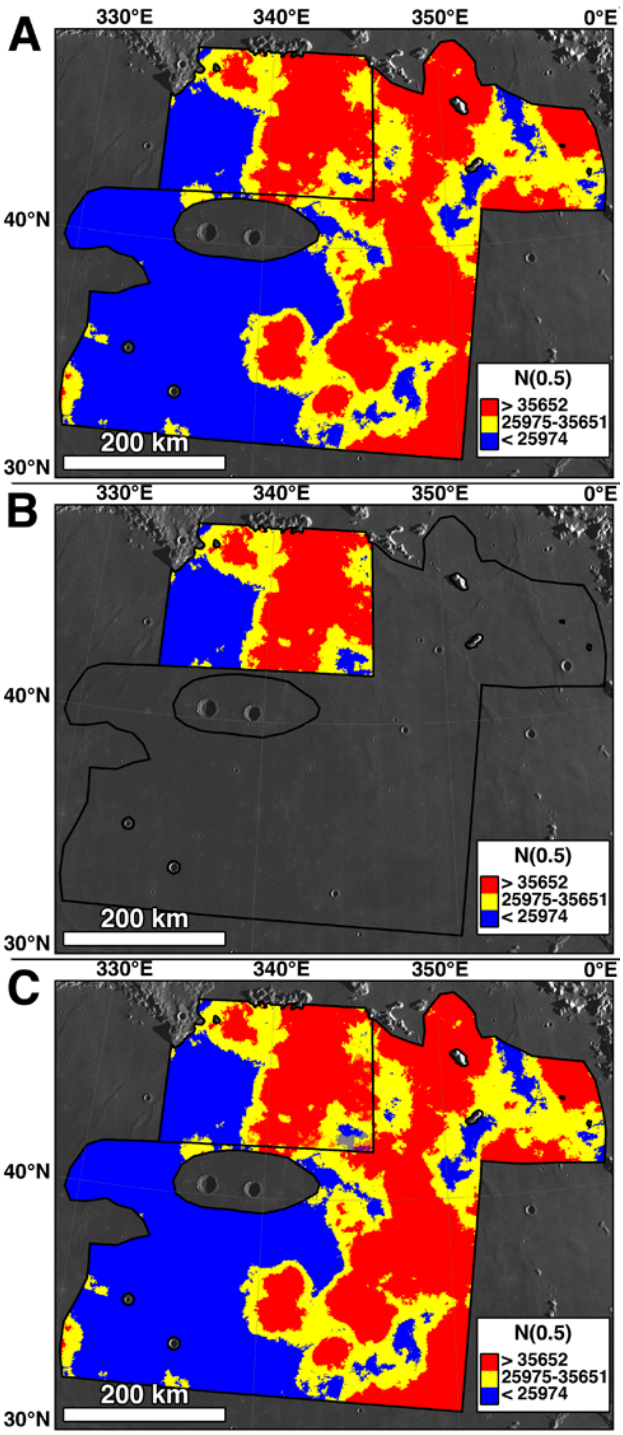

Figure 3.6. (A) ACD for the entire study region (2.27×10^5 km^2), subarea boundary (4.48×10^4 km^2) overlaid for reference. (B) Subarea ACD shown in relation to entire study region. (C) ACDs: subarea (50% transparency) overlaid on entire study region. Solid colors reflect the same density measurements between the subarea and the entire study region. Partially transparent areas (e.g., lower right corner of the subarea) reflect differences in density measurements (Figure 3.9), limited to within 25 km of the subarea edge.

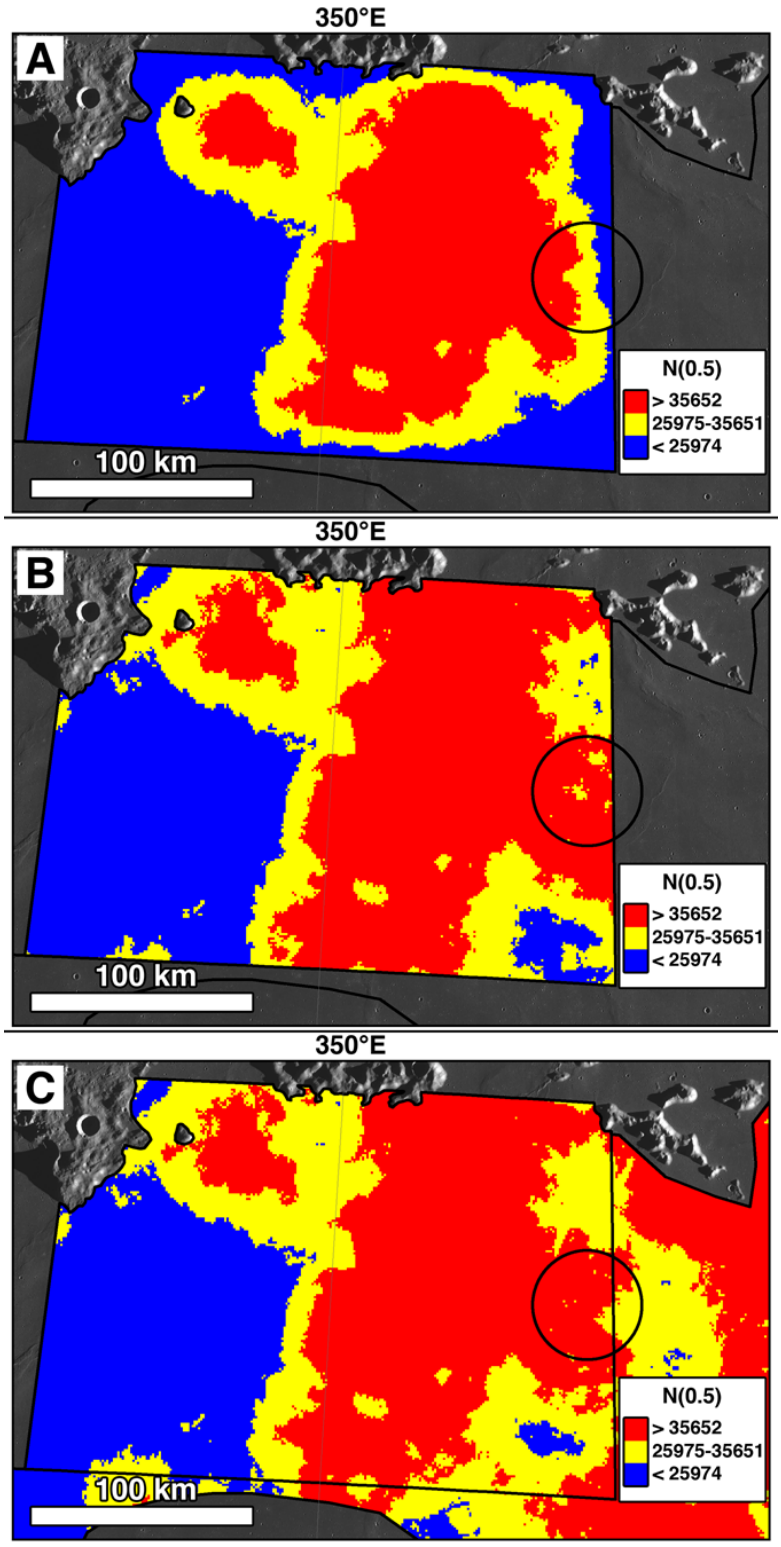

Figure 3.7. (A) Subarea uncorrected ACD. (B) Subarea corrected ACD. (C) ACD map for the entire study area, centered within the subarea. Black circle (25 km radius) is a representative neighborhood area used to observe differences between density measurements (Figure 3.9).

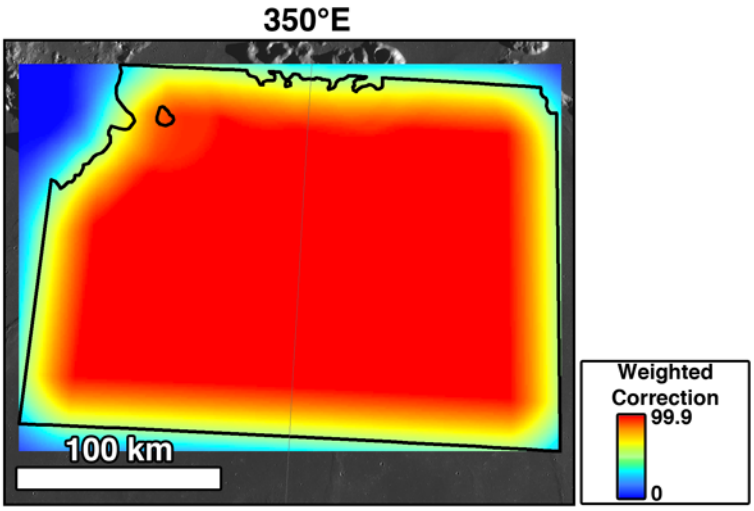

Figure 3.8. Point density for the 100 m spaced point correction applied to the observed ACD for the subarea within Mare Imbrium. The point correction is derived by dividing each point density value by the maximum value (99.9) to calculate the proportion of valid data within the neighborhood area.

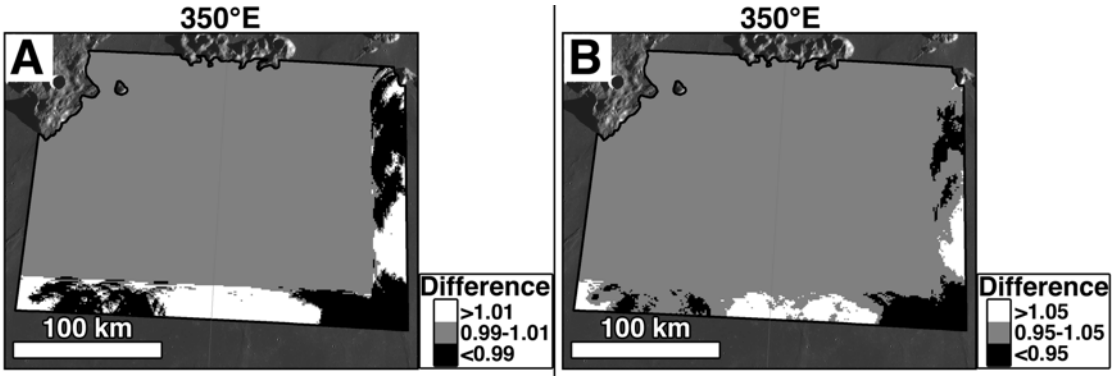

Figure 3.9. ACD difference maps created from the subarea and entire study region measurements (Figure 3.6, 3.7); (A) one percent and (B) five percent difference maps. Differences are limited to ≤25 km from the subarea boundary and reflect the addition of data beyond the subarea boundary for calculation of the entire study region density.

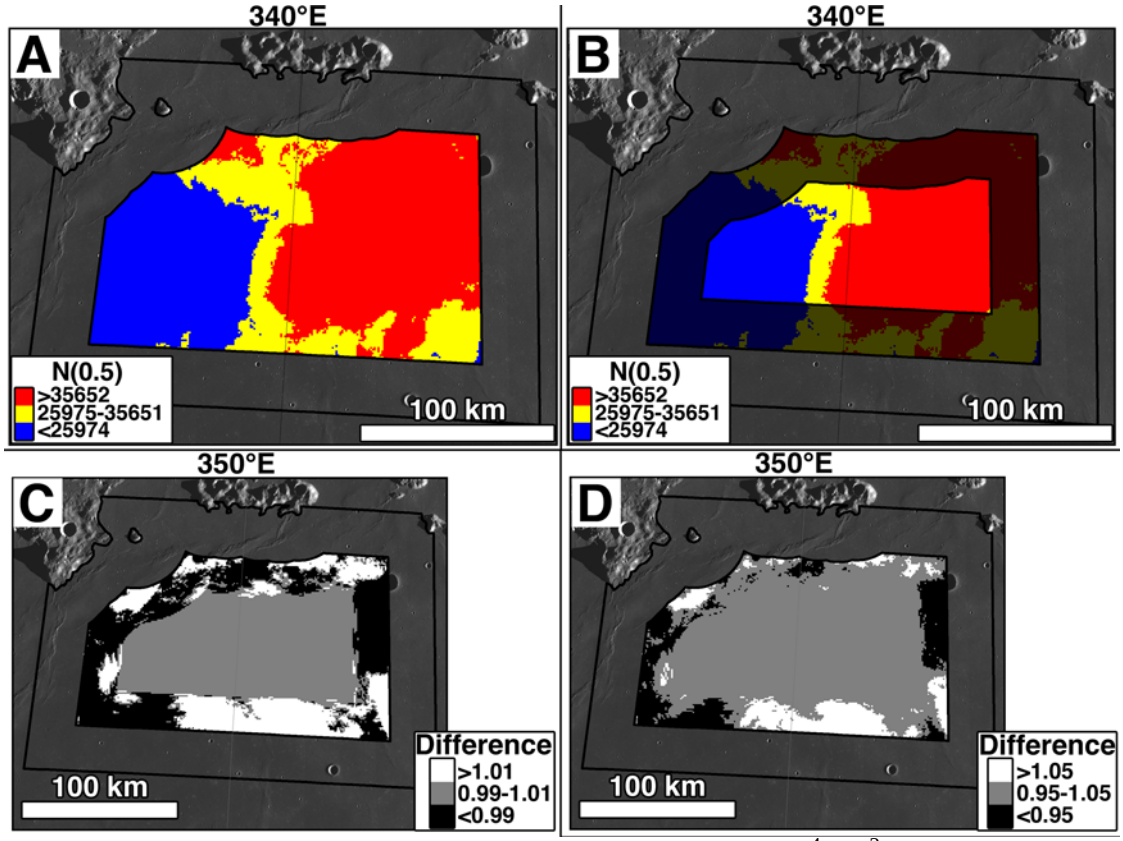

Figure 3.10. Measured ACD for the smallest subarea (2.16×10^4 km^2), and two distinct density units are observed (A). (B) ACD map where the area within 25 km of the boundary is shadowed to show the valid measurement area of ~8800 km^2 (i.e., no difference in density magnitude). (C) One percent and (D) five percent difference maps, created from the ACD measurements for the original subarea and a 30 km buffered smaller area and from which the valid measurement area for the smallest subarea was derived.

3.2.3.4. Statistical Versus Geologic Variations

To establish where ACD values reflect real geologic differences compared to variation resulting solely from poor statistics (i.e., small numbers of counted craters), synthetic ACD maps were generated for the study region using the measured crater frequencies and by employing the Create Random Points tool in ArcMap 10. This tool calculates a random distribution for a specified number of points within a feature, requiring user-input of a polygon boundary and the number of points to be distributed within the polygon.

Two different types of synthetic density maps were generated. One version considered the approximate crater frequency for the entire study area, to explore regional variations and the extent to which the measured ACD regional variations have geological meaning. For the study area as a whole, 7100 points, the combined measured cumulative crater frequency for D ≥500 m rounded to the nearest hundred, were randomly distributed (Figure 3.11). The second synthetic ACD map used the approximate cumulative crater frequency for each spectral unit, to explore the extent of local variation that is expected statistically within a geologic unit. Random points were generated for the separate spectrally red and blue geologic, with 4900 and 2200 points distributed within the unit boundaries (measured cumulative crater frequencies for D ≥500 m, Figure 3.12). The two distributions were then merged, and synthetic ACDs were calculated from these combined data.

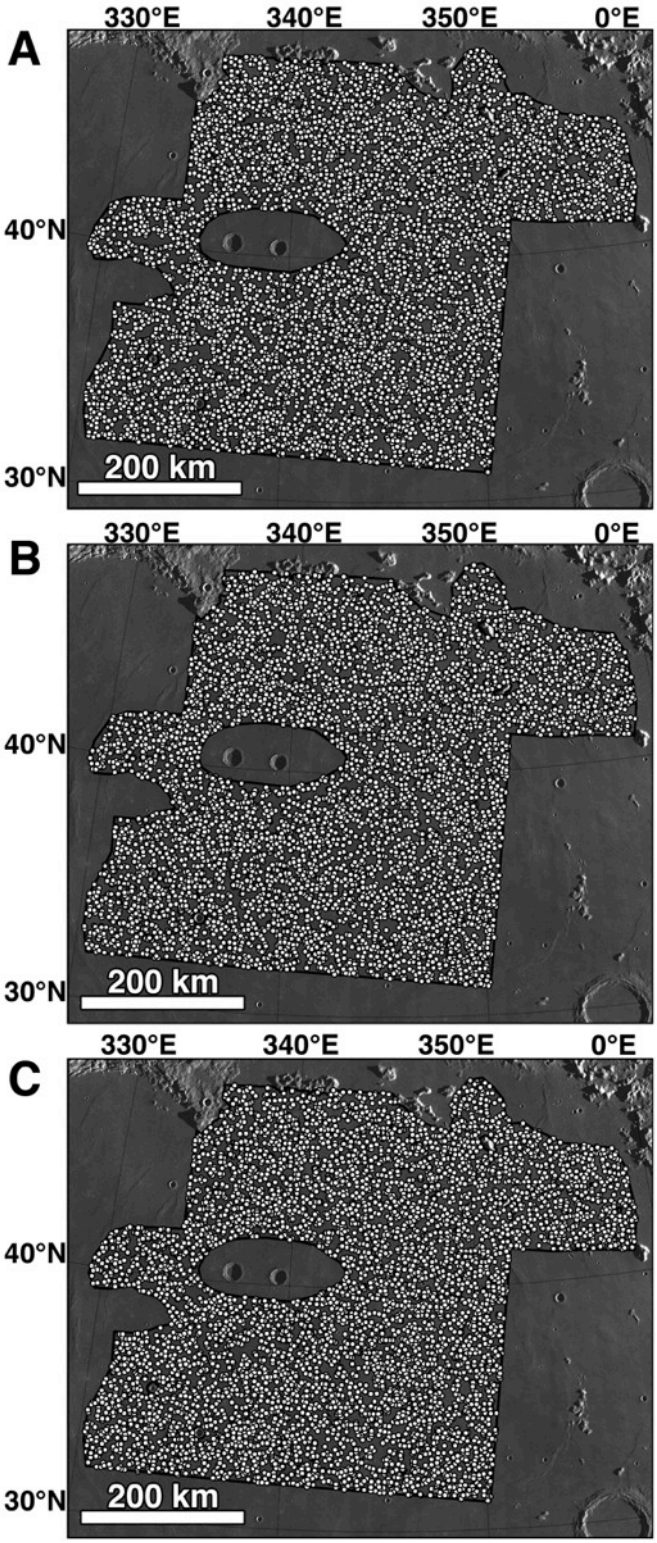

Figure 3.11. Three different random point distributions used to create synthetic areal density maps, reflecting the overall crater frequency (7100 points) for the study area. Each point represents one crater center. Resulting density maps shown in Figure 3.24, ACD values presented in Table 3.8.

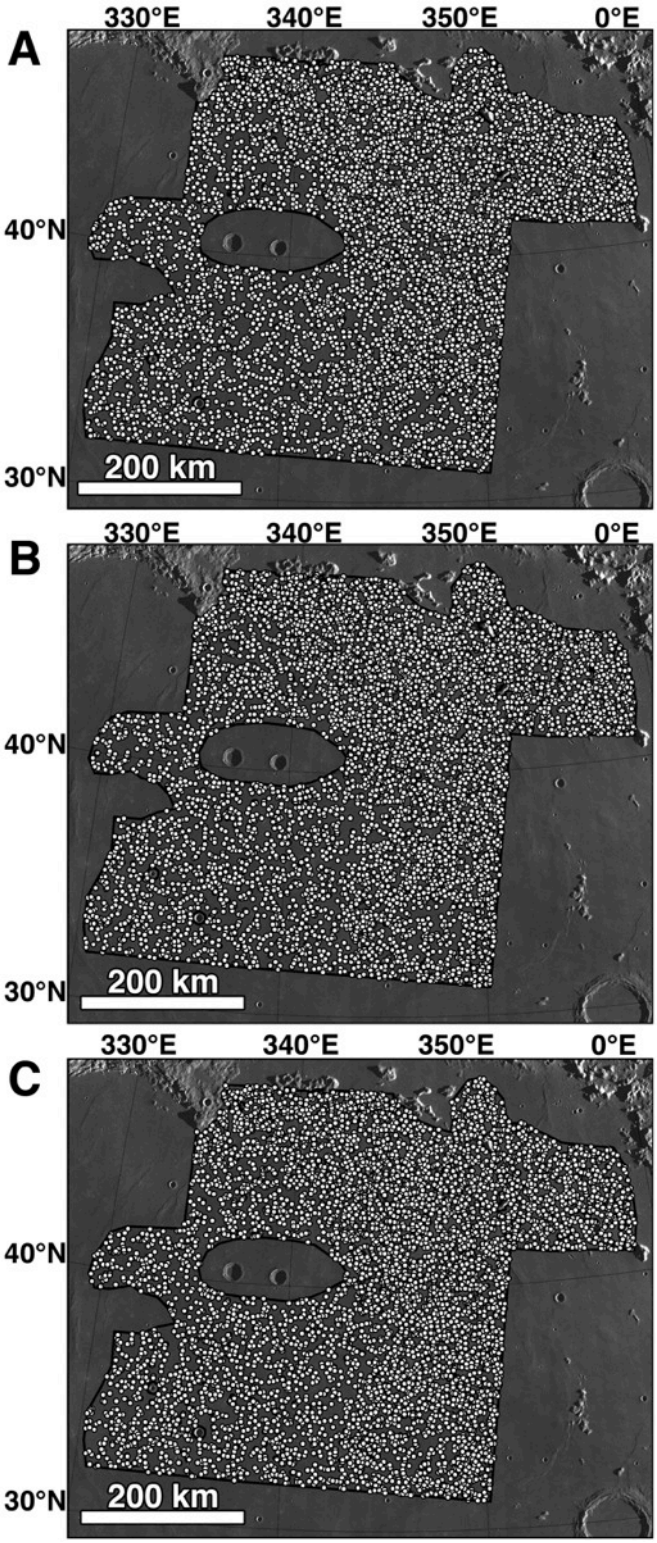

Figure 3.12. Three different random point distributions used to create the synthetic areal density map, reflecting the measured crater frequencies of the red (4900 points) and blue (2200 points) spectral units. Each point represents one crater center. Resulting synthetic ACD maps are shown in Figure 3.25, and ACD values are presented in Table 3.9.

3.3. Results

3.3.1. Crater Counts

All circular, non-overlapping craters were counted within the two units defined by spectral differences in the Mare Imbrium study area (Figure 3.13). From the measured crater frequencies (Table 3.2, 3.3), N(0.5) = 40711 ± 584 and N(1) = 3037 ± 159 for the red unit, and N(0.5) = 20535 ± 436 and N(1) = 1852 ± 131 for the blue unit. The crater retention ages are statistically distinguishable, and from my crater counts, the absolute model age for the red unit is ~3.3 Ga (3.3 +0.05/-0.06 Ga) and the blue unit is ~2.2 Ga (2.2 ±0.16 Ga) when the chronology (Neukum et al., 2001a) is fit to D ≥1 km craters (Figure 3.14). The model ages are in agreement with previously published average age ranges for the regional red (3.1–3.5 Ga from Hiesinger et al., 2000; 3.0–3.3 Ga from Bugiolacchi and Guest, 2008) and blue spectral units (2.6–3.0 Ga from Hiesinger et al., 2000; 2.2 Ga from Bugiolacchi and Guest, 2008). Thus, the presence of two geologic units of mare material located within the study region is confirmed on the basis of both absolute model and relative crater retention ages, and that the spectrally red unit is older than the spectrally blue unit.

Table 3.2. Mare Imbrium Cumulative Size-Frequency Distribution Data – Red Unit.*

D (km)[a]	Ncum[b]	Area (km^2)	Frequency	Uncertainty[c]
0.50	4866	1.20E+05	4.07E-02	6.89E-04
0.71	1378	1.20E+05	1.15E-02	3.62E-04
1.00	363	1.20E+05	3.04E-03	1.87E-04
1.41	99	1.20E+05	8.28E-04	1.07E-04
2.00	39	1.20E+05	3.26E-04	7.91E-05
2.83	22	1.20E+05	1.84E-04	5.31E-05
4.00	10	1.20E+05	8.37E-05	5.92E-05
5.66	8	1.20E+05	6.69E-05	3.86E-05
8.00	5	1.20E+05	4.18E-05	2.09E-05
11.31	1	1.20E+05	8.37E-06	8.37E-06

[a]Diameter (km) for lower bin limit.
[b]Cumulative number of craters per diameter bin.
[c]Uncertainty estimates are calculated from the square root of the number of craters for a given bin.
*Crater center points are shown in Figure 3.13; cumulative size-frequency plot shown in Figure 3.14.

Table 3.3. Mare Imbrium Cumulative Size-Frequency Distribution Data – Blue Unit.*

D (km)[a]	Ncum[b]	Area (km^2)	Frequency	Uncertainty[c]
0.50	2214	1.08E+05	2.05E-02	5.08E-04
0.71	582	1.08E+05	5.40E-03	2.76E-04
1.00	200	1.08E+05	1.86E-03	1.66E-04
1.41	75	1.08E+05	6.96E-04	9.38E-05
2.00	20	1.08E+05	1.86E-04	4.96E-05
2.83	6	1.08E+05	5.57E-05	2.78E-05
4.00	2	1.08E+05	1.86E-05	1.31E-05

[a]Diameter (km) for lower bin limit.
[b]Cumulative number of craters per diameter bin.
[c]Uncertainty estimates are calculated from the square root of the number of craters for a given bin.
*Crater center points are shown in Figure 3.13; cumulative size-frequency plot shown in Figure 3.14.

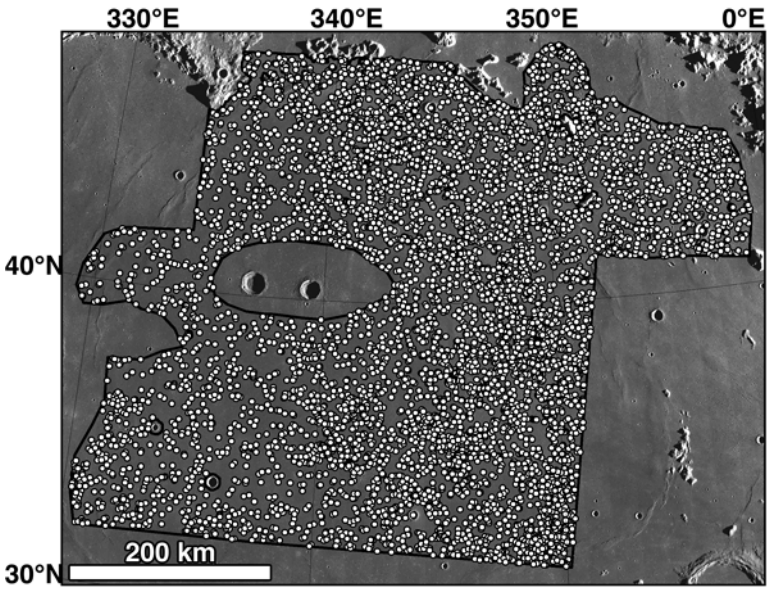

Figure 3.13. Distribution of craters with D ≥500 m, measured on the LROC WAC normalized reflectance mosaics. Each point represents one crater center. Resulting ACD shown in Figure 3.3A.

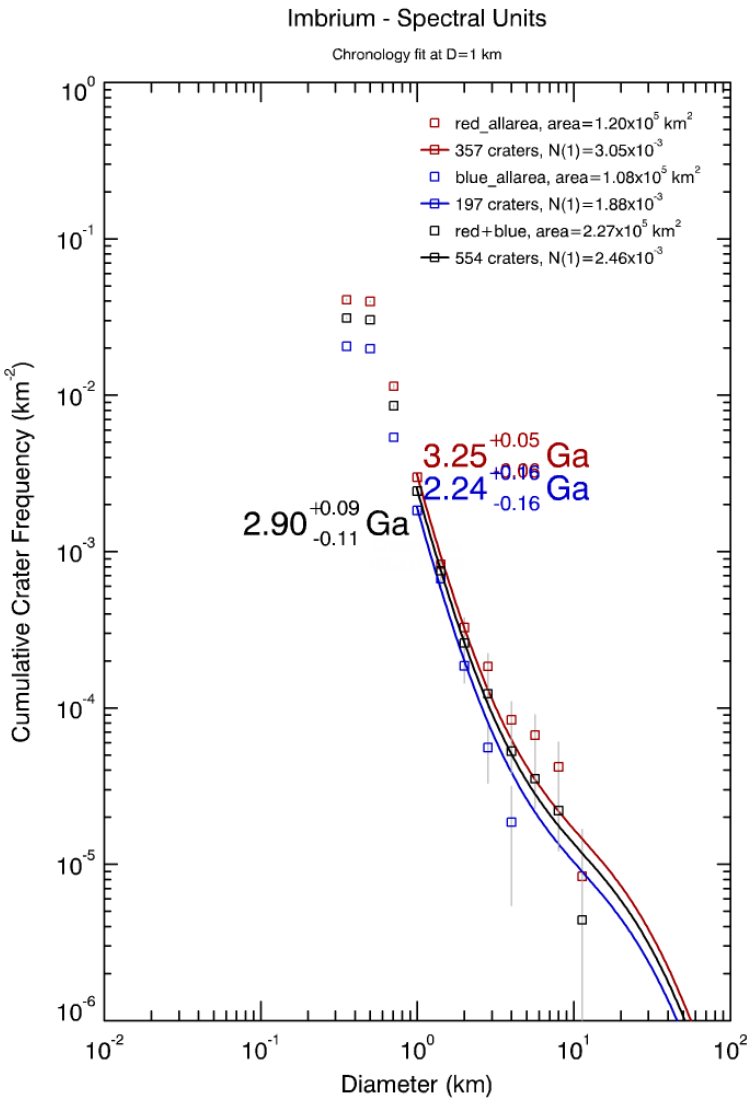

Figure 3.14. Cumulative crater size-frequency distribution and absolute model ages for the spectrally red and blue units in Mare Imbrium, derived from the measured counts in this investigation using the Neukum et al. (2001a) chronology function and tied to D ≥1 km. Tabulated binned crater data presented in Table 3.2, 3.3.

3.3.2. Areal Crater Density (ACD)

Two statistically separable, expansive regional units are observed in the ACD map (Figure 3.3A), and the ACD ranges between N(0.5) = 5936 ± 77 (12 craters per neighborhood) to N(0.5) = 80530 ± 284 (158 craters per neighborhood) (Table 3.4). The average regional ACD is N(0.5) = 30844 ± 176 (61 craters per neighborhood). Extending

approximately northwest to southeast is an irregularly shaped boundary between contiguous regions of high and low density units that is similar to the identified boundary between the red and blue spectral units.

To the west of the irregular boundary (Figure 3.3A) there is a large contiguous area of low density occurring within the blue spectral unit, with an average N(0.5) or $N(0.5)_{avg}$ = 15788 (Figure 3.15, 3.16A, 3.16B; Table 3.5). There are several areas with local, small area density variation ~50 km in width that have intermediate density magnitudes, and an area ~80 km in length (north-south direction) contains high density values at the southwestern study boundary (Figure 3.3A). High density areas within the low density region are observed adjacent to the irregular boundary (Figure 3.17) and north of Le Verrier crater (Figure 3.1A, 3.3A) and are not associated with substantial spectral variations (i.e., comprising a size greater than one neighborhood area).

Higher density magnitudes are observed to the east of the irregular boundary (Figure 3.3A) in the spectrally red unit. Regionally expansive, the high density unit has an $N(0.5)_{avg}$ = 50768, (Figure 3.18, 3.19; Table 3.6). More so than the low density unit, the high density region contains spatially limited local variations in ACD. Several areas of intermediate to low density are present within the expansive high density area (Figure 3.3A, 3.16C-F, 3.20).

Intermediate ACD values range N(0.5) = 24955–35850, with $N(0.5)_{avg}$ = 30569. Intermediate values occur along the boundary between and in localized areas within the high and low density regions and are rarely observed in isolated occurrences (Figure 3.3A, Table 3.7). Figures 3.21 and 3.22 show the locations for three intermediate density areas that are contained within a representative measurement neighborhood.

Table 3.4. Areal Crater Densities for Large Areas.

Density Class	Minimum N(0.5)	Maximum N(0.5)	Average N(0.5)[a]
High	32844	80530	50768 ± 225
Moderate	24955	35850	30569 ± 175
Low	5936	26154	15788 ± 126

[a]Uncertainty estimates were calculated from the square root of the number of average craters.

Table 3.5. Areal Crater Densities: Selected Low Density Neighborhoods.

Location	Latitude (°N)	Longitude (°E)	Minimum N(0.5)	Maximum N(0.5)	Average N(0.5)[a]
1	36.117	335.837	7130	14811	10321 ± 102
2	44.571	336.557	13750	23428	18700 ± 137
3	41.029	350.396	19863	35141	26018 ± 161
4	34.220	347.523	18844	38706	25919 ± 161
5	40.603	331.608	7130	19863	13709 ± 117
6	38.712	341.804	12732	23672	19642 ± 140
Range (1-6)	–	–	7130	38706	19044 ± 138

[a]Uncertainty estimates were calculated from the square root of the number of average craters.

Table 3.6. Areal Crater Densities: Selected High Density Neighborhoods.

Location	Latitude (°N)	Longitude (°E)	Minimum N(0.5)	Maximum N(0.5)	Average N(0.5)[a]
1	45.555	342.356	47365	73339	58959 ± 243
2	38.184	348.324	41762	74866	56696 ± 238
3	32.191	349.144	39216	78703	66401 ± 258
4	35.317	341.082	32595	49911	41777 ± 204
Range (1-6)	–	–	32595	78703	55957 ± 237

[a]Uncertainty estimates were calculated from the square root of the number of average craters.

Table 3.7. Areal Crater Densities: Selected Moderate Density Neighborhoods.

Location	Latitude (°N)	Longitude (°E)	Minimum N(0.5)	Maximum N(0.5)	Average N(0.5)[a]
1	44.692	347.096	24955	38706	38658 ± 197
2	42.956	355.843	23428	36425	30135 ± 174
3	34.811	343.091	30866	30135	31813 ± 178
Range (1-6)			23428	38706	30938 ± 176

[a]Uncertainty estimates were calculated from the square root of the number of average craters.

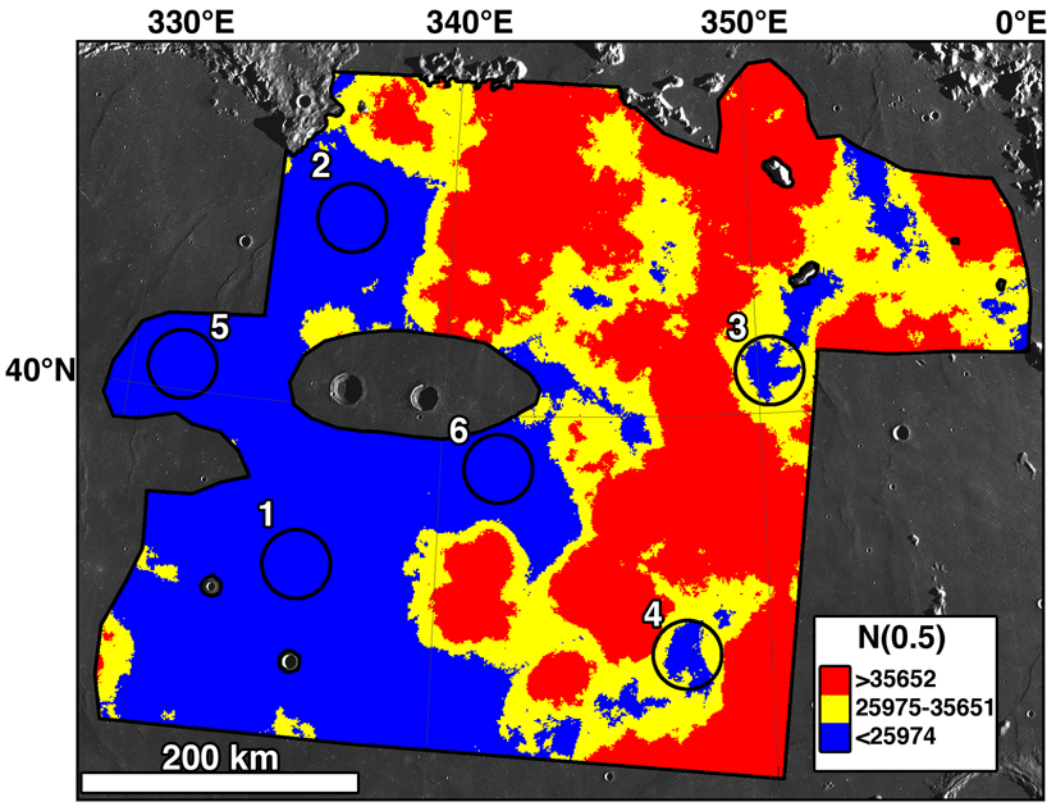

Figure 3.15. ACD map with six example neighborhoods (radius = 25 km) selected for the low density region. All but two example low density neighborhood areas are contained within the large low density region. Center coordinates for neighborhoods and density magnitudes within the neighborhoods are presented in Table 3.5, and close up views of three example neighborhoods are shown in Figure 3.16.

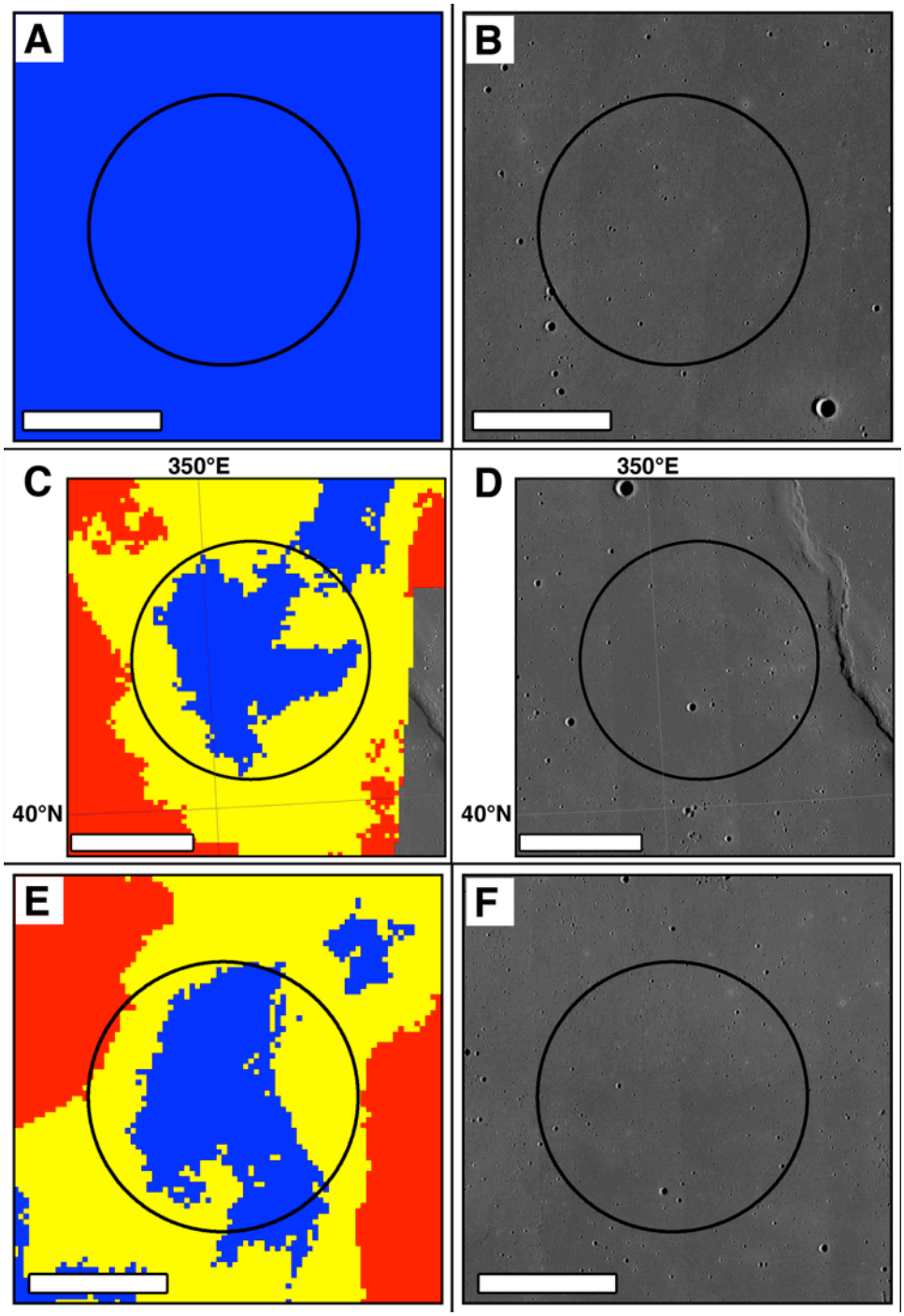

Figure 3.16. ACD map (left; same colorscale as Figure 3.15) and LROC WAC 75° incidence angle mosaic (right) for example neighborhood 1 within low density region (A, B). Example neighborhood 3, centered on a low density area within the large high density region (C, D). Example neighborhood 4, centered on a low density area in the southeastern portion of the study area (E, F). Scale bar is 25 km. Locations visually presented in Figure 3.15, center coordinates for each location and density values are provided in Table 3.5.

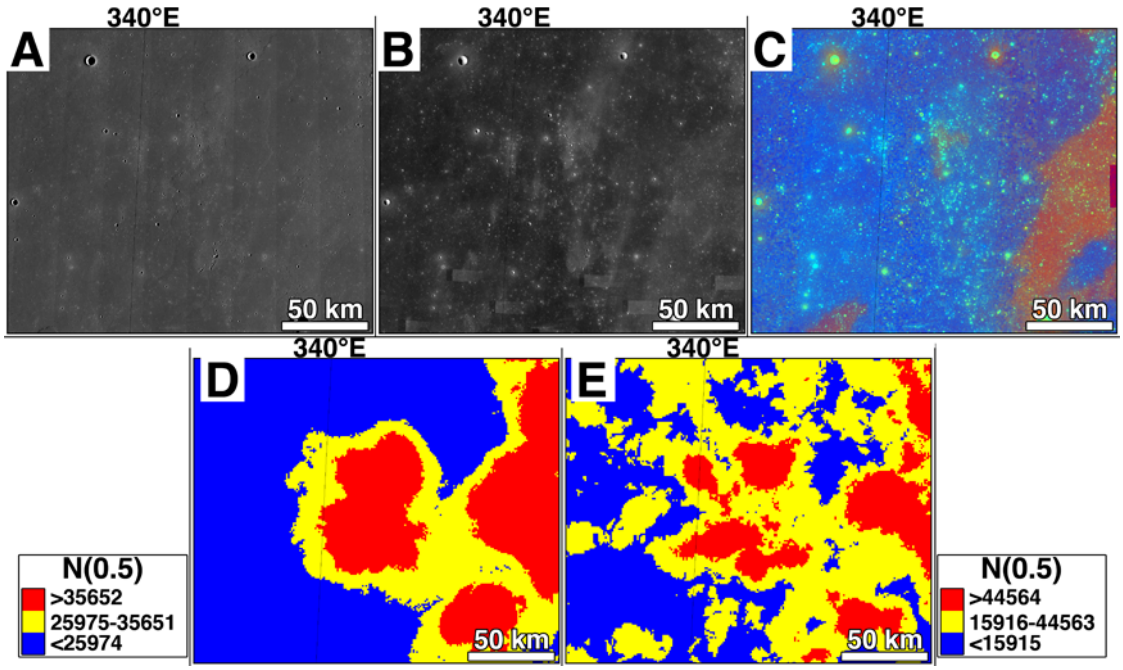

Figure 3.17. An isolated high density measurement within the low density region, located proximal to the spectral unit boundary (35.769°N, 341.217°E). This region is also shown in Figure 3.19 and density measurements are listed in Table 3.6. (A) LROC WAC normalized reflectance 75° incidence angle mosaic, (B) LROC WAC normalized reflectance 57° incidence angle mosaic, (C) Clementine multispectral ratio (R=750/415, G=750/950, B=415/750), (D) ACD with a 25 km neighborhood radius, (E) ACD derived using a 10 km neighborhood radius.

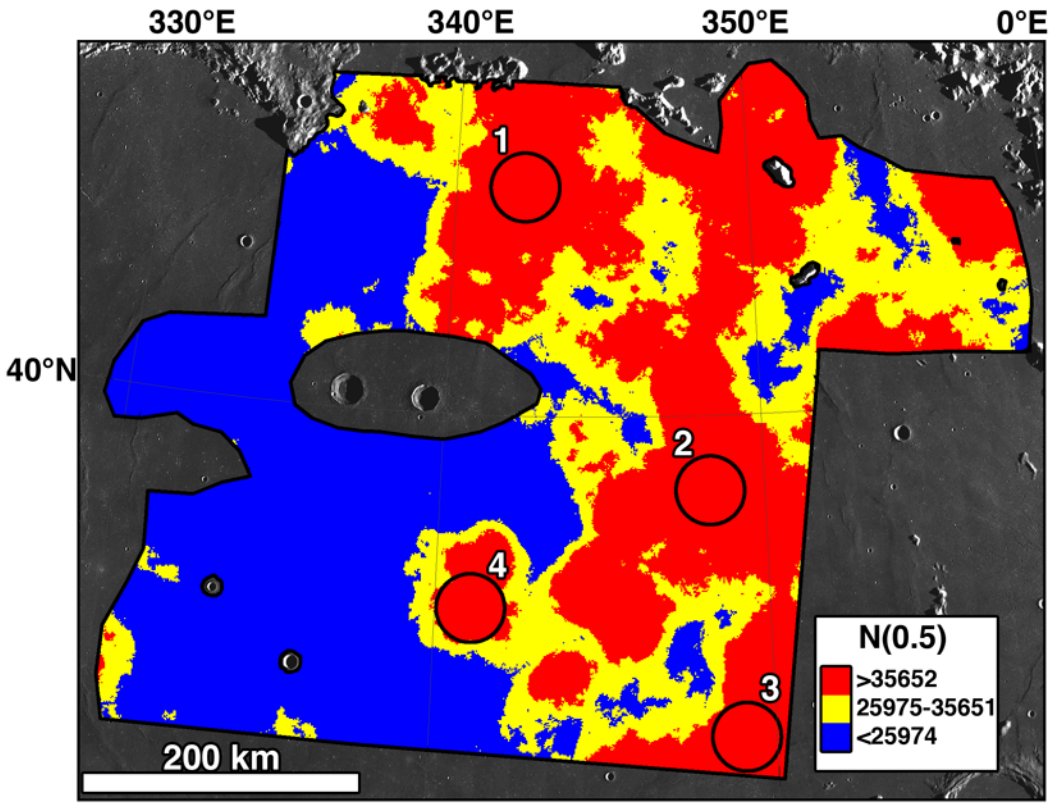

Figure 3.18. ACD map with four example neighborhoods (radius = 25 km) selected for the high density region. Center coordinates for neighborhoods and the density magnitudes within the neighborhoods are presented in Table 3.6. Close up view of example neighborhood 3 is shown in Figure 3.19. Neighborhood 1 is detailed in Figure 3.27 and neighborhood 2 is shown in Figure 3.28.

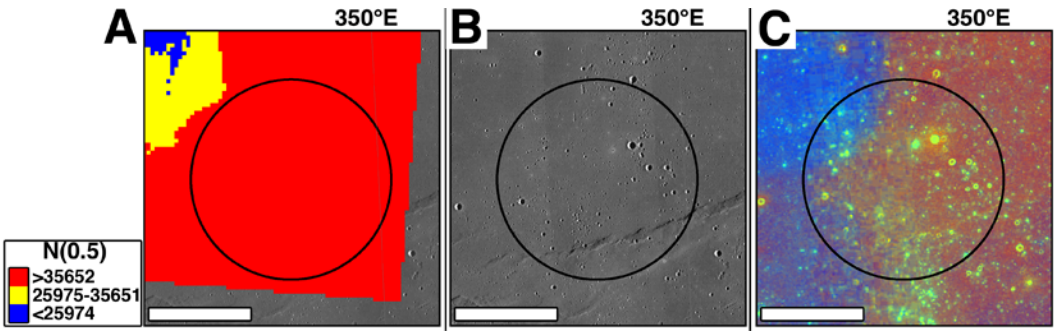

Figure 3.19. Example neighborhood 3 for the high density region (location in study region shown in Figure 3.18, center coordinates and density values listed in Table 3.6). (A) ACD, (B) LROC WAC 75° incidence angle mosaic (C) Clementine multispectral ratio (R=750/415, G=750/950, B=415/750). Scale bar is 25 km.

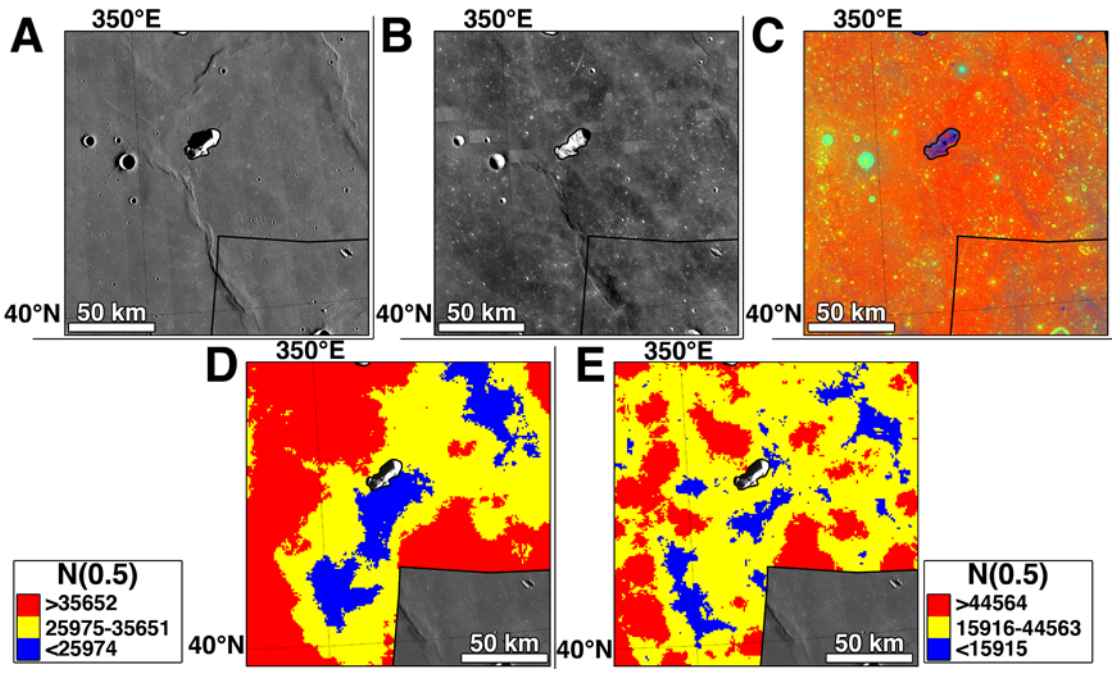

Figure 3.20. Example of local variation within the high density region (42.162°N, 351.267°E). This region is also shown in Figure 3.15, 3.16C,D, and density values are listed in Table 3.5. (A) LROC WAC 75° incidence angle mosaic (B) LROC WAC 57° incidence angle mosaic (C) Clementine multispectral ratio (R=750/415, G=750/950, B=415/750), (D) ACD with a 25 km neighborhood radius, (E) ACD derived using a 10 km neighborhood radius.

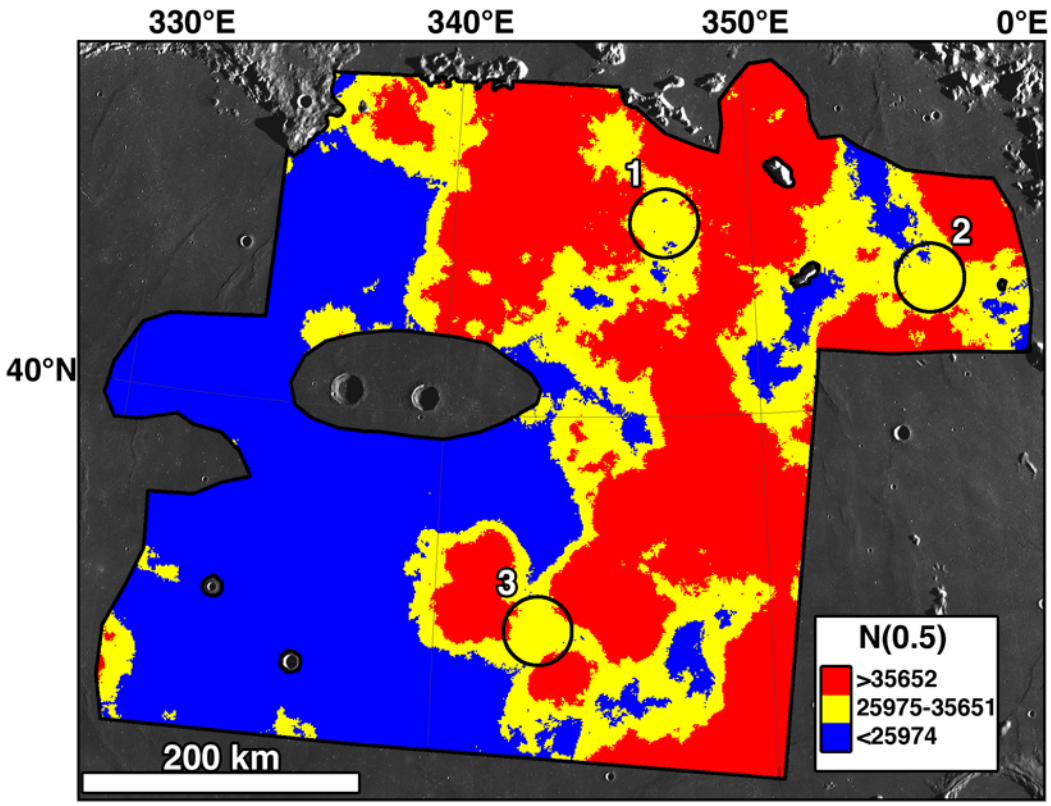

Figure 3.21. ACD map with three example neighborhoods with 25 km radii selected for the intermediate density regions. Each neighborhood area was selected to contain a maximum of intermediate values. Center coordinates for neighborhoods and the density magnitudes within the neighborhoods are presented in Table 3.7. Detailed views of the example neighborhoods are shown in Figure 3.22.

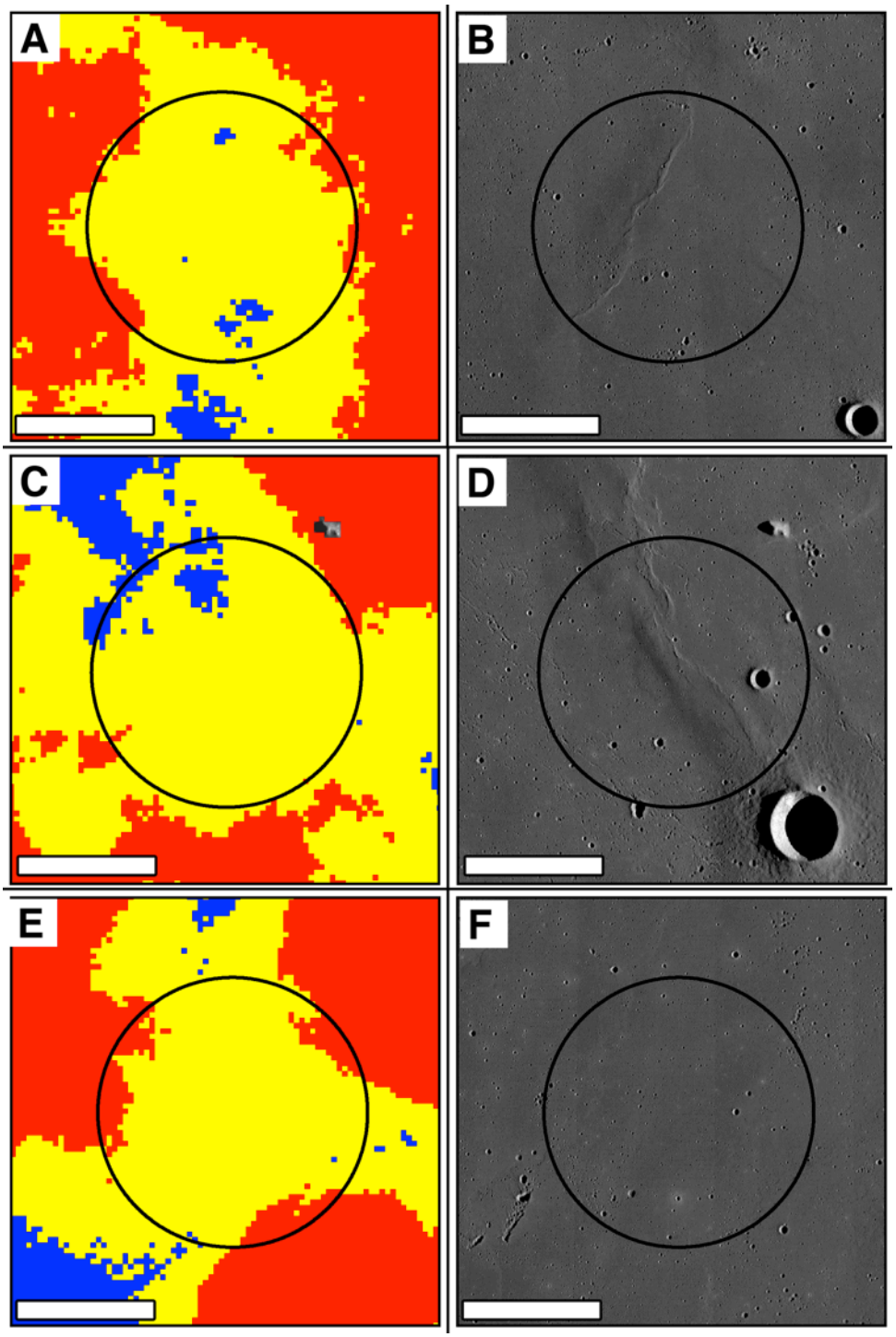

Figure 3.22. ACD on the left (same colorscale as Figure 3.21), LROC WAC 75° incidence angle mosaic on the right for intermediate density regions selected in Figure 3.21. (A, B) Example neighborhood 1, (C, D) example neighborhood 2, and (E, F) example neighborhood 3. Scale bar is 25 km. Center coordinates and density magnitudes are presented in Table 3.7.

3.4. Discussion

3.4.1. Areal Crater Density: Statistical Versus Geologic Variations

In the Mare Imbrium study region, the ACD map exhibits a boundary that is interpreted to represent the geologic contact between two previously mapped regional color units (Figure 3.1C). Crater density differences correspond with contiguous geologic units identified by strong spectral contrasts interpreted as variations in wt% FeO and TiO_2 (e.g., Charette et al., 1974; T. V. Johnson et al., 1977; Pieters, 1978; J. R. Johnson et al., 1991; Lucey et al., 2000) within the extruded mare basalts. However, the boundary observed in the density measurement does not precisely align with that determined from spectral variation (Figure 3.23). There are two plausible explanations for the boundary mismatch. The first reflects limits to the measurement technique. The moving neighborhood technique promotes smoothing of sharp contacts since the resulting output cell considers all the data contained within one neighborhood. Thus, distinct boundaries are reflected as intermediate density magnitudes such that potential uncertainty distinguishing the spectral contact in the ACD map will be present within ±25 km of the spectral boundary (Figure 3.23B). This factor is likely partly responsible for the boundary mismatch. The second explanation concerns the observed crater frequencies for the study region and their representation of real age differences. The ACD maps are dependent on measured crater frequencies and are expected to represent a random point distribution since impact cratering is assumed to be a random process (e.g., McGill, 1977). Thus, synthetic ACD maps (Figure 3.24, 3.25) derived from random point distributions (Figure 3.11, 3.12), with the number of points equal to the observed number of craters rounded to the nearest hundred, will determine if there is a geologic difference responsible for the

unit boundary mismatch or simply statistical variations affecting the observed crater population.

Synthetic ACD maps were generated to establish where measured ACD values reflect real age differences compared to variations resulting poor sample sizes, in addition to investigate how much local variation might be expected statistically within a geologic unit. Three models of regional synthetic ACD exhibit widespread intermediate density values with localized high and low density regions distributed across the measurement area (Figure 3.24; Table 3.8). This result is expected based on the random distribution of points composing the synthesized density maps: using the Poisson probabilities for classification boundaries, 80% of the distribution is of intermediate density, which is also expected because of the nature of the Poisson distribution. The remaining 20% of the random distribution is naturally classified within the high or low density categories. Thus, the synthetic density measurement for the combined crater frequency of this region (Figure 3.24) confirms that the boundary observed in the measured ACD is real, reflecting the contact between two geologic units of different interpreted composition and with different crater frequencies (age).

Three synthetic density maps were created from the cumulative crater frequencies of the red and blue spectral units to investigate observed statistical variation within the units (Figure 3.25; Table 3.9). As expected, all three maps show two distinct regions of high and low density, bounded by an intermediate density area. Within the high and low density regions, there are smaller regions of intermediate density that represent random variation (Figure 3.25). Consequently, while some local variation may be expected to occur within the measured ACD map due to the randomness of the impact cratering

process, significant differences between the synthetic ACD maps and the measured ACD map, particularly within the high or low density units, likely represent true age differences and are not solely explained by statistical variation.

The observed regional ACD differences reflect two distinct periods of volcanic activity in Mare Imbrium. However, small area variations in regional crater density may not always have an obvious origin, complicating identification of resurfaced areas in volcanic smooth plains. With respect to impact cratering in particular, the randomness of the cratering process, surface modification due to large crater formation and ejecta emplacement (i.e., erasure of the cratering record surrounding a larger crater), and formation of circular, non-overlapping clustered craters that may be secondary craters may act as a primary means promoting variations in ACD at the small (local) scale. Careful observations of the surface may reveal the cause of small area density variations, however, an unambiguous origin may not always be apparent.

In the low density region, there are two high density areas that do not appear in the synthetic ACD map (Figure 3.25) and do not follow the measured ACD trends surrounding the spectral unit boundary (e.g., Figure 3.23B). The first area, located in the southern portion of the region, is isolated but located spatially near the spectral unit boundary and $N(0.5)_{avg} = 66401 \pm 258$ (Figure 3.17). Secondary crater chains and three groupings of non-overlapping craters (500 m to ~1.6 km in diameter) surrounded by higher albedo material that I interpret to be crater ray material are observed in the LROC WAC mosaics. When considering the regional context, the groupings of spatially close, non-overlapping craters within the higher albedo rays are traced southward to Copernicus crater, located ~770 km to the south, and therefore represent secondary craters and ejecta

material. These observations are in agreement with geologic maps of Mare Imbrium (Carr, 1965; Moore, 1965; Hackman, 1966; Schaber, 1969; Page, 1970; M'Gonigle and Schleicher, 1972), which were made using Lunar Orbiter photographs with limited variations in solar incidence angles. A second high density area with similar attributes (i.e., clustered, non-overlapping 500 m to ~1.2 km diameter craters) is located north of Le Verrier crater, and similarly I interpret this local, small area ACD variation to result from secondary craters attributed to Copernicus (~1000 km distant) based on the dominant north-south high albedo ray elongation.

In the high density region, a prominent small area with low density is observed in the northeastern portion of the study area at 42.16°N, 351.27°E (Figure 3.20). Observations of the area in the LROC WAC mosaics reveal secondary crater chains and substantial ray material extending from the southeast to northwest from Aristillus crater (~340 km away from this location) and possibly from Autolycus crater as well, both of which are located to the east. Lower albedo areas are interspersed among the higher albedo rays and reflect the absence of ejecta. Although few secondary crater chains are identified in the geologic map, extensive crater ray material is mapped at this location (Schaber, 1969; Page, 1970).

Unfortunately, interpreting local, small area variation in ACD is, at times, more complicated. For example, the low density representative neighborhood number four (Figure 3.15) may reflect the superposition of the blue spectral unit onto the red spectral unit (Figure 3.23A), but the irregular shape and relatively small extent affects the ACD calculation and interpretation. Very few output cells will contain measurements from neighborhoods contained completely within the spectrally blue unit and this area is

affected by the ±25 km uncertainty at the spectral contact (Figure 3.23B). Comparison of the measured and synthetic ACD maps indicates that the presence of this low density area is not a random statistical variation and instead reflects real differences in measured crater frequency. Nevertheless, although the shape of the low density area in the observed ACD is different than in the synthetic maps, observations of the available image data and geologic maps suggest that secondaries and at least one, maybe two, ejecta rays from Copernicus contaminate this area. Unraveling the geologic and ACD relationships in this location therefore emphasizes the necessity of considering all available data, in addition to the importance of comparison to synthetic ACD maps.

Table 3.8. Synthetic Densities: Overall Region.

Synthetic Test #	**Minimum N(0.5)**	**Maximum N(0.5)**	**Average N(0.5)[a]**
Syn1ce[*]	13501	48781	30987 ± 176
Syn2ce	14193	52414	31004 ± 176
Syn3ce	13914	49787	30957 ± 176

[a]Uncertainty estimates were calculated from the square root of the number of average craters.
[*]Syn1ce = Synthetic density, example 1, corrected and masked.

Table 3.9. Synthetic Densities: Region with Red and Blue Units Defined.

Synthetic Test #	**Minimum N(0.5)**	**Maximum N(0.5)**	**Average N(0.5)[a]**
SynRB1ce[*]	10197	60606	30943 ± 176
SynRB2ce	9450	60107	30935 ± 176
SynRB3ce	7459	56778	30968 ± 176

[a]Uncertainty estimates were calculated from the square root of the number of average craters.
[*]SynRB1ce = Synthetic density, Red and Blue units, example 1, corrected and masked.

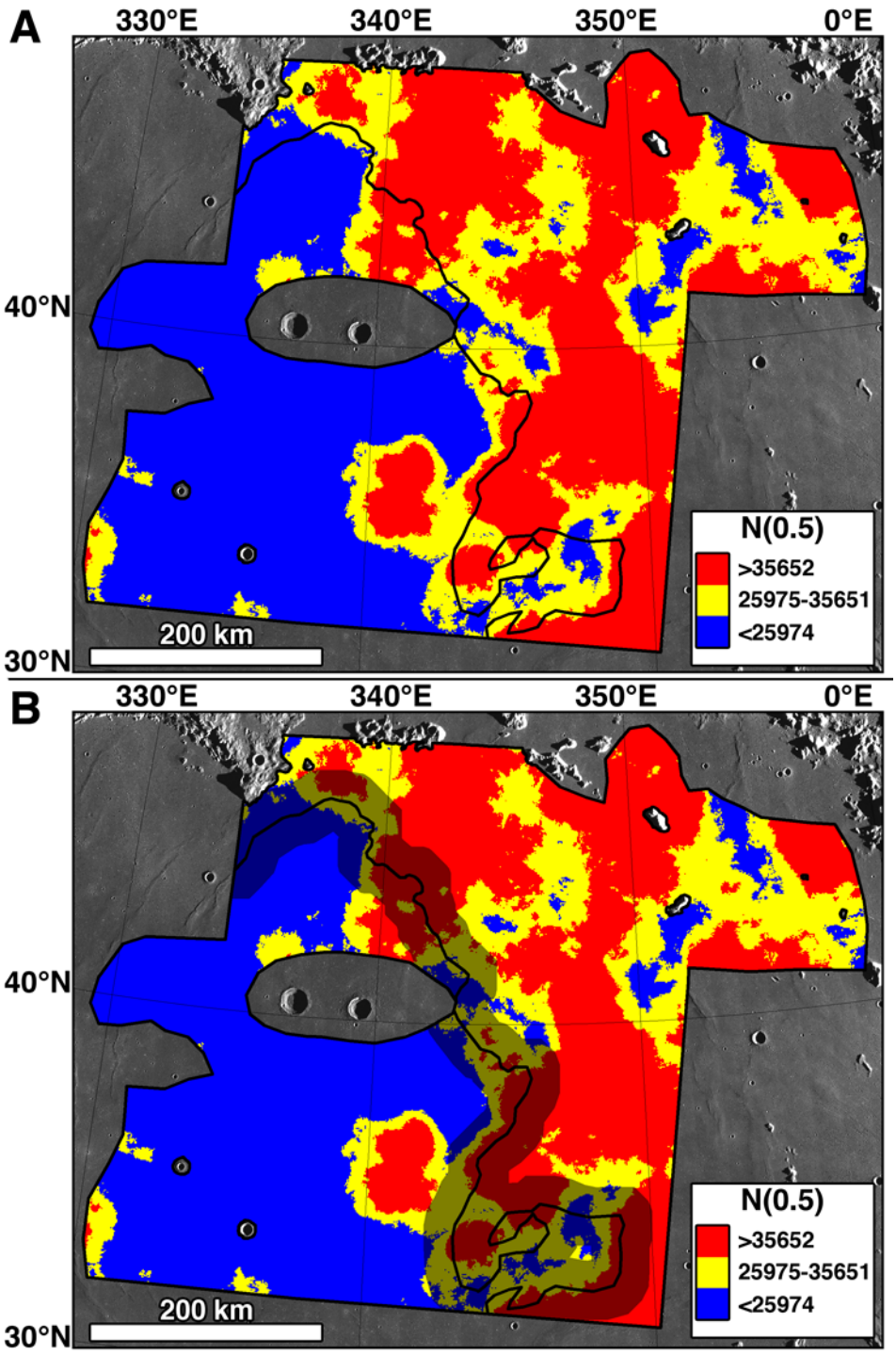

Figure 3.23. ACD map with spectral boundary drawn in black (A). (B) ±25 km distance from the boundary shadowed to illustrate potential uncertainty in ACD measurements at the spectral contact due to smoothing.

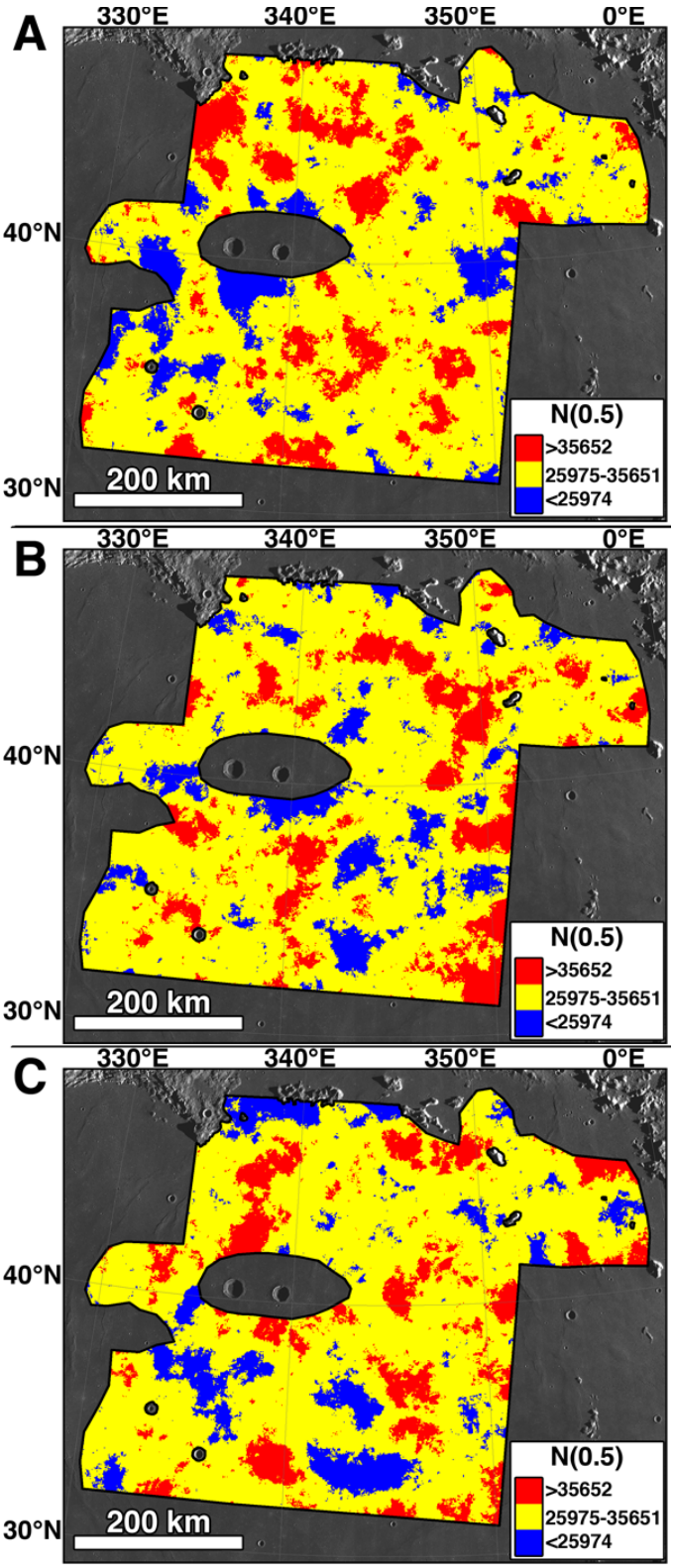

Figure 3.24. Synthetic areal density maps derived from three different random point distributions of 7100 points (cumulative crater frequency of D ≥500 m for this region). Point distributions shown in Figure 3.11 and Table 3.8 lists density values.

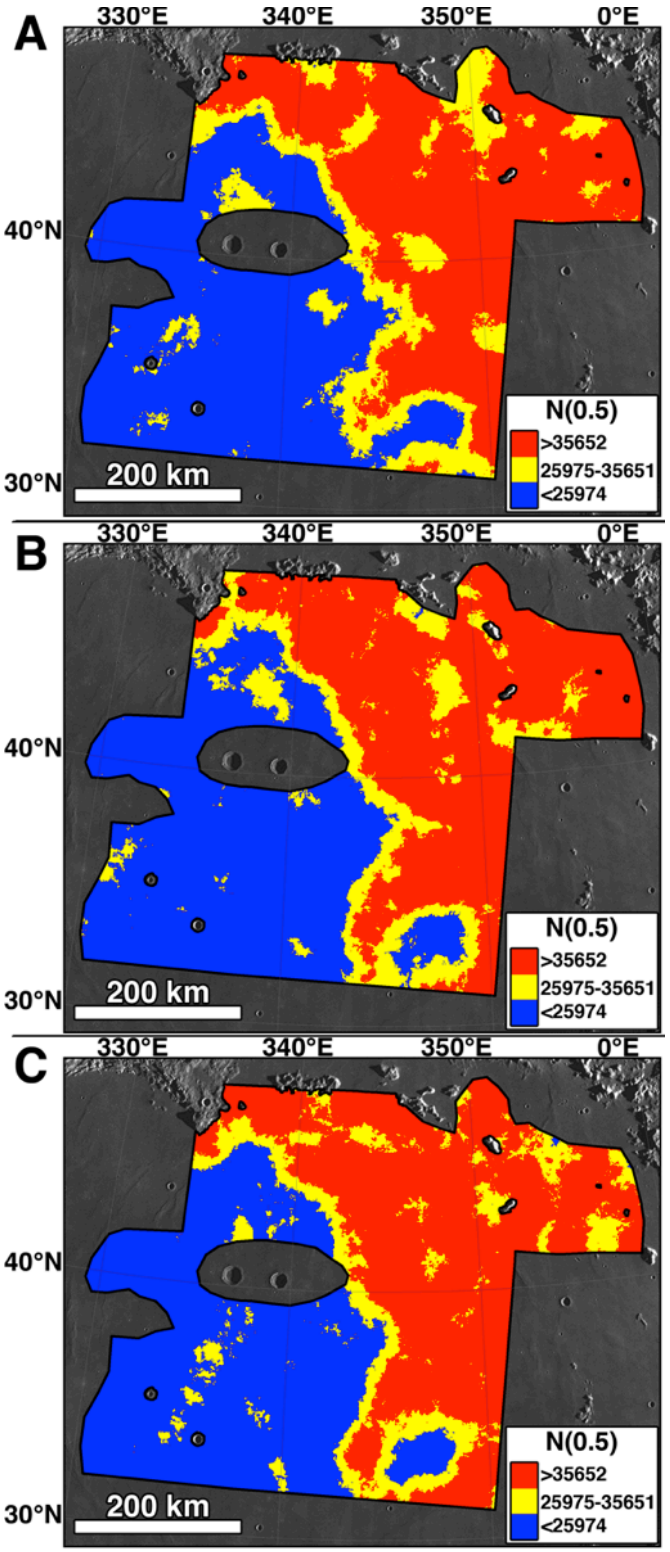

Figure 3.25. Synthetic areal density maps derived for three different random point distributions created from the crater frequencies of the red (4900 points) and blue (2200 points) spectral units. Point distributions shown in Figure 3.12 and density magnitudes are provided in Table 3.9.

3.4.2. Detection of Far-Flung, Non-Obvious Secondary Craters

The ACD measurement reflects the accumulation of impact craters over time and includes all observed circular, non-overlapping craters with D ≥500 m. I assume that the circular, non-overlapping craters are primary craters, a case necessary for valid age determination. In some cases, the circular, non-overlapping craters are spatially clustered (grouped) within a higher albedo region than the surrounding terrain, indicating that these groupings are evidence of secondary craters and crater ray materials. Measurements of the crater diameters within the groupings interpreted to be secondaries range from 500 m to ~2 km, and at least four parent craters contribute to the expansive crater rays and secondary crater chains observed within the study region: Copernicus to the south (9.62°N, 339.92°E, D ~96 km), Aristillus (33.88°N, 1.21°E, D ~54 km) and Autolycus (30.68°N, 1.49°E, D ~39 km) to the east, and Aristarchus to the west (23.73°N, 312.51°E, D ~40 km). Therefore, it is possible that at least some portion of the grouped non-overlapping craters represent far-flung secondaries, similar to those observed at Tycho crater (Dundas and McEwen, 2007) and Zunil crater on Mars (McEwen et al., 2005).

What is the effect of including these far-flung secondaries in crater frequency measurements? Secondary craters that occur in chains, with the herringbone pattern, or in overlapping clusters are immediately recognized and excluded, along with the surface area they cover. However, groupings of craters described above are not as easily identified. Previous lunar image datasets, such as Lunar Orbiter, had limited repeat coverage of an area at different solar incidence angles, so identifying non-obvious secondaries (non-overlapping clusters of craters within a higher reflectance unit) was perhaps difficult. The possibility of secondary contamination is considered for the lunar

chronology, with an estimated <10% uncertainty for the standard distribution curve between 0.8–3 km (Neukum et al., 1975a; 2001a). In fact, Neukum et al. (1975a) estimated a <5% contribution of secondary craters (e.g., those in chains, herringbone pattern) to the overall crater population observed in Mare Serenitatis using Lunar Orbiter photographs. Moreover, for the mare, absolute ages are determined using craters with D ≥1 km to limit inclusion of potential secondary craters (e.g., Neukum et al., 1975a; Hartmann et al., 1981; Neukum, 1983; Neukum et al., 2001a; McEwen and Bierhaus, 2006). In Mare Imbrium, the majority of measured grouped craters interpreted to be non-obvious secondaries are between 500 m to ~850 m in diameter, suggesting that while non-obvious secondary craters with D ≥1 km exist on the lunar surface, their presence is probabilistically low (hypothetically the percentage of unrecognized secondary craters in crater counts is <5%; e.g., Werner et al., 2009). Thus, absolute model age determinations will be minimally influenced by inclusion of non-obvious secondaries, especially if the potential inclusion of non-obvious secondaries is minimized through reference to published geologic maps, use of images with multiple illumination conditions, and consideration of counted crater locations with local and regional geology (e.g., proximity of count region to Copernicus crater and presence or absence of crater rays and prominent secondary crater chains).

Measures of ACD may aid in identification and determination of far-flung, non-obvious secondary craters, particularly when small neighborhood sizes (e.g., 10 km for Mare Imbrium) are used. Small neighborhoods emphasize local, statistical variations, so systematic local trends in groupings of craters, which are expected for clusters of far-

flung secondaries, will be visible (Figure 3.26). The resulting ACDs, in conjunction with image data, may assist in determination of potential origin direction.

Within small neighborhoods, crater clusters are a primary component of the higher ACD values in some areas. By identifying these higher than average density regions, and then observing the crater and surface morphology (including associated regional terrain), potential secondary crater groupings are identified if they are indeed the source for the higher density magnitudes. For example, an “X” shaped cluster of craters was identified (Figure 3.27, centered at 45.09°N, 343.00°E) in the LROC WAC basemap. The “X” has a higher albedo than the surrounding terrain and is located entirely within the spectrally red unit. In the ACD map with a neighborhood radius of 25 km, $N(0.5)_{avg} = 58959 \pm 243$ for the “X” (Figure 3.18, neighborhood 1; Table 3.5), contributing to the overall regional high density in the northern portion of the study area. When a 10 km neighborhood radius is used to create an ACD map (Figure 3.26), the “X” observed in the LROC WAC mosaic is emphasized (Figure 3.27). A linear high density region extending in the northeast-southwest direction is revealed, along with the northwest-southeast linear portion of the “X”. These groupings of craters are mapped as secondary crater material and ray material in the USGS geologic map (Schaber, 1969), and one possible source for the northeast-southwest trending portion of the “X” is Aristoteles crater located ~710 km away, to the northeast of Mare Imbrium (50.24°N, 17.32°E, D ~88 km). Should the “X” (craters and area) be removed from the measurement, I would expect the higher density region to remain unchanged with the exception of an “X”-shaped gore in the density map.

Similarly, at the eastern boundary of the study region (38.77°N, 348.08°E), the 10 km neighborhood radius ACD map (Figure 3.26, 3.28) reveals high density linear regions (not seen in Figure 3.3A) in a portion of the regional high density unit identified in the 25 km neighborhood radius ACD map. Comparison of the high density linear areas (Figure 3.28) to LROC WAC mosaics and the geologic map (Page, 1970) indicate that the high density areas reflect circular, non-overlapping craters within high albedo rays from Copernicus, Aristillus, and Autolycus craters. While it is possible that some craters in these linear high density areas may superpose the crater rays, there are no distinguishing features indicative of later crater formation (e.g., high albedo ejecta surrounding a crater).

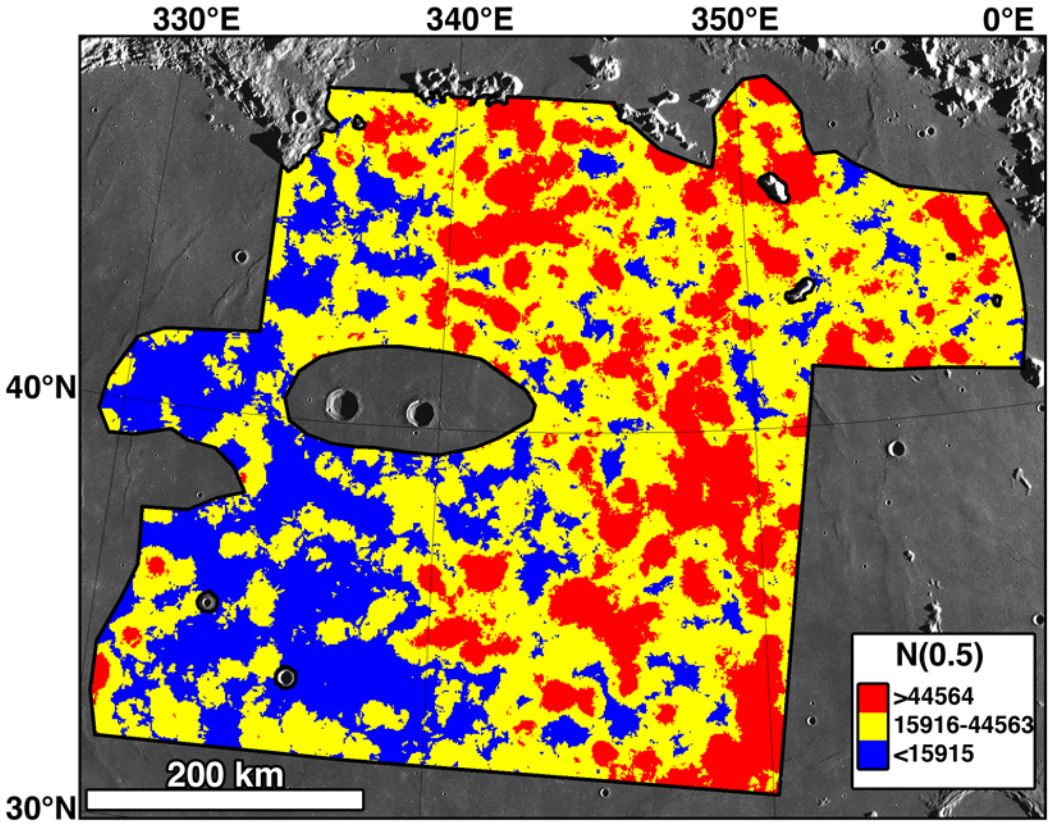

Figure 3.26. ACD map created using a 10 km neighborhood radius and 1 km output cell from the measured crater population (Figure 3.13).

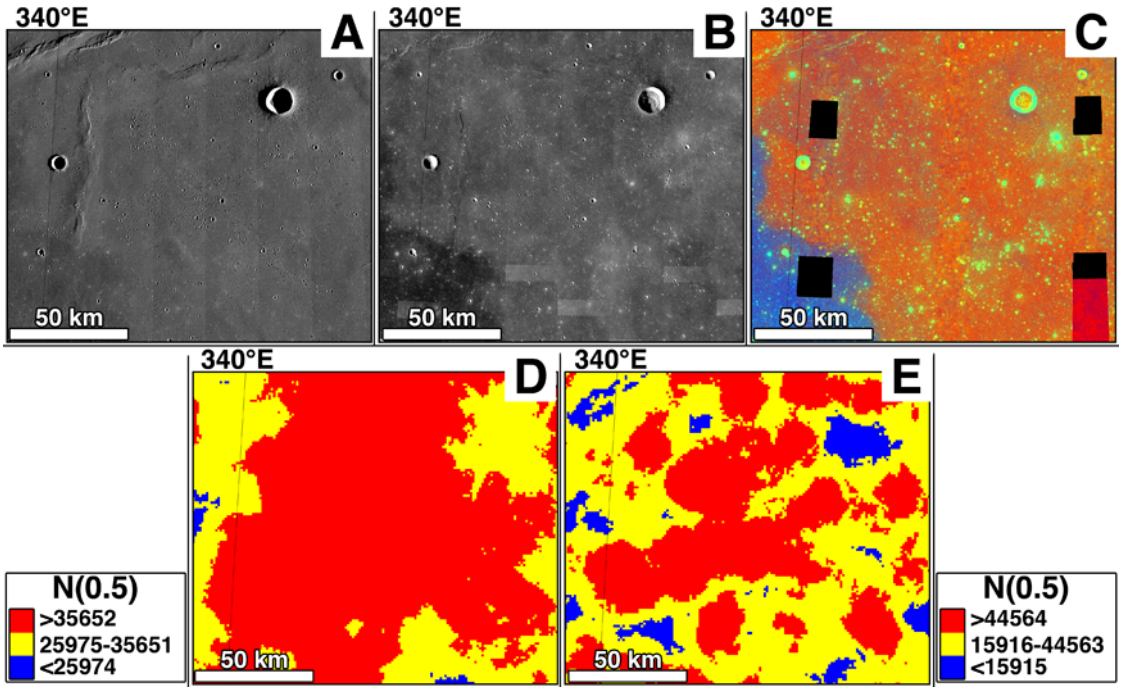

Figure 3.27. Portion of the high density area in the northwestern portion of the study area (45.091°N, 342.998°E), also shown in Figure 3.18 (neighborhood 1; associated density values are presented in Table 3.6). (A) LROC WAC 75° incidence angle normalized reflectance mosaic, (B) LROC WAC 57° incidence angle normalized reflectance mosaic, and (C) Clementine multispectral ratio (R=750/415, G=750/950, B=415/750) mosaics. This region is observed within the regional high density area in the 25 km neighborhood radius density map (D). On the basis of linear-like high density areas in the 10 km neighborhood radius ACD map (E), the "X" shape is interpreted to reflect far flung, non-obvious secondaries.

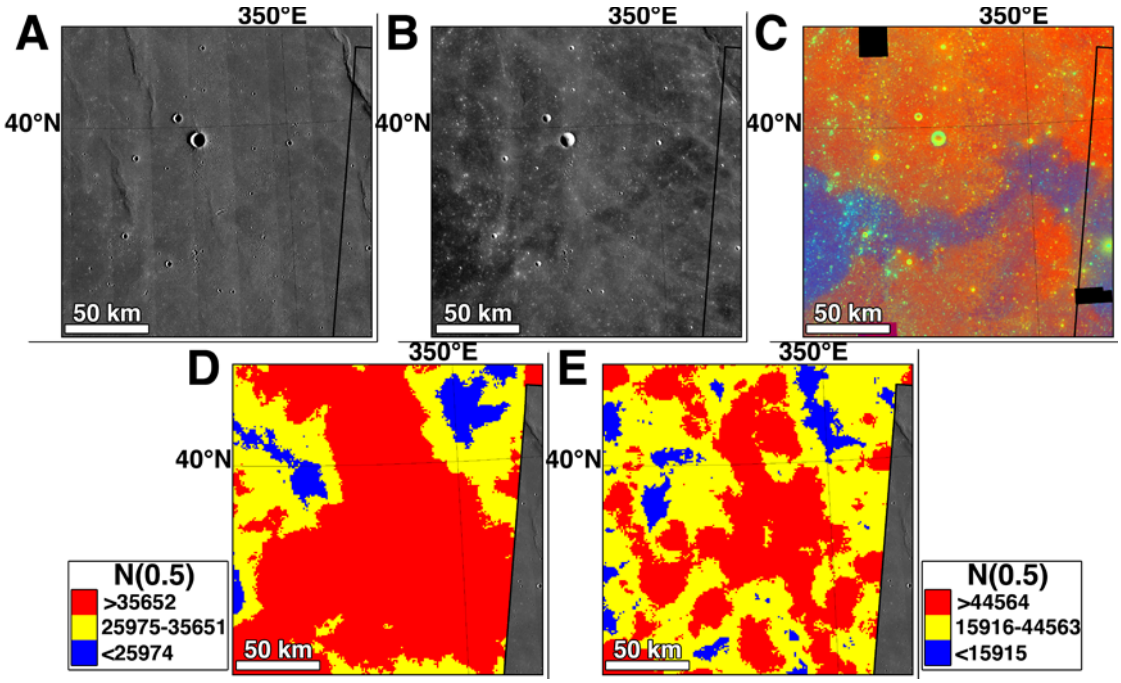

Figure 3.28. (A) LROC WAC 75° incidence angle normalized reflectance mosaic, (B) LROC WAC 57° incidence angle normalized reflectance mosaic, and (C) Clementine multispectral ratio (R=750/415, G=750/950, B=415/750) mosaic of an area within the eastern high density region observed in the 25 km radius ACD (D; Figure 3.18, neighborhood 2). Linear-like high density features are more prominent in the 10 km neighborhood radius ACD map (E) reflect far flung, non-obvious secondaries. Corresponding density magnitudes are provided in Table 3.6.

3.4.3. Potential Statistical Limitations

As with all studies concerning crater size-frequencies, the region of interest must contain a statistically significant number of craters at the desired diameter sizes from which to derive relative and absolute ages. Integral to obtaining a statistically robust crater sample population is identifying a region of uniform age unit covering a substantially large area. On the Moon, and on other planets, different measurement area sizes should be considered for dating different terrain types (e.g., older highlands versus younger mare, older versus younger mare, older mare versus younger impact melt). Unfortunately, there is no simple equation or relationship to invoke as a means to define the ideal measurement area size. Often, measurement area size is determined by the areal

extent of the unit in question, for example, the spatial extent of impact melt deposits surrounding and within a specific crater. Nevertheless, the results of this investigation constrain measurement area size recommendations for relative and absolute dating of the lunar mare, a topic usually avoided by workers due to the difficulty of presenting convincing, quantitative evidence for area size-determination arguments. Initially, a 4.48×10^4 km^2 subarea was selected from the entire study region to examine the point correction effectiveness (Figure 3.7B), and differences in ACD between the subarea and the entire region reflect the addition of data beyond the subarea boundary (Section 3.2.3.3). Even after the subarea is approximately halved, the resulting ACD map (Figure 3.10A) displays two dominant density units in an ~8800 km^2 area unaffected by boundary proximity. For this smallest area, N(0.5) = 35732 ± 1285 and n = 70; as the area size decreases, the statistical uncertainty and influence of small number statistics increase. Thus, on the basis of distinguishing two distinct, statistically separable crater populations representing two geologic units, selecting measurement areas $\geq 1 \times 10^4$ km^2 in spatial extent is ideal, whenever possible, for dating mare surfaces of all ages.

Given that some craters in the size range 500 m to ~850 m in diameter are more likely to be far-flung, non-obvious secondary craters on the basis of proximity to other craters (grouping or clustering), association with high albedo crater rays, and observation of an obvious source crater, it is useful to examine the ACD for Mare Imbrium when the crater frequencies are limited to D ≥1 km. Examining the effects of this size range on the ACD measurement is a helpful exercise since absolute ages for the mare are frequently derived for craters with D ≥1 km (Neukum et al., 1975a; Neukum, 1983; Neukum et al., 2001a). For the entire study area, N(1) = 2476 ± 104, corresponding to an n = 5 for an

average neighborhood with a 25 km radius, but an average of 5 craters per neighborhood for the majority of Mare Imbrium is not statistically significant (e.g., Silverman, 1986; Davis, 2002). Therefore, to create a statistically meaningful ACD map using ≥1 km diameter craters, either a greater neighborhood radius is required or the study area size must be increased. However, increasing the study area size is not ideal because ejecta and prominent secondary crater materials (chains, disrupted terrain) from Aristillus and Autolycus to the east, Copernicus to the south, and Aristarchus to the west contaminate the mare surface. Instead, increasing the neighborhood radius is more feasible, and by increasing the neighborhood radius to 50 km, n = 19, and there is a 10% chance of a neighborhood containing ≤13 craters and an 11% chance of ≥25 craters in a neighborhood (Figure 3.29A). When the neighborhood radius is increased to 75 km, n = 44, and there is a 10% chance of a neighborhood containing ≤35 craters and a 13% chance of ≥52 craters in a neighborhood (Figure 3.29B). As discussed previously (Section 3.2.3.2), larger neighborhood sizes smooth regional variation and thus limit observations of local variation. The ACD map for the 50 km neighborhood radius exhibits several discrete regions of high and low density, bordered and surrounded by intermediate density values. The high density regions correspond to those observed in the 25 km neighborhood radius map derived from D ≥500 m (Figure 3.3A), as does the largest low density area in the southwest, but the remainder does not correlate well. In contrast, the ACD derived with a 75 km neighborhood radius agrees better with the 25 km neighborhood radius ACD map: there are larger, broader regions of high density separated from a large, low density region by an intermediate density area (Figure 3.29). Moreover, the intermediate density forms a distinct northwest-southeast division of the

high and low density regions that corresponds to the spectral boundary between the red and blue units, albeit greatly smoothed. In this case, both the neighborhood size and smaller statistics (n(D ≥1 km) = 44 for a 75 km neighborhood radius, n(D ≥500 m) = 61 for a 25 km neighborhood radius) contribute to the differences in detail between the two ACD maps, but the overall trend of a higher density region to the east and a lower density region to the west remain similar. Furthermore, the locations of the large, broad high density regions do not change between the two maps: there is a high density region in the north and to the east in both. In the D ≥500 ACD map, I identified non-obvious secondaries that contributed in part to the high density magnitudes in these locations (Figure 3.3A, 3.27, 3.28), but the presence of high densities in the same locations (Figure 3.29B) in the D ≥1 km ACD map indicates that these high densities do not solely reflect the inclusion of likely non-obvious secondaries. Therefore, measures of ACD determined using D ≥500 m provide valid information about statistically separable crater populations, particularly when multiple datasets (i.e., image data, geologic maps, ACD maps with different neighborhood sizes) are employed in analysis to identify the influence of potential non-obvious secondaries on the ACD measurement.

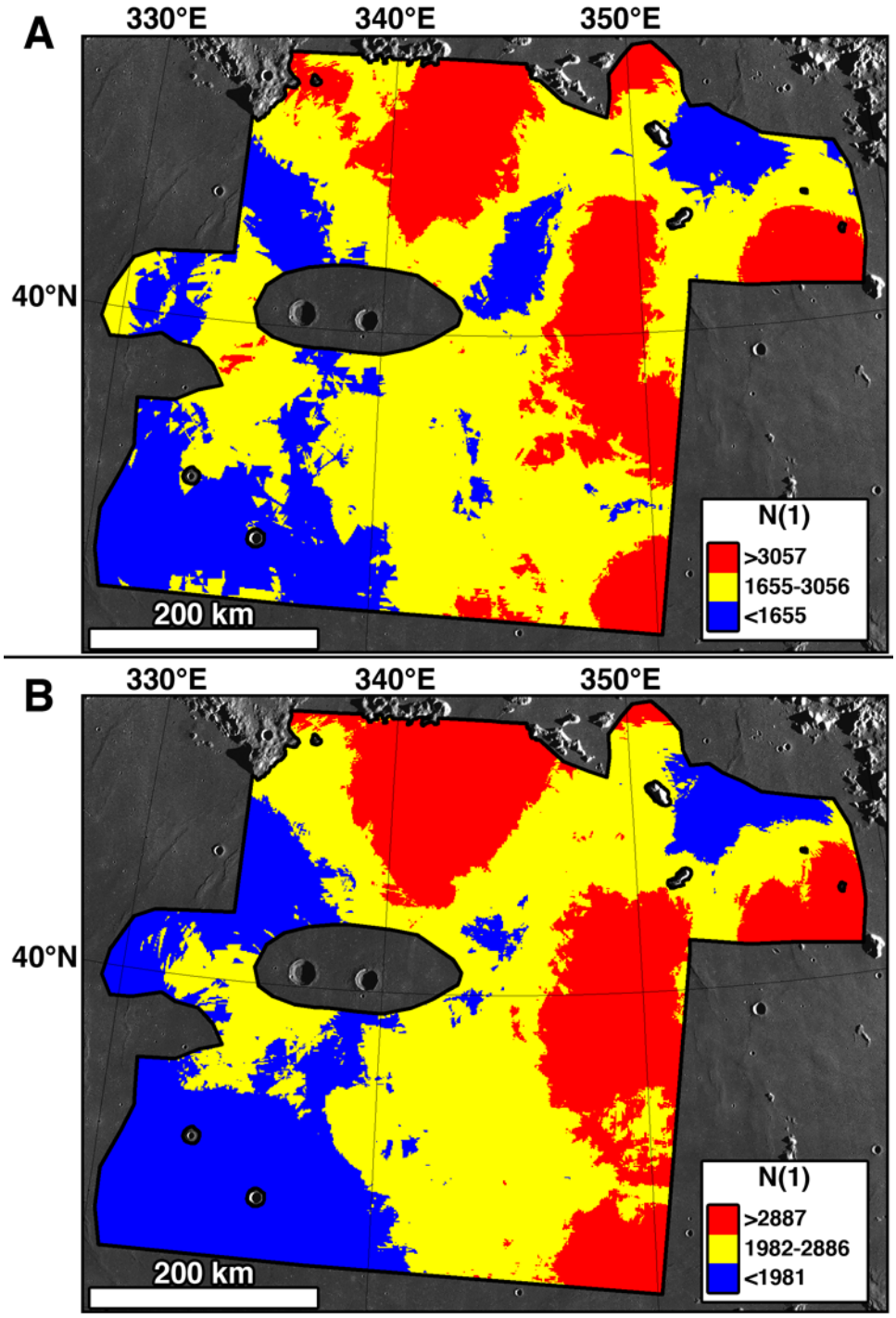

Figure 3.29. ACD maps derived from craters with D ≥1 km; (A) 50 km neighborhood radius, (B) 75 km neighborhood radius. Color classification scale determined from 10th percentile of measured crater population.

3.4.4. Absolute Model Age Assessment

Measurements of ACD derived from measures of crater frequency provide a means to test the significance of accepted model ages. The ACD map (Figure 3.3A) reproduces two statistically separable crater populations with different relative ages contained within adjacent regional spectral units that correspond to a modeled age difference of 300–500 million years (Hiesinger et al., 2000) to ~1 billion years (Bugiolacchi and Guest, 2008). Within the regional spectral units identified in Mare Imbrium (my study area, Figure 3.1C), Hiesinger et al. (2000) identified eight geologic units based on subtle spectral variation recorded in the Galileo Earth/Moon Encounter 2 images, and each individual color unit was assumed to be of uniform age. However, there are no obvious boundaries observed in the ACD map that correspond to the eight spectral units identified with model age differences less than 300–500 million years (Hiesinger et al., 2000). More recently, Bugiolacchi and Guest (2008) used Clementine multispectral data to identify geologic units in Mare Imbrium, and grouped color units according to compositional types (wt% FeO and TiO_2) and measured crater frequencies. Their results are also consistent with the ACD map, separating volcanic activity into two major eruptive phases for my defined study area in Mare Imbrium (Bugiolacchi and Guest, 2008). Thus, my findings suggest that while the observed spectral variations indicate changes in the mineralogy of the extruded mare lavas, emplacement of the eight smaller units identified by Hiesinger et al. (2000) occurred over a period of geologic time that was too short to accumulate statistically separable crater populations. The two regional geologic units distinguished within the ACD map and from relative crater retention ages

agree with the grouped geologic units (Hiesinger et al., 2000; Bugiolacchi and Guest, 2008), both on the basis of crater frequency and absolute model age range (2.2–3.3 Ga).

Therefore, a point to consider is whether model age differences of several hundred million years between spectrally determined units within the mare are geologically meaningful. Hiesinger et al. (2000) selected representative regions to date within each spectrally determined unit, assuming that each unit contained homogenous spectral features that were significantly different and each spectral unit represented a single age. However, the representative regions may not accurately represent the spectral unit for several reasons. First, most of the combined representative count areas are small, $<1 \times 10^4$ km^2, and as a result may not contain a statistically robust population of D ≥1 km craters (e.g., at least ~30; Silverman, 1986; Davis, 2002). From the N(1) values reported, a range of ~15 to 40 craters with D ≥1 km were measured (Hiesinger et al., 2000), and when statistical uncertainties are examined, there are only two, not eight, statistically significant crater populations (a relatively old unit and a younger one). To compare, only three units were smaller than 1.26×10^4 km^2 in size out of the thirteen grouped units dated by Bugiolacchi and Guest (2008). Furthermore, when crater counts on LROC WAC mosaics are completed for the mapped spatial extent of the eight units identified by Hiesinger et al. (2000), only two of the units are $<1 \times 10^4$ km^2 and the measured crater frequencies (i.e., N(1) values) are statistically separable into only two primary age groupings. From these data, I am unable to reproduce either absolute model ages for the eight units reported by Hiesinger et al. (2000) or absolute model ages for the two statistically separable units created by summing the values reported by Hiesinger et al. (2000). In contrast, my absolute model ages for the two regional units agree with those

derived by Bugiolacchi and Guest (2008). In addition to problems arising from small count areas, disparity in model ages may also reflect differences due to crater counting methods, in addition to subjectivity of crater recognition resulting from the effects of erosion, burial, illumination, and image quality on crater identification. Therefore, although there may be eight or more spectrally distinct units observed within the Mare Imbrium study region (Hiesinger et al., 2000; Bugiolacchi and Guest, 2008), I could only statistically distinguish two units from crater populations, suggesting that insufficient geologic time passed between emplacement of spectrally distinct volcanic eruptions to accumulate statistically separable crater populations for many of the spectral units identified by Hiesinger et al. (2000) and Bugiolacchi and Guest (2008).

3.4.5. Application to Mercury

The observation of a large-scale volcanic resurfacing boundary using ACD measurements indicates that spectral data is not a prerequisite for identification of relative age differences between expansive volcanically modified terrain. The ACD measurement may be combined with crater frequency statistics (e.g., N(1)) to test relative ages of large regions of volcanic smooth plains. The ability of ACD analysis to distinguish age units in the absence of spectral data in Mare Imbrium imply that this technique may be applied to other bodies to distinguish between different geologic subunits such as the northern smooth plains on Mercury (**Chapter 4**; Ostrach et al., in preparation). While strong multispectral contrasts observed within the lunar maria are used to define units, Mercury's smooth plains do not exhibit detectable spectral variation within individual contiguous units (e.g., Robinson et al., 2008; Denevi et al., 2009; 2013a). The utility of measuring ACD is that useful crater frequency information, in addition to relative age

relationships, may be determined independent of spectral differences and are applicable to expansive regions of volcanic smooth plains.

3.5. Conclusions

Using absolute model dating and determination of areal crater density, two spatially expansive, statistically separable mare units were determined from the measured crater frequencies for a large region within Mare Imbrium. The older, spectrally red unit is located in eastern Mare Imbrium and has an absolute model age of ~3.3 Ga old, and the younger, spectrally blue unit in western Mare Imbrium is ~2.2 Ga old. These ages agree with previous assessments of relative (e.g., Boyce and Dial, 1975; Schaber et al., 1975) and average absolute model (Hiesinger et al., 2000; Bugiolacchi and Guest, 2008) ages. However, although the ACD technique distinguishes between the two large geologic units with an age difference estimated between ~500 million years (Hiesinger et al., 2000) to ~1 billion years (Bugiolacchi and Guest, 2008), I am unable to reproduce either the 500 million year age difference in my dating efforts or distinguish subunits within the two large units reported by Hiesinger et al. (2000). Further examination using cumulative crater frequency measurements to determine relative crater retention ages indicate that several of the subunits reported (Hiesinger et al., 2000) are not statistically separable, and when coupled with my results, suggest that small model age differences on the order of hundreds of millions of years likely are not geologically meaningful.

My interpretation of areal crater densities (partly informed with spectral and normalized reflectance information) also reveal the presence of secondary craters of $D \geq 500$ m to ~2 km with non-diagnostic morphologies, in that the secondaries are not

observed as typical crater chains, herringbone pattern, or overlapping clusters. In most cases, the origins of the far-flung, non-obvious secondaries are identified, and these non-overlapping groupings of circular craters may be genetically associated with Copernicus, Aristillus, Autolycus, and Aristarchus craters, and in at least one case, Aristoteles crater. Therefore, although craters with $D \geq 1$ km are used for the absolute model age derivation and the contribution of unrecognized secondaries to the chronology is estimated at <5–10% (e.g., Neukum et al., 1975a; Werner et al., 2009), recognizing the potential for inclusion of non-obvious secondaries into measurements is important and all available datasets, including geologic maps, should be considered during selection of study areas for crater counting.

Measures of ACD can be used to distinguish previously reported age units that were defined with multispectral data within lunar mare for age contrasts >300–500 million years and spatial extents $>1 \times 10^4$ km^2, and the technique described here provides an effective method to determine relative ages of mare units independent of color boundaries. By employing the moving neighborhood approach to calculate ACD, any sharp contacts or boundaries are smoothed and reflected as intermediate densities, and because the density map reflects regional variations, substantial variations in crater density remain observable. Consequently, the spectral contact observed in the Clementine multispectral mosaic is reproduced in the ACD map within error of approximately ±one neighborhood radius (±25 km). Comparisons of ACD results for different sized subareas within Mare Imbrium also suggest measurement areas for crater counting should exceed 1×10^4 km^2 whenever possible. Moreover, the ability to distinguish surface units of different ages from measures of crater frequencies in Mare Imbrium, without using

spectral data, show that the ACD technique may be applied to other planetary bodies, such as Mercury, to search for age boundaries within contiguous smooth plains units. For example, the northern smooth plains on Mercury do not exhibit resolvable spectral variation, so my density method can be used to test hypotheses concerning timing of smooth plains emplacement (**Chapter 4**; Denevi et al., 2013a; Ostrach et al., in preparation).

CHAPTER 4

CONSTRAINING THE TIMESCALE OF NORTHERN SMOOTH PLAINS EMPLACEMENT ON MERCURY

4.1. Introduction

The MESSENGER spacecraft was inserted into orbit around Mercury on 18 March 2011, and soon thereafter the Mercury Dual Imaging System (MDIS) (Hawkins et al., 2007) began systematic mapping of the planet. Previous Mariner 10 and MESSENGER flyby image coverage (e.g., Murray et al., 1974a; Danielson et al., 1975; Trask and Guest, 1975; Solomon et al., 2001; 2008) of the north polar region (NPR; 50°N to 90°N, 0°E to 360°E) at illumination (solar incidence angle ≥65°, measured from the surface normal) and viewing geometries favorable for morphologic studies was limited, but showed large regions of smooth plains surrounded by more heavily cratered terrain (HCT) (e.g., Danielson et al., 1975; Trask and Guest, 1975; Robinson et al., 1999; Solomon et al., 2008). MDIS orbital images of the NPR provide full coverage at resolutions higher than those attained previously, low emission angles (intersection of the camera boresight with the surface, measured from the surface normal), and at illumination favorable for morphologic assessment.

Two major terrain units dominate the NPR: heavily cratered terrain (HCT) and smooth volcanic plains. The HCT is characterized by impact craters that are closely packed and overlapping (Murray et al., 1974b; Trask and Guest, 1975; Gault et al., 1977). An intercrater plains unit was mapped by Trask and Guest (1975), described as gently rolling ground between and around large craters of the HCT, but the relationship between the intercrater plains and HCT is complex; obvious superposition relations were not

commonly observed in Mariner 10 images (e.g., Trask and Guest, 1975; Malin, 1976; Leake, 1982). As a result and because of the difficulty in separating these two units, the intercrater plains and HCT were frequently combined into a single unit for crater counting purposes (Strom et al., 1975a; Trask, 1975; Guest and Gault, 1976), which I adopt in this investigation.

The northern smooth plains (NSP) are relatively flat with fewer superposed impact craters than the HCT (Murray et al., 1974b; Strom et al., 1975b; Guest and Gault, 1976), and are morphologically similar to the lunar maria (e.g., Murray et al., 1974a; 1974b; Murray, 1975; Strom et al., 1975b; Head et al., 2008; 2011). Smooth plains units identified in the Mariner 10-based studies (e.g., Murray et al., 1974b; 1975) have a lower crater size-frequency distribution (SFD) than the HCT, indicating that the smooth plains are substantially younger. Although no diagnostic volcanic features or constructs were conclusively identified in the Mariner 10 images, possibly due to resolution and illumination limitations (Schultz, 1977; Malin, 1978; Milkovich et al., 2002), a volcanic origin for much of the smooth plains was favored based on their widespread distribution, embayment relations with surrounding topography, observations of tectonic features, difference in crater density relative to the HCT, and visible color properties (e.g., Murray et al., 1974b; Strom et al., 1975b; Trask and Strom, 1976; Kiefer and Murray, 1987; Spudis and Guest, 1988; Robinson and Lucey, 1997; Robinson and Taylor, 2001). Although a volcanic origin for the smooth plains was called into question (Wilhelms, 1976b; Oberbeck et al., 1977), and while it is certainly possible that some smooth plains deposits are impact-generated products (i.e., fluidized ejecta, impact melt), the widespread smooth plains regions are now interpreted as volcanic effusive products,

much like the lunar maria (e.g., Murray et al., 1974b; 1975; Trask and Guest, 1975; Strom et al., 1975b; Trask and Strom, 1976; Kiefer and Murray, 1987; Robinson and Lucey, 1997; Head et al., 2008; 2009; 2011; Murchie et al., 2008; Robinson et al., 2008; Solomon et al., 2008; Denevi et al., 2009; 2013a; Ernst et al., 2010; Fassett et al., 2009; Kerber et al., 2009; 2011; Watters et al., 2009; Prockter et al., 2010; Freed et al., 2012; Goudge et al., 2012; Klimczak et al., 2012; Watters et al., 2012; Byrne et al., 2013; Hurwitz et al., 2013).

Using the impact cratering record of volcanically resurfaced regions, including partial crater floor flooding to regional plains formation and large-scale burial of pre-existing terrain, the extent and influence of volcanism over geologic time on Mercury is examined. This investigation defines the local stratigraphy for the NPR and complements previous studies of other regions (notably Trask, 1975; Strom, 1977; Spudis and Guest, 1988; Strom and Neukum, 1988; Strom et al., 2008; 2011; Fassett et al., 2009; Denevi et al., 2013a), providing insight into the global stratigraphic record and the relative ages of key geologic units on Mercury. The results presented here add to the understanding of the volcanic history of Mercury by comparing the relative ages of the NSP to the Caloris smooth plains (Spudis and Guest, 1988; Strom and Neukum, 1988; Strom et al., 2008; Fassett et al., 2009; Denevi et al., 2013a) and the surrounding NHCT; and the NHCT are compared to HCT elsewhere on Mercury (e.g., Strom et al., 2008; 2011; Fassett et al., 2011). The relative timing of NSP emplacement is explored using crater size-frequencies, measures of areal crater density, and stratigraphic relations, the results of which show evidence for multiple resurfacing of the NSP over a short geologic timescale. I also present regional NSP thickness and volume estimates derived from embayed craters,

providing a minimum approximation of volcanic material contained within this occurrence of smooth plains.

4.2. Methods and Data

I constructed a 400 meter pixel scale monochrome mosaic in polar stereographic projection from 0°E to 360°E and 50°N to 90°N from MDIS wide-angle camera (WAC) images (749 nm) (Hawkins et al., 2007; Figure 4.1). On the basis of morphologic observations, two distinct geologic units were defined in the NPR, HCT and NSP, comprising a total surface area of 9.26×10^6 km^2 (Figure 4.1). To prevent confusion when relating the results of my investigation to previous work, I adopt the term "heavily cratered terrain" to describe the combined HCT and intercrater plains units present on Mercury, identifying "northern heavily cratered terrain" (NHCT) when referring to HCT specific to the NPR.

The NHCT occupies 3.67×10^6 km^2 of the polar region (~40% total study area; ~5% surface area of Mercury). Impact crater morphologies in the NHCT range from pristine with visible ejecta ray systems and a sharp rim (Class 1 craters) to barely discernable and highly degraded craters (Class 4 and 5 craters; Arthur et al., 1963). Primary craters identified in the NHCT are as large as ~350 km in diameter, and there is a profusion of secondary craters intermingled with the primaries.

There are two large areas of smooth plains within the NPR, occupying a total area of 5.59×10^6 km^2 (~60% total study area, ~7% surface area of Mercury). The larger region of smooth plains (*SP1* in Figure 4.1b) is 3.79×10^6 km^2 in area, and extends beyond my study region to ~40°N between ~40°E to 80°E (Head et al., 2011). An area of

smooth plains occupying 2.92×10^5 km^2 not previously discussed by Head et al. (2011) is included in *SP1*. The smaller region, *SP2* (Figure 4.1b), extends from ~50°N to 65°N and ~120°E to 220°E and is 1.51×10^6 km^2 in area. The region *SP1* is connected by flooded craters and a series of broad valleys filled with smooth plains material (interpreted as flooded impact-sculpted terrain by Byrne et al., 2013). The smaller region of smooth plains (*SP2*) has contributions of material from both the proposed lava channels and the Caloris exterior smooth plains (much of this region is mapped as Caloris exterior smooth plains by Denevi et al., 2013a), suggesting multiple source regions.

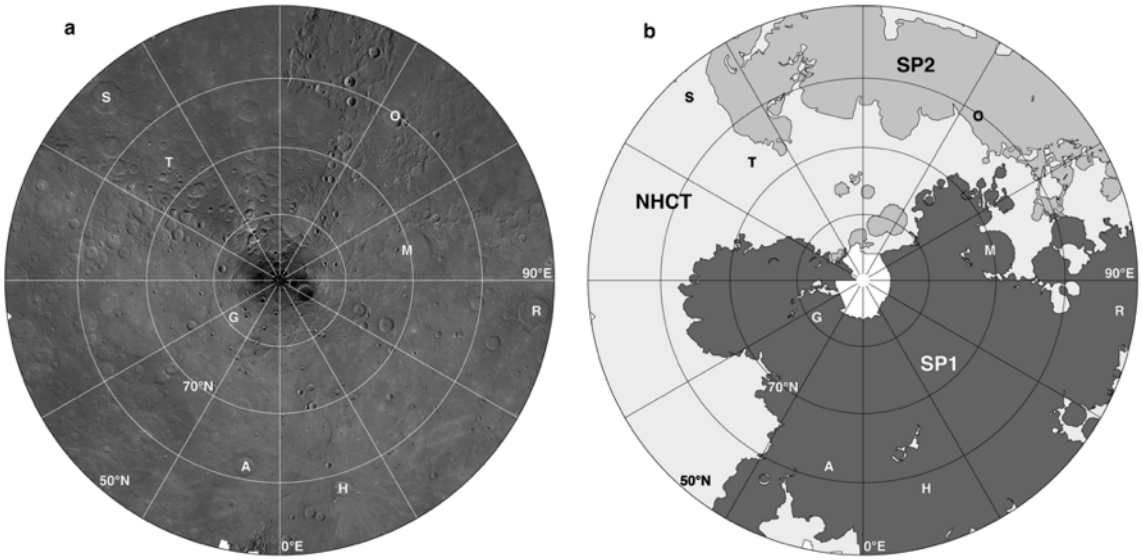

Figure 4.1. (a) MESSENGER MDIS WAC orbital monochrome mosaic of the NPR at 400 meter pixel scale in polar stereographic projection, extending from 0°E to 360°E, 50°N to 90°N, and covering an area 9.26×10^6 km^2. Eight impact craters are identified with capital letters: *A*, Abedin 61.76°N, 349.35°E, diameter (D) = 116 km; *G*, Goethe 81.50°N, 306.17°E, D = 317 km; *H*, Hokusai 57.75°N, 16.90°E, D = 114 km; *O*, Oskison 60.38°N, 145.36°E, D = 122 km; *M*, Mendelssohn 70.07°N, 102.55°E, D = 291 km; *R*, Rustaveli 52.55°N, 82.59°E, D = 200 km; *S*, Strindberg 53.21°N, 223.44°E, D = 189 km; *T*, Turgenev 65.63°N, 223.64°E, D = 136 km. (b) Sketch map denoting NPR units. *SP1* (dark gray) and *SP2* (light gray) comprise the NSP (5.59×10^6 km^2); *NHCT* is the northern heavily cratered terrain (3.67×10^6 km^2). Select craters are marked as described above. A region at the pole was excluded from mapping because of difficulty determining stratigraphic relations.

4.2.1. Crater Counts

I used the CraterTools extension (Kneissl et al., 2011) for the ESRI ArcMap 10 geographical information system (GIS) program to collect crater density measurements. This extension computes a best-fit circle to three user-defined points on a crater rim and records the center latitude, longitude, and diameter to a project database. Primary impact craters were identified on the basis of having nearly to entirely contiguous, approximately circular shapes. Obvious secondary craters, identified by their occurrence in chains, herringbone patterns, or clustered groups, were excluded. Secondary craters on Mercury are larger in diameter with respect to primaries compared to the Moon; a distinct upturn in the relative SFD plot (R-plot) at diameters around 8 km to 10 km is interpreted to be due to these larger secondaries (e.g., Gault et al., 1975; Trask, 1975; Strom, 1977; Strom et al., 2008; 2011). Thus, while primary craters with smaller diameters are present on the NSP, I restricted the crater frequencies used in age determination to those craters ≥8 km in diameter to limit inclusion of secondaries in my analysis.

A variety of plotting techniques are used to analyze crater size-frequency distributions; two methods are used in this investigation. I generated both cumulative SFD plots and R-plots to characterize crater populations using the standard root-2 binning and calculating uncertainties from the square root of the number of craters for a given bin, which represent ±one standard deviation (Crater Analysis Working Group, 1979). However, because cumulative SFD plots tend to look similar as a result of representing the cumulative distribution of craters, the R-plot is sometimes used to enhance subtle differences within and between crater populations. By displaying the differential size distribution (dN/dD, e.g., Crater Analysis Techniques Working Group, 1979) of the

measured crater population, the R-plot emphasizes the tendency of crater populations to exhibit a power law function (**Chapter 2**, Section 2.3.2, Equation 2.2) with a slope $b = -3 \pm 1$ (Crater Analysis Techniques Working Group, 1979; Neukum and Ivanov, 1994; Strom et al., 2005). Consequently, the R-plot essentially reflects the ratio between the measured crater distribution and a reference distribution with a -3 slope,

$$R(D) = D^{-3} \times \frac{dN}{dD} \qquad \text{(Equation 4.1)}$$

and from Equation 4.1, R-plot values, evaluated at the geometric mean of a given bin (usually using root-2 bins), are calculated from the discrete equation

$$R(D) = (D_a D_b)^{3/2} \left(\frac{N(D)_a - N(D)_b}{D_b - D_a} \right) \qquad \text{(Equation 4.2)}$$

where R(D) is the relative value and D_a and D_b are the bin minimum and maximum, respectively (Crater Analysis Techniques Working Group, 1979). Crater populations will plot as horizontal or moderately sloping lines in the R-plot; a differential distribution with $b = -3$ will plot as a horizontal line, a differential distribution with $b = -2$ will slope down to the left at a 45° angle, and a differential distribution with $b = -4$ will slope down to the right at a 45° angle (Crater Analysis Techniques Working Group, 1979; Neukum and Ivanov, 1994; Strom et al., 2005). Measured crater density is reflected by the vertical position of the relative values; higher relative values reflect greater crater density per unit area (e.g., Neukum and Ivanov, 1994; Strom et al., 2005).

I also calculated the crater retention age, which is the cumulative number of craters, *N*, equal to or larger than a given diameter, and normalized to a unit area (usually 10^6 km^2). This measure of relative crater frequency allows quantitative comparison of

crater populations across studies and provides a means to determine relative ages of different geologic units.

4.2.2. Mapping Buried Craters

Two crater populations are observed in the NSP: superposed primary impact craters (referred to hereafter as "post-plains craters") and partially to entirely embayed impact craters (referred to hereafter as "buried craters"). Completely buried craters were mapped by identifying arcuate wrinkle ridges that are thought to have nucleated above, and so demarcate, buried crater rims (Watters, 1993; Klimczak et al., 2012; Watters et al., 2012), and partially buried craters were mapped when ≤25% of the crater rim was exposed. Although there are overlapping craters in the post-plains population, identifying the craters is not difficult, whereas buried craters are more susceptible to complete removal from the observed cratering record by the formation of post-plains craters and their associated ejecta deposits. As a result, the buried crater measurement area is limited to a subsection of *SP1*, comprising an area 3.79×10^6 km^2 to exclude NSP modified by the Rustaveli impact. The *SP2* region was excluded from mapping due to modification by recent impacts, including Oskison crater, and poor illumination conditions for discerning buried craters. To maintain consistency with measurements of the NHCT and post-plains crater populations, I used buried craters ≥8 km in diameter for age determination.

I adopted a conservative mapping approach to promote unambiguous identification of relict, completely buried craters. Images with large solar incidence angles (>65°) typically have long shadows that emphasize subtle morphologic variations such that surface ridges marking buried craters are identifiable. In contrast, smaller buried craters (less than ~25–30 km diameters) are more difficult to unambiguously distinguish

on the basis of tectonic structures, even at large solar incidence angles, because of the widespread occurrence and complexity of wrinkle ridges and lobate scarps within the NSP as a whole (Head et al., 2011; Watters et al., 2012). Thus, the total number of identified buried craters in the region is a minimum.

4.2.3. Estimating NSP Regional Thickness and Volume

The thickness of the NSP was estimated using crater depth to diameter morphologic relationships defined by Pike (1988) (Table 4.1) and recently verified using MESSENGER flyby data (Barnouin et al., 2012). Buried crater diameters were measured using visible remnants of the crater rim, if visible, and by assuming arcuate wrinkle ridges represented original crater diameters. Original pre-flooding crater rim height was estimated assuming fresh crater morphology (Pike, 1988) and embayment with just enough material to cover the crater rim. Volume was then estimated by multiplying the rim heights for the smallest and largest fully buried craters unambiguously identified, representative of thickness, by the subsection of the *SP1* area of the NSP study region.

There are several limitations to using this technique. Mathematical relationships between crater diameter and rim height were only developed for mercurian craters between 2.4 km and 43 km diameter owing to limited coverage of larger partially shadowed craters (Pike, 1988). Although recent work revisiting crater depth to diameter relationships (e.g., Barnouin et al., 2012) shows that the previously derived relationships are valid, the Pike (1988) equations may overestimate the crater rim height because the ratio of diameter to depth tends to begin to flatten out for larger craters (>30 km), particularly for morphologic transitions between crater types (e.g., immature complex to mature complex) (e.g., Williams and Zuber, 1998; Baker et al., 2011; Barnouin et al.,

2012). Moreover, because the crater preservation state at the time of embayment is unknown, these equations likely further overestimate crater rim heights for degraded craters, whose rim heights tend to be lower than pristine craters. The NHCT and post-plains crater populations contain craters of various degradation states so it is likely that the buried crater population does as well. Furthermore, when a crater is completely filled and embayed, the thickness of the volcanic material above the crater rim is unknown; therefore, calculated crater rim heights will underestimate the thickness of volcanic material and provide minimum estimates. Nonetheless, this method was employed to produce first-order estimates of volcanic deposit thicknesses for the lunar maria (c.f., De Hon, 1974) and in this investigation.

Table 4.1. Rim Height and Depth to Diameter Equations, Pike (1988).

Crater Type[a]	**Rim Height**		**Depth to Diameter**	
	Diameter (km)	**Equation**	**Diameter (km)**	**Equation**
Simple	2.4 – 12	$0.052D^{0.930}$	0.2 – 14.4	$0.199D^{0.995}$
Immature Complex	13 – 43[b]	$0.150D^{0.487}$	9.5 – 29	$0.410D^{0.490}$
Mature Complex	–[c]	–[c]	30 – 175	$0.353D^{0.496}$

[a]Refer to Pike (1988) for detailed descriptions of crater morphology.
[b]Extrapolated to larger diameters, per verification by Barnouin et al. (2012).
[c]Equations not derived by Pike (1988).

4.2.4. Areal Crater Density

I applied a measure of statistical point density to determine if individual subunits with the NSP were identifiable using the post-plains crater population. Since older surfaces have accumulated more craters than younger surfaces, a measure of areal crater density should reflect variations in crater retention and thus indicate regions of resurfacing. Using the methodology of Ostrach and Robinson (2013), I modified the procedure to minimize edge effects by employing a weighted edge correction. I determined the areal density of all circular craters ≥4 km in diameter for the NSP.

Although some craters ≥4 km to 8 km may be unrecognized secondaries, I limited possible secondary inclusion by mapping only circular, non-overlapping craters. This technique of extending down to diameters where non-obvious secondary craters become prevalent was employed successfully for measures of areal crater density on the Moon (Ostrach and Robinson, 2013). Moreover, measurements including craters ≥8 km in diameter do not provide statistically robust areal crater density results (e.g., >30 samples; Silverman, 1986; Davis, 2002). For this region on Mercury, I used a moving neighborhood radius of 250 km and an output cell size of 10 km to ensure that geological differences related to age were emphasized, and real spatial variations were observed.

The moving neighborhood approach considers the number of craters within a defined circular region about each output cell; varying the neighborhood radius alters the spatial structure observed in the density plot such that small neighborhood sizes emphasize local (possibly statistical) variations whereas larger neighborhood sizes tend to smooth real variation. For the chosen neighborhood radius of 250 km, the number of craters per average neighborhood, n, is 53 and the standard deviation (estimated as $n^{0.5}$ for n craters) is 7.3, meaning the calculated density map is robust at the ~13% level against the crater count statistics (N(4)). Most of the variations in areal crater density reflect statistically significant differences in crater frequency, which are related to real relative age differences, as opposed to statistical noise. Given that impact cratering is assumed to be a random process (e.g., McGill, 1977), the statistical significance of the areal crater density measurement may be considered to be a random (Poisson) point distribution (e.g., Silverman, 1986; Davis, 2002). Accordingly, Poisson probabilities can be calculated to assess the statistical significance related to neighborhood selection.

When the 10th percentile is calculated for the average neighborhood (250 km radius) with n = 53 craters, there is a 12% chance that a neighborhood will contain ≤44 craters or ≥62 craters, and only a 1% chance that a neighborhood will contain ≤35 craters or ≥70 craters. These Poisson probabilities show that 80% of average neighborhoods will contain between 45 and 61 craters, and because the average sample size is 53 and considered to be a statistically robust sampling, average neighborhoods with ≤44 or ≥62 craters are statistically significant. However, when the neighborhood radius is decreased to 100 km, n = 9 and there is a 12% chance that the neighborhood will contain ≤5 craters or ≥13 craters, indicating that most of the density variation is statistical noise and the neighborhood area is too small. In contrast, when the neighborhood radius is increased to 500 km, n = 214. There is a 10% chance that the neighborhood will contain ≤195 craters or ≥223 craters, and although the average sample size is statistically robust, determining the influence of statistical noise within the crater frequency at the regional scale will be difficult and regional boundaries, if present, will be overly smoothed, suggesting that a 500 km radius is too large.

4.3. Results: Mercury North Polar Crater Statistics

4.3.1. Northern Heavily Cratered Terrain (NHCT)

I was unable to confidentially distinguish subunits within the NHCT based on crater statistics, morphologic relations, or color properties. The color properties of the NHCT are distinct from the NSP (Figure 4.2), and a definitive color difference following the defined morphologic boundary is observed; this relationship is analogous to those between HCT and probable volcanic plains mapped elsewhere on Mercury (Robinson

and Lucey, 1997; Robinson and Taylor, 2001; Robinson et al., 2008; Denevi et al., 2009; 2013a). Subtle regional color variation is difficult to determine within the NHCT because the current photometric correction is limited at large solar incidence angles found at high latitudes (>60°N) (Domingue et al., 2013), and calibration artifacts may further complicate determination of spectral subunits within the NHCT (Keller et al., 2013). In conjunction with the color observations, morphology observations identify stratigraphic relations at the local scale (e.g., impact crater superposition relations) within the NHCT, but any further attempt to define regional subunits is difficult.

In an effort to distinguish subunits, I divided the NHCT into three arbitrary subareas of comparable surface area, and determined the cumulative SFDs. To provide robust results and minimize bias, I repeated this process twice more, shifting the areal boundaries. At most diameters, the NHCT cumulative SFDs are statistically indistinguishable (Figure 4.3, Appendix D), exhibiting similar distributions and slopes. At diameters ≥50 km, the cumulative frequencies of the three subareas diverge as a result of small number statistics, and within the largest diameter bins there may be as few as one crater. The broadly massive and contiguous regions (areas 1 and 2 in Figure 4.3b, 4.3c) are statistically indistinguishable from each other as well as the cumulative frequency for the entire NHCT, but the dissected region of NHCT (area 3 in Figure 4.3b, 4.3c) has an overall lower cumulative frequency. N(20) values for the subareas are provided in Appendix D Table D1. NHCT craters are as large as ~350 km in diameter. In the NHCT, N(10) = 234 ± 8 and N(20) = 104 ± 5. The NHCT cumulative SFD exhibits an approximately constant slope (Figure 4.4a). In the R-plot, the NHCT has similar crater

frequencies compared with the “average” HCT, which was determined from multiple regions elsewhere on Mercury and was reported by Strom et al. (2008) (Figure 4.4b).

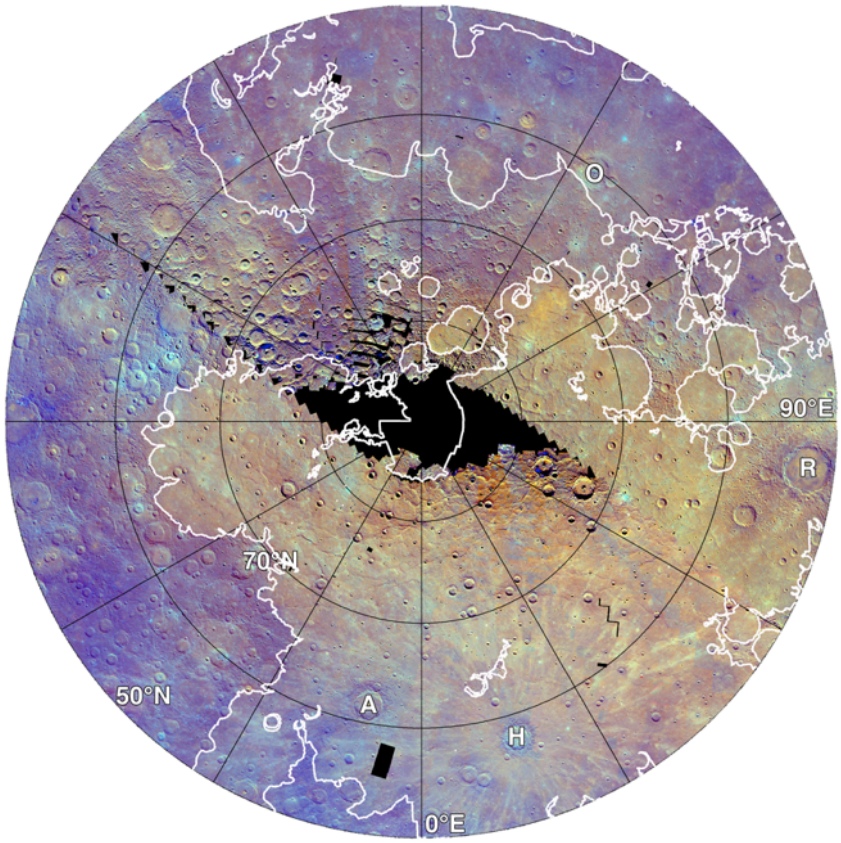

Figure 4.2. MDIS WAC principal component and ratio composite (second principal component in red, first principal component in green, and 430/1000 nm ratio in blue; Denevi et al., 2009) for the NPR. Mosaic is 665 meter pixel scale in polar stereographic projection, and black regions are due to gores in the color coverage. For orientation purposes: *A*, Abedin 61.76°N, 349.35°E, D = 116 km; *H*, Hokusai 57.75°N, 16.90°E, D = 114 km; *O*, Oskison 60.38°N, 145.36°E, D = 122 km; *R*, Rustaveli 52.55°N, 82.59°E, D = 200 km.

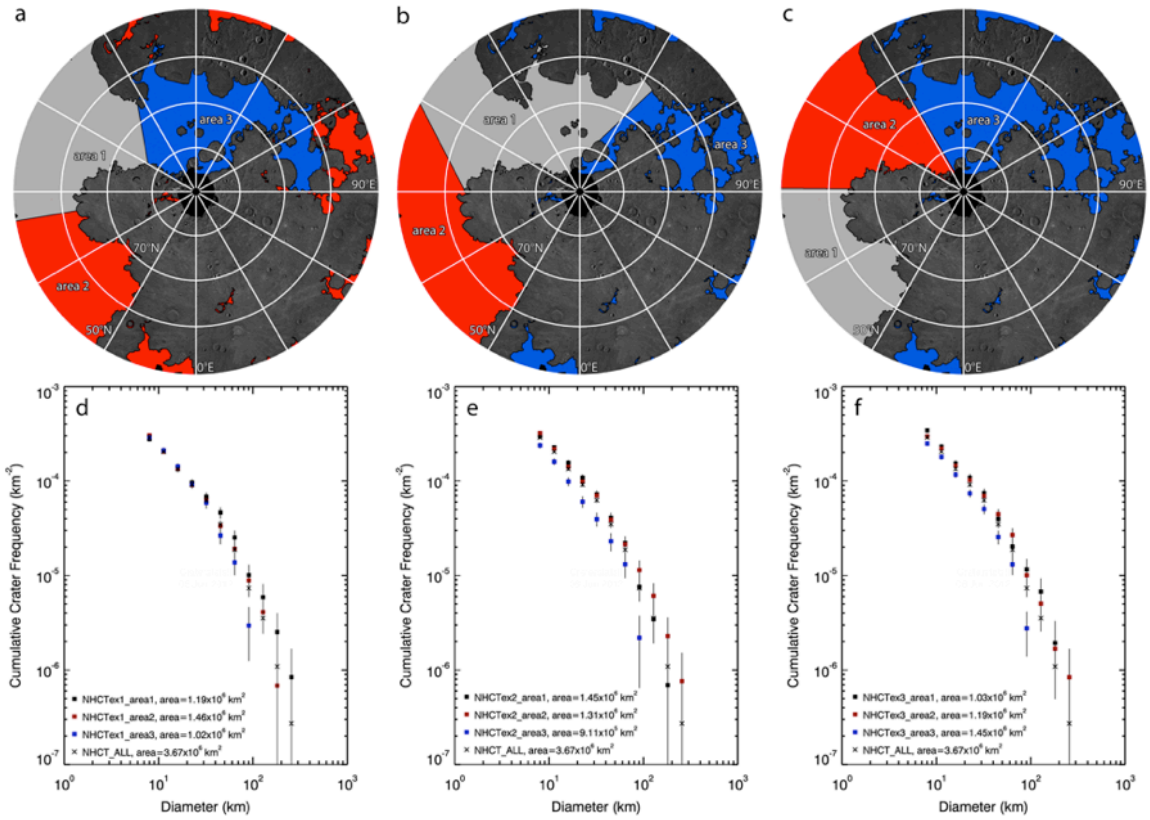

Figure 4.3. Subdividing the NHCT (measurement area 3.67×10^6 km^2) does not reveal statistically distinguishable subunits in cumulative SFD plots. Three subdivisions of the NHCT (a-c) and their corresponding cumulative SFD plots (d-f), plotted against the entire NHCT distribution for comparison. Refer to text for detailed discussion.

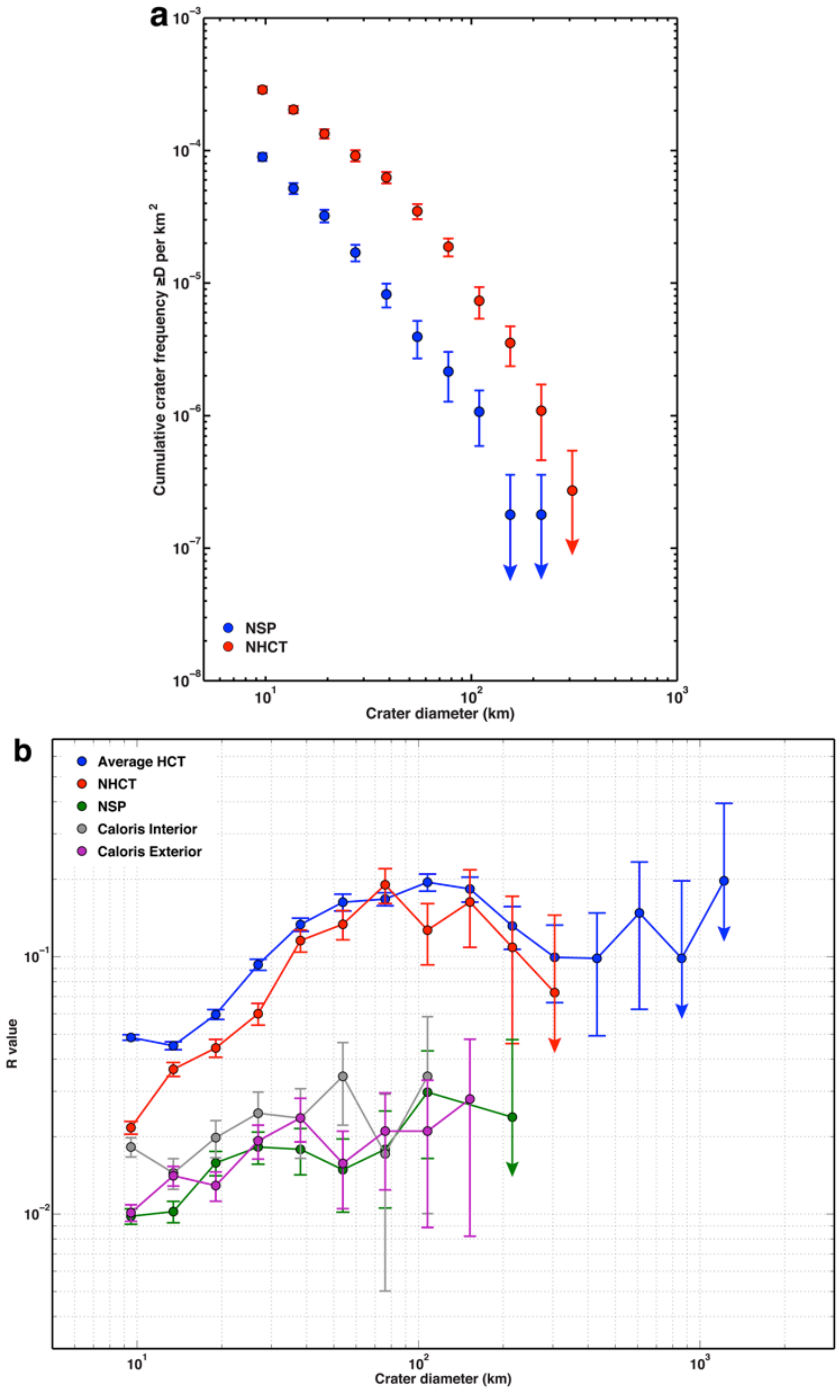

Figure 4.4. Cumulative SFD and R-plot for the NHCT (measurement area 3.67×10^6 km^2) and NSP (5.59×10^6 km^2). (a) Cumulative SFD. The NHCT has higher crater frequencies than the NSP. (b) R-plot of NPR crater populations, with "average" HCT (9.04×10^6; Strom et al., 2011) and Caloris interior and exterior post-plains crater populations (1.94×10^6 km^2 and 4.75×10^6 km^2, respectively; Strom et al., 2011). Uncertainty estimates are calculated from the square root of the number of craters for a given bin, and arrows extending toward the abscissa indicate diameter bins that include a single crater.

4.3.2. Northern Smooth Plains (NSP) Post-Plains Craters

Similar to the NHCT, I was unable to distinguish subunits within the NSP. MDIS color shows that the NSP exhibit a distinct color signature from the surrounding NHCT but are internally homogeneous (Figure 4.2). Variation in color within the NSP (excluding materials excavated by impact) at the regional scale is similar to the uncertainties remaining in the calibration (Domingue et al., 2013; Keller et al., 2013). Although local morphologic relations are present in the NSP (e.g., impact crater superposition, embayed craters), no evidence for the presence of morphologic or color subunits was observed.

Of the two NSP crater populations, post-plains craters are relevant to calculating crater densities and determining relative ages and stratigraphic relationships. To search for statistically distinguishable subunits within the NSP post-plains crater population, I divided *SP1* into four subareas covering similar areas in three separate iterations (Figure 4.5). The *SP2* area was not included because post-plains SFD comparisons between *SP1* and *SP2* reveal that these two regions are statistically indistinguishable (Figure 4.6). The absence of ≥100 km diameter craters within *SP2* is attributed to the substantially smaller count area than *SP1*, contributing to poor count statistics at larger crater diameters. The cumulative SFDs for all the arbitrary subareas in the NSP are statistically indistinguishable over all diameters (Figure 4.5) and N(10) values are nearly identical (Appendix D Table D2). At diameters ≥40 km, the cumulative frequencies noticeably diverge due to statistically small sample sizes.

The post-plains cumulative SFD plot has a lower frequency than the NHCT and a constant slope for craters in bins ≤100 km diameter and does not exhibit kinks (Figure

4.4a). Post-plains craters are as large as ~190 km in diameter, and in the NSP, N(10) = 63 ± 3 and N(20) = 23 ± 2. These crater retention ages are consistent with both Caloris exterior and interior plains counts (Strom et al., 2008; Fassett et al., 2009; Denevi et al., 2013a). The R-plot is relatively flat, exhibiting a different shape and slope than the NHCT distribution (Figure 4b). Additionally, the post-plains crater population is statistically indistinguishable to the Caloris plains crater densities (Figure 4.4b) (Strom et al., 2008).

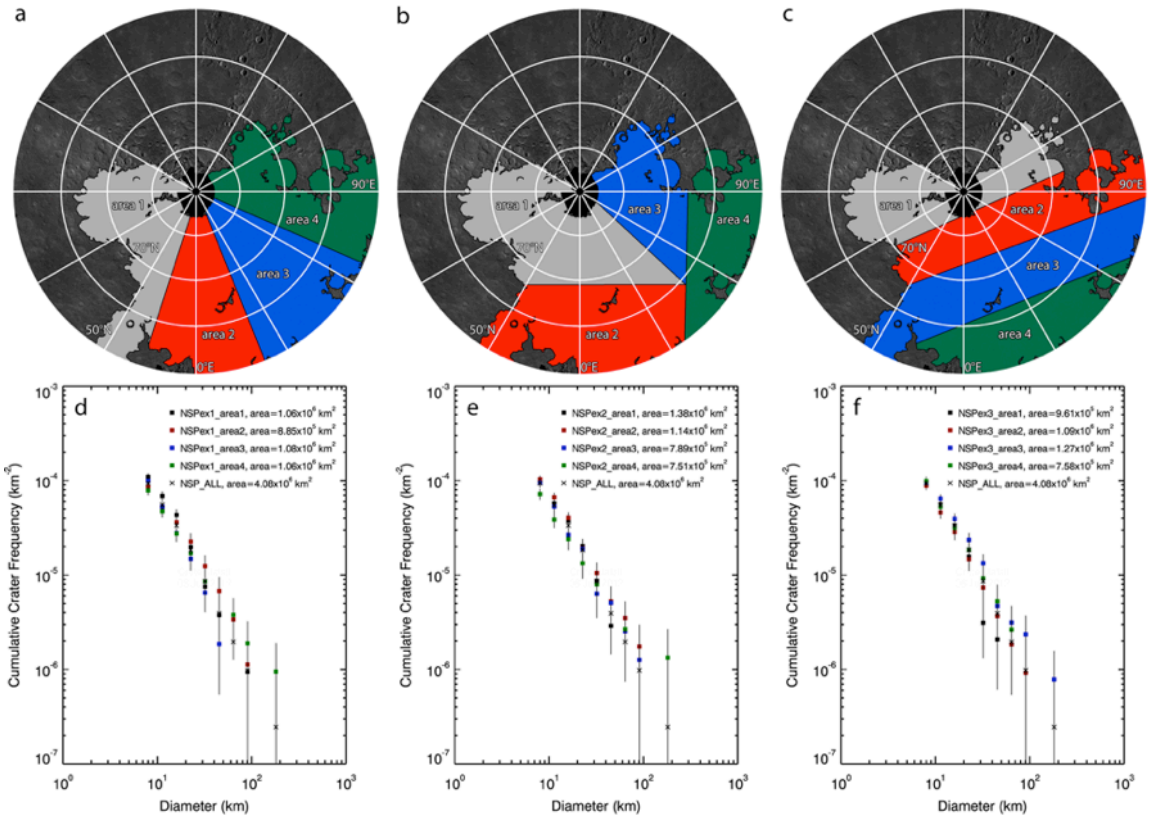

Figure 4.5. Subdividing the NSP (measurement area 4.08 × 10^6 km^2) does not reveal statistically distinguishable subunits in cumulative SFD plots. Three subdivisions of the NSP (a-c) and their corresponding cumulative SFD plots (d-f), plotted against the entire NSP distribution for comparison. Refer to text for detailed discussion.

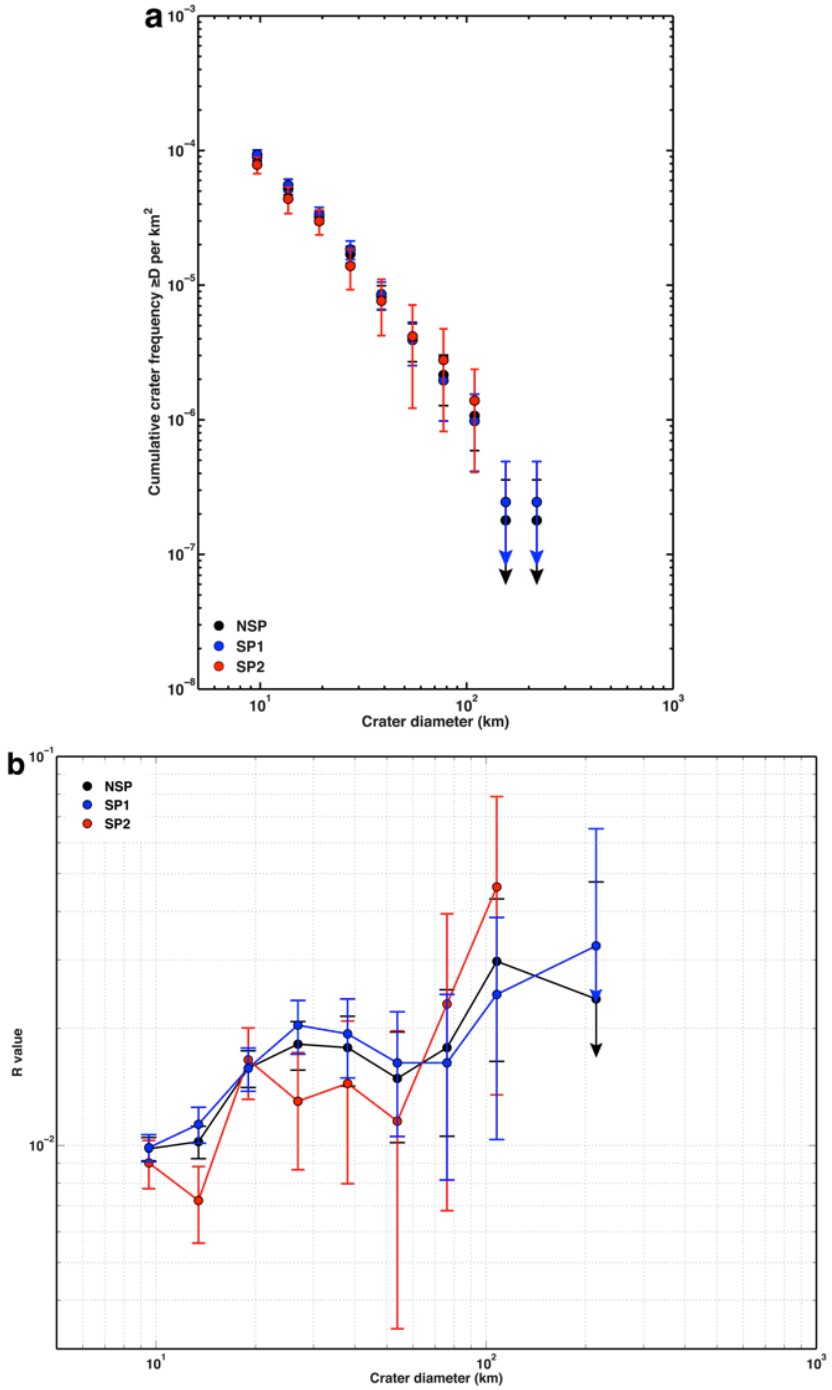

Figure 4.6. Cumulative SFD plot and R-plot for the NSP post-plains crater population (measurement area 5.59×10^6 km^2) plotted against the two subareas, *SP1* (4.08×10^6 km^2) and *SP2* (1.51×10^6 km^2). (a) Cumulative SFD; *SP1* and *SP2* are statistically indistinguishable. (b) R-plot; *SP1* and *SP2* have subtle differences in crater frequencies, and although statistically indistinguishable, the *SP2* crater frequencies exhibit large uncertainties reflecting the smaller count area. Statistical uncertainty estimates are calculated from the square root of the number of craters for a given bin, and arrows extending toward the abscissa indicate diameter bins that include a single crater.

4.3.3. NSP Buried Craters

4.3.3.1. Morphologic Relations

There is abundant evidence of embayment relations between NSP and pre-existing craters. There are remnant crater rims (Figure 4.7, 4.8a), partially embayed craters and basins (e.g., Goethe, Figure 4.8a), and tectonic features interpreted to represent deformation caused by relict craters rims (Figure 4.8; e.g. Klimczak et al., 2012; Watters et al., 2012). Additionally, there are partially filled craters with and without rim breaches within the NSP (Figure 4.7b, 4.7c) and in the NHCT near the unit boundary (Figure 4.7c).

All but a small region of the Goethe basin rim (81.50°N, 306.17°E, 317 km diameter) was buried by smooth plains material, and well-formed arcuate wrinkle ridges denote the estimated buried rim location (Figure 4.8a, 4.8d). Using the morphologic relationships derived by Pike (1988), I estimate the Goethe basin rim height to be greater than 2.2 km and the basin depth to exceed 4 km. Additional wrinkle ridges deform the smooth plains within the basin interior, and arcuate wrinkle ridges and interior fractures define two buried craters located near the basin center (e.g. Klimczak et al., 2012; Watters et al., 2012). Using their diameters of ~45 km and ~60 km, estimates of original rim heights are 0.96 km to 1.1 km and crater depths are 2.3 km to 2.7 km, respectively.

Unambiguous superposition relations are observed for many buried craters in the NSP and are not limited to the largest impact basins (Figure 4.8). Tung Yuan crater (75.22°N, 296.51°E, 60 km diameter) superposes an unnamed basin (76.21°N, 284.16°E, ~250 km diameter), where original rim height and interior depth estimates are greater than 2.2 km and 4 km, respectively (Figure 4.8b, 4.8e). There are two large (~40 km and

~55 km diameters) craters buried near the basin rim, with estimated rim heights of 0.93 km and 1.1 km and original crater depths of 2.3 km and 2.6 km, respectively. Within the basin, numerous smaller craters (~10–35 km in diameter) are partially or completely buried within the basin interior. I estimate these crater rim heights to range between 0.45 km and 0.85 km and depths to be between 2.0 km and 2.1 km. Egonu crater (67.40°N, 60.80°E, 25 km diameter) superposes an unnamed basin (66.60°N, 60.86°E, ~155 km diameter; Figure 4.8c, 4.8f) with an estimated original rim height of 1.8 km and depth greater than 4 km. The basin interior contains one large buried crater (~80 km in diameter), with a rim height estimate of 1.3 km and a depth of 3.1 km. The buried crater is offset from the basin center, and interior tectonic fractures are present within the buried crater.

In addition, although I unambiguously identified the buried crater population for diameters ≥25 km, there is evidence for widespread burial of craters in the 4 km to 25 km diameter range (Figure 4.9; Figure 4 in Klimczak et al., 2012). I confidently identified 285 buried craters in the smaller size range, although additional buried craters may exist (Section 4.2.2) as evidenced by the steep decrease in frequency below 10 km diameter that likely reflects sampling bias at these smaller diameters (Figure 4.10). Rim height and interior crater depth estimates for buried craters in the 4–25 km diameter range are 0.19–0.73 km and 0.79–2.00 km, respectively. The smaller buried craters are not limited to flooded crater interiors (Figure 4.9, 4.10), although >50 buried craters do occur within the largest partially buried basin (Borealis, ~680 km in diameter, located at 69.91°N, 280.68°E; Figure 4.9), and are frequently are observed in the NSP among and between the larger buried craters.

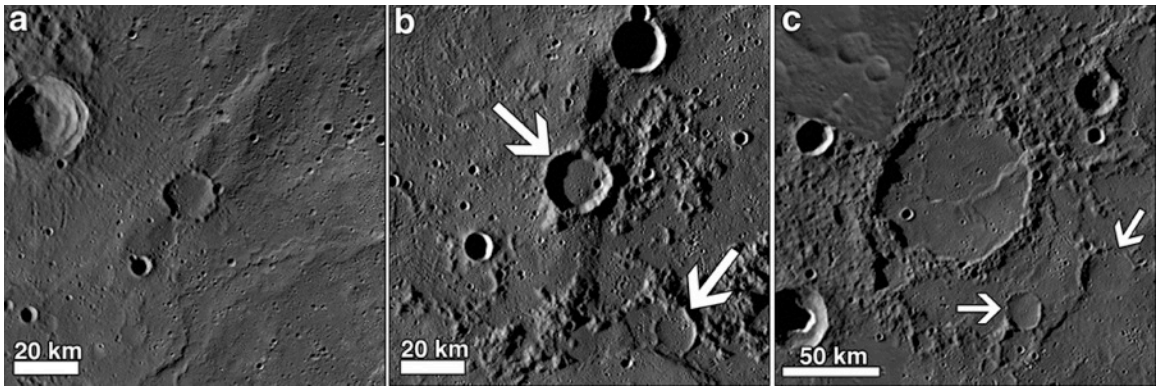

Figure 4.7. (a) Embayed crater in NSP (center, 77.79°N, 246.59°E, ~18 km diameter), with only the crater rim exposed at the surface. (b) Crater (center, 82.59°N, 274.18°E, ~20 km diameter) in NHCT subsequently embayed by NSP. Embayed ~15 km diameter crater (lower right). (c) Crater located at an NHCT and NSP boundary (image center; 61.09°N, 328.58°E, ~80 km diameter), partially embayed with smooth material within the crater interior. Two unnamed smaller craters (arrows, lower right) were also embayed and nearly buried by smooth plains material. MDIS WAC monochrome mosaic, 400 meter pixel scale.

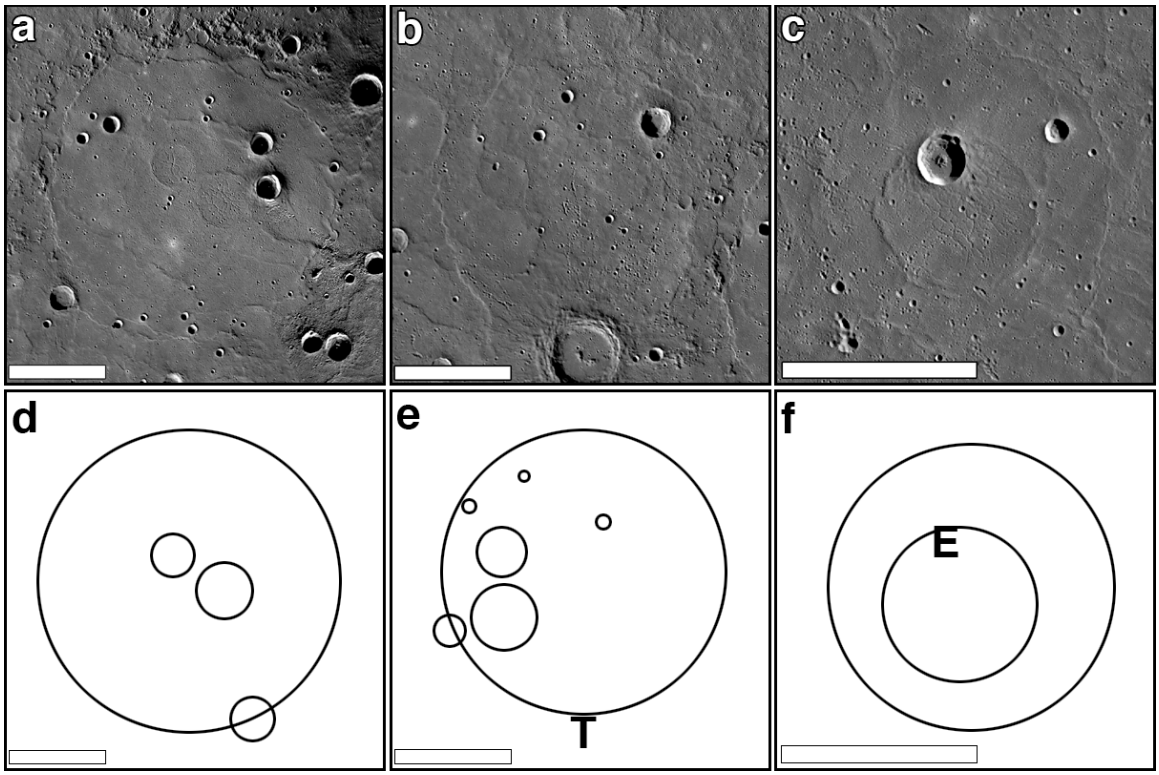

Figure 4.8. Observations of buried craters within the interiors of larger craters and basins (a-c), sketch maps of buried craters (d-f), scale bars are 100 km. (a, d) Goethe basin (81.50°N, 306.17°E, D = 317 km) is the classic example, with a partially buried rim and two well-defined buried craters near the basin center (D = ~45 km and 60 km). (b, e) Unnamed basin (76.21°N, 284.16°E, D = ~250 km) located to the east of Goethe and superposed by Tung Yuan crater (75.22°N, 296.51°E, D = 60 km; *T* in e). Two large (~45 km and 60 km diameter) craters and numerous smaller craters (D = ~10 to 35 km) are buried within the basin interior. (c, f) Unnamed basin (66.60°N, 60.86°E, D = ~150 km) superposed by Egonu crater (67.40°N, 60.80°E, D = 25 km; *E* in f). The basin interior contains one large buried crater (D = ~80 km) with interior tectonic fractures, offset from the basin center.

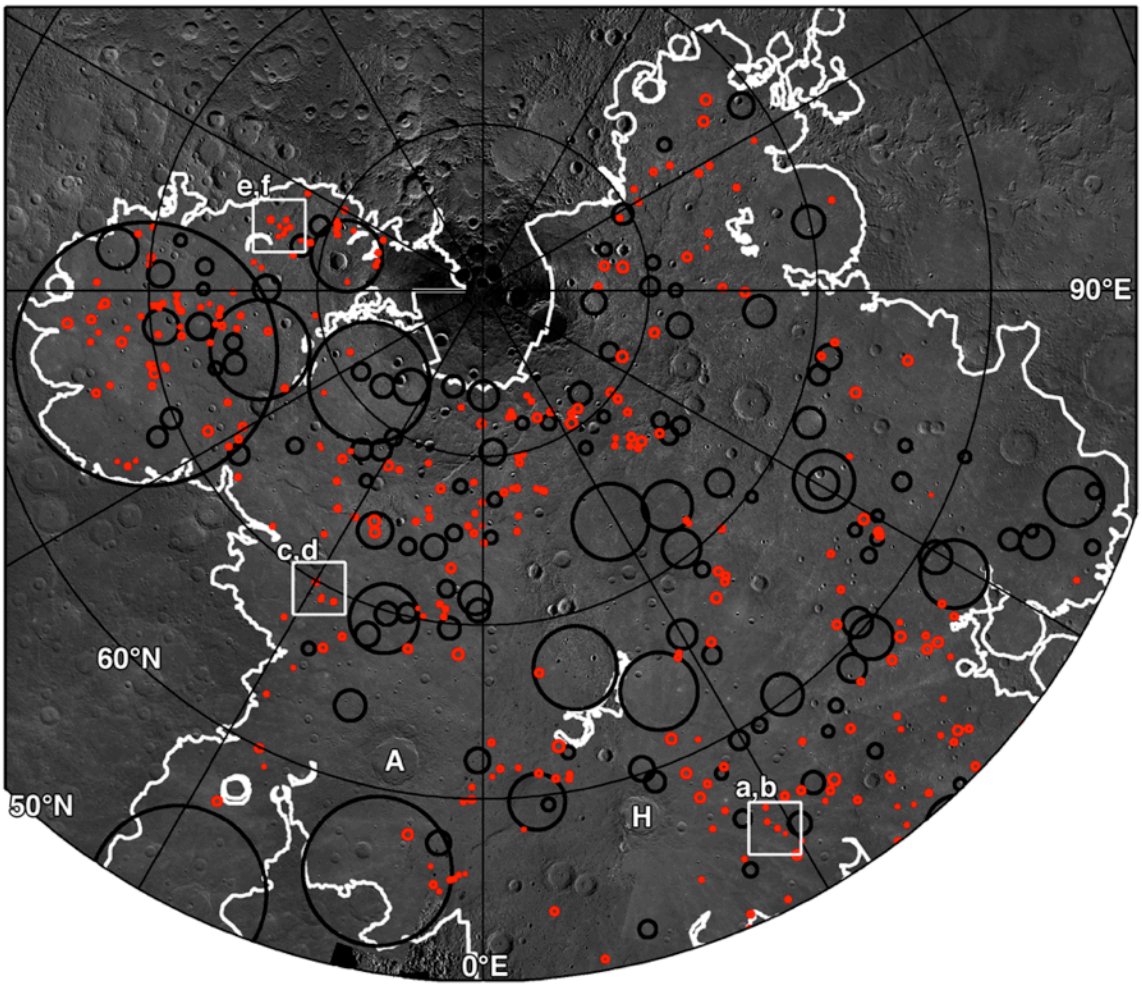

Figure 4.9. Partially to entirely buried craters mapped in the NSP; red circles denote buried craters 4 km to 25 km in diameter, black circles denote buried craters >25 km in diameter. These small buried craters are distributed widely across the NSP and are evidence for a hiatus in volcanic activity. The three white boxes note the locations of the detailed views in Figure 4.10. Abedin (*A*, 61.76°N, 349.35°E, D = 116 km) and Hokusai (*H*, 57.75°N, 16.90°E, D = 114 km) craters marked for orientation purposes.

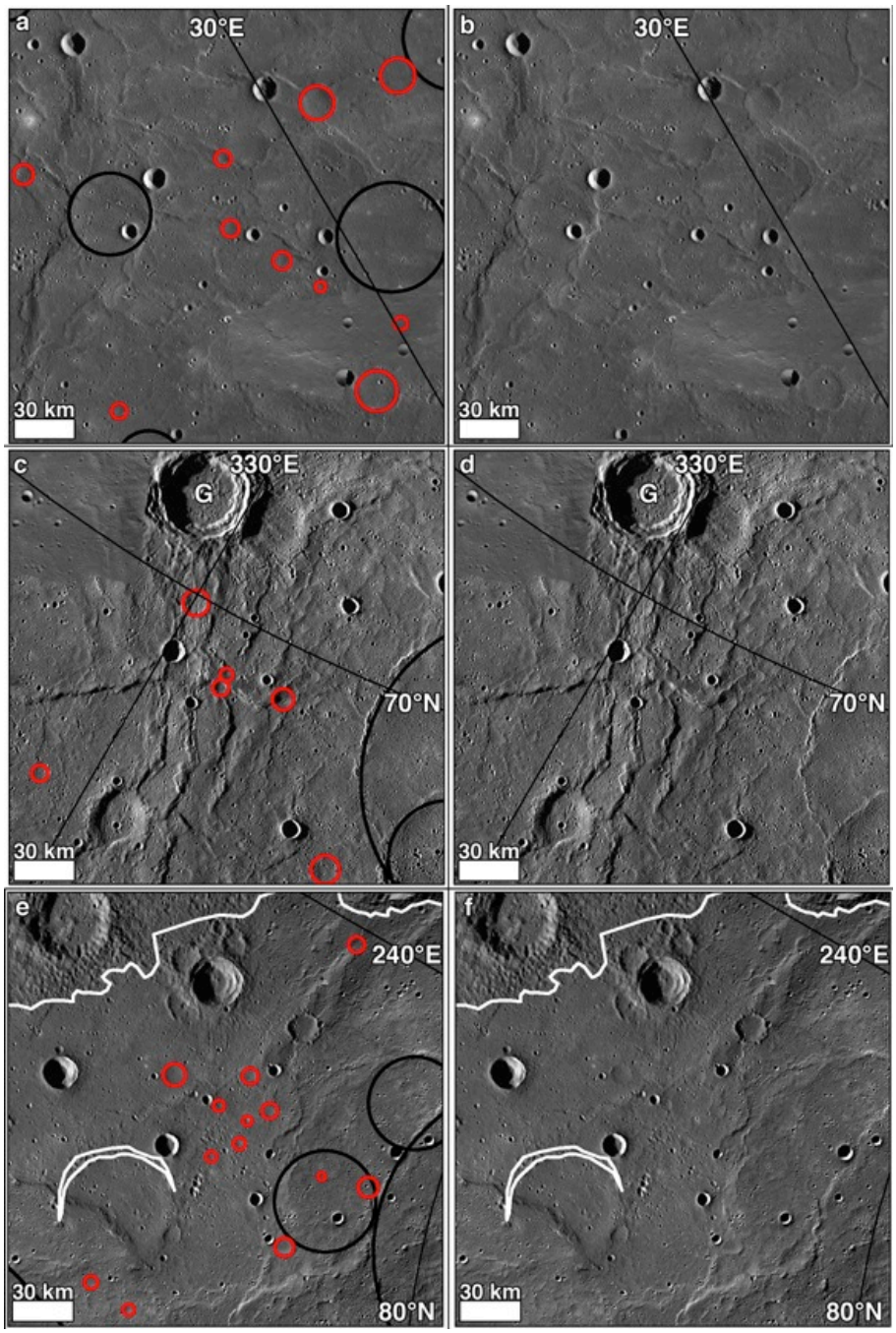

Figure 4.10. Detailed views of three representative NSP locations with small (4–25 km diameter) buried craters outlined in red. (a, b) Small buried craters to the east of Hokusai; centered at 54.80°N, 28.19°E, where a post-plains crater ~7 km in diameter is located adjacent to a buried crater ~9 km in diameter. (c, d) Substantial tectonic deformation deforms this area south of Grotell crater (*G*, 71.11°N, 328.24°E, D = 48 km), and several small buried craters are sharply defined by wrinkle ridges (centered at 69.16°N, 332.23°E on buried crater doublet, ~7 km and ~8 km diameters). (e, f) Small buried craters near the NSP–NHCT boundary, centered on a buried crater ~6 km in diameter with a post-plains crater ~5 km in diameter at 77.13°N, 252.35°E.

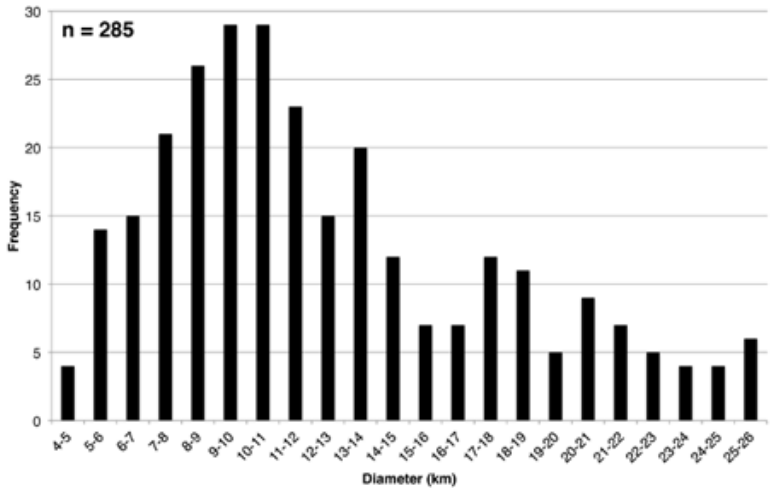

Figure 4.11. Histogram of buried craters in the 4–25 km diameter range, with 285 buried craters identified. The sharp drop-off below 10 km diameter reflects the increasing difficulty of confidently identifying buried craters. For this population, the median diameter is 11.1 km, the average diameter is 12.5 km, and the standard deviation is 5.2 km.

4.3.3.2. Buried Crater SFDs

Buried craters are widespread and randomly distributed across the NSP. The total number of buried craters, particularly for smaller diameters (less than ~30 km), may be greater than reported here, resulting primarily from illumination conditions (discussed in Section 4.2.2). Furthermore, there are likely craters of variable sizes that were buried to depths that effectively removed the craters from observation.

Fully buried craters are as large as ~260 km in diameter. For the buried craters, $N(10) = 79 \pm 5$ and $N(20) = 42 \pm 3$. The cumulative SFDs of the NSP post-plains craters, buried craters, and NHCT are markedly different (Figure 4.12). At diameters ≤30–60 km, the buried crater cumulative SFD slope shallows and begins to converge with the post-plains population at 8 to 10 km diameter (Figure 4.12a). The buried crater cumulative SFD slope is distinct from the post-plains and NHCT populations between ~30–100 km diameter, and is statistically indistinguishable from the NHCT between ~100–130 km

diameter. For craters ≥128 km in diameter, the buried crater cumulative SFD has a similar slope to NHCT. Like the post-plains crater population, the buried crater cumulative SFD does not exhibit kinks (Figure 4.12a). The R-plot shows that the buried crater population has a similar shape and slope as the NHCT crater population, particularly for diameters ≤60 km, but a lower overall crater density for diameters ≤150 km (Figure 4.12b).

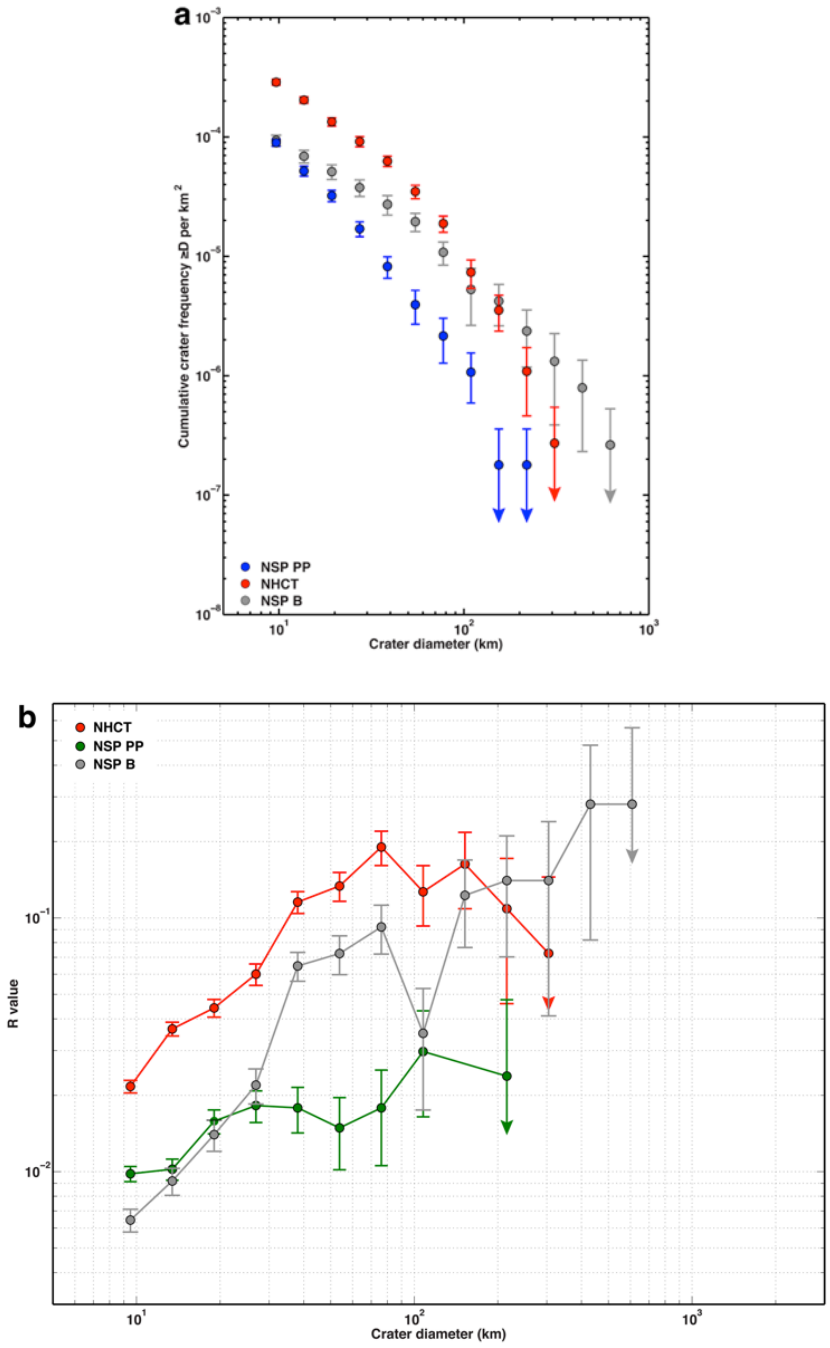

Figure 4.12. Cumulative SFD and R-plot for the NHCT (area 3.67×10^6 km^2), NSP post-plains (NSP PP, 5.59×10^6 km^2), and buried crater populations (NSP B, 3.79×10^6 km^2; selected from within *SP1* to exclude Rustaveli impact materials). (a) Cumulative SFD shows that the buried crater population has a lower frequency than the NHCT but a higher frequency than the NSP for diameters ≤130 km. (b) R-plot; buried crater population plots lower than the NHCT with a similar slope for diameters ≤60 km. Uncertainties are estimated from the square root of the number of craters for a given bin, and arrows are used for crater diameter bins with a single crater.

4.3.4. NSP Thickness and Volume Estimates

I use the diameters of buried craters to provide a first-order estimate of the depth of flooding in and around these craters and serving as a means to estimate smooth plains thickness. Rim height estimates for embayed craters with <25% rim remaining exposed range from 0.36–1.76 km for craters of diameters 8–157 km, respectively. For this diameter range, crater depth estimates are between 1.6 km to >4 km. However, although I identified ~300 buried craters in the 4–25 km diameter range, difficulties in confidently measuring the true population of these smaller craters (Section 4.2.2) prompted us to use 25 km as a minimum diameter for thickness and volume estimates for the NSP. With 25 km as the minimum diameter bound, the NSP are regionally on the order of 0.73 km to 1.76 km thick. Locally, NSP thickness may be deeper (or shallower), depending on the sizes of craters and depth of interior flooding.

Volume estimates use the rim heights for the smallest and largest completely embayed craters unambiguously identified, corresponding to diameters of 25 km and 157 km. The resulting rim height estimates are 0.73 km and 1.76 km, respectively. Using the area inclusive of all NSP units (*SP1* and *SP2*; 5.59×10^6 km^2) and assuming that *SP2* hosts a similar population of buried craters to *SP1*, I estimate the minimum regional NSP volume to be between 4.08×10^6 km^3 and 9.84×10^6 km^3.

4.3.5. NSP Areal Crater Density

The areal crater density map for the NSP is shown in Figure 4.13, and is classified into high, moderate, and low density regions (Section 4.2.4; Figure 4.14), where the "moderate" density class represents the classification of 80% of the sample population and both "high" and "low" density classes represent the upper and lower 10th percentile,

respectively. Representative neighborhoods were selected from within the three density types in the NSP, and Table 4.2 provides the average N(4) ($N(4)_{avg}$) for high, moderate, and low density regions. Much of the NSP is characterized by a moderate areal crater density (N(4) = 214–328, or 42–64 craters per neighborhood; Figure 4.14c, 4.14d); there are three broadly circular regions of lower density and large, relatively isolated higher density regions. The measured areal crater density distribution for the NSP is similar to synthetic areal crater density maps derived from random point distributions created using the measured crater frequency of the NSP (Figure 4.15), which show widespread moderate density and isolated high and low density regions.

In regions of high density, $N(4)_{avg}$, is 359 (70 craters per average neighborhood), and in regions of low density, $N(4)_{avg}$ = 170 (33 craters per average neighborhood). The large, relatively isolated high density regions are located throughout the NSP, and no volcanic vents, flow fronts, or embayment relations are observed on the surface surrounding these high density regions (Figure 4.13, 4.14a, 4.14b). One high density region (centered at 56.20°N, 211.21°E) is geographically proximal to Strindberg crater (53.21°N, 223.44°E) and contains secondary craters that meet the mapping criteria (circular, non-overlapping, D ≥4 km). However, the remaining high density regions do not exhibit similar relationships with the surroundings. In contrast, the well-defined circular regions of lower crater density are geographically associated with the surface modification resulting from three large, relatively recent impact craters: Rustaveli ($N(4)_{avg}$ = 130), Abedin ($N(4)_{avg}$ = 187), and Hokusai ($N(4)_{avg}$ = 194). In these areas, the crater formation and emplacement of ejecta obliterated the adjacent NSP and removed the post-plains cratering record (Figure 4.14e, 4.14f).

Table 4.2. Average N(4) for Areal Crater Densities Identified in the NSP.

Density Class[a]	Minimum N(4)	Maximum N(4)	Average N(4)
High	267	454	359
Moderate	214	328	273
Low	116	240	170

[a]Three circular regions with a radius of 250 km were selected within the density class region to average, and each neighborhood may contain minimal output cells from other density classes.

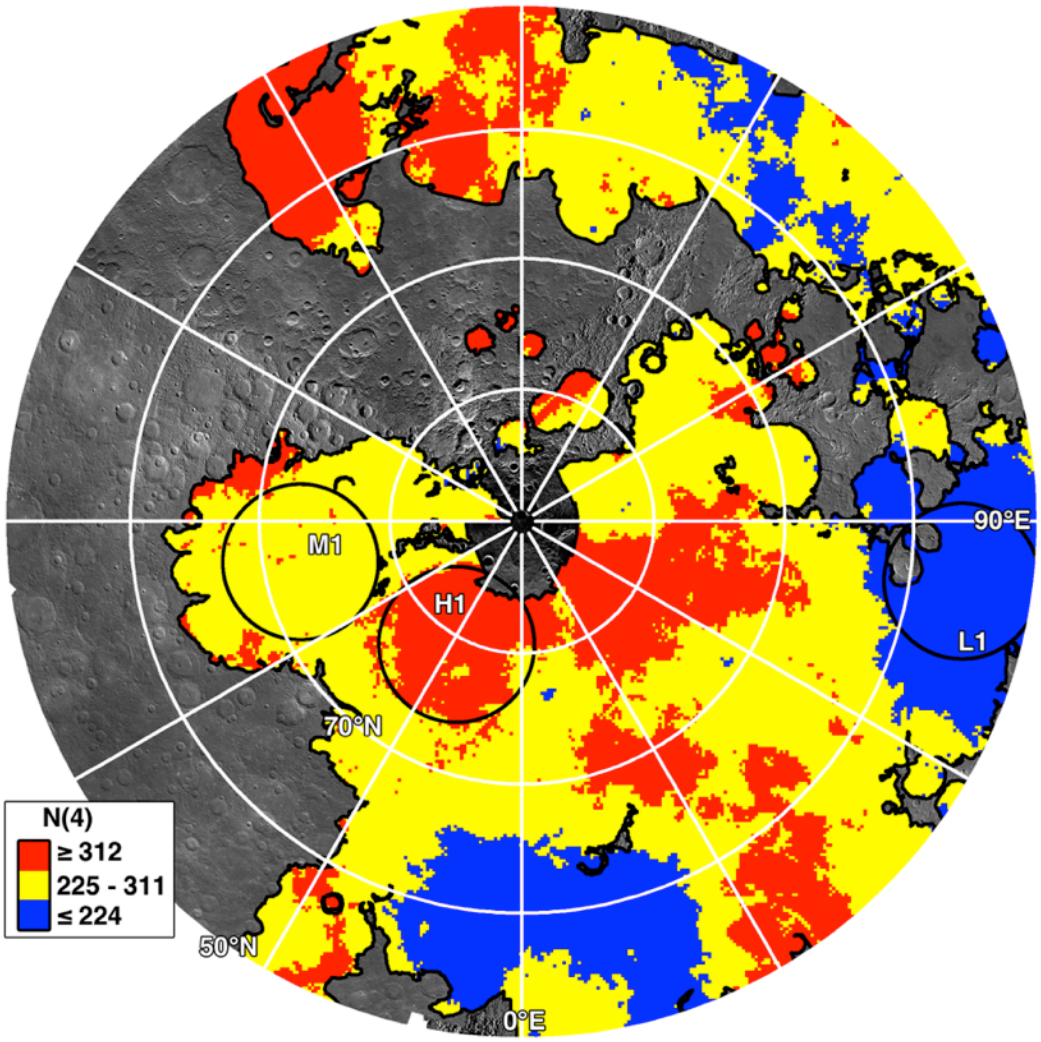

Figure 4.13. Areal crater density for the NSP in Lambert Azimuthal Equal-Area projection (neighborhood radius = 250 km, output cell = 10 km, craters D ≥4 km). Black circles with 250 km radius represent example neighborhood areas for low (L1), moderate (M1), and high (H1) densities (Figure 4.14). Color classification was determined by calculating Poisson probabilities for the measured crater population, in agreement with statistical assessment of neighborhood size selection (Section 4.2.4).

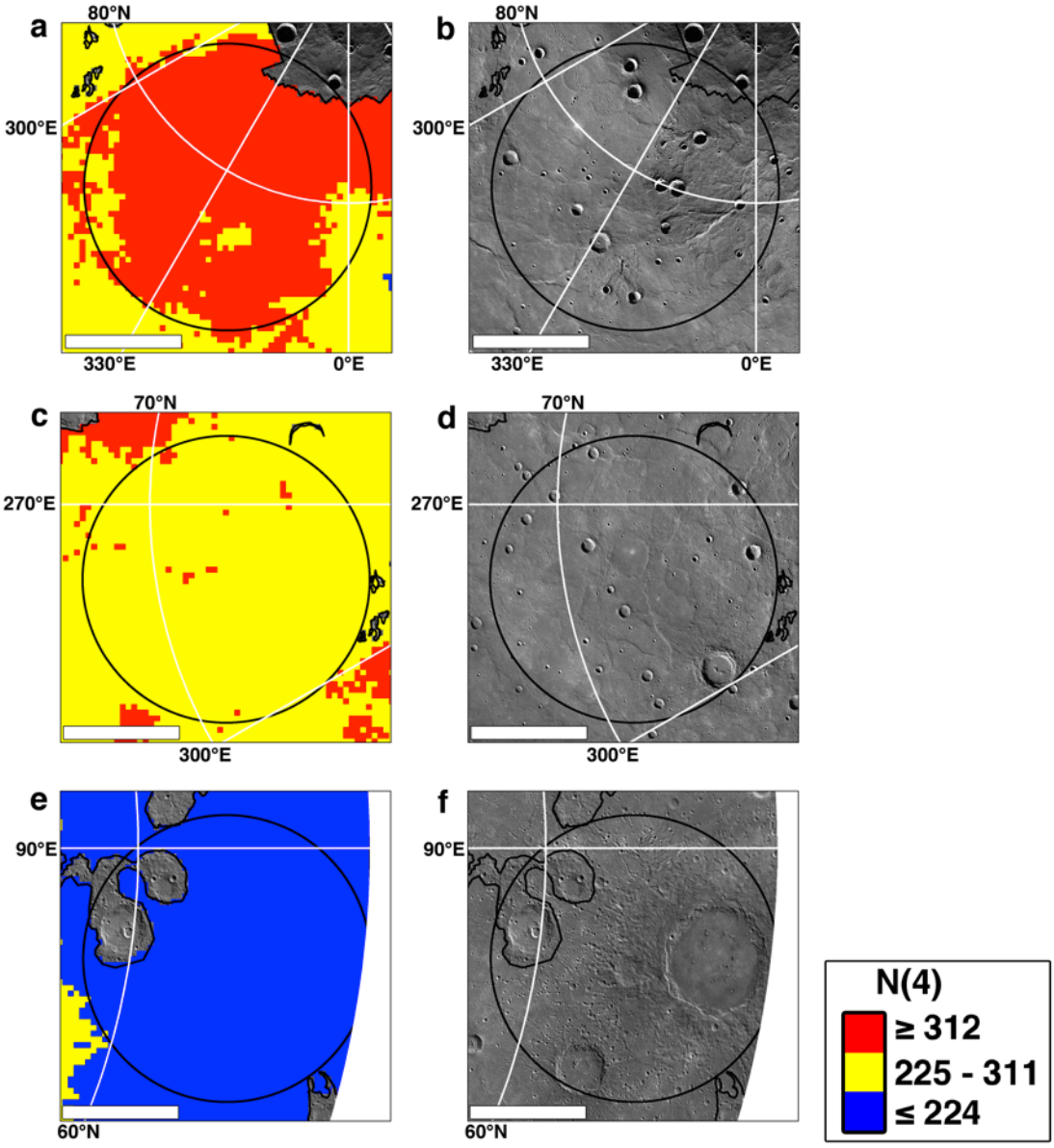

Figure 4.14. Examples of high, moderate, and low areal crater densities for the NSP (a-f), identified in Figure 4.13 as H1, M1, and L1, respectively. Black circle with 250 km radius (one neighborhood area) in the areal crater density map (left) and the MDIS monochrome WAC mosaic (right) and white scale bar is 200 km. An isolated high density region (a, b), there are no visible geologic boundaries indicative of resurfacing. Moderate areal crater density (c, d) is prevalent in the NSP. Low density regions are attributed to the formation of impact craters, Rustaveli (e, f; 52.54°N, 82.59°E, D = 200 km) is the largest example in the NSP.

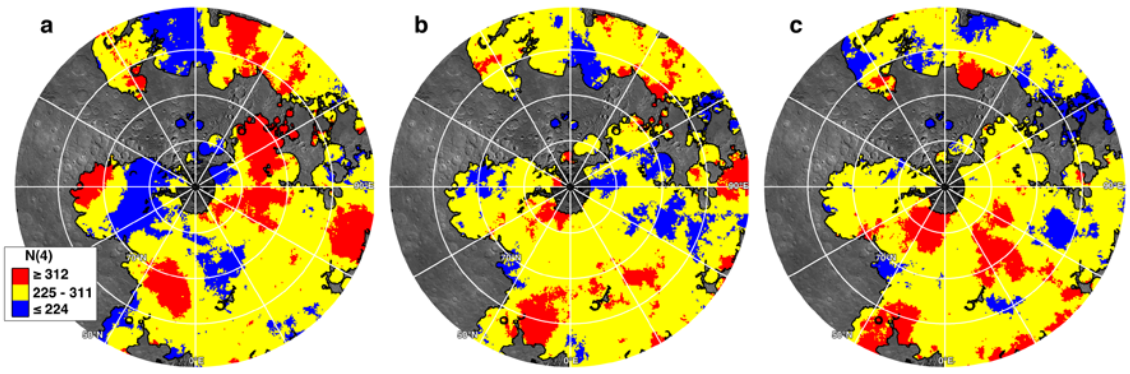

Figure 4.15. Three iterations (a-c) of synthetic areal crater density for the NSP determined from different random distributions each containing 1500 points. Output cell is 10 km, neighborhood radius is 250 km. Colors classified according to the 10th percentile calculated for the Poisson probabilities from the distribution.

4.4. Discussion

4.4.1. NHCT: Old, Part of Global Unit

When divided into arbitrary subareas, some divisions of NHCT (Figure 4.3a, 4.3d; areas 1 and 2 in Figure 4.3b, 4.3c, 4.3e, 4.3f; Appendix D Table D1) are statistically indistinguishable, particularly at the smaller diameters (the largest diameter bins may have only a single crater). However, two arbitrary divisions of NHCT create a subarea that has a lower crater frequency than the others (area 3 in Figure 4.3b, 4.3c, 4.3e, 4.3f). The lower crater frequency for area 3 compared to areas 1 and 2 (Figure 4.3b, 4.3c, 4.3e, 4.3f).) leads to a possible interpretation that area 3 is a statistically distinguishable sub-unit within the NHCT. While this interpretation may be valid statistically, it is unlikely that area 3 represents a younger NHCT region compared to areas 1 and 2 based on geomorphologic observations of area 3. Area 3 is more strongly affected by NSP embayment than areas 1 or 2. Area 3 is composed of several discontinuous regions of NHCT scattered throughout the NPR, as well as an NHCT area (50° to 70°N, 90° to

120°E) that is substantially modified by smooth plains materials. The modification of NHCT by NSP emplacement erased part of the NHCT crater population, evidenced by incompletely filled NHCT craters at the NHCT-NSP boundary, as well as flooded craters connected by broad valley-like pathways (Figure 4.3b, 4.3c). The dissection of the NHCT by NSP in area 3 results in a decrease in crater frequency for this selected subarea. However, when portions of the discontinuous and modified regions of NHCT are included with the larger contiguous units (Figure 4.3a), the cumulative SFDs for the three subareas are statistically indistinguishable, indicating that the cumulative SFD for area 3 is substantially affected by the contamination of NSP embayment and NHCT crater burial.

Both the cumulative SFD and R-plot show that the NHCT is older than the NSP (Figure 4.4). Additionally, the R-plot shows that the NHCT crater frequency for diameters >40 km is statistically indistinguishable from that of a global "average" of HCT, with the exception of the 100 km diameter bin (Figure 4.4b). However, for diameters <40 km, the NHCT exhibits a similar downward-sloping crater density in the R-plot and is statistically distinct from the global "average" of HCT (Figure 4.4b; Strom et al., 2008; 2011; Fassett et al., 2011). The overall trend of the NHCT in the R-plot, where crater density increases from D = 8 km to ~80 km and then levels off until beginning to decrease at D = ~110 km (Figure 4.4b), is broadly consistent with the presence of a globally distributed unit (Strom et al., 2011).

The crater frequency variations of the NHCT compared to that of the "average" HCT in Figure 4.4b represent a unique, regional resurfacing history for the NHCT. The observed downturn in the NHCT curve at crater diameters <50 km represents differences

in the degree of resurfacing relative to the "average" HCT and not poor statistics, and is consistent with other observations of a downturn for counts of other portions of the HCT, regardless of count area size (Strom et al., 2008; 2011). Morphologic observations of embayed and filled craters within the NHCT support the removal of smaller craters by volcanic resurfacing or impact-related basin ejecta emplacement (i.e., deposits comparable to the Cayley Plains on the Moon; Wilhelms, 1976b; Oberbeck et al., 1977). These local crater frequency variations with NHCT indicate that at least one period of major resurfacing occurred prior to emplacement of the NSP. In this case, the term "period" may represent continuous or discrete volcanic activity, or basin ejecta emplacement (e.g., resulting from the Caloris impact), and distinguishing between these sources with the available data is not possible. Strom et al. (2011) interpreted crater density differences between HCT regions to represent intercrater plains emplacement, assuming that most intercrater plains are volcanic in origin.

Furthermore, previous work using Mariner 10 data (notably Strom, 1977) and MESSENGER flyby data (e.g., Strom et al., 2011; Fassett et al., 2011) compared the crater SFDs of the Mercury HCT to the lunar highlands to show that both geologic units have the highest crater frequencies compared to other surfaces, although the HCT on Mercury is less cratered than the lunar highlands (e.g., Fassett et al., 2011). The high crater frequencies of these surfaces, which are dominated by Population 1 craters, indicate that they likely date to the Late Heavy Bombardment (Strom et al., 2005; 2008, 2011). Additionally, the large-scale resurfacing of the NHCT, by volcanic or basin ejecta emplacement (or both), must have occurred during the Late Heavy Bombardment because the resurfaced area, represented by a slightly lower crater density at diameters

≤50 km, still retains the shape of Population 1 craters, in addition to the more recent Population 2 craters (Strom et al., 2005; 2008; 2011).

4.4.2. NSP: Young, Regionally Distributed

The post-plains cumulative SFD and R-plot reveal a lower crater frequency than the NHCT and thus the NSP represents a younger geologic unit (Figure 4.4). The SFDs of *SP1* and *SP2* are indistinguishable, enabling us to combine these two NSP regions for statistical treatment (Figure 4.6). No statistically separable subunits are revealed when arbitrary subareas are selected (Figure 4.5; Appendix D Table D2), indicating that the NSP may be considered as being emplaced over a brief period of geologic time.

The relatively low frequency and flat distribution for the NSP post-plains population indicates that these craters are predominately Population 2 (Strom et al., 2005; Fassett et al., 2011). When compared to the Caloris interior and exterior post-plains crater populations (Figure 4.4b), the NSP post-plains population has a similar crater frequency and slope (and thus age) to the Caloris plains. Previous work showed that the Caloris plains postdate basin formation (e.g., Spudis and Guest, 1988; Murchie et al., 2008; Fassett et al., 2009) and were likely emplaced near the end of the Late Heavy Bombardment (e.g., Strom et al., 2008; 2011). More recently, mapping of additional major smooth plains units interpreted to be volcanic (i.e., Rudaki plains, plains south of Rachmaninoff, and plains within Beethoven and Rembrandt basins) revealed a limited range of crater retention ages (Fassett et al., 2012; Denevi et al., 2013a) that also overlap those of the Caloris plains (Spudis and Guest, 1988; Strom et al., 2008; Fassett et al., 2009; Fassett et al., 2012; Denevi et al., 2013a). The overlap in uncertainty estimates for all major smooth plains units indicates that their relative ages are statistically

indistinguishable from the NSP. Thus, any further statistical variation between the geologic units cannot be assessed beyond concluding that the NSP, the smooth plains of the Rudaki plains, those south of Rachmaninoff, and those associated with Beethoven, Rembrandt, and Caloris basins formed contemporaneously.

When a planetary surface is resurfaced (due to ejecta emplacement or volcanism), the erasure of craters of given sizes may manifest as kinks or elbows in the cumulative SFD for the superposed crater population (e.g., Neukum and Horn, 1976; Hiesinger et al., 2002), particularly if the interim between initial emplacement of material and resurfacing comprised a substantial period of geologic time. Although designating an age difference between the original surface and the resurfacing event is poorly constrained and remains an outstanding question, recent studies suggest a time difference of ~1.5–0.5 Ga is observable in the SFDs (Michael and Neukum, 2010; Neukum et al., 2010). However, the NSP post-plains crater population cumulative SFD does not exhibit kinks (Figure 4.4a) even though buried craters are visible. It may be that the interval(s) between episodes resurfacing in the NSP were of insufficient length to allow a statistically appreciable number of craters with D ≥8 km to form and be observed as kinks in the cumulative SFD. Or, equally plausible, a late-stage volcanic emplacement episode may have near-completely resurfaced the NSP up to the largest diameters, in which case the cumulative SFD records only the post-plains craters formed since the most recent resurfacing of this region and kinks would be unexpected.

4.4.3. NSP Absolute Age

At present, there are three principal chronologies for Mercury. Neukum et al. (2001a; 2001b) updated the absolute age chronology for Mercury originally derived by Strom and Neukum (1988) by incorporating newer data related to asteroid populations, cratering rate relative to the Moon, and improvements in crater scaling models. Using the Neukum et al. (2001b) chronology and the crater counts of this investigation, the NSP have an absolute model age of 3.73 ± 0.01 Ga, where the uncertainties are formal statistical estimates. This age for the NSP is consistent with previous results (Head et al., 2011) and for other major regions of smooth plains with estimated ages of ~3.7–3.9 Ga (Denevi et al., 2013a), which were derived using the Strom and Neukum (1988) chronology.

More recently, two new model production functions (MPF) were developed that improved upon the Neukum et al. (2001b) model by incorporating additional parameters (e.g., modeled relative global impact fluxes, improved crater scaling, two impactor populations, changing target properties) and newer data (Marchi et al., 2005; 2009; 2011; Le Feuvre and Wieczorek, 2011). For example, the Le Feuvre and Wieczorek (2011) MPF fit to crater counts for the Caloris interior plains (Fassett et al., 2009) produced a model age of 3.30 ± 0.3 Ga old. As the NSP crater counts are statistically indistinguishable from the Caloris counts, under this MPF the NSP are dated at 3.30 ± 0.3 Ga. Finally, the MPF calculated by Marchi et al. (2009; 2011) result in model ages for the NSP ranging from 2.5 ± 0.3 Ga to 3.1 ± 0.6 Ga. For this younger case, the range in absolute model age dates is partially dependent on the crater size range chosen to anchor the best MPF fit. Anchoring the MPF to intermediate crater sizes produces the age

of 2.5 ± 0.3 Ga, compared to an age of 3.1 ± 0.6 Ga when the MPF is anchored to the largest crater sizes, but the χ^2 test used to assess the MPF fit is not statistically favorable for the larger crater diameters and should not be used (Marchi, personal communication, 2012). Table 4.3 summarizes the absolute model ages for the three MPFs.

Although the MPFs produce model ages that are statistically distinguishable, differences of several hundred million years are not reflections of real geological meaning due to the nature of the calculation and inherent assumptions. For example, the range for the newest MPFs for the NSP is ~2.5 to ~3.3 Ga old, whereas the Neukum et al. (2001b) MPF estimates a value of ~3.7 Ga. The ages returned by these newest chronologies suggest that the NSP are younger than previously thought, and while no absolute age was derived for the NSP from Mariner 10 efforts, for the Caloris interior plains, a relative crater retention age of N(20) = 39 ± 12 was determined (Spudis and Guest, 1988) as was an absolute model age of 3.85 Ga (Strom and Neukum, 1988). Given that the NSP are statistically indistinguishable from the Caloris plains, an absolute model age of 3.85 Ga is assigned to the NSP under the Strom and Neukum (1988) MPF. Thus, the wide range in absolute age estimates between the three absolute model age chronologies indicate that more work is required, particularly since samples of known surface provenance do not exist for Mercury, to make certain that the assumptions inherent to modeling absolute ages and meaningful error bounds for Mercury are adequately addressed.

Table 4.3. Absolute Model Ages for the NSP.

Model Production Function	Model Age (Ga)
Neukum et al. (2001b)	3.73 ± 0.01[a]
Le Feuvre and Wieczorek (2011)	3.30 ± 0.03
Marchi et al. (2009)	2.5 ± 0.3 – 3.1 ± 0.6

[a]Formal statistical uncertainty estimates.

4.4.4. Buried Craters: Evidence for Volcanic Resurfacing

4.4.4.1. Morphologic Relations

Embayment relations provide abundant evidence for volcanic emplacement of the NSP. In the NSP and near NHCT-NSP boundaries there are partially flooded craters (Figure 4.7c) that are morphologically similar to Archimedes crater on the Moon (Figure 4.16). These crater embayment and infilling relations are defined by the stratigraphic relationships between an impact crater and nearby volcanic smooth plains units. Archimedes crater on the Moon is the type example (Figure 4.16), where mare materials within Imbrium basin embayed the Archimedes ejecta deposits and the crater interior was filled with mare material from a different source vent(s), as indicated by the absence of an obvious crater rim/wall breach (Wilhelms and McCauley, 1971; Head, 1982).

Other relations between buried craters are observed within the NSP (Figure 4.8), and comparing estimates of volcanic fill thickness provides compelling evidence for a minimum of two periods of volcanic resurfacing. Considering the smaller, buried craters (≥30 km to ~70 km in diameter) located within partially to completely buried larger craters and basins lends support to the hypothesis for multiple phases of smooth plains emplacement. Estimates of original crater depths and rim heights (Pike, 1988) for three basins and their buried craters (Figure 4.8) produce original basin depths that likely exceeded 4 km, and the buried craters within the basins have original rim heights

between 0.5–1.3 km. By assuming that completely buried craters are flooded so that the rim lies just beneath the volcanic surface, an assumption required for the rim height estimates since I observe tectonic deformation and not remnant crater rims, a minimum thickness of 1.3 km of volcanic material is required to bury the craters superposed within the basins. Yet I estimate at least 4 km volcanic material is needed to fill the basin interiors. These estimates suggest that the smaller craters must have formed on a thick fill that modified the original basin floor. Although the deepest depth to which a crater can be buried by volcanic material and result in subsequent tectonic deformation of the final surface is unknown, the buried crater rim heights are less than half the estimated basin depths, and the observations of varying amounts of tectonic deformation are in agreement with hypothesized differences in burial depths of craters (e.g., Freed et al., 2012; Watters et al., 2012). The presence of polygonally-arranged graben in some flooded craters (e.g., those within Goethe basin, Figure 4.8a) and absence in neighboring craters of similar diameter (e.g., Figure 4.8b) were interpreted to suggest different amounts of volcanic flooding across the NSP over the course of emplacement based on the results of finite element models (Freed et al., 2012; Klimczak et al., 2012; Watters et al., 2012).

Therefore, if the finite element models are truly representative of the subsurface geologic conditions within the NSP (Freed et al., 2012), then a first resurfacing episode was responsible for initial flooding of the larger basins, to an unknown depth, (e.g., Figure 4.8) and erasure of smaller craters within the NPR. It is plausible that basin ejecta was distributed within the NPR to initially resurface the region in a manner similar to the Imbrium basin materials on the Moon (i.e., the Fra Mauro Formation; e.g., Wilhelms, 1987), and the most likely candidate to provide a thick, regional fill of basin material is

Caloris. The Odin Formation, mapped in the circum-Caloris region and composed of knobby plains, was interpreted as basin ejecta from Mariner 10 images (Murray et al., 1974a; Strom et al., 1975; Trask and Guest, 1975). While stratigraphic relations suggest that the Odin Formation is composed of basin ejecta with portions embayed by younger volcanic deposits, crater size-frequency analyses are not consistent with the observed stratigraphic relations (Fassett et al., 2009; Denevi et al., 2013a). Moreover, the Odin Formation does not extend into the larger NSP region *SP1* (e.g. Fassett et al., 2009) where the buried crater population is observed, indicating that a substantial amount of basin ejecta was not likely emplaced in this region. Moreover, besides Borealis and Goethe, there are no additional basins unambiguously identified in MLA data (Zuber et al., 2012; Fassett et al., 2012), and the ejecta emplaced by these basins would be spatially limited in extent, unable to resurface the NPR on a regional scale. Thus, I suggest that the initial resurfacing in the NPR was by volcanic emplacement.

Subsequent to initial resurfacing, craters formed on the modified surface, which were then buried by at least one later episode of volcanic emplacement. I suggest that the buried craters identified in flooded basin interiors reflect a second volcanic resurfacing of the NSP, during which the basins were filled and interiors, including superposed craters, were buried. Additional evidence for at least a second volcanic resurfacing episode is the population of buried craters ≤25 km in diameter that are widely distributed across the NSP. If the smallest buried craters were spatially limited in extent, topographic variation beneath the NSP would explain their presence. If grouped about one location, the smallest buried craters may have formed on a local topographic high, but because the craters are dispersed within the NSP, it is improbable that all 4–25 km diameter buried

craters (n = 285) are perched on topographic highs. Similarly, the close proximity of these smaller craters to larger buried craters, particularly within Borealis basin, suggests stratigraphic relations inconsistent with the smallest buried craters having formed on the pre-NSP surface. Moreover, the morphology of surface deformation interpreted to represent the rims for the smallest buried craters is sharp and distinct (Figure 4.10) across the NSP, regardless of location (e.g., proximity to the NHCT-NSP boundary or near the center of the NSP), suggesting that these smallest craters are not buried to substantially different depths (e.g., Freed et al., 2012; Watters et al., 2012). A thickness of 0.19–0.73 km material, with an average of 0.54 km, is required to bury the smallest crater rims, and partially buried craters and kipukas near the NSP-NHCT boundary (presumably with thinner NSP than elsewhere; Figure 4.10c) are consistent with a burial thickness of at least ~0.2 km to ~0.5 km. However, the larger buried craters in the central NSP (~70°N, ~30°E) require ~1.5 km to ~2 km of material to bury the rims, yet buried craters ≤25 km in diameter persist with sharp morphology. Therefore, the smallest buried craters likely were flooded during a late (or last) stage of emplacement over a voluminous unit.

An alternative hypothesis to multiple phases of volcanic resurfacing may be that, prior to NSP emplacement, the NPR had irregular topography. However, this possibility is inconsistent with MESSENGER Mercury Laser Altimeter (MLA) data, which show that the NSP can be characterized as a lowland area ~2 km deeper than the surrounding NHCT, distinguished by a negative free-air gravity anomaly suggesting local isostatic compensation (Smith et al., 2012; Zuber et al., 2012). Unexpectedly, a broad topographic rise was observed, and on the basis of craters with inclined floors upon the rise that were

likely level-floored originally, the topographic rise formed after NSP emplacement concluded (e.g., Balcerski et al., 2012; Solomon et al., 2012; Zuber et al., 2012).

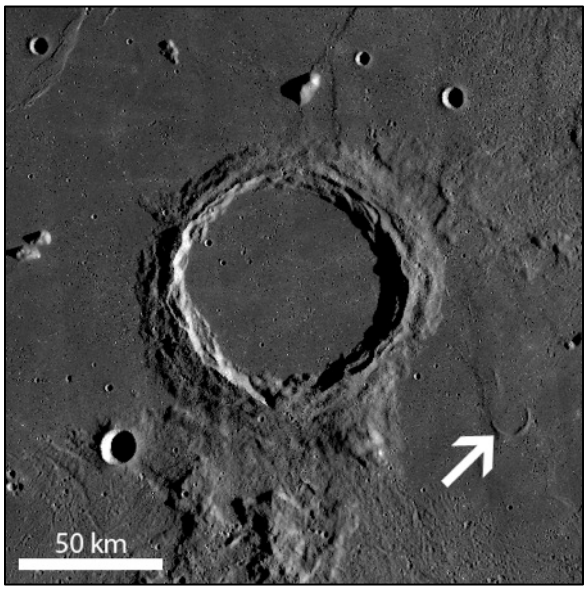

Figure 4.16. Archimedes crater (29.72°N, 356.01°E, diameter ~80 km), located in eastern Mare Imbrium on the Moon, is filled with volcanic smooth plains materials (mare basalts). Mare basalts embayed Spurr crater (arrow; 27.92°N, 358.74°E, ~13 km diameter), such that only about half of the crater rim is visible. LROC WAC monochrome mosaic, 400 meter pixel scale, illumination from the right.

4.4.4.2. Buried Crater SFDs

The post-plains and buried crater populations exhibit a large range in diameters (as large as ~190 km, ~260 km, and ~680 km for the post-plains, fully buried, and partially buried crater populations, respectively; Appendix D), and the buried crater cumulative SFD has a shallower slope than both the NSP and NHCT cumulative SFDs (Figure 4.12). The shallow cumulative SFD slope suggests that volcanic resurfacing affected the accumulation of buried craters that now persist in the measured population, an interpretation furthered by morphologic observations. The absence of kinks in the cumulative SFD, paired with the morphology, also suggests that minimal geologic time separated the resurfacing episodes that affected the buried crater population.

The trend for the buried craters in the R-plot (Figure 4.12b) demonstrates that the buried crater population is composed primarily of Population 1 craters, and the deficit at smaller diameters (≥25–30 km) reflects resurfacing resulting from volcanic or ejecta emplacement or a combination of both. The crossover of the NHCT and buried crater cumulative SFDs at ~130 km diameter (Figure 4.12a) indicates that ≥130 km, the buried crater population reflects embayment of the original NHCT surface. At ~60 km diameter, there is a stepped decrease in the buried crater frequency in the R-plot (observed as a shallower slope in the cumulative SFD) that may be due to volcanic resurfacing as well as the constraints on definitive crater identification discussed for smaller diameters (Figure 4.12b, Section 4.2.2). Furthermore, assuming I unambiguously identified all buried craters in the 4–25 km diameter range, the dip below the NSP post-plains crater population frequency suggests that at diameters ≤25–30 km, Population 2 craters dominate the buried crater population and represent craters that formed in NSP that was subsequently resurfaced.

4.4.5. Volume of NSP

Although the cumulative SFDs do not exhibit the characteristic kinks associated with resurfacing events (e.g., Neukum and Horn, 1976), all buried craters must have formed prior to the post-plains crater population, and stratigraphic relations show that successive volcanic emplacement likely occurred. Using the buried crater population, I estimate the regional volume of the NSP to be between 4.08×10^6 km^3 and 9.84×10^6 km^3. The total estimated volume for all lunar mare is ~10^7 km^3 (e.g., Head and Wilson, 1992) whereas the Columbia River Flood Basalts and the Deccan Traps on Earth are estimated to have a volume of 1.3×10^6 km^3 and 8.2×10^6 km^3, respectively (e.g.,

Coffin and Eldholm, 1994 and references therein). When compared to the largest-known flood basalts on the Earth and Mars, the NSP prove to be small: the Hesperian Ridged Plains on Mars, which cover ~30% of the planet, have an estimated volume of ~4×10^7 km^3 (Head et al., 2002), whereas the volume of the terrestrial Ontong Java Large Igneous Province is estimated to be ~$4–8 \times 10^7$ km^3 (Coffin and Eldholm, 1994).

4.4.6. Areal Crater Density

Ostrach and Robinson (2013) used areal crater density as a means of identifying resurfacing boundaries originally identified as color units within Mare Imbrium on the Moon. Multispectral color differences are absent (or currently undetectable) within the NSP, so the ability to distinguish age units with a modeled difference of ~500 million years to 1 billion years (Ostrach and Robinson, 2013) using statistical methods and crater counts show that this areal crater density mapping technique may be applied to Mercury to search for age subunits within the NSP.

The NSP exhibit widespread moderate areal crater density, consistent with a randomly distributed sample population based on the synthetic density maps derived from measured crater frequencies (Figure 4.13, 4.15). Three iterations of synthetic areal crater density maps all exhibit patchy high and low density areas interspersed within a spatially extensive moderate density region, indicating that such density variations are expected for a random distribution. Thus, while high and low density regions observed in the measured areal crater density map likely represent statistically significant variations, visual assessment of such areas must be made to determine if the high and low density regions represent geological differences as opposed to statistical noise.

Visual observations confirm that low density values primarily result from impact-related modification of the NSP. The low crater density regions reflect obliteration and modification of the surrounding area to approximately two diameters from the crater rim by formation, ejecta emplacement, and auto-secondary impacts (Figure 4.13, 4.14c; similar density trends were observed surrounding Orientale basin on the Moon in a study of global crater density by Head et al., 2010). In some cases, such as the areas surrounding the Abedin, Hokusai, Rustaveli, and Oskison impact craters, the irregular boundaries between the low and moderate density values reflect both the geological effects of distance from the craters and their ejecta and smoothing inherent in the density technique. For each calculation of areal crater density within one neighborhood area at a particular output cell position, all craters contained within the neighborhood are considered. Thus, the lowest density values occur within the interiors of the large impact craters. As the output cell position moves outward relative to the crater interior, the density magnitude increases, provided the surrounding region is of higher density, to produce moderate density values.

Similarly, the absence of observed volcanic resurfacing contacts surrounding the high density areas indicates that for all but one large high density region in the NSP, variations in areal crater density reflect the randomness of the cratering process (e.g., Figure 4.13, 4.14a, 4.14b, 4.15). The single exception in high density results from the likely inclusion of circular, non-overlapping secondaries from Strindberg crater (53.21°N, 223.44°E). Smaller, isolated high density patches (e.g., 72.00°N, 120.00°E) and the scatter of high density output cells such as those surrounding large high density regions (e.g., H1 in Figure 4.13) may reflect statistical noise in the areal crater density

measurement expected for a random population based on the results of the synthetic density maps.

The spatially expansive moderate areal crater density across the NSP, coupled with the low density regions attributed to impact-related obliteration of the preexisting surface and the high density regions reflecting random impact cratering, is consistent with a final volcanic resurfacing over a relatively short period of time. Moreover, the measured areal crater density reflects a randomly distributed crater population without observed volcanic resurfacing boundaries as demonstrated by comparison to synthetic areal crater density determined from random point distributions. These results suggest that the most recent (and probably last) episode of large-scale volcanic resurfacing within the NSP encompassed nearly the entire region, an interpretation consistent with morphologic observations (Section 4.4.3.1). This explanation is also consistent with the homogeneous MDIS color observations, the presence of Archimedes-like partially flooded craters, absence of resurfacing kinks in the cumulative SFD for both the post-plains and buried crater populations, and is in agreement with earlier studies (e.g., Head et al., 2011; Freed et al., 2012; Klimczak et al., 2012).

4.5. Conclusions

MESSENGER MDIS orbital image data provide the first complete view of Mercury's NPR at favorable illumination for morphologic and crater count studies. Although Mariner 10 and the MESSENGER flybys imaged the full extent of the NSP, the illumination for similar observations of morphology was not optimal until orbital data from MESSENGER were acquired. The areal coverage of the smooth plains in the NPR

(0°E to 360°E, 50°N to 90°N) is ~7% of the surface area of Mercury and is one of two major occurrences of widespread smooth plains on Mercury. The two units of smooth plains identified in the NPR, *SP1* and *SP2*, comprise 5% and 2% of the surface area of Mercury, respectively. Therefore, the NSP cover slightly less surface area than the 9% of the Caloris plains (interior and exterior combined). Thus, at least ~14% of Mercury's surface is covered by volcanic material comprising the NSP and the Caloris plains (the *SP2* region is genetically associated with the Caloris exterior plains), with the remaining ~13% of smooth plains occurring elsewhere (Denevi et al., 2013a). Furthermore, although no conclusive volcanic edifices are identified in the NSP, the morphologic and structural evidence, including the presence of flow-modified channels closely associated with vent-like features (Head et al., 2011; Byrne et al., 2013) and extensional tectonic landforms hosted by impact craters and basins filled with material interpreted to be volcanic (Freed et al., 2012; Klimczak et al., 2012; Watters et al., 2012), supports the hypothesis that NSP were formed rapidly by large volumes of high-temperature, low-viscosity lava. Using buried crater rim height estimates, the minimum regional NSP volume is between 4.08×10^6 km^3 and 9.84×10^6 km^3.

The NSP post-plains crater frequencies, observed in both the SFDs and the areal crater density maps, are homogeneous. From the crater distributions I interpret that the NSP formed in voluminous outpouring of volcanic material over a short period of geologic time. In particular, the areal crater density reveals that the post-plains crater distribution is considered to be a statistically random population, and from the areal density I conclude that the last resurfacing encompassed the current NSP extent. Observations of buried craters and tectonic deformation associated with flooded impact

structures indicate that the NSP were volcanically modified and resurfaced. Stratigraphic relations among buried craters show that at least two periods of volcanic modification occurred prior to the formation of the post-plains crater population. The absence of kinks characteristic to volcanic resurfacing (e.g., Neukum and Horn, 1976) in the cumulative SFDs for the post-plains and buried crater populations, together with measures of areal crater density, suggest that episodes of volcanic emplacement likely occurred over a relatively short period of geologic time and included a hiatus between resurfacing, during which the dominant crater population switched from Population 1 to Population 2. The three current absolute age models result in ages for the NSP spanning 1.2 Ga (~3.7–2.5 Ga) so these models must be interpreted with care.

Subunits within the NSP were not detected with MDIS multispectral observations, and coupled with the crater size-frequency distributions, these observations together suggest that the composition of extruded lava did not significantly change over the formation time of the surface upon which the post-plains crater population formed. This hypothesis is supported by MESSENGER X-Ray Spectrometer (XRS) measurements for several locations within the NSP showing that the Al/Si, Ca/Si, and Mg/Si ratios are most consistent with a magnesian basalt, and that the composition of the NSP does not appreciably vary across the sampled region (Nittler et al., 2011; Stockstill-Cahill et al., 2012; Weider et al., 2012).

Relative crater size-frequency distributions for the NHCT are consistent with those for “average” Mercury HCT, with some variation in crater density observed because crater SFDs on Mercury are highly sensitive to resurfacing (volcanic and impact-related) and secondary cratering. This variation is consistent with widespread, complex

resurfacing that likely resulted from the emplacement of a combination of volcanic and impact-related basin material during the Late Heavy Bombardment through modification and burial of HCT (e.g., Murray et al., 1975; Strom et al., 1975b; Trask and Guest, 1975; Malin, 1976; Strom, 1977; Whitten et al., 2012; Denevi et al., 2013b). If further analysis confirms a volcanic origin for the intercrater plains, the earlier activity responsible for intercrater plains formation would provide additional evidence that widespread volcanism occurred through much of Mercury's early history.

The comprehensive cratering history of the mercurian NPR may now be put into context with other smooth plains and HCT identified on Mercury. Morphologic observations of two expansive regions of smooth plains units in the NPR are comparable to the Caloris smooth plains (interior and exterior) in both age and expanse based on measures of crater frequencies. Likewise, the NSP are comparable in age to regions of smooth plains located in other areas (e.g., Rudaki plains, plains south of Rachmaninoff, plains within Beethoven and Rembrandt basins; Denevi et al., 2013a). Consequently, the majority of smooth plains regions on Mercury are too young relative to the youngest large basins to be basin-generated products, disproving previous arguments against a volcanic origin for most of the smooth plains regions (e.g., Wilhelms, 1976b; Oberbeck et al., 1977).

CHAPTER 5

EFFECTS OF SHAKING ON DENSITY SORTING IN GRANULAR MATERIALS: IMPLICATIONS FOR PLANETARY REGOLITHS

5.1. Introduction

The regolith of an airless body is defined as a layer of fragmental debris overlying largely coherent rock (e.g., Shoemaker et al., 1969; Oberbeck et al., 1973) and is formed by successive impact cratering events. Detailed knowledge of the lunar regolith (including grain size distributions, thickness variations, compositional variations with depth) is important because the regolith is globally distributed, and most remote sensing observations are of the regolith (not bedrock). Since various remote sensing techniques can sample different depths within the regolith, small-scale compositional variations with depth may bias estimates of the regolith's bulk composition for a given technique.

The goal of this investigation is to determine whether the lunar regolith may undergo compositional sorting due to seismic shaking. Seismic shaking is an active process on the Moon; measurements from returned drill cores and drive tubes, along with surface photographs, determined that the lunar regolith is compacted within the top few centimeters of the surface (e.g., Carrier et al., 1972; 1973). It is possible that seismic shaking also causes grain redistribution in the lunar regolith at the few 100 μm to 10 cm depth scale. For example, ilmenite ($FeTiO_3$) is a high-density oxide that is sometimes abundant in returned lunar regolith samples (e.g., Heiken, 1975; Basaltic Volcanism Study Project, 1981; Papike et al., 1982; 1998). Compositional information derived from Clementine UV-VIS spectral reflectance (CSR) is based on measures of spectral absorptions (415 nm to 1000 nm) of the lunar surface materials (e.g., Nozette et al., 1994;

McEwen and Robinson, 1997), and estimates of titanium abundance (Ti or TiO_2) are inferred to result primarily from the presence of ilmenite (e.g., Blewett et al., 1997; Lucey et al., 1998; Giguere et al., 2000; Lucey et al., 2000; Gillis et al., 2003). The Lunar Prospector Gamma Ray and Neutron Spectrometers (LP GRS and NS; Feldman et al., 1996; 1999; 2004) measured gamma ray and neutron absorption from which TiO_2 abundance was estimated (e.g., Elphic et al., 1998; 2000; 2002; Prettyman et al., 2006). LP TiO_2 abundance estimates do not everywhere match well with CSR values (Elphic et al., 2000; 2002; Prettyman et al., 2006), and CSR samples only the top few micrometers while LP GRS and NS sense to a depth greater than 10 cm (Feldman et al., 1999; 2004). Thus, it is relevant to know if ilmenite content varies in the top ten centimeters of the lunar regolith and whether the differences in TiO_2 abundance reported by LP GRS and CSR studies represent true compositional vertical stratification (at the 10 cm scale) or are simply measures of the imprecision of one or both methods.

To examine potential compositional vertical stratification of ilmenite occurring within the lunar regolith, I designed experiments modeling a bimodal granular mixture of materials with strong density contrasts and varying grain sizes. The experiment test bed was perturbed with vertical and horizontal vibrations to represent the effects of seismic shaking. In the experiments, particles with higher densities sink into the matrix material that serves as a simulated regolith, even when the denser particles are smaller than the particles composing the matrix. Moreover, the denser particles sank into the matrix under both vertical and horizontal vibration regimes. Although these experiments were not performed under simulated lunar conditions and are therefore not a perfect analog, the results represent a meaningful first order demonstration when considering compositional

remote sensing measurements of the lunar, and other planetary, surfaces with surficial regolith.

5.2. Background

5.2.1. Returned Samples and Remotely Sensed Compositions

From the Apollo sample collection it is known that the mean grain size of lunar regolith, which is dependent on the degree of evolution or maturity of the soil (e.g., time exposed at the surface, degree of rock fragment and mineral comminution, and amount of fresh material introduced via impact), is ~40–800 μm (Heiken, 1975), averaging mostly between ~55–80 μm (McKay et al., 1974). Different minerals within the regolith are proposed to comminute at different rates in the lunar environment (e.g., Korotev, 1976; Devine et al., 1982; Papike et al., 1982; Hörz et al., 1984; Hörz and Cintala, 1997). Regolith samples reveal that concentrations of ferromagnesian minerals, such as ilmenite, decrease with decreasing grain size (Lindstrom et al., 1977; Vaniman et al., 1979; Basu et al., 1980; Labotka et al., 1980; Papike et al., 1982; Hörz et al., 1984; Taylor et al., 2000), suggesting that ilmenite may persist in larger grain size fractions than other regolith components. On the lunar surface, the top millimeter of regolith is considered to be the primary mixing zone due to the prevalence of micrometeorite bombardment (e.g., Gault et al., 1974), and continuous perturbation and mixing due to micrometeorite bombardment, in addition to ejecta deposition and seismic shaking from larger impacts, may promote mechanical sorting of the topmost layer where denser particles may preferentially sink. If particle sorting does occur, the distribution of ilmenite may vary within the top 10 cm (or more) depending on factors such as regolith maturity and

parental rock composition (bulk soil TiO_2 abundances may be lower than basalt samples due to injection of highland components and preferential comminution, e.g., Papike et al., 1982). Furthermore, mineral-specific comminution experiments suggest that differential comminution could significantly influence remote sensing compositional studies (Hörz et al., 1984). Comminuted fines may dominate the measurement surface and coat larger mineral grains and rock fragments preventing an accurate bulk regolith determination and thus biasing the compositional measurement (Hörz et al., 1984).

Analyses of regolith cores indicate that the regolith at any one location reflects a unique stratigraphy that primarily depends on the composition of the underlying bedrock, but substantial variation in composition and grain size occur within sample drill cores and drive tubes (within a single core/drive tube, as well as from location to location at one site, e.g., Papike et al., 1982). Therefore, remotely sensed measurements of the optical surface (less than 100 μm, e.g., Morris, 1985) may not accurately represent the bulk regolith (meter depth scale), even at a few centimeters depth. Comparing the TiO_2 abundances derived from CSR and LP GRS allows the variability in composition estimated by the two datasets, which are derived from sampling different regolith depths, to be investigated. The 2002 PDS-released reduced 2° LP GRS titanium elemental abundance data resampled to 0.5° pixel scale (http://pds-geosciences.wustl.edu/missions/lunarp/reduced_special.html) converted to TiO_2 abundance was compared to the CSR TiO_2 abundance determined from the Lucey et al. (2000) algorithm from the five-band Clementine multispectral global mosaics resampled to 0.5° pixel scale. Figure 5.1, created by subtracting the LP GRS from CSR abundances, provides a guide to regions exhibiting significant differences in TiO_2 on the Moon.

In Figure 5.1, there are regions with small TiO_2 abundance differences (primarily the titanium-poor highlands (e.g., Papike et al., 1982; Korotev et al., 2003), with approximately 0 to -3 wt% TiO_2 difference) and regions of significant abundance differences (i.e., titanium-rich maria, with >5 wt% TiO_2 difference). The maximum difference, where CSR exceeds LP GRS values, is 13 wt% TiO_2 and the minimum difference, where LP GRS exceeds CSR values, is -10 wt% TiO_2, and both minimum and maximum differences in TiO_2 abundance occur in the nearside maria. Figure 5.2 is a histogram of the CSR and LP GRS TiO_2 abundances for the nearside maria, and although both datasets have a mean in the 4–6 wt% TiO_2 bin, for <8 wt% TiO_2, LP GRS abundances exceed the CSR estimates, and at >8 wt% TiO_2, CSR abundances exceed the LP GRS estimates.

Most CSR and LP GRS TiO_2 abundances are between 0 and 8–10 wt% TiO_2 when the CSR and LP GRS TiO_2 abundances for the nearside maria are plotted against their difference (Figure 5.3). The positive trend of the CSR abundance between ~10 and 18 wt% TiO_2, where the CSR–LP GRS difference increases, reflects higher CSR TiO_2 abundances than LP GRS, but CSR abundances become increasingly uncertain (>~1–2 wt% TiO_2 uncertainty) at high values. It is possible that CSR overestimates true TiO_2 abundance for >8–10 wt% TiO_2 primarily because none of the returned soils have abundances in excess of 8.5 wt% TiO_2 (e.g., Blewett et al., 1997), so high values are extrapolated by the algorithm (e.g., Blewett et al., 1997; Lucey et al., 2000). Another source of uncertainty in the CSR estimate of TiO_2 abundance is that elemental titanium begins to partition into other mineral phases, such as pyroxene, at high values (e.g., Lucey et al., 1998). Therefore, CSR TiO_2 abundance estimates >8–10 wt% may not

reflect real surface compositions, although the high titanium regions probably are enriched relative to other, lower titanium areas (e.g., Mare Tranquillitatis/Apollo 11 Landing Site compared to Hadley Rille/Apollo 15 Landing Site; Table 5.1).

A distinct cut-off is observed in the LP GRS data, following a negative linear trend (Figure 5.3). When the CSR and LP GRS TiO_2 abundances of a farside highlands region (where TiO_2 abundance is expected to be low; e.g., Korotev, 1999; Jolliff et al., 2000; Korotev et al., 2003) are compared (Figure 5.4), CSR TiO_2 values exhibit a narrow range, from 0–1 wt% TiO_2 (uncertainty is ~±1 wt%; Lucey et al., 2000). In contrast, LP GRS TiO_2 abundance ranges from 0–2 wt% TiO_2. The range in LP GRS TiO_2 abundance data for the highland area (Figure 5.4) is reflected as a distinct cut-off and negative trend in the nearside maria data (Figure 5.3). Since TiO_2 abundances of returned regolith samples of highland lithologies are low (<1 wt% TiO_2 for Apollo 16 regoliths; e.g., Blewett et al., 1997), it is likely that the CSR TiO_2 abundance reflects the minimal TiO_2 expected to be contained in highland regoliths and that the large range in LP GRS TiO_2 values indicates noise in the system (abundance is below minimum threshold detection limit). Thus the uncertainty in TiO_2 abundance measured by LP GRS, is ~±1–1.5 wt%.

In some regions of the nearside maria, the CSR technique (Lucey et al., 2000) predicts higher TiO_2 abundances when compared to LP GRS values, a finding in agreement with other LP GRS and NS studies (e.g., Elphic et al., 2000; 2002; Prettyman et al., 2006). CSR TiO_2 abundance exceeds LP GRS estimates in 49% of the nearside maria, and the higher CSR TiO_2 values predominantly occur in western Oceanus Procellarum, southern Mare Serenitatis, Mare Tranquillitatis, Mare Fecunditatis, and Mare Crisium (Figure 5.5). LP GRS TiO_2 abundances exceed CSR estimates for 22% of

the nearside maria, and these values are found primarily in eastern Oceanus Procellarum and Mare Imbrium. Within the nearside maria, 29% of the TiO_2 abundances are ≤1 wt% TiO_2, and uncertainty for both the CSR and LP GRS estimates are both about 1%. However, the higher TiO_2 abundances estimated by CSR for half of the nearside maria may partly result from the dependence of the CSR algorithm calibration to the lunar sample suite (Blewett et al., 1997; Lucey et al., 1998; 2000), where high-titanium basalt (9–14 wt% TiO_2) samples from the Apollo 11 and Apollo 17 landing sites are well-represented, as are low- and very low-titanium basalts (1–5 wt% and <1 wt% TiO_2, respectively) but intermediate-titanium basalt (5–9 wt% TiO_2) samples are not (e.g., Papike and Vaniman, 1978a; 1978b; Basaltic Volcanism Study Project, 1981; Papike et al., 1998; Giguere et al., 2000; Gillis et al., 2003). TiO_2 abundances derived from both CSR and LP GRS for Apollo landing sites (Table 5.1) agree to within the factor of uncertainty for both methods (±1–2 wt% for CSR (Lucey et al., 1998), ~±1 wt% for LP GRS determined here; otherwise relative elemental LP GRS uncertainties are 4–15% (Lawrence et al., 2000)), with the exception of the Apollo 11 landing site in Mare Tranquillitatis. The 8% difference in TiO_2 abundances at the Apollo 11 site (11 wt% in CSR, 3 wt% in LP GRS) does not have an obvious explanation (e.g., the landing site is situated more than 50 km from the mare-highlands boundary). My observations suggest that the CSR–LP GRS TiO_2 abundance mismatch may result from remaining systematic uncertainties in the CSR algorithm calculation (e.g., Blewett et al., 1997; Lucey et al., 1998; Gillis et al., 2003), contribution of highland components to the LP GRS footprint (at the equator, 1° is approximately equal to 30 km) (Feldman et al., 1999; Lawrence et al., 2000; 2003; 2004; Prettyman et al., 2006), or a combination of these factors.

Table 5.1. Apollo Landing Site TiO_2 abundance in wt%.

Landing Site	**Latitude**	**Longitude (°E)**	**Sample TiO_2***	**CSR TiO_2**	**LP GRS TiO_2**
Apollo 11	0.67°N§	23.47	7.5	10.93	2.65
Apollo 12	3.01°S	336.58	3.1	5.24	4.28
Apollo 14	3.65°S	342.53	1.7	1.75	1.25
Apollo 15	26.13°N	3.63	1.5	2.24	2.18
Apollo 16	8.97°S	15.50	0.6	1.02	0.16
Apollo 17	20.19°N	30.77	8.5	3.33	4.07
Luna 16	0.51°S†	56.36	3.3	7.43	5.52
Luna 24	12.71°N	62.21	1.0	5.23	1.28

*TiO_2 abundances for regolith samples, from Blewett et al. (1997).
§Landing Site coordinates for the Apollo Lunar Modules (Davies and Colvin, 2000).
†Landing Site coordinates for the Luna descent stages (Robinson et al., 2012).

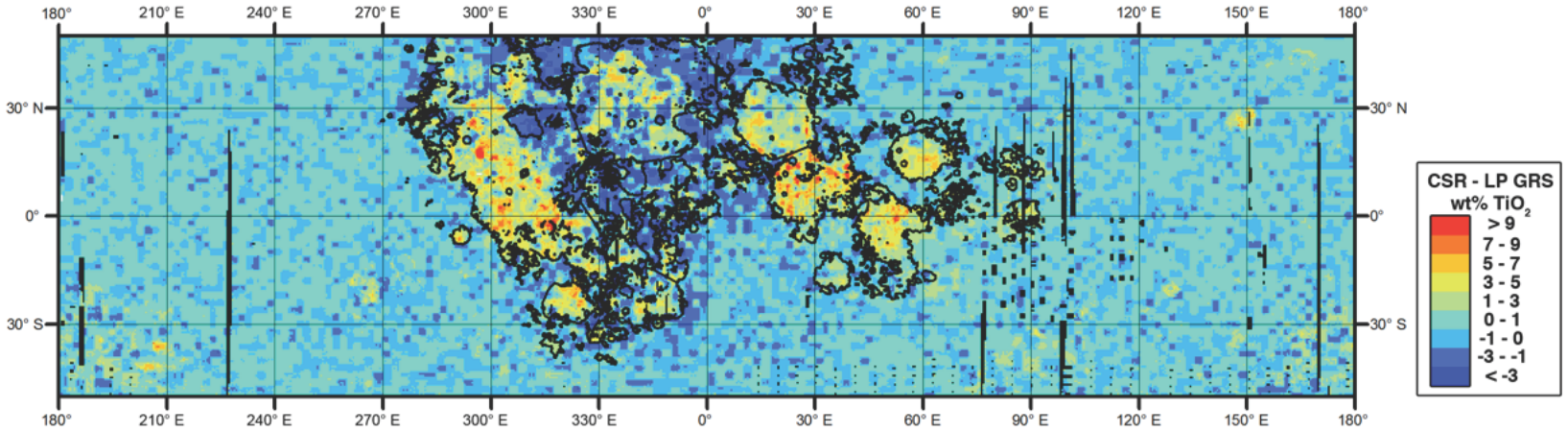

Figure 5.1. TiO_2 abundance difference map created by subtracting LP GRS from CSR values; simple cylindrical projection with 0.5° pixel scale (~15 km per pixel at the equator) for the latitude range 50°N–50°S. The largest differences between the CSR and LP GRS TiO_2 abundances are observed in the nearside maria (outlined in black, Figure 5.2).

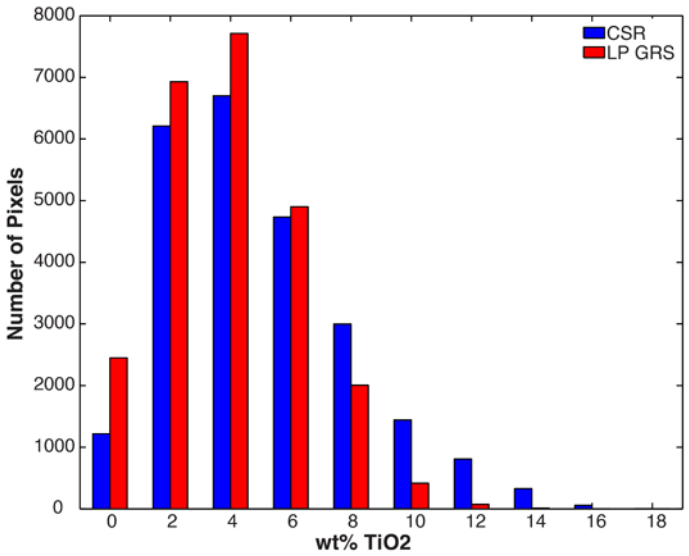

Figure 5.2. Histogram of the CSR and LP GRS TiO_2 abundances for the nearside maria, determined for two-value bins with the bin maximum value shown (i.e., the smallest value bin is -2 to 0 wt% TiO_2, and 0 is shown). The means for both CSR and LP GRS TiO_2 abundances lie within the 4–6 wt% bin (5.0 and 3.9 wt% TiO_2, respectively).

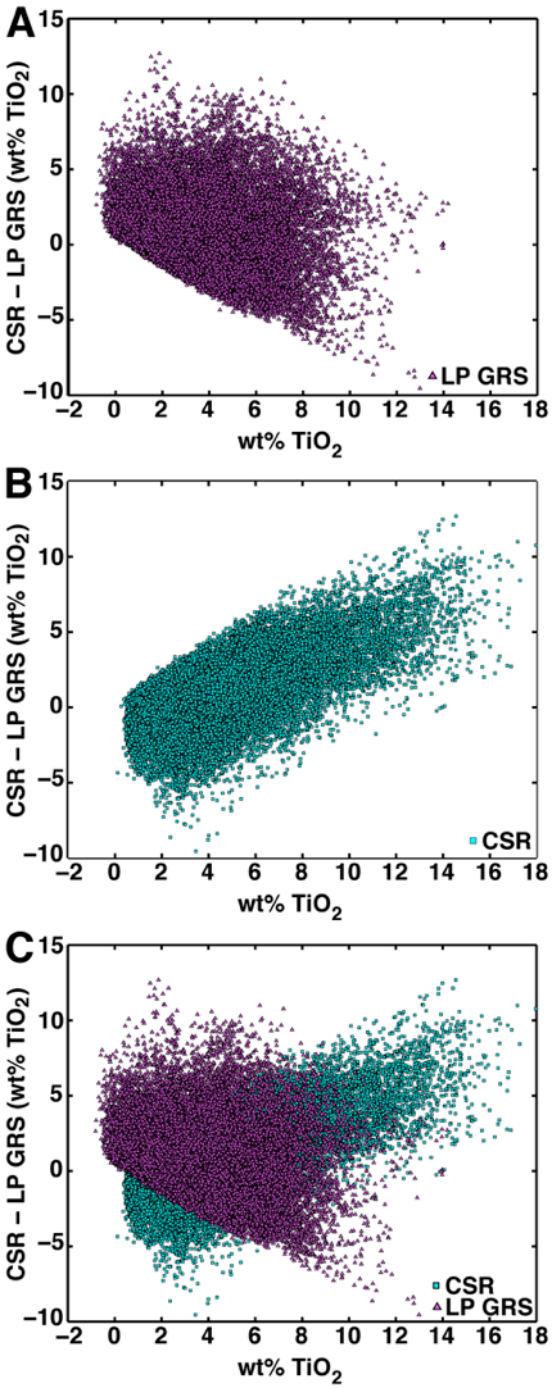

Figure 5.3. TiO_2 abundances determined for 0.5° binned data by (A) LP GRS and (B) CSR for the nearside maria are compared to (C) their difference (CSR – LP GRS). As CSR TiO_2 abundance increases, the difference between the CSR and LP GRS TiO_2 abundance increases, indicating that CSR estimates exceed those of LP GRS. The opposite trend is true for LP GRS TiO_2 abundances and as LP GRS TiO_2 abundance increases, the difference between CSR and LP GRS wt% TiO_2 decreases, indicating that LP GRS values exceed CSR estimates. The abrupt cut-off observed in the LP GRS data is the detection threshold for elemental Ti for the LP GRS system (Figure 5.4).

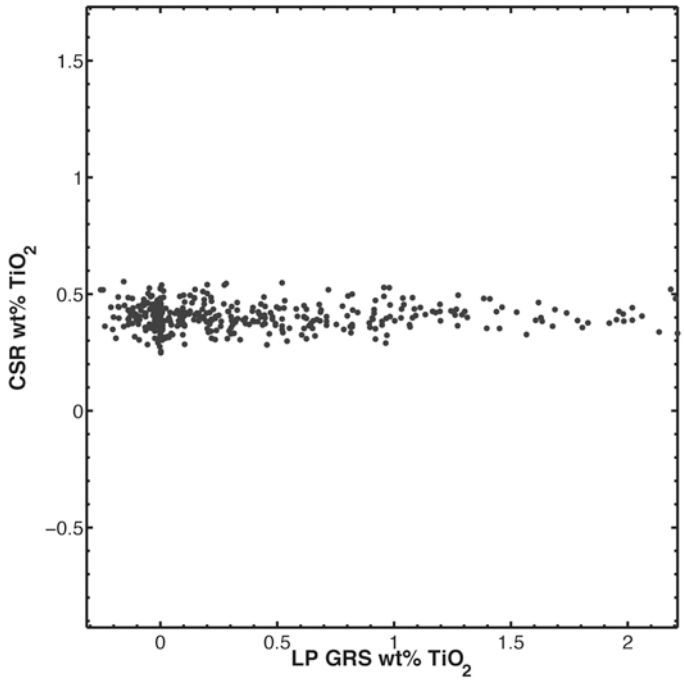

Figure 5.4. TiO_2 abundances in a farside highland area (4.02°N, 158.86°E, ~9.8×10^4 km^2); determined from 0.5° binned data for CSR as a function of LP GRS. TiO_2 abundance in the highlands should be low, and CSR TiO_2 abundance ranges within 0–1 wt%. However, LP GRS TiO_2 abundances range from 0–2 wt%, exceeding the CSR estimates by a minimum of ±1 wt% TiO_2.

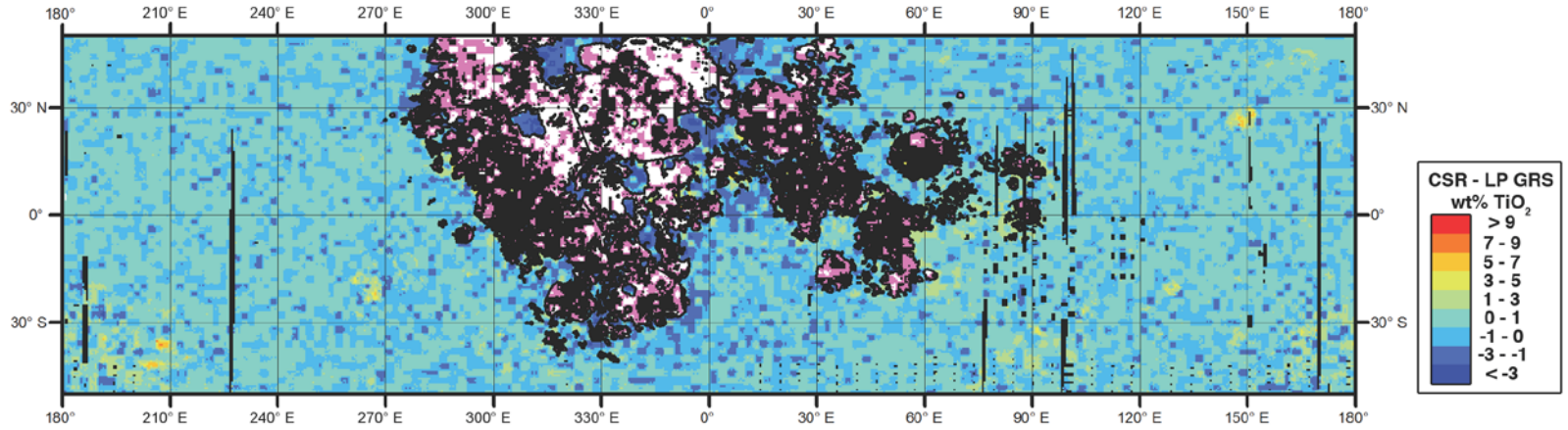

Figure 5.5. TiO_2 abundance difference map from Figure 5.1, with the nearside maria classified according to whether the CSR or LP GRS TiO2 abundance is higher. TiO_2 abundance differences >1 wt%, when CSR TiO_2 values exceed LP GRS estimates, are colored black and comprise 49% of the nearside maria. TiO_2 abundance differences <-1 wt%, when LP GRS TiO_2 values exceed CSR estimates, are colored white and comprise 22% of the nearside maria extent. 29% of the nearside maria contain TiO_2 abundances between -1 and 1 wt% (which is the range in uncertainty for both methods, colored pink) where the true TiO_2 values may overlap.

5.2.2. Particle Size Segregation: The "Brazil-Nut Effect"

The "Brazil-Nut Effect" (BNE) is a colloquial expression for the size segregation of particles during vertical shaking that results in large particles rising to the top of a granular mixture (Rosato et al., 1987); a process known as kinetic sieving. The effects of shaking on particle segregation within granular mixtures is of particular interest to industry, because of the granular materials involved in pharmaceuticals, building construction (e.g., dry cement mixtures, materials involved with road construction), freight transport of commodities (e.g., coal, grains), and food processing (e.g., flours, boxed mixes, cereals) (e.g., Rippie et al., 1964; Bridgwater, 1976; Jaeger and Nagel, 1992; Rosato et al., 2002; Shinbrot, 2004).

Particle and powder segregation have been topics of study since the 1960s (e.g., Rippie et al., 1964). Theoretical and experimental investigations have attempted to further explain the complicated behavior of granular particulates since that time (e.g., Bridgwater, 1976; Parsons, 1976; Williams, 1976; Harwood, 1977; Rosato et al., 1987; Devillard, 1990; Gallas et al., 1992; Jullien et al., 1992; Knight et al., 1993; Vanel et al., 1997; Shinbrot and Muzzio, 1998; Hong et al., 2001; Möbius et al., 2001; Breu et al., 2003; Huerta and Ruiz-Suárez, 2004; Shinbrot, 2004), and most of these works suggest that agitation of granular mixtures by shaking in cylindrical or rectangular containers, or by pouring through chutes, promotes size sorting of the particulates. Containers used in physical experiments usually have a base diameter or width of $\leq$10 cm and a material height of $\leq$20 cm, although some experiments are smaller-scale (e.g., 4 cm × 1 cm × 5 cm with a material depth of 2 cm; Burtally et al., 2003) (e.g., Knight et al., 1993; Möbius et al., 2001; Breu et al., 2003; Burtally et al., 2003; Huerta and Ruiz-Suárez, 2004).

Particulate materials involved in physical experiments include glass ballotini beads, beads and spheres made of bronze, chrome steel, aluminum, polypropylene, wood, and food materials such as poppy seeds, almonds, and brazil nuts, which have variable densities and diameters commonly ranging in size from 0.5 mm to >22 mm (e.g., Rippie et al., 1964; Knight et al., 1993; Möbius et al., 2001; Breu et al., 2003; Burtally et al., 2003; Huerta and Ruiz-Suárez, 2004; Metzger et al., 2011). Early investigations found that among the various physical properties affecting particle segregation, including particle size, shape, and density, particle size differences tended to be the most influential during segregation (Williams, 1976), and fines tended to sift toward the bottom of the experimental container (e.g., Bridgwater, 1976; Parsons, 1976), but some experiments found that the particle density contrasts substantially influence segregation (e.g., Rippie et al., 1964). Later numerical simulations suggested that sorting occurred regardless of density contrasts in widely differing experimental systems and that the segregation mechanisms depended weakly on the system details (e.g., particle shape distribution; e.g., Rosato et al., 1987; 2002), but subsequent experiments indicate that particle density is an important factor in grain segregation (e.g., Jullien et al., 1993; Shinbrot and Muzzio, 1998; Möbius et al., 2001; Breu et al., 2003; Shinbrot, 2004; Ciamarra et al., 2006; Schröter et al., 2006; Metzger et al., 2011). Several simulations and experiments (e.g., Hong et al., 2001; Möbius et al., 2001; Breu et al., 2003; Ciamarra et al., 2006) suggest that a threshold exists between the size and density ratios of the particles, and this threshold defines the cross-over between the canonical BNE, where large grains rise to the top of the mixture, and the “Reverse Brazil-Nut Effect” (RBNE), where large grains sink to the bottom. Work by Huerta and Ruiz-Suárez (2004) attributes particle behavior

to the frequency and amplitude of the shaking; however, the mechanisms controlling vibration-induced segregation remain poorly understood (e.g., Knight et al., 1993; Duran and Jullien, 1998; Hong et al., 2001; Schröter et al., 2006).

In addition to industrial application, the size segregation and sorting resulting from shaking involved in geologic processes are also of interest, including landslides and avalanches (e.g., Jaeger and Nagel, 1992; Jaeger et al., 1996). From the planetary perspective, seismic shaking produced by impacts was used to explain observations of subdued topography surrounding large impact craters and basins on the Moon (Schultz and Gault, 1975) and later suggested as a primary means of erosion and downslope movement on asteroids (e.g., Cintala et al., 1978; Carr et al., 1994; Asphaug et al., 1996; Greenberg et al., 1996; Thomas et al., 2002; Richardson et al., 2005; Miyamoto et al., 2007). Following the discovery of smooth ponded deposits composed of fine-grained (sub-centimeter) material on 433 Eros (e.g., Robinson et al., 2001; Veverka et al., 2001; Robinson et al., 2002), impact-induced seismic shaking was invoked as a probable formation mechanism for ponds on 433 Eros (e.g., Asphaug et al., 2001; Cheng et al., 2002). Cheng et al. (2002) developed a model, based on the BNE/RBNE (e.g., Rosato et al., 1987; Knight et al., 1993; Shinbrot and Muzzio, 1998), to explain pond formation as a result of fine-grained material redistributing to form ponds on the surface of 433 Eros following seismic shaking by impact events. In this model, seismic agitation mobilizes fine-grained regolith on slopes, the regolith moves downslope in a fluidized manner to create ponds, and the ponds then experience size-sorting and burial of large objects so that the finer-grained particles remain on the surface (Cheng et al., 2002). Other workers (Benoit et al., 2003; Izenberg and Barnouin-Jha, 2006a; 2006b) invoked the BNE in a

physical experimental setting to investigate the possibility of grain-size sorting of an asteroidal regolith induced by seismic shaking. Benoit et al. (2003) experimented with an analog chondritic regolith composed of varying grain sizes and densities; their experiments consisted of a bimodal mixture of larger, less dense quartz sand particles mixed with smaller, denser iron-metal grains. These experiments were shaken laterally in a glass beaker by hand and although the mixture contained particles of different densities, the results were consistent with earlier simulations and experiments studying the BNE (large grains rising to the top) (e.g., Rosato et al., 1987; Jullien et al., 1992; Knight et al., 1993; Möbius et al., 2001). However, the results of Benoit et al. (2003) may not completely represent an asteroidal or planetary surface exposed to impact gardening, primarily because these experiments did not test size variations among particles of different densities and considered only horizontal motion; regolith mixing involves "in situ reworking" that requires a vertical component of movement between particles (McKay et al., 1974). Later experiments by Izenberg and Barnouin-Jha (2006a; 2006b) used the vibration lab at Johns Hopkins University Applied Physics Laboratory to investigate vertical and horizontal agitation on slope erosion and crater degradation. Playground sand was used as a regolith simulant inside a 1 m × 1 m × 40 cm Plexiglas container, and experiments used two modes of shaking, single jolts and continuous shaking, with different magnitudes and directions (horizontal or vertical) (Izenberg and Barnouin-Jha, 2006a; 2006b). Initial results indicated that single jolts were more destructive on crater morphology and slopes were eroded more rapidly with large accelerations (Izenberg and Barnouin-Jha, 2006a; 2006b), but these experiments did not investigate size-sorting with respect to the effects of perturbation on different sized

particles or particles with different densities. To more accurately test mechanisms that may promote sorting of a planetary regolith, experiments should consider vertical and horizontal perturbations with varying particle size and density. Therefore, I designed a series of experiments to investigate the possibility of vibration-induced mechanical sorting in the lunar regolith in the context of the grain-sorting hypothesis explaining the observed compositional differences between Lunar Prospector and Clementine measurements.

5.3. Methods

To examine physical mixtures of particles representing a lunar regolith and promote size-sorting, I created an experimental procedure to partially mimic the process of seismic shaking resulting from impact events (e.g., Cintala et al., 1978; Asphaug and Melosh, 1993; Asphaug et al., 1996; Cheng et al., 2002; Richardson et al., 2005) and moonquakes (e.g., Nakamura et al., 1974; 1979; 1982). Impact events form not only craters and ejecta blankets but also create seismic waves. Near the surface, these seismic waves agitate unconsolidated regolith and may mobilize the particles, acting as a degradational or sorting mechanism (e.g., Schultz and Gault, 1975; Cintala et al., 1978; Veverka et al., 2001; Cheng et al., 2002; Richardson et al., 2005). Another scenario that may prove important to regolith particle segregation is the initial emplacement of ejected material during an impact event, which may in itself act as a mechanical sorting mechanism, due to ballistic sedimentation (Oberbeck, 1975). In this study, three experiments were designed to investigate particle size and density segregation of granular mixtures under different shaking conditions and in different sized containers. Measured

bulk densities and grain size fractions for the particulates used in the experiments are provided in Tables 5.2 and 5.3, and the densities for other common minerals are provided in Table 5.4.

Table 5.2. Experimental materials: grain sizes.

Material	Grain size fraction[a]
Basalt chips	2–8 mm
Glass ballotini beads	80–149 μm
Quartz sand	300–600 μm
Anorthosite	>4 mm
	2–4 mm
Ilmenite	>4 mm
	2–4 mm
	600 μm – 1.18 mm
	300–600 μm
	150–300 μm
	<150 μm

[a]Materials were sieved and the grain size fractions listed were used during experimental runs.

Table 5.3. Experimental materials: measured bulk density.

Material	Bulk Density (g/cm^3)*
Anorthosite	1.4–1.5
Glass ballotini beads	1.5–1.6
Quartz sand	1.6–1.7
Ilmenite	2.6–2.7

*Bulk density was measured on the uncompacted dry materials, and the 300–600 μm size fraction was used for anorthosite, ilmenite, and quartz sand. The 80–149 μm size fraction was used for the glass ballotini beads.

Table 5.4. Reported densities of common minerals and glass ballotini beads.

Material	Density (g/cm^3)*
Glass Beads	~2.46–2.49
Flood Basalt	2.40–3.10
Anorthite	2.76
Enstatite	3.21–3.96
Olivine	3.22–4.39
Diopside	3.44–3.55
Ilmenite	4.70–4.78

*Mineral densities reported by Deer et al. (1966), flood basalt reported by Lide, ed. (2007), and glass ballotini bead density reported from the MSDS provided by McMaster-Carr Co.

5.3.1. Experiment One: Vertical Tabletop Shaker

The first experimental setup used a metal rectangular bread pan (23.5 cm × 13.3 cm × 7.0 cm) filled with ~80–149 µm size fraction glass ballotini beads, an abrasive blasting media manufactured by the McMaster-Carr Company. The pan was placed on a Syntron Jogger model J-1-B, an electromechanical vertical shaking table designed for jogging and packing of material with a load limit of 4.5 kg. The tabletop dimensions of the shaker were 17.8 cm × 25.4 cm and the pan was surrounded by a foam buffer to prohibit movement of the pan off the shaker table. The shaker provides a 60 Hz frequency and a 0.15 cm unloaded amplitude at its lowest setting. The shaker has a rheostat marked from 0 – 100 to allow changes to the unloaded amplitude, and for all tests the rheostat was set to 0.

The shaker was positioned on a copy-stand with adjustable lights and a digital camera (Figure 5.6). A white reference image was captured first as part of the experimental procedure, and then the test materials were placed on the surface of the glass beads. An anti-static pistol was discharged above the container before the larger particles were placed and before the shaking began to minimize electrostatic effects. For each run the shaker was turned on for increments of two minutes, for a total of ten minutes run time. The ten minute test period was defined as an experimental run based on preliminary testing made while finalizing the experimental setup. Increments of two minutes allowed sufficient time for particle movement to take place and be recorded by the digital camera, but after ten minutes of run time (that is, five increments of two minutes), no substantial changes to the experimental media were observed in the digital

images. An image was shuttered between each two minute period, when the shaker was turned off.

This procedure was followed for mixtures of glass beads (1.5 g/cm^3; Table 5.3) and ilmenite chips (4.7 g/cm^3; Table 5.4) and glass beads and basalt chips (2.4 g/cm^3; Table 5.4). The ilmenite and basalt chips were irregularly shaped and ranged in size from ~2 mm to ~8 mm across their widest dimension. Between experiment runs, all materials were removed from the container. The ilmenite and basalt chips were separated from the glass bead matrix, and the fine-grained glass beads were removed from the container and then replaced. This procedure effectively un-compacted, or aerated, the glass beads in addition to maintaining the bimodal mixture of rock chips and finer-grained glass bead matrix.

Initial tests revealed significant edge effects in the experimental setup, mostly due to the small size of the largest container that could fit on the shaker and the mass of material filling the container. Tests using containers of various shapes (e.g., square, rectangle, circle) with various side angles showed that circular containers with side angles between ~45° and 60° decreased edge effects. Three circular containers were designed with different dimensions (base diameters 14.0, 17.8, and 25.0 cm) and side angles (from horizontal: 45°, 60°, and 60°, respectively) to mitigate edge effects and provide a large sample volume to test grain size fractions more closely matched (e.g., <150 μm ilmenite powder and the glass beads). The shaker table load limit (4.5 kg) constrained the mass of the sample and thus the size of the container, influencing the relationship between maximum container size and maximum glass bead depth. Similar to the first phase procedures, ilmenite and basalt chips ranging from ~2 mm to ~8 mm in

size were placed on the surface of the glass beads in the circular pan, discharged the anti-static pistol, and captured photos at appropriate time intervals (between each two minute period, when the shaker was turned off). For this set of experiments, fine-grained ilmenite powder sieved to contain the <150 μm size fraction was also incorporated.

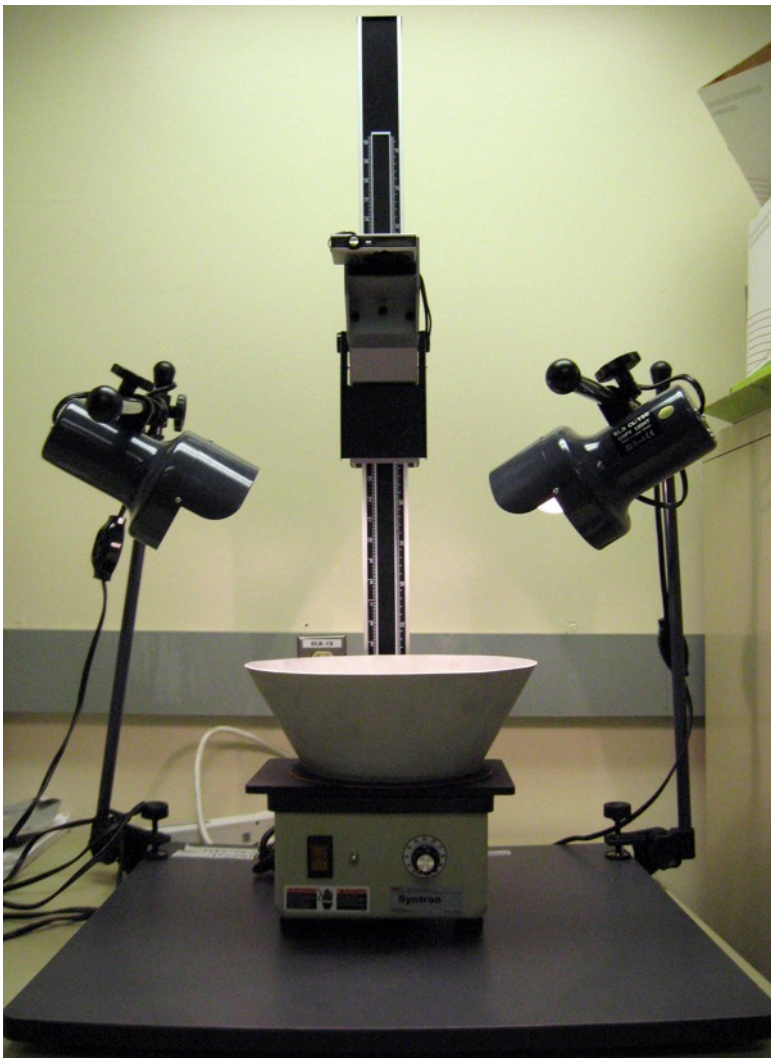

Figure 5.6. Vertical tabletop shaker (Syntron Jogger J-1-B) experimental setup, with the 17.8 cm diameter custom-built circular pan. A circular rubber pad was placed between the shaker and the circular pan to minimize pan movement during shaking. This assembly was placed on the lab floor during experiments to limit vibrations of the copy-stand, which were observed when the setup was placed on the lab counter.

5.3.2. Experiment Two: Vertical Large Shaker

The experimental setup was expanded to incorporate the Syntron Jogger VP-181, which is a larger electromechanical vertical shaker with tabletop dimensions of 76.2 cm × 76.2 cm and a load limit in excess of 315 kg. This larger shaker had the same frequency (60 Hz) and unloaded amplitude (0.15 cm) as the smaller shaker. A custom-made circular pan with an inner or base diameter of 71.1 cm and an outer or top diameter of 91.2 cm was designed for the VP-181 and could accommodate greater than 15 cm depth of fine-grained material (Figure 5.7). For this second experimental procedure, more realistic geologic materials were incorporated into the experimental setup so that the finer-grained matrix mixture more closely resembled a lunar regolith sample (e.g., replace the spherical glass ballotini beads with particles of variable roundness, sphericity, and angularity). For the fine-grained matrix, four 100-pound bags (~182 kg) of coarse quartz sand (#30 silver sand from P.W. Gillibrand Co.) were sieved to acquire the 300–600 μm size fraction. The 300–600 μm size fraction was chosen because this size fraction yielded the most volume, which was equivalent to a sand of ~15 cm in the custom-made. I did not formally measure the moisture content of the sand, ilmenite, or anorthosite samples, but all of the experiments were performed under similar conditions in a laboratory that was constantly air conditioned at the same temperature over a period of several weeks during the summer months in Tempe, AZ. The outside relative humidity was typically ~20% (climate records obtained from NOAA, http://www.ncdc.noaa.gov/) and I assume the inside was comparable. The digital camera was attached to a tripod and a photograph was recorded every two minutes.

For this set of experiments, crushed ilmenite and anorthosite samples in several size fractions were incorporated to characterize the mechanical sorting promoted by the vertical shaking. Both ilmenite and anorthosite samples exhibited similar sinking behavior into the sand for different size fractions, however, due to the poor contrast in digital images between the anorthosite particles and the quartz sand, image interpretation is difficult. Therefore, I focus on presenting figures and discussion for the ilmenite samples that display an obvious contrast with the sand. Rock chips a few mm in size are observed in lunar regolith samples but are not monomineralic (e.g., Papike et al., 1982), therefore, using smaller size fractions of ilmenite and anorthosite is more representative of the mineral fragments observed in the returned lunar regolith. As in previous phases, the container was filled with the fine-grained matrix material (sieved sand), and denser ilmenite or anorthosite particles of a given size fraction were selected and then distributed on the surface of the sand in the container. The denser particles were placed on the sand surface toward the center of the container to limit edge effects.

The sand was initially gently poured into the container and then aerated between each test by thoroughly mixing the sand and de-compacting it post-shaking (substituting for removal and refilling as per the smaller experiment). A 3 cm diameter wooden dowel was used to manually aerate the sand by inserting the dowel into the sand at the container wall, making sure the dowel touched the bottom of the container, and then pulling the dowel through the sand to the other side. This motion was repeated across the diameter of the container in one direction and then again in a roughly perpendicular direction. Following these steps, the sand was further disturbed by creating depressions and hills that were then smoothed very light pressure from the experiment operator’s hands.

To finish the aerating process, the sand surface was smoothed to be approximately level and then, to smooth out any hand indentations, gently brushed with a hand-broom while keeping the surface as loose as possible. These methods decompacted the compacted sand and mixed in the small ilmenite and anorthosite grains (<600 μm) to make a more uniform mixture after experiment runs.

Figure 5.7. Large vertical shaker (Syntron Jogger VP-181) experimental setup, with the custom-built circular pan (base diameter 71.1 cm, top diameter 91.1 cm) filled to ~15 cm depth with sand (300–600 μm size fraction). A rubber non-skid carpet pad was placed between the shaker and the container to minimize movement of the pan during shaking. A tripod was stationed to the lower left of the shaker table (out of the field of view) to which the camera was attached.

5.3.3. Experiment Three: Horizontal Shaking

Graduating from the observations of particle sorting influenced by vertical shaking movement, a wooden box was constructed to test particle sorting in a horizontal shaking environment. The wooden box was constructed using a sheet of plywood for the

base and four wood planks (3.8 cm thick and 19.0 cm tall); final dimensions of the "sandbox" were 112 cm × 112 cm × 20 cm. Each corner was gusseted with plywood to provide stability and seams were caulked to prevent sand leakage. In contrast to the vertical shaking experiments, the horizontal experiments were not mechanically controlled. Horizontal shaking was induced using a 4.5 kg sledge-hammer against one wall of the wooden box, and the selected wall remained constant through all shaking tests. To protect the sandbox wall from hammer blows, a wooden hammer cushion was constructed to span the length of one side of the box. The hammer cushion was also designed to distribute the energy transmitted by the hammer blow from a point-source to a line-source and was constructed using three 122 cm × 20 cm pieces: one piece was the length of the box and the other two pieces were attached to the ends of the first piece so that the central third of the hammer cushion had a void space to promote decoupling between the point-source hammer blow and the wall of the sandbox receiving the blow (Figure 5.8). Additionally, a piece of ~0.6 cm steel plate was attached where the hammer contacted the wood. To fill the box to a depth of ~10 cm, I mixed all previously sieved size fractions of sand.

An experimental run was defined as 100 hits with the sledge-hammer. This method required two operators, one person held the sledge-hammer handle and the second person picked up the sledge head and dropped it from the same height each time, ~45° from vertical (Figure 5.9). Another 122 cm × 20 cm plank was placed as a beam across the top of the box to provide a platform for the person holding the sledge-hammer handle. To promote regularity in the horizontal shaking experimental procedure, four tests were completed at once by defining four ~15 cm × ~15 cm areas in the center of the

sandbox, along with four “repeat” areas (away from the center of the box) designed to provide observations of different regions of the sandbox (Figure 5.8). As before, the anti-static pistol was discharged above the sand surface before the test particles were placed and again before the hammering began. For the horizontal shaking tests, a digital video camera was used to continuously record the experimental procedures and observations over the experimental run, and stills from the videos were captured to document results.

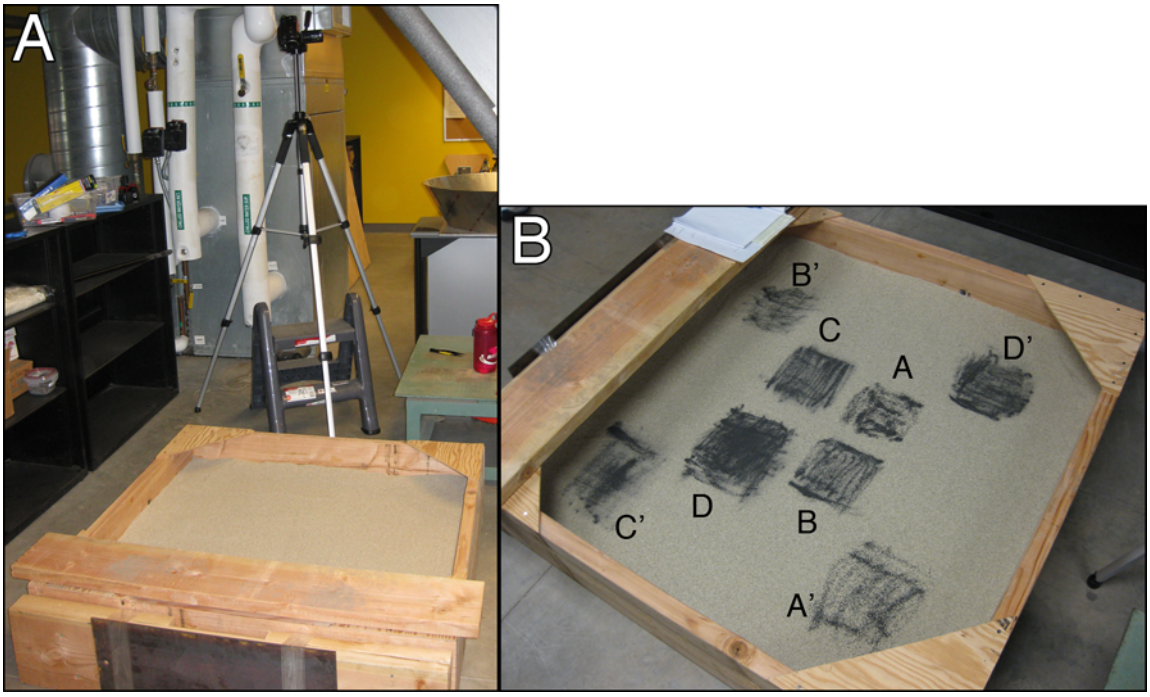

Figure 5.8. (A) Horizontal shaking experimental setup with the sandbox (112 cm × 112 cm × 20 cm) filled to a depth of ~10 cm and the steel plate attached to the wooden hammer cushion in front. (B) Sandbox setup with ilmenite particles distributed in ~15 cm × 15 cm areas, with the following size fractions: A, 600 μm – 1.8 mm; B, 300–600 μm; C, 150–300 μm; D, <150 μm; A’, 600 μm – 1.8 mm; B’, 300–600 μm; C’, 150–300 μm; D’, <150 μm. Steel plate and wooden hammer cushion placement as in (A).

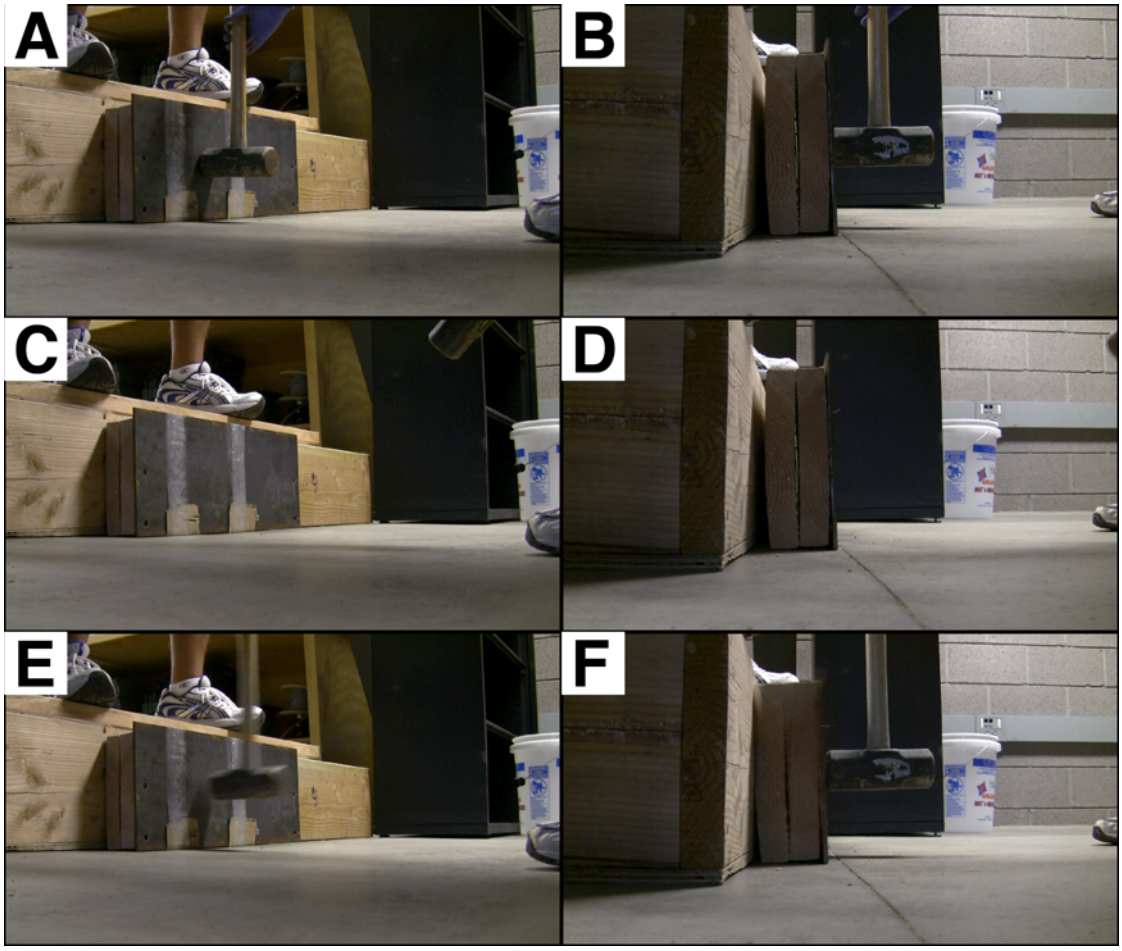

Figure 5.9. Front and side view of one sledge-hammer hit to the sandbox. (A) Front view and (B) side view of initial placement of the sledge-hammer on the steel cushion, (C) front view and (D) side view of lifted sledge-hammer, and (E) front view and (F) side view of the sledge-hammer hitting the steel cushion.

5.4. Results

5.4.1. Experiment One: Vertical Tabletop Shaker

Over the ten minute test period, the coarse fragments of basalt and ilmenite (~2–8 mm) sank into the glass beads in a rectangular container (Figure 5.10). The higher-density ilmenite sank more completely than the basalt. In most of the tests, the majority of the ilmenite sank completely with only a small depression at the surface above the location of the buried chips. In the tests using basalt, the chips did not sink completely

below the surface of the glass beads. During initial tests, rock chips (basalt or ilmenite) placed close to the walls and corners of the rectangular container moved toward the walls when the shaker was turned on. During shaking, these rock chips were pushed against the container walls by glass bead movement. The movement of the glass beads at the container edges was examined by sprinkling a small amount of fine-grained ilmenite powder (<150 μm) on top of the glass beads. During shaking, the ilmenite powder completely disappeared at the container edges, revealing glass beads, while the ilmenite in the center of the container did not completely disappear. However, because edge effects dominated in the rectangular container, a larger, circular container with angled sides was developed.

Similar to the previous tests, the ilmenite and basalt chips sank in the glass bead matrix in the three circular custom-made containers (Figure 5.11). In these tests, edge effects were prominent for the circular containers with base diameters 14.0 cm and 25.0 cm, with 45° and 60° angled sides, respectively. The 17.8 cm diameter circular container (60° angled sides) did not exhibit enhanced edge effects; when the fine-grained ilmenite powder (<150 μm) was sprinkled on the surface of the glass beads, there was minimal observed movement of material at or toward the container walls. The 17.8 cm diameter container with 60° angled sides accommodated a glass bead depth of 7.0 cm at the center, corresponding to a volume equivalent to 4.3 kg, and during shaking the container sides remained rigid. In contrast, the 14.0 cm and 25.0 cm diameter custom-made containers exhibited wall-warping during the course of the experiment runs when the shaker was turned on (due to the metal-work machining required to bend and affix the wall metal to the container base) and accommodated a glass bead depth <7.0 cm.

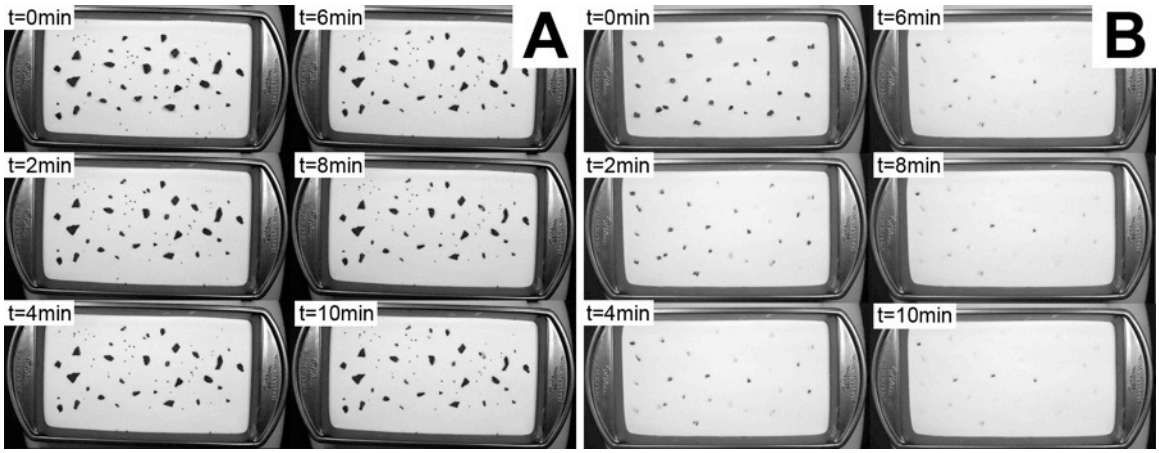

Figure 5.10. Ten minute experimental runs on the tabletop shaker for coarse-grained, denser (A) basalt and (B) ilmenite fragments initially placed on the surface of fine-grained, less-dense glass beads in the rectangular pan. The greater density of the ilmenite fragments promoted more sinking than the basalt (Table 5.4).

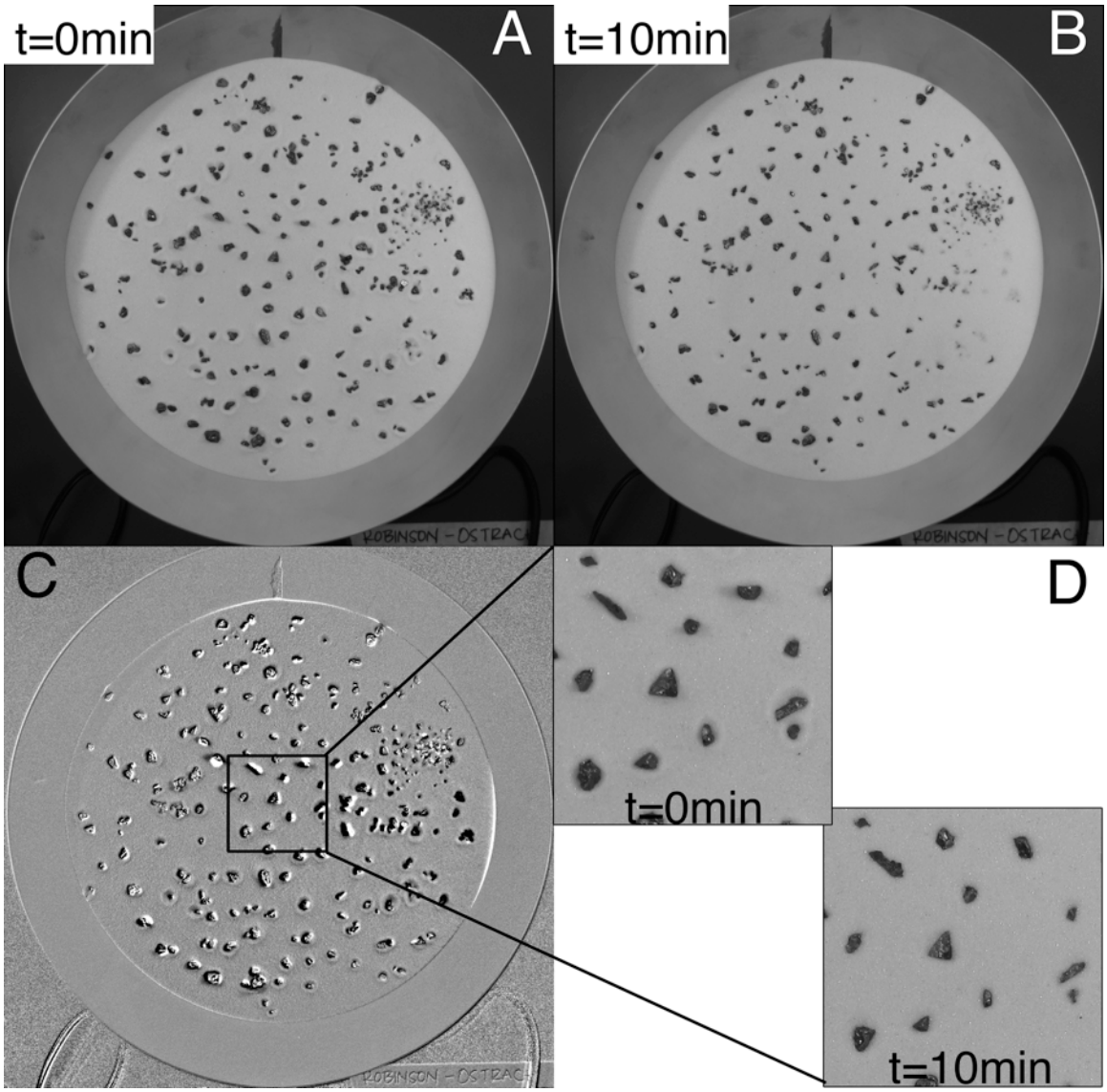

Figure 5.11. (A) Initial setup prior to shaking on the tabletop vertical shaker using the 17.8 cm base diameter custom-made circular container. Ilmenite chips (~2-8 mm diameter) distributed on the glass bead surface (80–149 μm). (B) After ten minutes of intermittent shaking, the ilmenite fragments partially sank into the glass beads. (C) Ratio image of (A) and (B); the gray background throughout the image reflects areas that are the same in both images, black areas represent the locations of ilmenite fragments in the initial setup (no shaking), and white areas represent the locations of ilmenite fragments after ten minutes. Black box shows the central area selected for detailed view in (D). (D) Close up views of the center area from (A) and (B), displaying the change in orientation and partial sinking of ilmenite fragments over the shaking test period.

5.4.2. Experiment Two: Vertical Large Shaker

For the experiments with the large shaker table that used the custom-made container (71.1 cm basal diameter), ilmenite and anorthosite particles (>4 mm size fraction) that were much larger than the sand particles (300–600 μm size fraction) were selected for the first test runs. Similar to the previous tests in the small shaker, the denser, larger particles of ilmenite and anorthosite sank into the fine-grained sand mixture, and the denser ilmenite sank about twice as much as the anorthosite. A pair of fine-tipped tweezers was used to grab the particles at the level of sand on the particle, and the dimensions of the base of the chip (the part that was under the sand) to the level of the tweezer tip were measured, along with the whole height of the chip. This process was repeated for a few grains of each rock type. For a test with ilmenite and anorthosite particles >4 mm with sand particles 300–600 μm, ilmenite pieces sank to about half their height and anorthosite pieces sank to about one quarter to one third their height.

Next, I tested ilmenite particles that were the same size as the sand particles (300–600 μm; Figure 5.12), ilmenite particles half the grain size of the sand (150–300 μm; Figure 5.13 and 5.14), and superfine ilmenite particles (<150 μm; Figure 5.15 and 5.16). In all three cases, the majority of ilmenite particles sank completely below the surface of the sand. The sand surface activity in the central area of the container was similar in the large shaker table setup as in the small shaker table setup. In both cases, away from the container sides where edge effects were assumed to be absent, there was no difference in sinking behavior when larger pieces of denser particles (e.g., hand-samples, >4 mm diameter pieces) or fine-grained particles (<600 μm) were used. The large experiment setup had the largest center surface area and no movement of material was observed at or

near the container sides in the large shaker table setup. As observed previously, the fine-grained component of the experiment compacted over the course of the experiment run. Moreover, in all three test cases, a circular region within the center of the large pan exhibited less sinking than the outer margins (Figures 5.12–5.16).

When first vibrated, the ilmenite and sand particles made small lateral movements on the surface. Over the course of two minutes, the sand grains laterally moved more than the ilmenite grains and the ilmenite grains began sinking. However, an appreciable amount of sinking was not observed at the top-most, visible surface in these first two minutes, although it is possible that ilmenite particles in direct contact with the sand grains were sinking during this time (ilmenite was distributed on the surface in thicknesses exceeding one ilmenite particle diameter). Over several minutes, the ilmenite gradually sank (but did not completely disappear) from the visible surface in the container and, throughout descent, the more angular grains of ilmenite appeared as little points sticking up through the surface layer of sand. Overall, the ilmenite grains were more angular and platy than the sand grains at the 300–600 μm size fraction. When the ilmenite grains were distributed on the sand surface prior to shaking, their orientations were dispersed and random. After six minutes in the run (from a total ten minute time period), many of the ilmenite grains were visible as a pointy tip or edge sticking out of the sand, so it is possible that many of the grains rotated 90 degrees (or close to 90 degrees) as they sank.

For the finer grain size fractions of ilmenite (150–300 μm, <150 μm), after most of the ilmenite particles disappeared from the surface, a shadow of the finest fraction (<150 μm) of ilmenite particles remained on surface, adhered to sand grains. I observed a

distinct outline where ilmenite was present beneath the surface sand grains. At the conclusion of ten minutes of intermittent shaking (Section 5.3.1), the depth to the first ilmenite grains for the 150–300 μm and <150 μm size fractions was between three and six sand grain diameters (300–600 μm), and greater than six sand grain diameters to reach the bulk of the ilmenite originally distributed on the top surface. These values were determined by placing a piece of clear packing tape on the experiment mixture surface, gently applying pressure to attract grains, carefully removing the piece of tape, photographing the piece of tape, and repeating the process on the same area until little to no ilmenite remained (Figure 5.17).

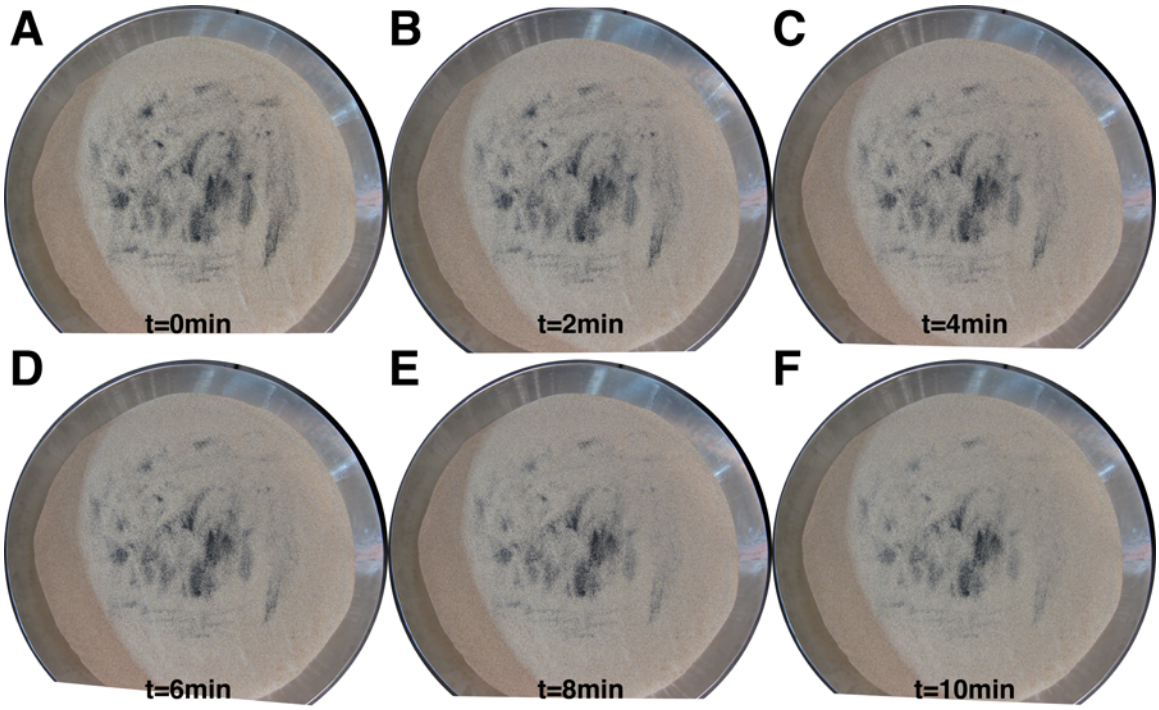

Figure 5.12. Large vertical shaker setup with custom-built circular pan (base diameter 71.1 cm, top diameter 91.1 cm; Figure 5.7) (A) Ilmenite particles 300–600 μm dispersed on the sand surface (300–600 μm). (B-F) Over the course of a ten minute period, the ilmenite particles sank into the sand. After ten minutes (F), much of the ilmenite distributed on the surface is not visible; the densest distributions of ilmenite particles (i.e., deposited thickest on the sand surface) remain visible but also experienced particle sinking.

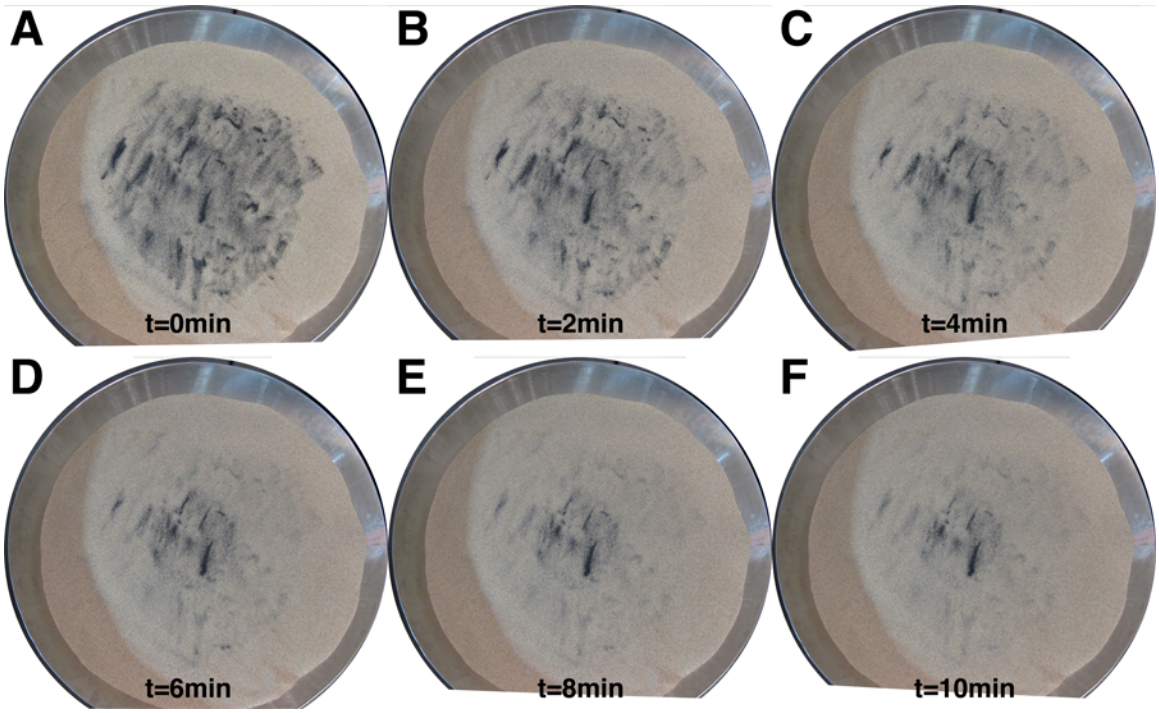

Figure 5.13. Large vertical shaker setup with custom-built circular pan (base diameter 71.1 cm, top diameter 91.1 cm; Figure 5.7). (A) Ilmenite particles 150–300 μm dispersed on the sand surface (300–600 μm). (B-F) Over the course of a ten minute period, the ilmenite particles sank almost completely into the sand. Sinking occurred rapidly after the onset of shaking, with most sinking occurring within the first six minutes (B-D). After ten minutes (F), almost no ilmenite distributed on the surface was visible. Pan top diameter 91.2 cm.

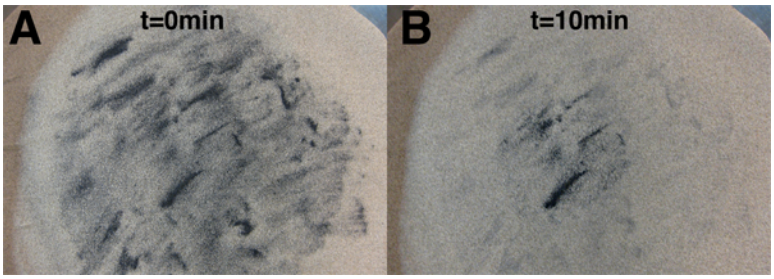

Figure 5.14. Close-up view of pan center on large vertical shaker from Figure 5.13, for (A) initial distribution of ilmenite prior to shaking and (B) after ten minutes of shaking. Ilmenite particles 150–300 μm overlaid on the sand surface (300–600 μm).

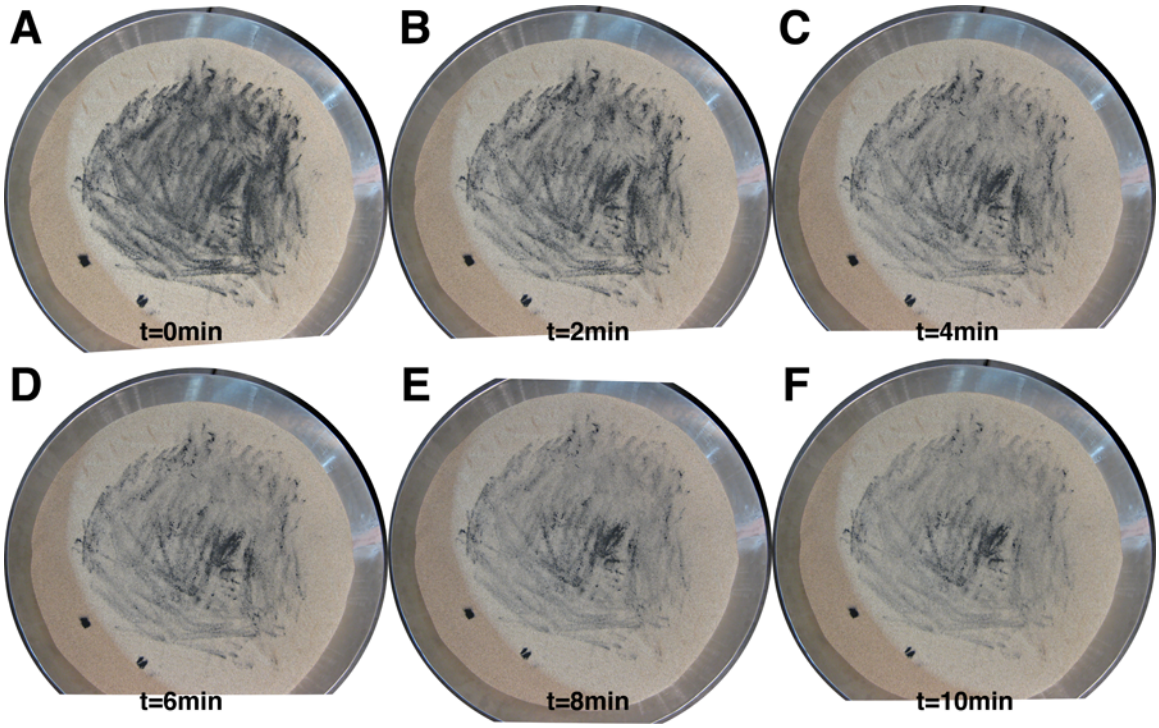

Figure 5.15. Large vertical shaker setup with custom-built circular pan (base diameter 71.1 cm, top diameter 91.1 cm; Figure 5.7). (A) Ilmenite particles <150 μm dispersed on the sand surface (300–600 μm). (B-F) Over the course of a ten minute period, a significant fraction of the ilmenite particles sank into the sand. As before (Figure 5.12, 5.13), sinking occurred rapidly after the onset of shaking, with most sinking occurring within the first six minutes (B-D). After ten minutes (F), most of the ilmenite sank beneath the surface of the top layer of sand grains and an ilmenite "shadow" remained on the sand surface, where particles <<150 μm stuck to the much larger sand grains.

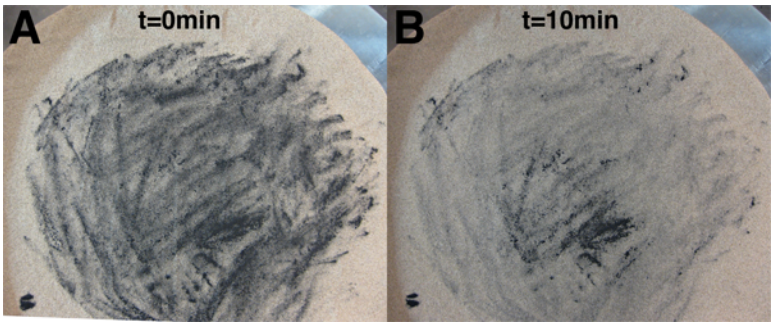

Figure 5.16. Close-up view of pan center on large vertical shaker from Figure 5.15, for (A) initial distribution of ilmenite prior to shaking and (B) after ten minutes of shaking. (A) Ilmenite particles <150 μm overlaid on the sand surface (300–600 μm) before the onset of shaking. (B) After ten minutes, an ilmenite "shadow" remained on the sand surface, and visual observations of the sand grains revealed an ilmenite powder (<150 μm) coating. Observations of depth of ilmenite sinking were made using clear packing tape (Figure 5.17).

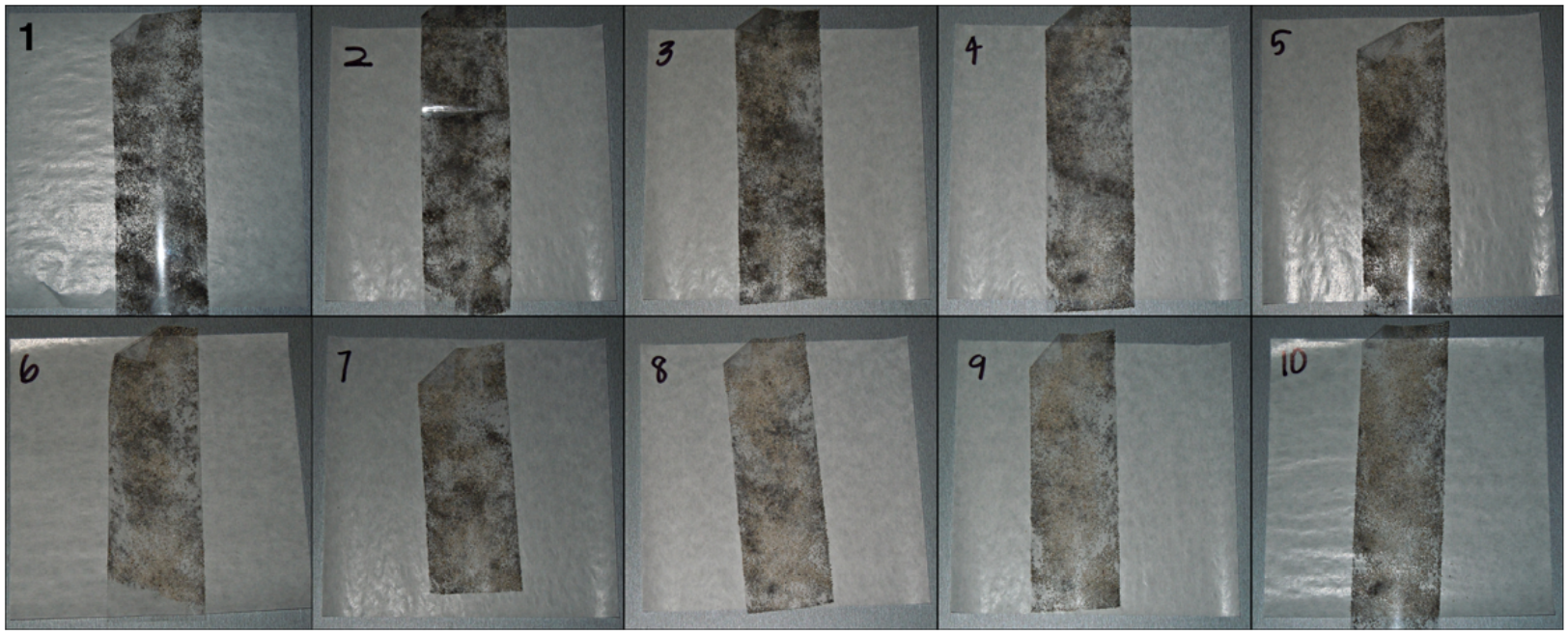

Figure 5.17. Ilmenite particle variation with depth for <150 μm ilmenite grains and 300–600 μm sand grains after ten minutes of intermittent shaking in the large vertical shaker experimental setup (Figure 5.7). Sample 1 was collected from the top surface of the sand-ilmenite mixture and subsequent samples (2-10) were obtained from the same location. The darker color of the samples 1-3 reflects the coating of sand grains by <150 μm ilmenite particles that occurred as the ilmenite sank. Width of packing tape is 4.8 cm.

5.4.3. Experiment Three: Horizontal Shaking

Two scenarios were tested in the horizontal shaking phase: the first case had the void of the hammer cushion centered on the sandbox front wall and the second case had a solid edge of the cushion centered on the sandbox front wall. In both cases, eight test areas were defined and contained the same material (Figure 5.8). With the void of the hammer cushion centered on the sandbox wall, the most ilmenite sank in the four "repeat" areas and a lesser amount of ilmenite sank in the four central areas (Figure 5.18). With the solid side of the hammer cushion against the sandbox front wall and the same ilmenite grain size configuration (Figure 5.8), the four central areas noticeably became more diffuse as ilmenite sank within ten hits of the hammer, and continued to sink over the experiment run of 100 hits (Figure 5.19). At the conclusion of the run, the observed sinking behavior was reversed from the first horizontal shake test: the "repeat" areas exhibited less sinking, although "repeat" areas C' and B' experienced some sinking, and the central areas exhibited the most sinking. In both hammer cushion configurations, after 100 hammer blows, the sand was compacted, but not as much as in the vertical shake tests. The hammer blows to the front side of the sandbox promoted horizontal movement of the sand along the sandbox side walls, observed in the digital video as small changes in the sand height on the sides (<~1–2 cm).

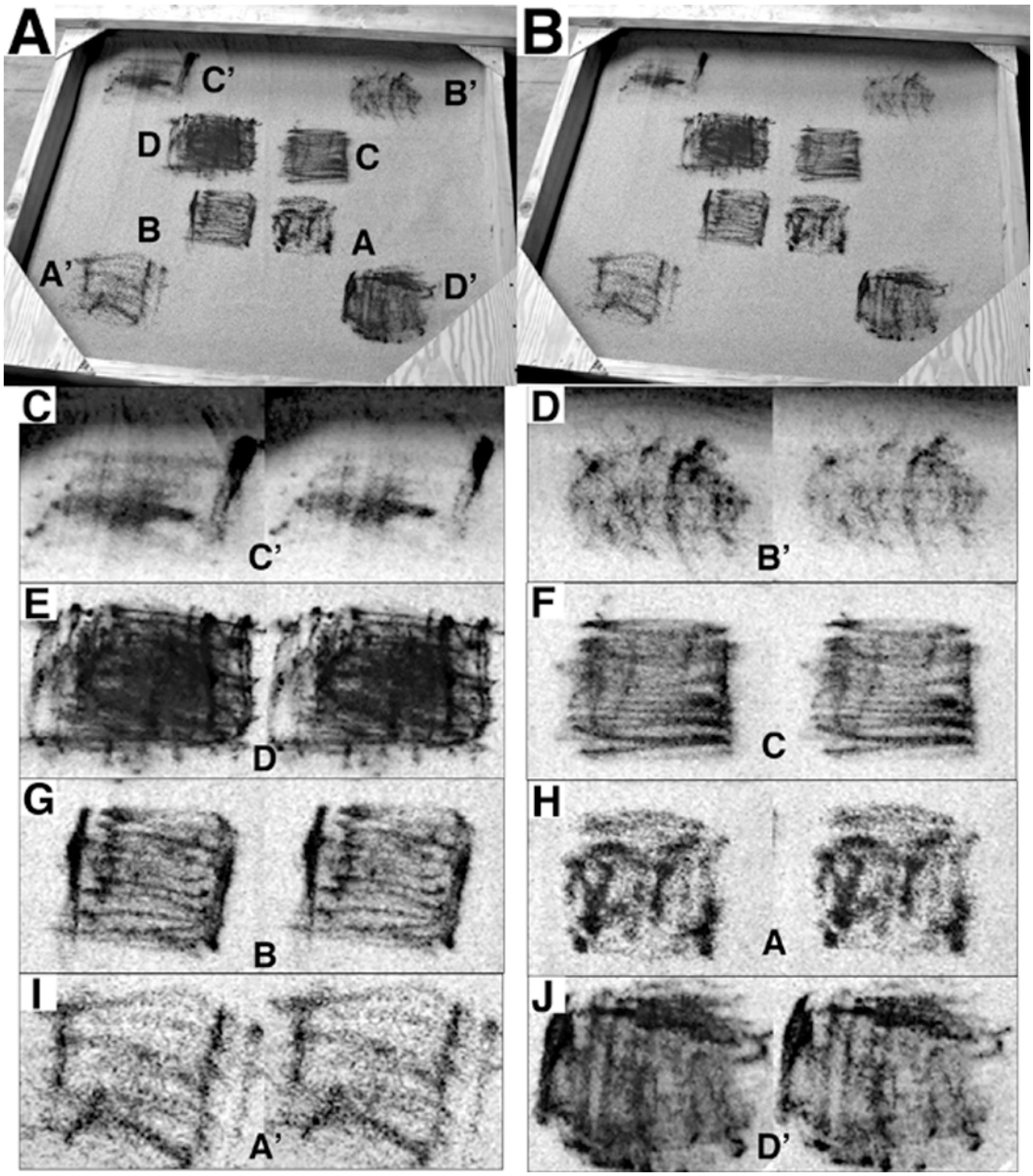

Figure 5.18. Horizontal shaking test during which the hammer cushion was placed with the void space at the center of the sandbox and the sledge-hammer hit the steel plate on the cushion at the void space. Hammer blows were applied to the edge of the sandbox at the top of these images. (A) Initial distribution of ilmenite particles in ~15 cm × 15 cm areas prior to hammer blows, with size fractions labeled: A, 600 μm – 1.8 mm; B, 300–600 μm; C, 150–300 μm; D, <150 μm; A', 600 μm – 1.8 mm; B', 300–600 μm; C', 150–300 μm; D', <150 μm. (B) Distribution of ilmenite particles after 100 hammer blows, showing the sinking of ilmenite into the sand mixture for all grain sizes. (C) through (J) are close-up views of each test area, before shaking (left) and after shaking (right).

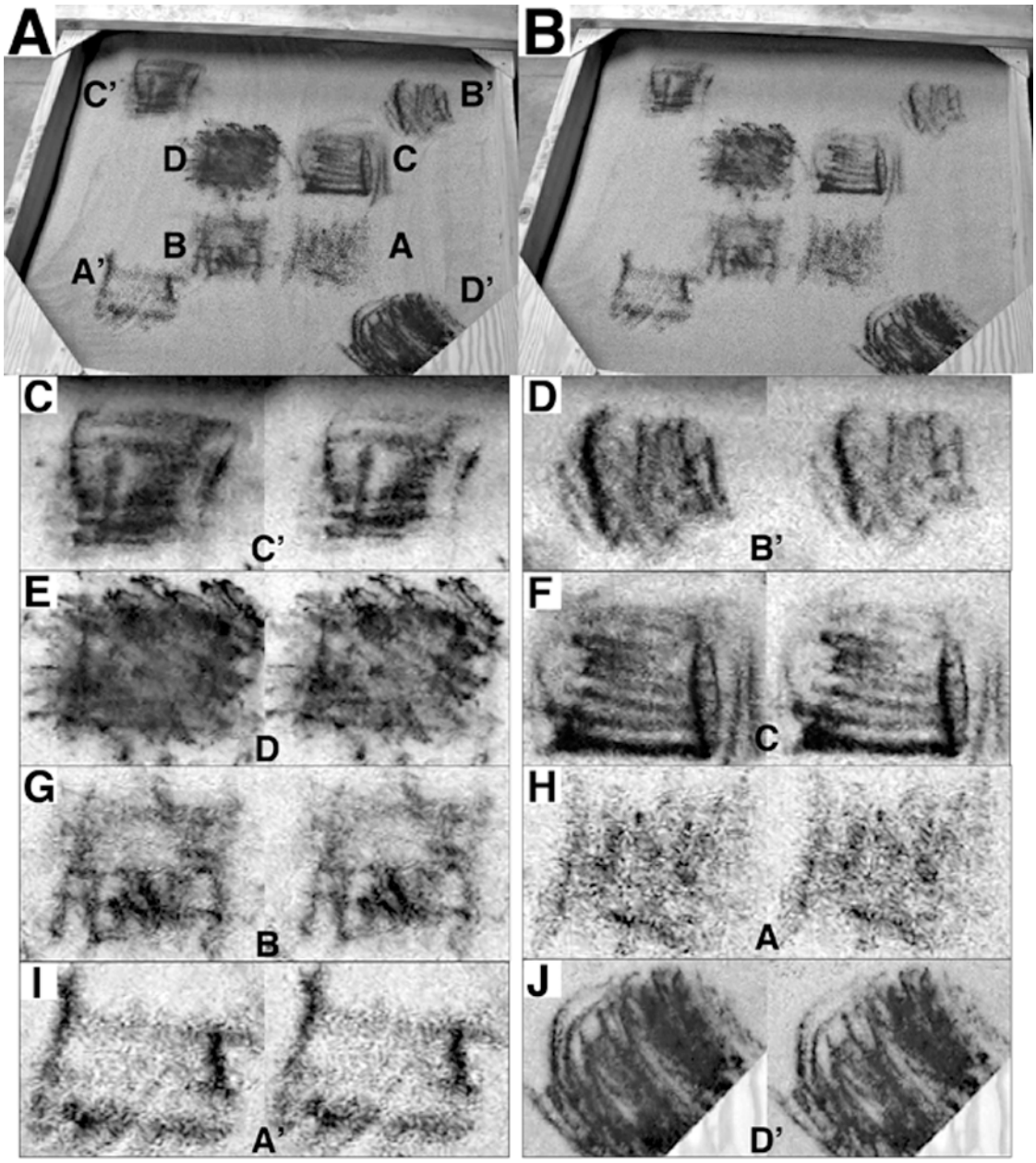

Figure 5.19. Horizontal shaking test during which the hammer cushion was placed with the solid end at the center of the sandbox and the sledge-hammer hit the steel plate attached to the cushion at the solid end. Hammer blows were applied to the edge of the sandbox at the top of these images. (A) Initial distribution of ilmenite particles in ~15 cm × 15 cm areas prior to hammer blows, with size fractions labeled: A, 600 μm – 1.8 mm; B, 300–600 μm; C, 150–300 μm; D, <150 μm; A', 600 μm – 1.8 mm; B', 300–600 μm; C', 150–300 μm; D', <150 μm. (B) Distribution of ilmenite particles after 100 hammer blows, showing the sinking of ilmenite into the sand mixture at all size-fractions. (C) through (J) are close-up views of each test area, before shaking (left) and after shaking (right).

5.5. Discussion

All three sets of shaking experiments indicate that granular mixtures of two different materials with density and grain size contrasts experience density-dependent mechanical size-sorting when vertically or horizontally perturbed. Under three significant experimental conditions, the denser particle of ilmenite sank into the less-dense matrix material, with the exception of the finest grain size fraction (<150 μm) that coated the matrix particles, regardless of grain size differences. In the first test case on the small tabletop vertical shaker, during which ilmenite and basalt fragments were vertically perturbed, the denser ilmenite sank deeper into the glass bead matrix than the less-dense basalt (Figure 5.10; Section 5.4.1). Subsequent tests using the large vertical shaker exhibited similar behavior with ilmenite, anorthosite, and sand, where the ilmenite sank more than the anorthosite into the sand, but poor contrast between anorthosite particles and the sand led to difficulties in image analysis for smaller grain size fractions. When three different size fractions of ilmenite particles were used in the large vertical shaker setup, ilmenite sank in all cases (Figures 5.12–5.17), suggesting that under ambient laboratory conditions (similar temperatures, humidity, and air pressure), the density contrast between the denser particles and the matrix affects the depth of descent of the denser grains. After vertical shaking, ilmenite grains (150–300 μm and <150 μm size fractions) were first observed at depths ranging from ~0.9 mm to ~1.8 mm and the bulk of ilmenite grains were observed at depths greater than ~1.8 mm to ~3.6 mm.

In all vertical shaking test cases, most of the sorting occurred in the first four to six minutes, suggesting rapid particle response to perturbation. It is unclear whether the ilmenite particles sank to their maximum depths within the first four to six minutes or

sank beneath the top sand grains surface during that time, sinking to deeper depths later. However, the matrix material (glass ballotini beads or sand) became compacted over the course of the experiment run, which may have influenced the depth of sinking for the ilmenite particles. Additionally, a circular area in the center of the large vertical shaker (VP-181) container remained relatively undisturbed and the ilmenite placed there did not exhibit as substantive sinking as the surroundings for tests of all size fractions. It is possible that at this location, the sand became compacted at or soon after (<2 minutes) the onset of shaking, preventing the sinking of ilmenite, due to the location of the vertical shaker table electromagnetic motor. The shaker is manufactured to distribute table vibrations across the entire table surface and the motor is installed directly beneath the center of the table. It may be that the material directly above the motor was most strongly affected by the vibrations and becomes compacted the fastest or, conversely, shaking vibrations were somehow attenuated by the experimental setup. These qualitative observations of particle compaction behavior resulting from shaking deserve additional investigation, in which quantitative measurements are made in a more lunar-like test setup. Analyses of regolith in returned drive tubes and drill cores, in addition to records of astronaut surface activities (e.g., hammer blows used to obtain a drive tube) and surface photographs (e.g., boot-print photographs), indicated that the density of lunar regolith varies vertically; that is, how the particles of the regolith are packed differs by location and is dependent on multiple factors, including geologic setting (proximity to fresh craters, location on slopes, age of surface, etc.) (e.g., Carrier et al., 1972; 1973).

In the horizontal tests, sinking of the ilmenite particles was observed within ten hammer blows, and sinking continued throughout the experiment run (100 hits). With the

hammer cushion void centered on the sandbox wall and the hammer blow centered on the void, the coupling of the hammer hit was distributed along the front wall similar to a line-source (something impacting along the length of the entire wall at one time), thus more evenly shaking the sandbox test bed. However, the force imparted to the experiment was attenuated as it traveled through the sand, and the ilmenite test areas toward the sandbox walls ("repeat" areas) experienced greater perturbation than the ilmenite test areas in the sandbox interior (center area). As a result, the central ilmenite areas exhibited a small amount of sinking while the "repeat" areas, particularly closest to the front wall, exhibited more sinking. In contrast, when the void space was removed by attaching the steel plate to the edge of the cushion, the hammer hit was applied directly to the cushion and simulated a point-source (discrete force of impact of hammer at one location). The coupling of the hammer hit directly to the sandbox wall at one location produced ilmenite test areas in the center of the sandbox that exhibited a greater amount of sinking than the "repeat" areas, although once again the "repeat" areas closest to the sandbox front wall exhibited more ilmenite sinking than those placed at the back wall. In both horizontal shaking tests, the ilmenite particles placed near the front wall of the sandbox (upon which the hammer blows fell) were affected more by the hammer perturbation so that more ilmenite sank in those regions than farther away. This sinking behavior is consistent with the attenuation of energy imparted to the sand from the front wall with increasing distance; the shaking is greatest closest to the hammer hit (front wall) and is least farthest away (sandbox back wall).

Previous work by Huerta and Ruiz-Suárez (2004) determined that vibration-induced segregation of particles in an experimental setting is strongly controlled by the

frequency and amplitude of the shaking. At higher frequencies, fluidization of the particulate mixture was observed, leading to a case where buoyancy dominantly controlled segregation (e.g., less dense particles are buoyant and denser particles sink) (Huerta and Ruiz-Suárez, 2004). The vertical shaker, operating at 60 Hz, is considered "high frequency" based on this previous work, and thus it is likely that the vertical shaker table experiments induced some amount of fluidization. The process of granular particle fluidization has frequently been applied to many geologic scenarios, especially those involving the transport of large volumes of material (e.g., debris flows in Vallis Marineris, Mars; Melosh, 1979; 1983), but there are few mentions of how fluidization scales to smaller geologic scenarios. However, the horizontal shaking tests were designed specifically to change the frequency of vibration (avoiding or mitigating fluidization) and to see if the same particle separation occurred as in the mechanical vertical vibration tests.

Translating experimental observations from the laboratory to geologic settings is complicated and understanding the relevance of experimental results in light of a geologic process is difficult. Laboratory experiments may not be completely transferrable to geologic applications because the experiments are small-scale and may not simulate a real geologic environment. For example, many of the experiments examining the BNE and RBNE are centimeters in scale (e.g., Knight et al., 1993; Hong et al., 2001; Möbius et al., 2001; Breu et al., 2003; Burtally et al., 2003; Huerta and Ruiz-Suárez, 2004; Metzger et al., 2011) and probably suffer from edge effects, which do not dominate a typical regolith on the Moon (e.g., in a central mare area). However, many of the small-scale experiments carried out by other researchers are directly applicable to industry (e.g.,

pharmaceuticals, food products), specifically addressing edge effects of packing containers and conveyor systems. In fact, some experimental observations focus on the effects of wall friction and the influence of container shape on particle sorting and convection (Knight et al., 1993). The experiments carried out here attempt to simulate a geologic environment by using as large a container size as possible, within financial and spatial means, to minimize edge effects. Although the large vertical shaker container surely experienced edge effects, the influence of the edge effects on the large container was minimal when compared to those observed on the small tabletop shaker. Furthermore, according to relationships between particle diameter and density (e.g., Hong et al., 2001; Breu et al., 2003), the ilmenite and sand experiments primarily fall into the RBNE realm, where the denser particles are expected to sink, although according to the particle diameter/density relationship, the shaking tests using ilmenite grains that were the same size as the sand grains theoretically could exhibit the BNE. The vertical shakers operate at frequencies much greater than shallow moonquakes measured by the Apollo Passive Seismic Experiments, which have frequencies commonly ranging between 2–4 Hz (e.g., Nakamura et al., 1979), and small meteoroid impacts with frequencies up to 8 Hz (e.g., Latham et al., 1970a). Furthermore, some terrestrial shallow nuclear explosions have measured frequencies of only about 0.03–1 Hz (Press et al., 1960). However, although the energy of the experimental system may be much greater than those observed geologically, the particle size and density sorting process is simulated in a manner that may be applicable to the Moon. While the experiments were conducted under terrestrial conditions (i.e., gravity, atmosphere, temperatures, humidity), the ilmenite sorting observations at all grain sizes do not solely reflect the presence of air-

driven separation due to pore space in the sand matrix (e.g., Burtally et al., 2002). Consequently, it is plausible to suggest that a similar size and density sorting mechanism may be occurring in the regolith of the lunar maria. Moreover, if such a sorting mechanism is active on the Moon, removing fine-grained ilmenite from the surface via seismic shaking will be efficient because the Moon's low seismic attenuation allows seismic energy to propagate for long distances and with great clarity (Latham et al., 1970b; e.g., 1970a; Dorman et al., 1978; Nakamura et al., 1982).

Two key shaking mechanisms should be considered when examining how particles may mechanically sort within the lunar regolith: sorting that occurs during impact ejecta emplacement and seismic shaking that results from either moonquakes or nearby impacts. When ejecta from an impact is initially emplaced on the lunar surface, ballistic sedimentation contributes to fragmentation of surface material (if the impact excavates through the regolith layer) and mixing of the upper regolith surface (Oberbeck, 1975). Micrometeorite bombardment over time comminutes particles at the regolith surface into smaller fragments in addition to jostling particles on a small scale (e.g., McKay et al., 1974). The mixing of the upper regolith surface by ejecta from larger impacts and micrometeorite bombardment redistributes mineral grains and may promote sorting by density as the minerals are churned, comminuted, and shaken. Moonquakes or nearby impacts may promote sorting in much the same way as observed in the vertical and horizontal shaking experiments because the seismic energy transmitted from shallow moonquakes or impacts will propagate through the lunar crust to shake the regolith. It is possible that such seismic activity promotes mechanical sorting, particularly because of the degradational landforms (subdued topography, morphology) surrounding and related

to lunar craters that are interpreted to result from seismic modification (Schultz and Gault, 1975).

Although completed under terrestrial conditions, the results of the vertical and horizontal shaking experiments suggest that size and density sorting may occur in the lunar regolith. If these experiments reproduce a sorting mechanism that is active on the Moon, then it is plausible that ilmenite content can vary in the top ten centimeters of the lunar regolith. CSR and LP GRS titanium abundance estimates agree within uncertainty for 29% of the nearside maria, and it is probable that in these regions, the reported TiO_2 abundances reflect ilmenite surface abundance that is observed at the optical surface by CSR (0.5° pixel scale) and at depth from LP GRS (0.5° pixel scale). However, the abundance differences for the remainder of the nearside maria (49% have higher CSR values, 22% have higher LP GRS values) may reflect contamination of the mare regolith by highland material, the competing effects of particle sorting and coating of surface grains by the smallest size fraction of ilmenite, imprecision of one or both titanium estimates, or a combination of the three, possibly with other unknown factors.

To investigate the disparity in TiO_2 abundance estimates between CSR and LP GRS, the 2° (natively collected) LP GRS titanium elemental abundance data were used, and CSR was resampled to 2° pixel scale. There is no evidence of a simple calibration error for either CSR or the LP GRS derived titanium values (Figure 5.20) that explains the differences between the two datasets. If the CSR and LP GRS titanium abundances agreed, the data would cluster along the unity line in Figure 5.20, but there is not a statistical correlation ($R^2 = 0.14$). Furthermore, a best-fit linear regression does not indicate a strong statistical correlation ($R^2 = 0.4$) between the 2° data. The locations

where CSR and LP GRS estimates agree (ranging from low to high titanium abundance; Figure 5.21) are scattered throughout the nearside maria and are not associated with particular geologic features (i.e. contacts, shield volcanoes, superposed impact craters, rays, etc.).

For low CSR titanium abundances (~0–2 wt% TiO_2), LP GRS titanium abundances range between 0 wt% and ~4 wt% TiO_2 (Figure 5.21D, 5.21E) and thus the differences are close to the expected range from the uncertainties in the two methods (regions with TiO_2 <2 wt% in both CSR and LP GRS datasets (cyan in Figure 5.21D, 5.21E; part of northwest Oceanus Procellarum, small areas in Sinus Iridum and northeast Mare Imbrium, much of Lacus Somniorum, and patches of maria surrounding Mare Crisium) and regions where CSR is <2 wt% TiO_2 and LP GRS is ~2–4 wt% TiO_2, (magenta in Figure 5.21D, 5.21E; remainder of northwest Oceanus Procellarum, Sinus Iridum, northeastern Mare Imbrium, Lacus Somniorum, and a small area of Lacus Mortis)). Although the differences in CSR and LP GRS for these regions may primarily reflect measurement uncertainties, lower CSR than LP GRS titanium abundances (e.g., 1 wt% compared to 4 wt% TiO_2, respectively; Figure 5.21D, 5.21E, 5.22A) may reflect real compositional differences resulting from contamination of the optical surface by highland components. Lateral (horizontal) transport of material on the Moon occurs through emplacement of impact crater ejecta that creates a thin blanketing (covering and mixing materials in the optical surface) of compositionally distinct materials (i.e., anorthositic highland material on the mafic maria). The absence of visible ejecta rays from highland impact craters superposed on the maria in northeastern Mare Imbrium, Sinus Iridum, and northwest Oceanus Procellarum weakens, but does not exclude, the

possibly for contamination of mare regolith by highland materials. For example, an anorthositic component attributed to highland materials was discovered in the Apollo 11 bulk regolith samples, and rays from Theophilus and Alfraganus craters are observed near (but not at) the landing site in Mare Tranquillitatis (e.g., Wood et al., 1970). It is thus possible to observe highland contamination of mare basalts without visible crater rays extending across the region. Furthermore, the absence of visible crater rays may also be explained by ballistic sedimentation (Oberbeck, 1975) coupled with the effects of space weathering (e.g., Hapke, 2001 and references therein) that churn and darken the regolith over time to promote the gradual disappearance of visible ejecta rays over time.

For some areas with moderate CSR titanium abundance (~2–5 wt% TiO_2), LP GRS titanium abundance is high (>5 wt% TiO_2; Figure 5.21D, 5.21E, 5.22B); these areas occur primarily within Mare Insularum and Oceanus Procellarum in locations geographically close to irregular mare boundaries. Regions such as the Aristarchus Plateau exhibit distinct compositional contacts, and lateral transport of highlands material to the maria via ejecta emplacement is one simple explanation for lower CSR titanium estimates than those measured by LP GRS. Similarly, the partially embayed highland regions within Mare Insularum will contribute anorthositic material laterally via impact crater ejecta emplacement to depress the CSR titanium estimates of the mare basalts (Figure 5.21D, 5.21E). Oceanus Procellarum may also have decreased CSR titanium abundance due to contribution of titanium-poor materials from Aristarchus and Kepler crater ejecta (relative to the surroundings; Figure 5.21D, 5.21E). However, observations of moderate CSR abundance and high LP GRS abundance may also be explained by the sinking of denser ilmenite grains as a result of seismic shaking (Figure 5.22B). Over time

and successive seismic shaking events, the ilmenite grains sink to increase the ilmenite content measured within the upper few centimeters of regolith relative to the optical surface (Figure 5.22B). Even if fine-grained ilmenite particles are stranded at the optical surface through the shaking process, promoting a moderate measure of ilmenite by CSR, the enrichment in coarser-grained ilmenite below the optical surface is detectable and will be reflected by high LP GRS abundance measurements.

Lastly, areas with high CSR titanium abundances (~5–10 wt% TiO_2) correlated with low to moderate LP GRS values (0 to ~5 wt% TiO_2) are primarily located either near mare boundaries or within Mare Crisium and Mare Fecunditatis (Figure 5.21D, 5.21E). The 2° pixel scale binning of LP GRS (footprint of ~45 km, Figure 27 in Prettyman et al., 2006) often results in portions of two or more geologic units within a pixel ("mixed-pixels"). Therefore near mare boundaries, particularly western Oceanus Procellarum, Mare Humorum, and Mare Nubium, high CSR and low–moderate LP GRS titanium abundances likely reflect contamination of LP GRS measurements by highland materials included within the footprint (Figure 5.21D, 5.21E). However, the disparate titanium abundances in Mare Crisium and Mare Fecunditatis (Figure 5.21D, 5.21E) cannot be explained by such mixed-pixels. Mare Crisium and Mare Fecunditatis contain the most discrepant geologic units on the Moon; neither CSR nor LP GRS titanium abundances match returned Luna 16 and 24 regolith samples (Table 5.1). Revisions to the location of the Luna 24 landing site in Mare Crisium using Lunar Reconnaissance Orbiter Camera Narrow Angle Camera (LROC NAC) images indicate that Luna 24 landed on the continuous ejecta blanket of a 65 m diameter crater (Robinson et al., 2012), and therefore, the returned sample is not representative of the regolith optical surface measured by CSR.

However, the Luna 24 regolith sample indicates the presence of a different compositional unit, further attesting to the complexity of the lunar regolith and changing volcanic compositions on the Moon over time. The higher CSR titanium estimates in Mare Crisium and Mare Fecunditatis are not consistent with the simple model of seismic shaking (Figure 5.22B) explored in the experiments, where the coarse-grained ilmenite particles sank into the sand matrix (Section 5.4, Figure 5.12–5.14). However, it may be that the higher CSR titanium estimate is due to a grain separation effect of the fine-grained ilmenite size fraction, similar to that seen in the shaking experiments (Section 5.4, Figure 5.15–5.17). In the experimental setup, as fine-grained (<150 μm) ilmenite particles sank into the bed of larger (300–600 μm), less-dense sand particles, an ilmenite "shadow" remained at the surface, coating the sand particles. This scenario, shown in Figure 5.22C, provides an explanation for high CSR, low–moderate LP GRS regions, where the finest of the fine-grained ilmenite particles are stranded in the optical surface as a result of seismic shaking. The experimental results suggest that seismic shaking promotes sinking of the fine-grained ilmenite until the pore space in between the sand grains are filled, and because there is more fine-grained ilmenite than can be accommodated by the available pore space, ilmenite is stranded within the optical surface. Although possible, this explanation is less likely because in the shaking experiments, all the coarse-grained, and most of the fine-grained, ilmenite sank, except for the finest of the fine-fraction that remained stranded at the surface coating sand grains.

The results presented here provide plausible explanations for the nearside maria differences between CSR and LP GRS titanium abundances, but intelligent acquisition of

additional samples is required to solve this problem. Sampling techniques that accurately capture the optical surface of the regolith, a depth of a few centimeters, and a depth to ~10 cm (or more) are desirable to better calibrate multispectral observations of the lunar surface and remotely sensed measurements of bulk regolith composition. For example, optical surface sampling could employ an adhesive surface, much like the tape pulls in my shaking experiments (Figure 5.17), to collect the top layers of the regolith in specific locations. Samples from different depths (e.g., a few cm, ~10 cm) are easily obtained in drive tube cores (e.g., McKay et al., 1974; Heiken, 1975; Papike et al., 1982) whereby the regolith is preserved in a vertical cross-section. Ideally, samples from each region discussed above should be obtained, so that the regions exhibiting the greatest disparities in titanium abundances (especially Mare Crisium and Mare Fecunditatis), in addition to a location where CSR and LP GRS agree, are represented.

Investigating the strengths and limitations of remotely sensed compositional measurements is integral to studies of small bodies, because sampling opportunities are few. For example, subtle color and compositional differences between the smooth ponds and the surrounding regolith are observed on 433 Eros (Robinson et al., 2001; 2002; Riner et al., 2008). Differences in regolith maturity, variations in grain size, and compositional variations due to sorting processes are invoked to explain the color properties of ponds, specifically focusing on a depletion of Fe–Ni metal (Robinson et al., 2001; 2002). Impact-induced seismic shaking was invoked as the primary process for smooth ponds formation on 433 Eros (e.g., Asphaug et al., 2001; Cheng et al., 2002), but little thought was previously given to seismic shaking as a compositional sorting mechanism. The results of this study raise the possibility that mechanical sorting

resulting from both size and density variations may account for a pond composition that is different than the surrounding terrain. Removing Fe–Ni from the regolith by density sorting of the regolith will decrease the spectral slope so that ponds are “less red”, as long as the silicate particle sizes remaining at the surface are <50 μm, (Riner et al., 2008). Although the compositional properties of ponds can be explained by multiple factors (Robinson et al., 2001; Riner et al., 2008), the results of my experiments indicate that seismic shaking density and size sorting of the Eros regolith is plausible.

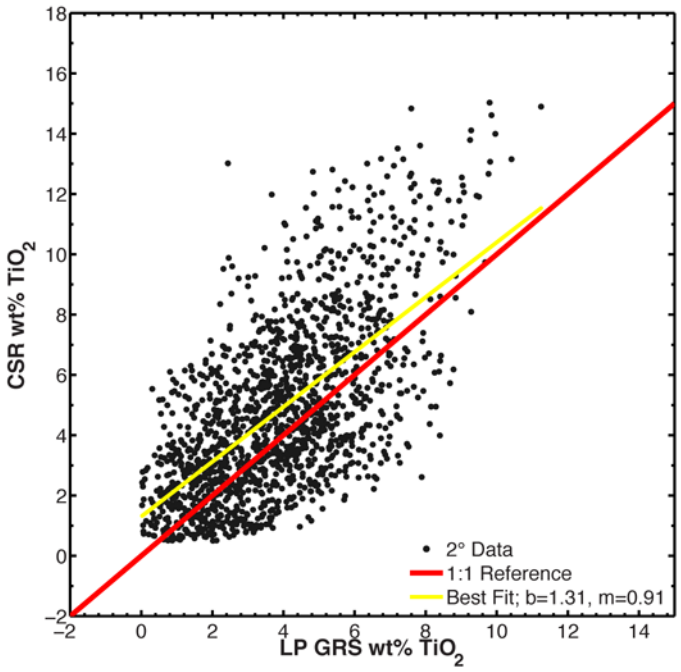

Figure 5.20. TiO_2 abundance derived from CSR compared to LP GRS. If the datasets were in agreement, the points would plot along the unity reference line (red; $R^2 = 0.14$). A best-fit linear regression is shown in yellow, and $R^2 = 0.40$.

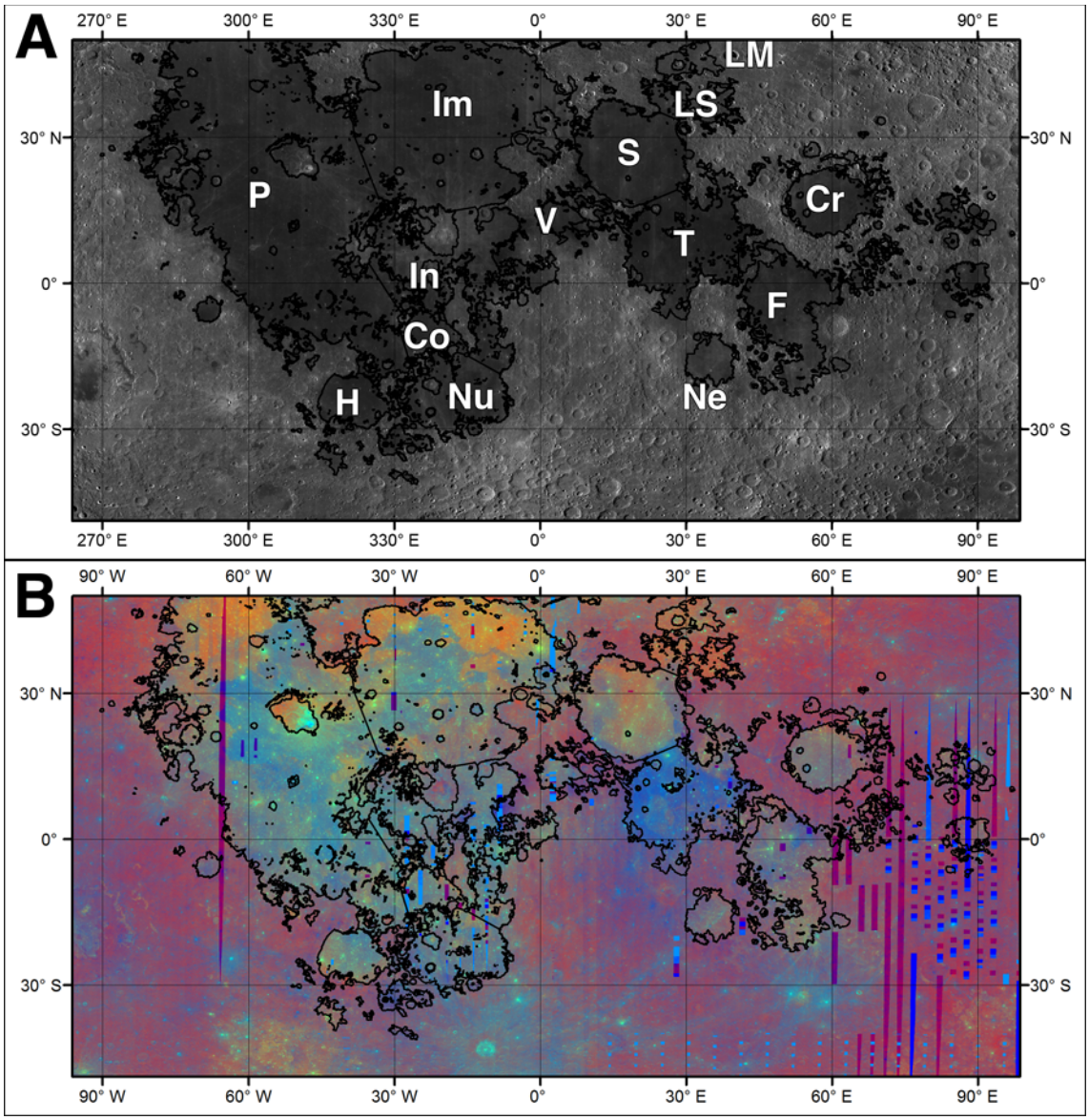

Figure 5.21. View of nearside lunar maria (centered at 0°N, 0°E); (A) LROC WAC normalized reflectance mosaic, (B) Clementine multispectral ratio mosaic (R=750/415, G=750/950, B=415/750). In (A), maria are named: Co, Cognitum; Cr, Crisium; F, Fecunditatis; H, Humorum; Im, Imbrium; In, Insularum; LM, Lacus Mortis; LS, Lacus Somniorum; P, Procellarum; Ne, Nectaris; Nu, Nubium; S, Serenitatis; T, Tranquillitatis; V, Vaporum.

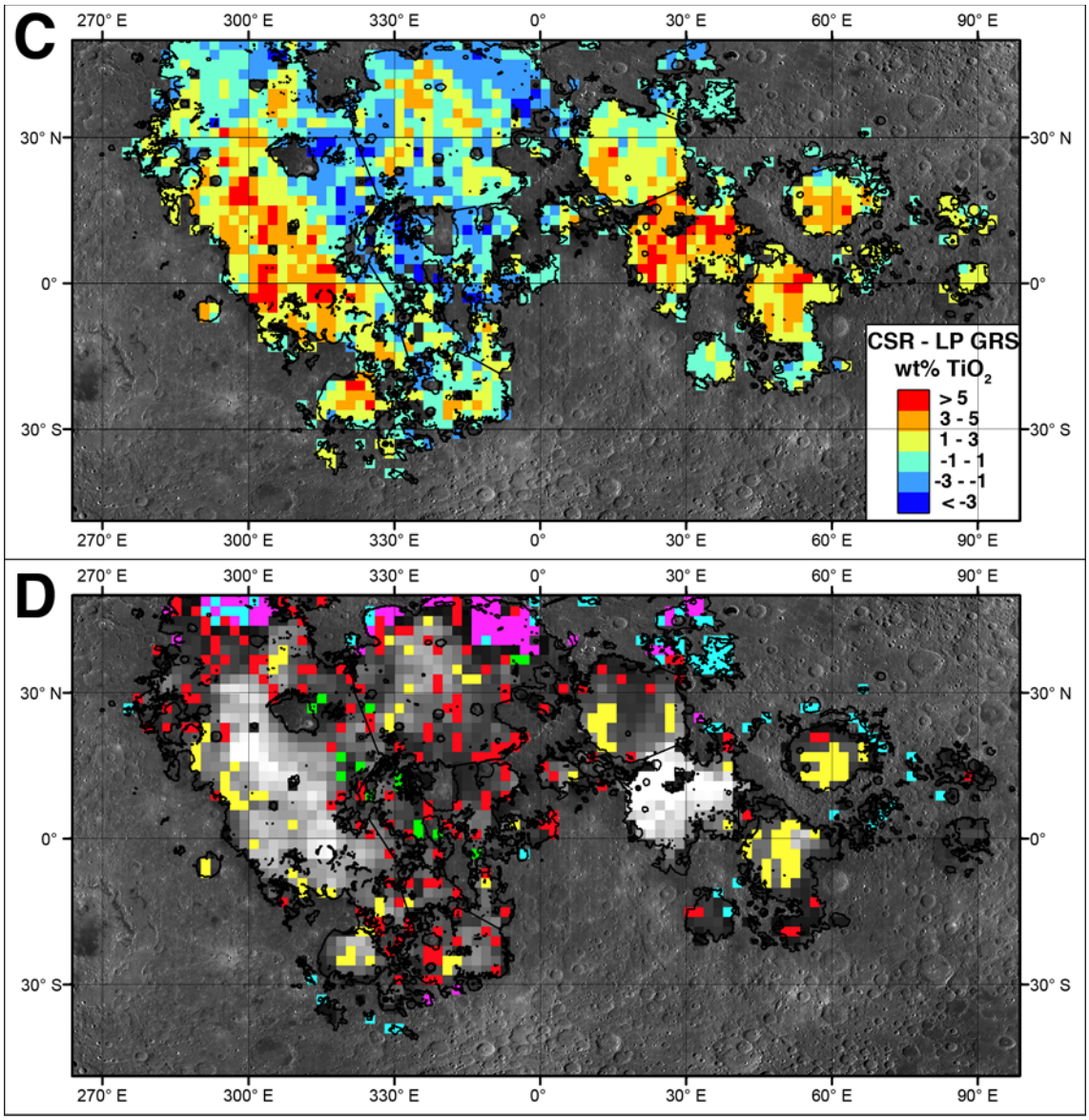

Figure 5.21, continued. View of nearside lunar maria (centered at 0°N, 0°E); (C) 2° pixel scale CSR–LP GRS difference map overlaid on LROC WAC normalized reflectance mosaic, (D) Color-classified 2° pixel scale CSR map created by selection of regions of interest in the CSR versus LP GRS wt% TiO_2 scatterplot (Figure 5.21E, below) overlaid on LROC WAC normalized reflectance mosaic.

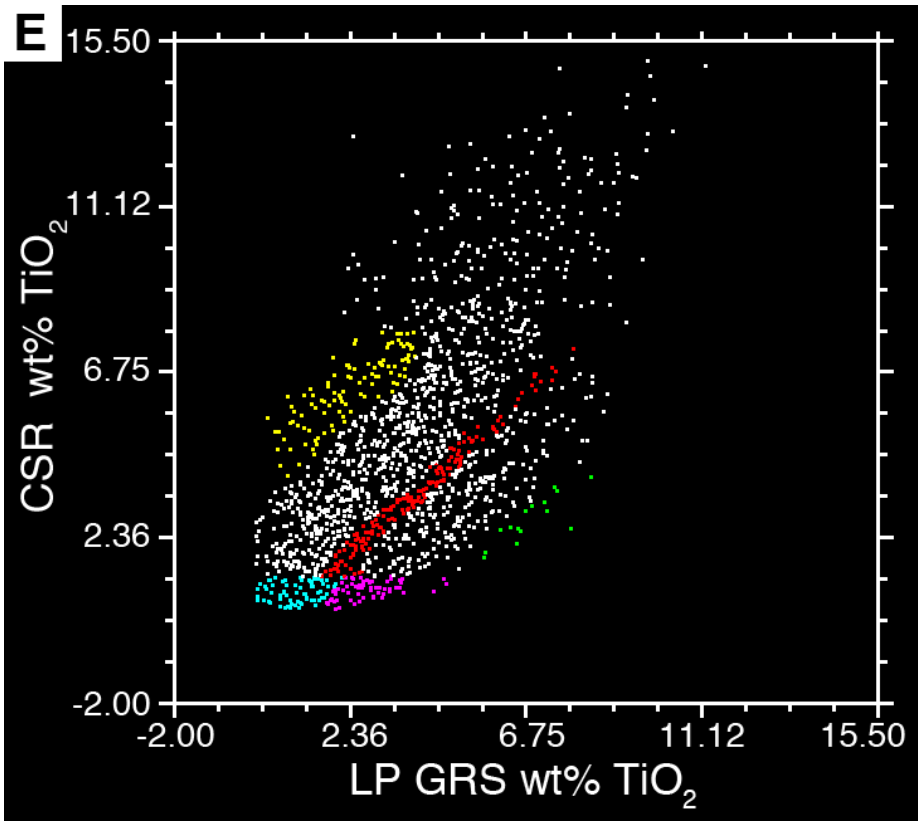

Figure 5.21, continued. (E) CSR titanium abundance as a function of LP GRS titanium abundance for 2° pixel scale measurements. Selected regions of interest shown in Figure 5.21D: red = approximate unity between CSR and LP GRS where the measurements agree; cyan = ~0–2 wt% TiO_2 in CSR and LP GRS (both low); magenta = ~0–2 wt% TiO_2 in CSR, ~2–4 wt% TiO_2 in LP GRS (CSR low, LP GRS moderate); green = ~2–5 wt% TiO_2 in CSR, >5 wt% TiO_2 in LP GRS (CSR moderate, LP GRS high); yellow = ~5–10 wt% TiO_2 in CSR, ~0–5 wt% TiO_2 in LP GRS (CSR high, LP GRS low to moderate).

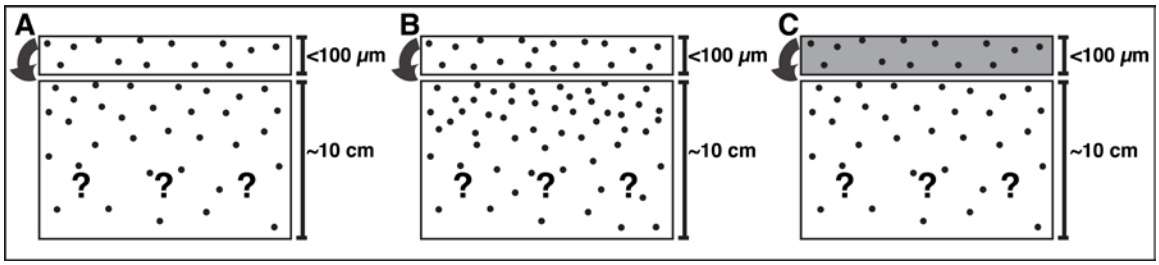

Figure 5.22. Cartoon illustrations, informed by the experimental results, depicting three scenarios for CSR and LP GRS titanium abundances observed in Figure 5.21D, 5.21E; black dots represent ilmenite grains, grayed area represents the finest size fraction of ilmenite occurring in the regolith. Due to the difference in measurement scales, the optical surface (<100 μm) measured by CSR is shown in the top rectangle and a measurement depth of ~10 cm for the LP GRS is shown in the bottom rectangle, although the depth to which ilmenite sinks is unknown. An arrow indicates that the optical surface comprises the top-most portion of the LP GRS measurement depth. (A) Low CSR (~1 wt% TiO_2), low–moderate LP GRS (~4 wt% TiO_2); measurements of the optical surface are similar to those in the top 10 cm. (B) Moderate CSR (~2.5 wt% TiO_2), high LP GRS (~7 wt% TiO_2); seismic shaking removes ilmenite from the optical surface, where it becomes concentrated in the top few centimeters and sampled by LP GRS. (C) High CSR (~6 wt% TiO_2), low–moderate LP GRS (~2.5 wt% TiO_2); the finest grain size fraction of ilmenite is stranded at the optical surface due to seismic shaking, enhancing the CSR abundance estimate.

5.6. Conclusions

Constraining the mechanical mixing properties, including grain size sorting, density sorting, and depth of sorting of a regolith, is essential to accurately interpreting remotely sensed measurements. Vertical and horizontal shaking experiments were conducted to simulate the effects of seismic shaking on a regolith mixture. Although completed under terrestrial conditions, the results of these experiments are relevant for the Moon and other airless planetary bodies with regoliths. Returned lunar regolith samples have a broad range of grain sizes, compositions, and densities, and the regolith for a location is genetically related to the underlying bedrock (e.g., Papike et al., 1982). Varying densities of minerals within a regolith may result in density-driven mechanical sorting, perhaps regardless of size. Two-component physical mixtures containing

particles of different size fractions and different densities were used to study the effects of shaking on particle sorting. In all cases, under vertical and horizontal perturbation, the denser materials sank into the less dense matrix material, even when there were small density differences. More importantly, all size fractions of the denser particles sank, even when the denser particles were smaller than the matrix. These experimental results indicate that the Brazil Nut Effect (e.g., Rosato et al., 1987) cannot directly be applied to explain most geologic features on planetary surfaces with regoliths, because experimental investigations of the Brazil Nut Effect (e.g., Knight et al., 1993; Möbius et al., 2001; Breu et al., 2003; Burtally et al., 2003; Huerta and Ruiz-Suárez, 2004) and the Reverse Brazil Nut Effect (e.g., Hong et al., 2001) were completed in small containers (≤10 cm diameter or width; Knight et al., 1993; Hong et al., 2001; Möbius et al., 2001; Breu et al., 2003; Burtally et al., 2003) that cannot be accurately scaled to larger dimensions and are prone to significant edge-effects. Future seismic shaking investigations would benefit from shaking tables with variable amplitudes, frequencies, and motion, such as that used by Izenberg and Barnouin-Jha (2006a; 2006b). The ability to change amplitudes and frequencies would enable better simulations of lunar-like seismic events by setting the shaker to approximate moonquakes and impact events of different magnitudes. Using both vertical and horizontal motion during a single test run might improve the experimental results by more realistically simulating a planetary surface affected by seismic shaking. In addition to using larger shaker tables with more advanced shaking settings, future investigations into seismic shaking as a planetary process should logically incorporate numerical models to appropriately apply the experimental results at the

planetary scale (such as those presented by Asphaug et al., 1996; Richardson et al., 2005).

The experiments undertaken in this investigation demonstrate the possibility of mechanical segregation of particles in the regolith and provide plausible explanations toward understanding the three types of inconsistencies between compositional remote sensing datasets. For example, my experimental results suggest that for some locations a simple model of seismic shaking, where ilmenite grains sink below the optical surface, is plausible. In other regions, there may be a competing effect between the dense ilmenite particles sinking (regardless of size) and the coating of surface particles by the finest of the fine size fraction of ilmenite, which may lead to incorrect interpretation of remotely sensed composition. Titanium abundance estimates derived from CSR and LP GRS agree for only 29% of the nearside maria, indicating that in these regions the different remote sensing methods are likely accurately determining composition (within the measurement uncertainties). However, the remaining 71% of the nearside maria exhibit higher titanium abundances in either the CSR or the LP GRS estimates. Both measurement techniques have limitations, and my observations suggest that while some regions exhibit low CSR and higher LP GRS titanium abundances due to density separation of ilmenite promoted by seismic shaking, the mismatch between datasets results primarily from remaining uncertainties in the CSR algorithm (e.g., Blewett et al., 1997; Lucey et al., 1998; Gillis et al., 2003) and contribution of highland components to the LP GRS footprint (Feldman et al., 1999; Lawrence et al., 2000; 2003; 2004; Prettyman et al., 2006).

Seismic shaking is likely an active process on all asteroids (e.g., Asphaug et al., 1993; 1996; Richardson, 2005), and the effects of compositional sorting resulting from

perturbation should be considered. Compositional remote sensing measurements may not always provide accurate information below the optical surface, so future sample return missions relying on these compositional data should acquire multiple samples from different depths on the asteroid whenever possible. The OSIRIS-REx mission to asteroid (101955) 1999 RQ36 is a perfect opportunity to compare the compositional information acquired by remote sensing to that of a collected sample. Ground- and space-based telescopic studies have extensively characterized asteroid (101955) 1999 RQ36, and the OSIRIS-REx current mission plan includes mapping the asteroid with multiple imagers and spectrometers (X-Ray, visible, infrared, and thermal) at different scales, and collection of >60 g regolith from the asteroid surface (Lauretta and Team, 2012). The OSIRIS-REx mission thus provides a unique opportunity to investigate discrepancies between surface and subsurface measurements, and intelligent sampling paired with remotely sensed compositional will improve understanding of potential disparity between remotely sensed compositions and samples of asteroidal regolith.

CHAPTER 6

DISTRIBUTION OF IMPACT MELT ON MERCURY AND THE MOON

6.1. Introduction

The surfaces of both Mercury and the Moon show evidence of substantial surface modification from the impact cratering process. Images taken by the camera instruments aboard the recent Lunar Reconnaissance Orbiter (LRO) mission to the Moon and the MErcury Surface, Space ENvironment, GEochemistry, and Ranging (MESSENGER) mission to Mercury provide key data to complete an investigation of impact craters and their products such as impact melt, formed by the vaporization and melting of target rock during impact. Impact melt is a particularly important product of the impact cratering process because it has no geological counterpart; impact melts form as a result of the nearly instantaneous melting of the target rocks soon after impact (e.g., French, 1998). Comparison of the distribution and extent of impact melt produced by the impact process on Mercury and the Moon should reveal significant clues pertaining to the formation and emplacement of impact melt in and around craters, in addition to providing quantitative measurements with which to assess melt-generation models. Determining the presence, spatial extent, and volume of impact melt on Mercury was difficult until March 2011, when MESSENGER entered orbit about Mercury and began a global mapping campaign, as the Mariner 10 or MESSENGER flybys did not acquire global coverage and few images were taken at favorable illumination and resolution for morphologic studies. Similarly, global maps acquired by LRO enable a more comprehensive investigation of impact melt distribution and examination of morphologic characteristics to improve upon previous studies of lunar impact melt.

Comparisons between lunar and mercurian craters were made following the Mariner 10 flybys (Murray et al., 1974; Gault et al., 1975; Murray et al., 1975; Gault et al., 1977; Guest and O'Donnell, 1977; Oberbeck et al., 1977; Strom, 1979), and many morphologic similarities were observed between the craters on both planets. Differences were also noted: craters on Mercury form wall terraces at smaller diameters than on the Moon, secondary craters are larger on Mercury yet secondary crater fields are located closer to the crater rims than their lunar counterparts, and continuous ejecta blankets have a restricted spatial extent on the innermost planet (e.g., Murray et al., 1974; Gault et al., 1975; Oberbeck et al., 1977). Many of these differences are attributed to the greater gravitational acceleration on Mercury than the Moon (3.7 m/s^2 vs. 1.6 m/s^2; e.g., Gault et al., 1975). As a result, the average impact velocity is ~2 times higher on Mercury than the Moon (e.g., Wetherill, 1974; Le Feuvre and Wieczorek, 2008), which substantially increases the volume of impact melt (Gault et al., 1975).

Previous studies of impact melt deposits discussed the presence of material interpreted to be impact melt in and around lunar craters (Shoemaker et al., 1968; El-Baz, 1972; Howard, 1972; Howard and Wilshire, 1975; Hawke and Head, 1977a; 1977b). However, on the basis of available data, these studies were not able to compile a comprehensive global dataset of craters with impact melt deposits; for example, Hawke and Head (1977a) examined exterior impact melt flows for 55 craters using Lunar Orbiter and Apollo Metric images. Moreover, impact melt studies of Mercury using the Mariner 10 data were sparse, with the exception of an abstract by Hawke and Cintala (1977) that mentioned the occurrence of smooth ponded deposits in several mercurian craters similar to ponded lunar impact melt. Crater scaling relationships and impact melt-generation

models predict that for similar sizes, craters on Mercury should produce greater volumes of impact melt due to the greater impact velocities than on the Moon (e.g., Gault et al., 1975; Grieve and Cintala, 1992; 1997). Previous workers were unable to quantitatively test these predictions due to the available data, but measurements from LRO and MESSENGER facilitate acquisition of comprehensive datasets to test these theoretical models.

Here I present initial results of a comparison between Mercury and the Moon regarding the distribution and areal extent of impact melt deposits within craters with diameters between 8 to ~160 km. Leveraging new data from LRO and MESSENGER, I selected two regions on the Moon and one region on Mercury for comparative study. The two lunar regions were chosen in order to sample both nearside terrain and farside highlands, and the mercurian region was selected to encompass heavily cratered terrain and exclude volcanically modified impact basins (e.g., Caloris, Beethoven, Rembrandt). For each of these regions, craters with ponded impact melt deposits were identified, the extent of those interior deposits were mapped, and melt pond area was calculated and used as an approximation for volume.

6.2. Methods and Data

Lunar Reconnaissance Orbiter Camera Wide Angle Camera (LROC WAC) (Robinson et al., 2010; Speyerer et al., 2011) and MESSENGER Mercury Dual Imaging System (MDIS) WAC and Narrow Angle Camera (NAC) (Hawkins et al., 2007) 200 meter pixel scale monochrome mosaics were made using images with favorable illumination for morphology (average 60° to 77° incidence angle). On Mercury, a region

centered at 0°N and 0°E extending ±30° latitude and ±60° longitude was selected in heavily cratered terrain, covering a surface area of 11.6×10^6 km^2 (~16% of the planet). On the Moon, two areas were selected (~23% of the planet): a region on the nearside centered at 0°N and 0°E extending ±30° latitude and ±60° longitude and covering an area of 6.3×10^6 km^2, and a region on the farside centered at 0°N and 145°E extending ±20° latitude and ±35° longitude with a surface area of 2.5×10^6 km^2.

ESRI ArcMap 10 and the CraterTools extension (Kneissl et al., 2011) were used to identify craters with ponded impact melt and to map the extent of these deposits. CraterTools computes a best-fit circle to three user-defined points on a crater rim and records the center latitude, longitude, and diameter to a project database. The deposit extents were mapped using the standard editing tools included with the ArcMap 10 software. An 8 km minimum diameter was defined for crater identification because secondaries can commonly be as large as 8 to 10 km on Mercury (**Chapter 4**; Strom et al., 2008). Craters with diameters >200 km were excluded because photogeological studies suggest that on Mercury, basins this size frequently have volcanic smooth plains associated with interior impact melt deposits (e.g., Prockter et al., 2010; Marchi et al., 2011).

Definitive identification of impact melt on Mercury is challenged by poor image resolution, so only the youngest age-groups of craters (Kuiperian/Mansurian on Mercury, and Copernican/Eratosthenian on the Moon) are included in the investigation, on the assumption that the youngest craters have interior deposits most easily identified due to a lack of substantial erosion and crater degradation. Such young craters were identified primarily on the basis of morphology, augmented by existing geologic maps. Improving

upon criteria used to identify impact melt in earlier detailed studies (c.f., Howard and Wilshire, 1975; Hawke and Head, 1977a; 1977b) by examining larger regions at consistent illumination for morphologic interpretation, melt deposits were distinguished on the basis of (1) Interior pond morphology (a smooth texture, few superposed craters, and a distinct fill-wall contact; e.g., Shoemaker et al., 1968; El-Baz, 1972; Howard, 1974; Howard and Wilshire, 1975), (2) The presence of exterior flows, ponds, and veneers (Howard, 1972; Howard and Wilshire, 1975; Hawke and Head, 1977a), and (3) The absence of embayed craters within the crater interior (indicative of a length of time between crater formation and infill, consistent with subsequent volcanism; e.g., Strom et al., 1975; Wilhelms, 1976b) (Figure 6.1). Furthermore, volcanic infill of lunar craters is often indicated by the presence of lower albedo material and compositional variation within the crater compared to outside; similar albedo and compositional variations are absent on Mercury (e.g., Robinson et al., 2008; Denevi et al., 2009).

Only interior impact melt deposits were included in mapping and area measurements. Exterior melt deposits were excluded from this investigation because confidently identifying the spatial extents of exterior melt was difficult. As topography data were not yet available, the spatial extents of interior melt pond areas were measured as an approximate proxy for volume. The volume of impact melt produced should scale with crater diameter (e.g., Grieve and Cintala, 1992; 1997; Cintala and Grieve, 1998a; 1998b), a hypothesis that is tested in this investigation. Thus, more melt should be retained in larger impact events (e.g., Grieve and Cintala, 1997) and for similarly sized craters, disparities in interior melt areal extents are assumed to reflect volumetric differences in melt produced.

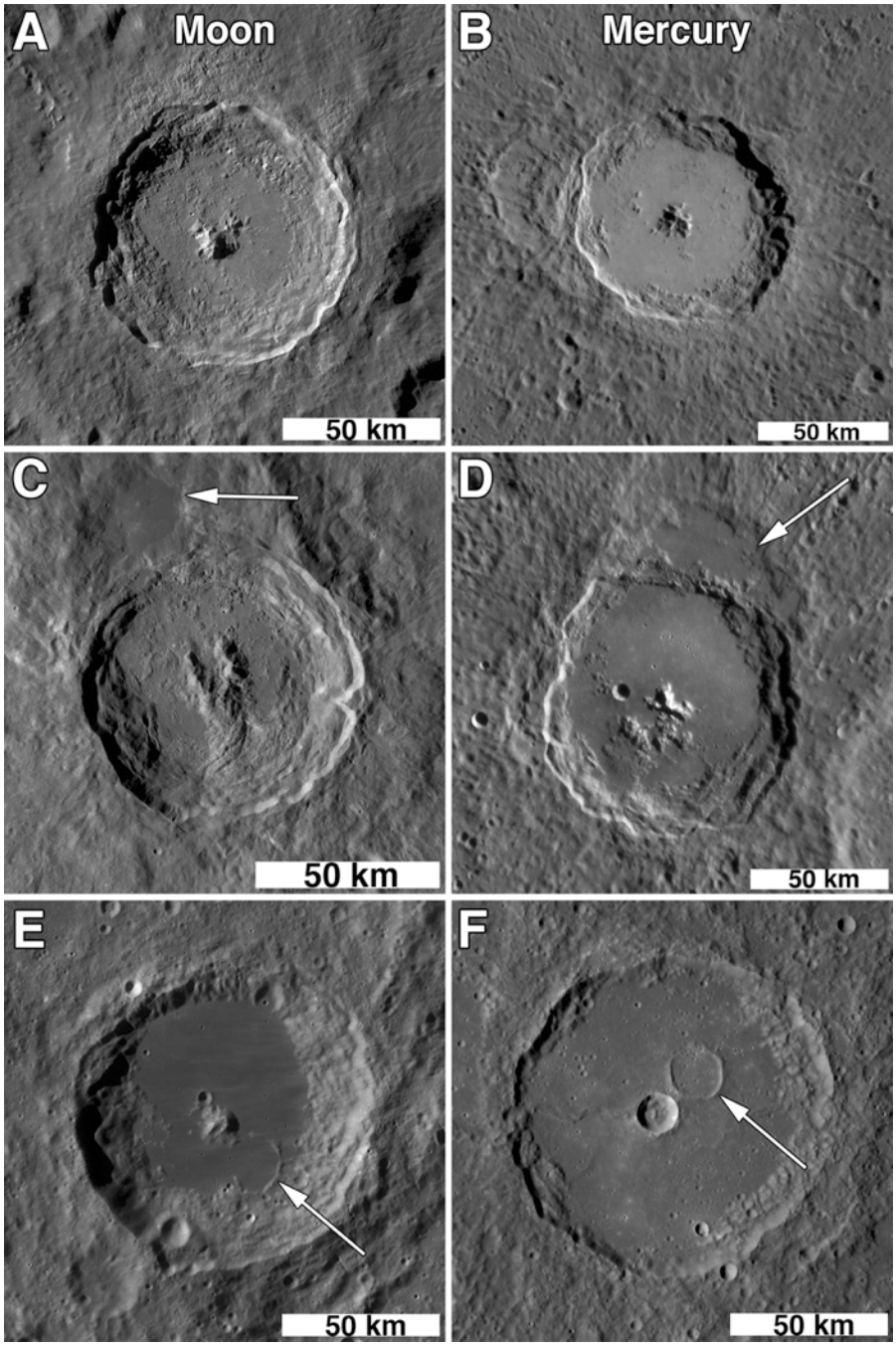

Figure 6.1. Representative craters illustrating distinguishing criteria for impact melt mapping: (1) Young craters with smooth deposits and well-defined contacts, (A) Tycho crater (43.41°S, 339.92°E, ~85 km diameter) and (B) Debussy cater (33.93°S, 12.55°E, ~80 km diameter); (2) Presence of exterior ponds or flows and perched ponds on crater wall terraces, (C) King crater (5.04°N, 120.43°E, ~78 km diameter) and (D) Sibelius crater (49.54°S, 214.75°E, ~94 km diameter), arrows note exterior ponds; and (3) Absence of embayed or filled craters (arrows) within smooth floor deposits, (E) Pauli crater (45.24°S, 137.52°E, ~100 km crater) and (F) Machaut crater (2.03°S, 277.74°E, ~104 km diameter), arrows note embayed craters.

6.3. Results

Ponded impact melt deposits were identified in 488 mercurian craters and 495 lunar craters for diameters ranging from 8 km to ~160 km. From the measured population, the average mercurian crater diameter with identifiable impact melt deposits is 24 km, with a maximum of 125 km and a median diameter of 17 km. The corresponding average lunar crater diameter is 16 km for the nearside, with a maximum of 100 km and a median diameter of 12 km; the average diameter is 19 km for the farside, with a maximum of 158 km and a median diameter of 13 km. Figure 6.2 is a histogram of craters containing ponded interior impact melt for diameters 8–53 km in 5 km bins, normalized to 10^6 km^2, and the general trend observed is the presence of high frequencies of melt-flooded craters in smaller bins that gradually decrease at larger crater diameters. For all three regions, the two smallest bins (8–13 km, 13–18 km) contain the highest crater frequencies per 10^6 km^2 (Figure 6.2). At 8–13 km, the lunar frequencies exceed those for mercurian craters by a factor of two (lunar nearside) or more (lunar farside), and for most bins, the lunar farside frequencies exceed those for Mercury (Figure 6.2). At diameters >13 km, the mercurian frequencies exceed the lunar nearside frequencies (Figure 6.2).

Both Mercury and the Moon show an increase in interior melt deposit area with increasing crater diameter (Figure 6.3). There is considerable variation in melt pond areas for craters 8 to ~30 km in diameter in all three regions (Figure 6.3). The average interior melt area is 219 km^2 on Mercury, with a maximum of 6517 km^2, a minimum of 0.5 km^2, and a median area of 27 km^2. On the lunar nearside, the average melt area is 52 km^2, with a maximum of 2320 km^2, a minimum of 0.6 km^2, and a median area of 6 km^2. On the

lunar farside, the average melt area is 112 km^2, with a maximum of 6515 km^2, a minimum of 0.3 km^2, and a median area of 7 km^2. At diameters <30 km, all three study areas overlap and have a range of estimated interior melt areas that is an order of magnitude; at 8 km diameter, the melt area ranges from 0.3 km^2 to ~10 km^2, at 25 km diameter, the melt area ranges from ~5 km^2 to ~100 km^2 (Figure 6.3). For craters ≥30 km in diameter, mercurian craters contain larger areal extents of interior ponded impact melt than their lunar counterparts (Figure 6.3). The craters measured on the lunar nearside and farside display a trend of increasing melt pond area with increasing diameter but do not exhibit a separation such as that observed between the mercurian and lunar data (Figure 6.3).

When the percent of crater area covered by impact melt is calculated, melt-covered interior pond percentages are clustered between 0–20% for craters <30 km diameter (Figure 6.4). Although the mercurian and lunar craters are densely clustered between 0–10%, some mercurian and lunar farside craters have melt ponds proportional to ~20% of the crater area. At diameters ≥30 km the mercurian and lunar craters trends separate. For ≥30 km diameter, mercurian craters have greater percentages of the crater area (~15–45%) covered by impact melt than lunar craters (~3–25%; Figure 6.4).

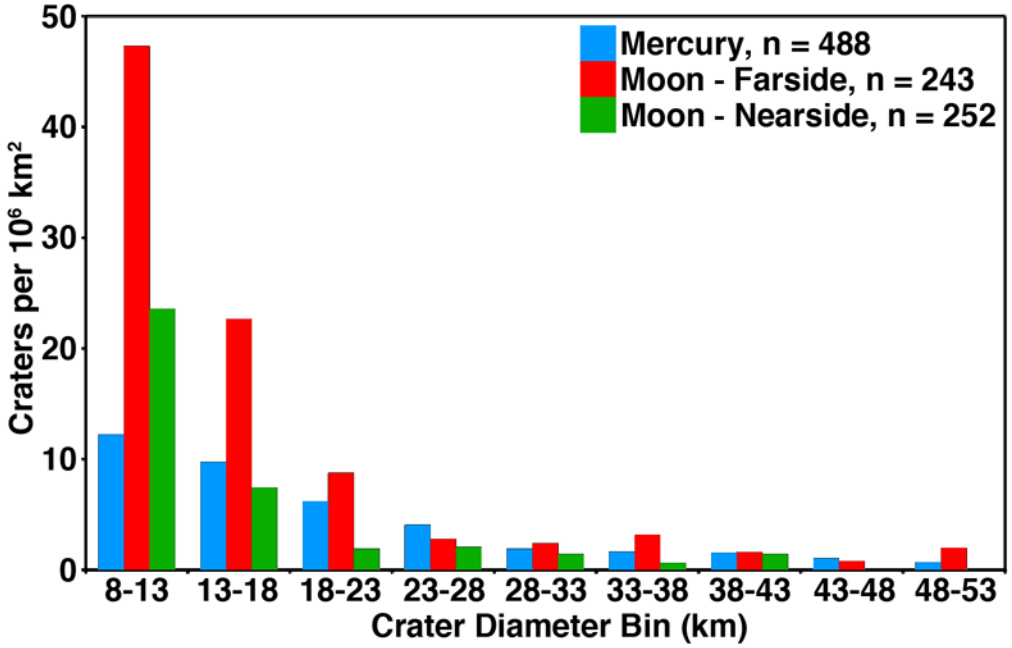

Figure 6.2. Distribution of craters with interior impact melt for 8–53 km, normalized to a unit area (10^6 km^2). In the largest bin, I measured 8 mercurian craters (normalized value is 0.69) and 5 lunar farside craters (normalized value is 1.99).

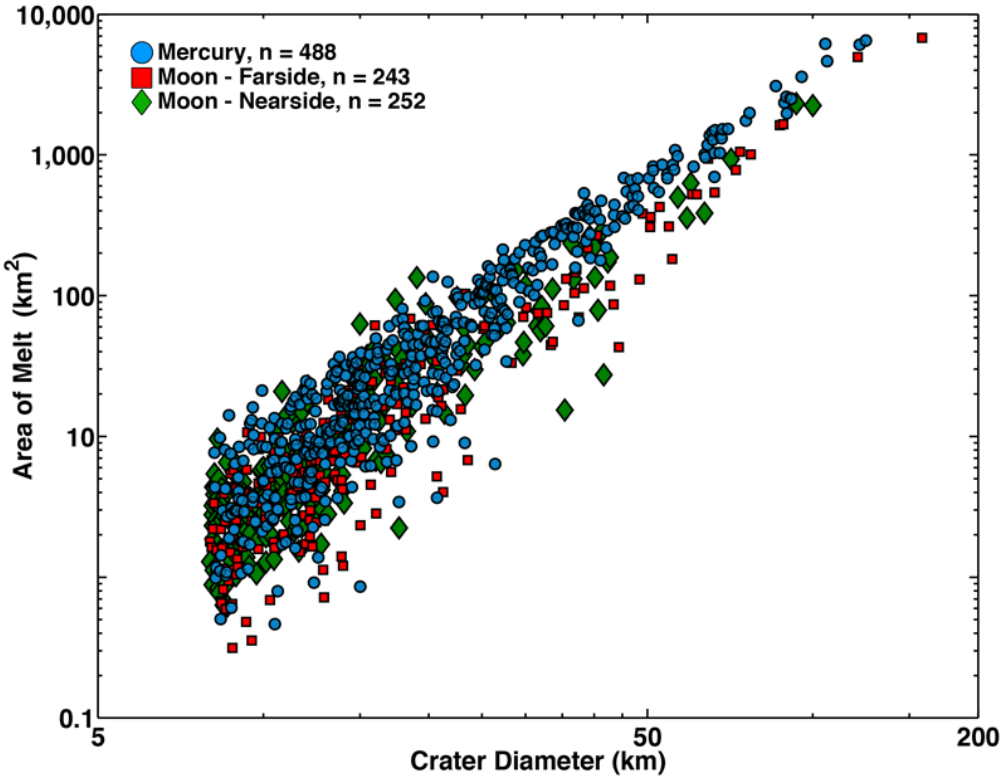

Figure 6.3. Impact melt area as a function of crater diameter for measured interior deposits. Including exterior deposits may change the distribution, especially for larger craters.

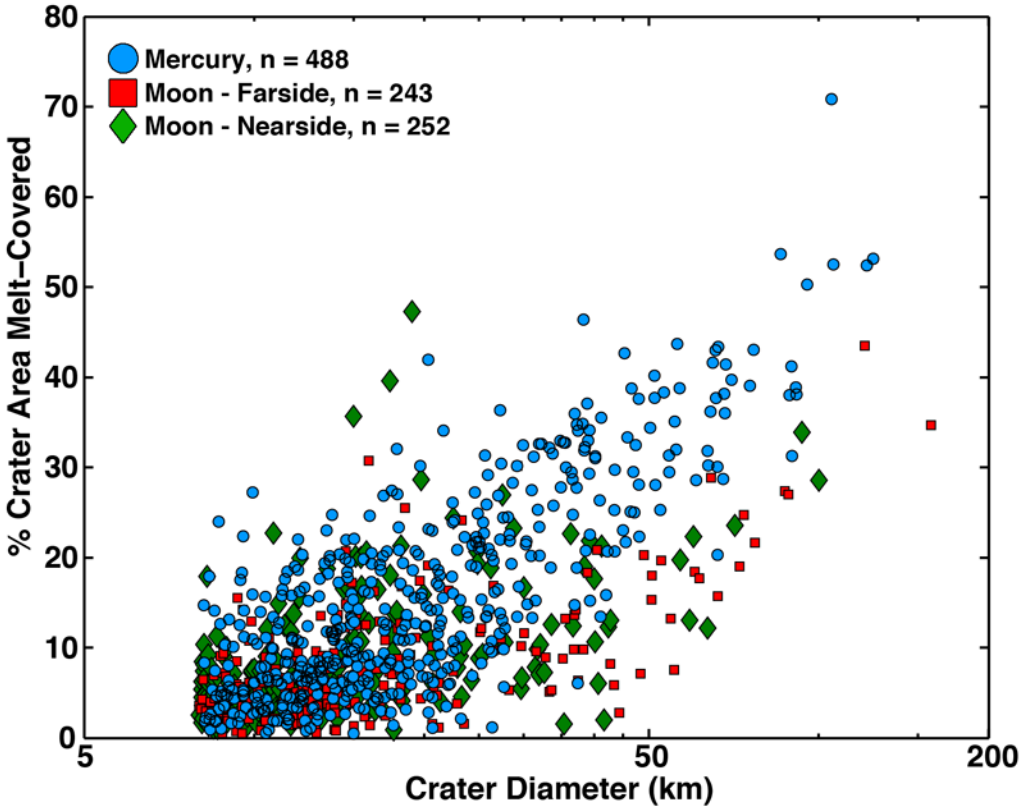

Figure 6.4. Percentage of the crater area (interior) that is covered in impact melt as a function of crater diameter. At diameters ≥30 km, mercurian craters exhibit a greater percentage of melt-covered areas than lunar craters.

6.4. Discussion

In this investigation, hundreds of craters are identified and mapped with interior impact melt deposits on Mercury and the Moon. More craters per unit area are identified with impact melt on the lunar farside than on Mercury for most crater diameter bins shown in Figure 6.2. This finding agrees with previous comparisons of global crater densities (Strom, 1977; Fassett et al., 2011; Strom et al., 2011) and is observed because the relative global impact flux on Mercury is 1.9 times that of the Moon (Cintala, 1992; Le Feuvre and Wieczorek, 2008). In this investigation, only craters interpreted to be young (Kuiperian/Mansurian on Mercury, Copernican/Eratosthenian on the Moon) on the

basis of sharp morphology were identified and mapped on Mercury and the Moon, and these results suggest that Mercury is deficient in young, impact melt-filled craters compared to the Moon. Future efforts to extend impact melt identification to older craters may provide insight, but currently an explanation for the observed deficiency remains elusive. If older crater populations on Mercury and the Moon exhibit the same relationship (deficiency in impact melt filled craters on Mercury relative to the Moon), it may be that resurfacing (e.g., volcanism, basin ejecta emplacement) removed an unknown portion of the global population of older craters with impact melt on Mercury.

Observations of lunar craters suggest a relationship between the impact melting process and crater morphology (e.g., Cintala and Grieve, 1998a; 1998b), which may explain the trends in the measured areal extents of interior impact melt (Figure 6.3, 6.4). A range of size-dependent morphologies were first identified and described for lunar craters (e.g., Shoemaker, 1962; 1971; Howard, 1974; Pike, 1977; Melosh, 1989), and the progression of crater morphologies with size are also observed and well-studied on Mercury (e.g., Gault et al., 1975; Oberbeck et al., 1977; Pike, 1988; Xiao et al., accepted). Morphologic descriptions and observations of impact melt for lunar craters are presented below, along with a discussion of my observations and examples of lunar impact melt. Simple craters (usually <15 km diameter) have a distinct bowl-shape, are parabolic to trapezoidal in profile, and may have a flat floor with blocky debris (Figure 6.5; e.g., Howard, 1974; Pike, 1977; Melosh, 1989). Impact melt observed in simple craters usually occurs as veneers covering most of the floor and on portions of the rim (Howard and Wilshire, 1975; Hawke and Head, 1977b); external melt flows and interior melt ponds are rare (Howard and Wilshire, 1975; Hawke and Head, 1977a; 1977b).

Therefore for craters <15 km, substantial ponded interior impact melt would not be expected and are, indeed, not generally observed in the measurements of melt pond areal extent (Figure 6.3). The range in distribution of measured pond areas reflects differences in melt produced (perhaps as a result of differences in target material) or potential measurement uncertainties (misidentification of eroded debris that appear smooth at the 200 meter pixel scale resolution or a 2–3 pixel analyst error in mapping). Transitional craters (usually 15–20 km diameter) exhibit some simple crater structures while beginning to develop features observed in complex craters such as crater wall terracing and central peaks (Figure 6.6; e.g., Howard, 1974; Melosh, 1989). Impact melt in transitional craters is observed as veneers and occasional ponds on the rim, and coalesced channels and flows terminate at ponds on the crater floor or perched on the poorly-formed wall terraces (Howard and Wilshire, 1975; Hawke and Head, 1977b). The increase in predicted impact melt volume is observed as increasing melt pond areas as diameter increases (Figure 6.3). The fairly broad range in mapped melt pond areas primarily reflects differences in melt produced for these craters, which may experience small- to large-scale wall slumping that can modify or bury interior impact melt ponds. Complex craters (usually >20 km diameter) have distinct terraced crater walls and a central peak or central peak cluster (Figure 6.1, 6.7; e.g., Howard, 1974; Hale and Head, 1979; Melosh, 1989). Impact melt is present at all scales in complex craters: thin veneers coating the continuous ejecta, flows and coalesced ponds exterior to the crater and on the crater rim, and ponds on the wall terraces and crater floor (e.g., Howard and Wilshire, 1975; Hawke and Head, 1977b). At diameters ≥30 km, the lunar and mercurian data separate and no distinction is observed between lunar nearside and farside measurements

(Figure 6.3). Mercurian craters have greater areal extents of impact melt when compared to lunar craters at the same sizes, verifying previous visual observations (e.g., Howard, 1974; Howard and Wilshire, 1975; Hawke and Head, 1977a). Furthermore, these findings confirm the results of calculations that predict greater volumes of melt relative to crater volume and more retained melt in crater interiors for increasing crater sizes (e.g., Gault et al., 1975; Cintala, 1992; Grieve and Cintala, 1992; 1997; Pierazzo et al., 1997; Cintala and Grieve, 1998a; 1998b; Barr and Citron, 2011).

Conversely, smaller craters (<30 km diameter) have a larger range of melt pond areas (Figure 6.3, 6.4). The measured impact melt pond areas for mercurian and lunar craters overlap in the 8–30 km diameter region, indicating that there is not an obvious distinction between lunar and mercurian craters at these diameters. These results are consistent with calculations that predict smaller volumes of melt at smaller crater diameters, where the volume of melt produced scales as a function of transient crater diameters (Cintala and Grieve, 1998a; 1998b). The volume of melt generated during impact is primarily a function of impact velocity, but the projectile density and size as well as the target density will influence the amount of melt produced for a given impact velocity (e.g., Grieve and Cintala, 1992). Thus, the range in measured impact melt pond areas for diameters 8–30 km likely result from a combination of several of these factors (e.g., melt pond area for a 10 km diameter crater is expected to differ for impact into a lunar nearside basalt compared to a lunar farside anorthosite). Flow features and ponded deposits are not commonly observed within simple crater interiors (Hawke and Head, 1977b), implying that impact melt within small craters (<10–15 km diameter) solidified relatively quickly. Veneers are observed on the walls smaller craters (<10–15 km

diameter; Hawke and Head, 1977a; 1977b), as are low-reflectance rays crossing crater walls and rims that are interpreted as sprays of solidified, glassy (melt-rich) ejecta (Howard, 1974). The floors of simple and transitional craters are often chaotic, and burial or mixture of impact melt with debris slumped from the crater walls may explain the varying measurements of interior impact melt pond area. Moreover, for smaller craters there is a greater opportunity for the entire volume of impact melt to interact with clastic debris in the crater cavity. If a thin layer of impact melt incorporated debris from the crater wall, the incorporation of debris would rapidly cool the impact melt. Depending on the volume of melt produced and the amount of entrained debris, the resulting deposit (melt plus clasts) may not morphologically resemble other instances of identified impact melt. Incorporating high-resolution LROC and MESSENGER NAC images to examine and map detailed impact melt morphology is necessary to continue this investigation, particularly for craters <30 km in diameter.

Interpreting crater morphology and observations of impact melt with respect to crater size for Mercury or the Moon, followed by comparisons between the two planets, requires additional calculations of impact melting and inclusion of crater scaling relationships (O'Keefe and Ahrens, 1977; Holsapple and Schmidt, 1982; Croft, 1985; Cintala, 1992; Grieve and Cintala, 1992; Holsapple, 1993; O'Keefe and Ahrens, 1993; Grieve and Cintala, 1997; Pierazzo et al., 1997; Cintala and Grieve, 1998a; 1998b; Barr and Citron, 2011). Crater scaling uses mathematical equations to derive quantitative relations for specific parameters (i.e., balancing equations of mass, momentum, and energy) and is necessary to investigations of the impact cratering process at a planetary scale (e.g., Holsapple, 1993). To continue this investigation, relations between impact

melt volume and transient crater cavity diameter are fundamental (e.g., O'Keefe and Ahrens, 1977; Holsapple and Schmidt, 1987; Grieve and Cintala, 1992; O'Keefe and Ahrens, 1993; Pierazzo et al., 1997; Cintala and Grieve, 1998a; 1998b); crater scaling must be incorporated before additional interpretation of differences in impact melt distribution for Mercury and the Moon are made.

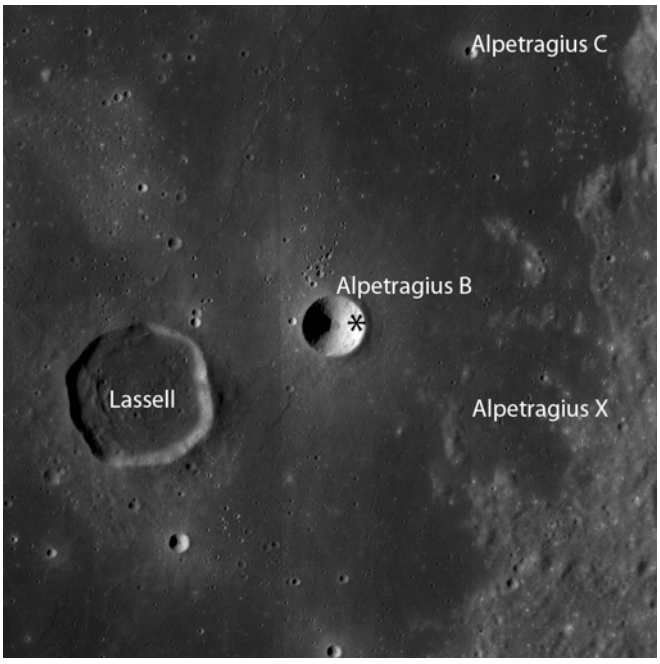

Figure 6.5. Alpetragius B, located in Mare Nubium (15.12°S, 353.25°E; ~10 km in diameter) is an example of a simple lunar crater. LROC WAC monochrome mosaic, asterisk notes granular debris flow visible in the LROC NAC Featured Image "Debris Channels" (Appendix A), image credit [NASA/GSFC/Arizona State University].

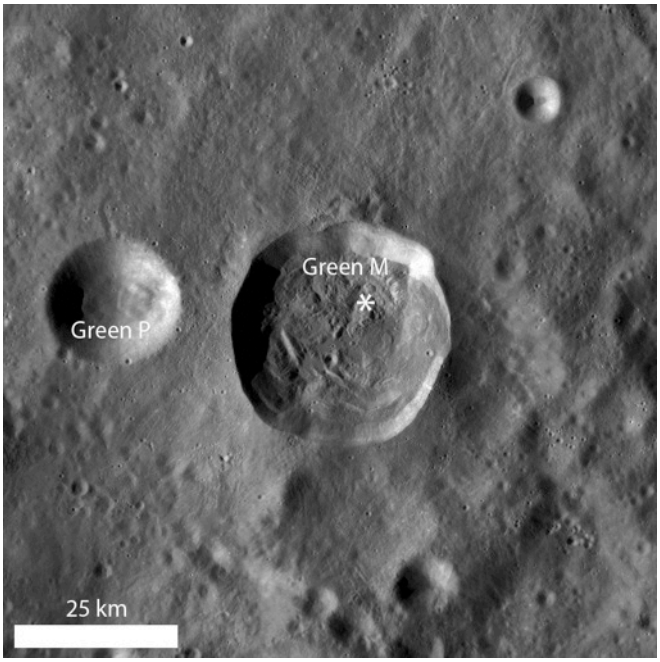

Figure 6.6. Green M, located southeast of Mendeleev crater (0.34°N, 133.12°E; ~35 km in diameter) is an example of a larger transitional lunar crater. LROC WAC monochrome mosaic, asterisk notes eroding impact melt visible in the LROC NAC Featured Image "On the floor of Green M" (Appendix A), image credit [NASA/GSFC/Arizona State University].

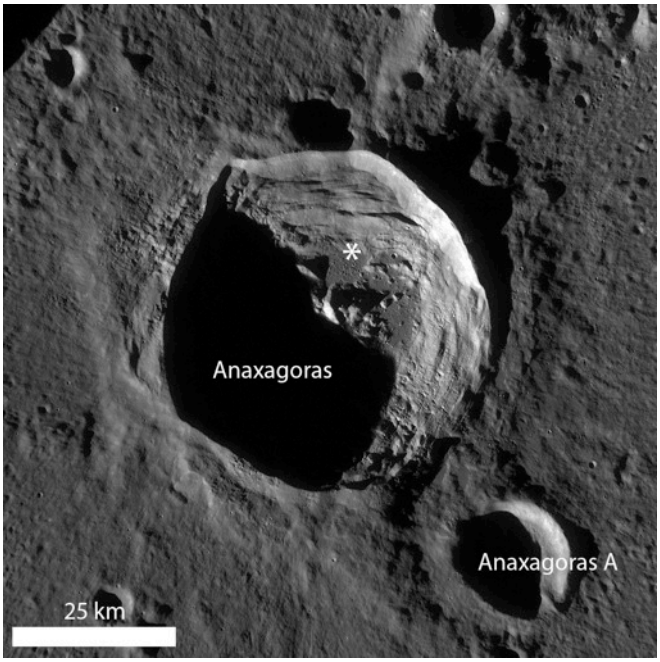

Figure 6.7. Anaxagoras crater, located on the lunar farside (73.46°N, 349.93°E; ~52 km in diameter) is an example of a complex lunar crater. LROC WAC monochrome mosaic, asterisk notes overlapping melt lobes visible in the LROC NAC Featured Image "Melt Overlap" (Appendix A), image credit [NASA/GSFC/Arizona State University].

6.5. Conclusions

This chapter presents the first exploration of how the distributions and areal extents of impact melt deposits compare between Mercury and the Moon. Utilizing new high-resolution global datasets obtained by LROC and MESSENGER, the criteria for distinguishing impact melt defined in previous studies (e.g., Howard and Wilshire, 1975; Hawke and Head, 1977a; 1977b) are revised. By examining larger regions at illuminations favorable for morphologic interpretation, impact melt deposits were identified on the basis of:

(1) Interior pond morphology (a smooth texture, few superposed craters, and a distinct fill-wall contact),

(2) Presence of exterior flows, ponds, and veneers, and

(3) Absence of embayed craters within the crater interior (indicating passage of time between crater formation and infill, consistent with subsequent volcanism).

Applying these criteria to three regions on Mercury and the Moon, more craters per normalized unit area were identified with impact melt on the lunar farside than on Mercury, a result consistent with studies of global crater densities (Strom, 1977; Fassett et al., 2011; Strom et al., 2011) and assessments of an increased impact flux and higher impact velocities on Mercury relative to the Moon (e.g., Wetherill, 1974; Gault et al., 1975; Cintala, 1992; Le Feuvre and Wieczorek, 2008). Considering the melt-filled crater population as a proportion of the global crater population, in addition to comparison of the melt-filled crater population to other defined crater populations (e.g., volcanic-filled, stratigraphically older, and for a particular size range) may provide additional insight into

the deficiency of young craters with impact melt on Mercury compared to the Moon. Greater areal extents of impact melt were mapped for craters ≥30 km in diameter on Mercury than on the Moon. For this initial investiation, area was used as an approximation for volume, and from the areal measurements, greater volumes of melt are inferred for larger-diameter craters on Mercury than on the Moon. These findings confirm theoretical melt-generation models (e.g., O'Keefe and Ahrens, 1977; Grieve and Cintala, 1992; 1997; Pierazzo et al., 1997; Cintala and Grieve, 1998a; 1998b; Barr and Citron, 2011) that predict greater melt production for mercurian craters compared to similar sized lunar craters (due to the twice larger average impact velocity on Mercury than on the Moon). A range in areal extents of impact melt were mapped for craters 8–30 km in diameter, and mapping using high-resolution LROC and MESSENGER NAC images in an attempt to account for measured differences (e.g., burial of melt by slumping, incorporation of clasts into the melt) is required. The next step toward a quantitative comparison of impact melt volume estimates and assessment of melt-generation models is incorporation of crater scaling laws to account for planetary variables influencing the impact cratering process (Holsapple and Schmidt, 1982; Housen et al., 1983; Croft, 1985; Holsapple and Schmidt, 1987; Holsapple, 1993; O'Keefe and Ahrens, 1993).

Over the course of my two-year postdoctoral program, I will continue these investigations. By examining the areal extent and distribution of impact melt within and around craters, estimating melt volumes, and characterizing melt deposit morphologies, a global dataset will be compiled. Differential crater scaling to account for planetary differences in melt production (e.g., Cintala and Grieve, 1998a; 1998b), topography data

from orbiting laser altimeters aboard LRO and MESSENGER, and high-resolution NAC images will be incorporated into future measurements. Using quantitative measurements, this research will improve understanding of the effects of planetary variables during the impact process and can be used to test accepted melt-generation models (Cintala, 1992; Pierazzo et al., 1997; Cintala and Grieve, 1998a; 1998b; Barr and Citron, 2011).

CHAPTER 7

CONCLUDING THOUGHTS

The work presented in this dissertation contributes to understanding the impact cratering process on the terrestrial planets. Fundamental concepts related to planetary science are addressed, focusing on SCEM Science Concepts (1) The Moon reveals the inner Solar System bombardment history, (6) The Moon is ideal for investigating the impact process at the planetary scale, and (7) The Moon is ideal for investigations of regolith processes (NRC, 2007). This work also investigates key science questions posed in the Planetary Decadal Survey (2011) by using crater measurements to improve understanding of the lunar and mercurian impact records, gain insight into the impact cratering process through observations of impact melt, and investigate the history of volcanic emplacement for specific regions on Mercury and the Moon.

The effects of solar incidence angle on consistent identification and measurement of craters are investigated in **Chapter 2**. Accurate small crater (<1 km diameter) population statistics are essential for determination of relative and absolute model ages (AMAs) of younger units (e.g., Neukum et al., 1975a; Schultz et al., 1977; Hiesinger et al., 2012) and estimations of regolith depths (Quaide and Oberbeck, 1968; Shoemaker et al., 1969; Wilcox et al., 2005). My results indicate that incidence angle affects AMA determinations and equilibrium crater diameter estimates. AMAs derived for three different study regions produce different ages, even though most AMAs agree within the statistical uncertainties. Using the same or similar incidence angles to measure crater size-frequency distributions (SFDs) is ideal for work concerned with absolute age comparisons between units and will provide the most consistent results, limiting

uncertainties arising from analyst interpretation (e.g., Hiesinger et al., 2012). My results demonstrate that an optimal incidence angle range for relative and absolute age dating studies is between ~65° and 80°. Conversely, equilibrium crater diameter estimates and inferred regolith depths are significantly influenced by changes in incidence angle over the ~65°–87° range used in this investigation. I find that estimates of equilibrium crater diameter decrease with decreasing incidence angle, which is consistent with previous work (Wilcox et al., 2005). The difference in estimated equilibrium crater diameter exceeds 30 m for images taken at incidence angles over an ~20° range, and the variation in crater equilibrium diameter directly influences estimates of average regolith depth. Measurements made on images acquired at smaller incidence angles underestimate crater diameters relative to those made on images at larger incidence angles, leading to equilibrium crater diameter estimates that are too small. Even though measurements made at larger incidence angles allow a more accurate measurement of the crater diameter (the break in slope at the perceived crater rim is emphasized) and thus a more accurate equilibrium crater diameter estimate, the pronounced shadows in the larger incidence angle images hide part of the small crater population in the shadows (e.g., Moore, 1972; Soderblom, 1972; Wilcox et al., 2005). Therefore, an ~80° incidence angle image enables equilibrium crater diameter estimates that are more accurate than crater measurements made at smaller incidence angles, while mitigating shadowing observed at larger incidence angles.

Chapter 2 tests the hypothesis that incidence angle affects an analyst's ability to both detect craters and accurately measure their diameters. In this investigation, three individuals collected crater measurements of the same region from images with different

incidence angles. Crater measurements collected by a single analyst reflect measurement errors based on his or her counting technique, experience, and the inherent statistical uncertainties. Potential differences resulting from more experience can be examined in an exercise where an analyst revisits an early measurement area after gaining experience; the ideal case would be for me to recount one of the Apollo Metric images now that I have several years of experience. Comparing the measurements ("early" versus "experienced") will quantify the improvements in analyst crater counting ability and determine individual measurement error. Similarly, the data collected by multiple individuals is affected by the errors and uncertainties associated with each separate measurement. Improvements for future studies employing multiple individuals might use time limits for measurement sessions (c.f., Greeley and Gault, 1970), and sessions could be implemented at similar times each day (e.g., two hours in the morning, to be repeated for the number of days required to finish the measurement area). To better conduct statistical comparisons between analysts and their reproducibility (between one another and against themselves), a calibration image will be selected for the analyst to crater count prior to beginning the daily measurement session; the calibration image will be small, perhaps containing 20–50 craters of different sizes. This exercise will allow analyses of variations between sessions and constrain the error per individual and uncertainties between individuals (similar to the investigation by Robbins et al., 2013a; 2013b).

In **Chapter 3**, absolute model age dating and measures of areal crater density (ACD) from crater counts reveal two spatially expansive, statistically separable mare units in Mare Imbrium. The older, spectrally red eastern unit is ~3.3 Ga old, and the younger, spectrally blue western unit is ~2.2 Ga old. These ages agree with previous

assessments of relative and average absolute model ages (e.g., Schaber et al., 1975; Hiesinger et al., 2000; Bugiolacchi and Guest, 2008) but I am unable to distinguish subunits identified within the large spectral units with reported age differences of <300–500 million years (Hiesinger et al., 2000). ACD measurements also reveal that optimal crater statistics result from count areas larger than 1×10^4 km^2 in size on the mare. The age difference sensitivity of the ACD technique will be examined in future investigations of additional units within other mare regions that have strong spectral contrasts, smaller age differences, and areas exceeding 1×10^4 km^2. The regional ACD map for Mare Imbrium reveals density units that correspond with color units, showing variations between density units that correspond to a previously proposed age boundary. The ACD maps are derived from a statistical point density calculation that considers only the spatial density of crater center points, neglecting the measured crater diameters. Future work will use statistical weighting techniques (e.g., Baddeley and Turner, 2005) to incorporate crater diameters on the ACD measurement. For example, the formation of one larger crater potentially destroys numerous smaller craters, leading to a possible low ACD that does not adequately reflect the relative age of the surface (more large craters accumulate on older surfaces).

ACD measurements confirm the presence of probable non-obvious secondary craters in with diameters ≥500 m to ~2 km that may be traced to possible parent craters in **Chapter 2**. Although the lunar chronology accounts for unrecognized secondaries (e.g., Neukum et al., 1975a; Neukum et al., 1975b; Werner et al., 2009), my findings suggest that using ≥1 km diameter craters for AMA derivation limits possible inclusion of non-obvious secondaries. Future investigations pertaining to potential secondary

contamination (e.g., McEwen et al., 2005; McEwen and Bierhaus, 2006; Dundas et al., 2007; Werner et al., 2009) will examine small crater depth to diameter ratios (Pike, 1978) measured using LROC Digital Terrain Models (DTMs). Secondary craters have a shallower depth to diameter ratio than primaries at diameters <1 km (Pike, 1978); identifying the presence of non-obvious secondaries in the mare will be valuable to interpretations of ACD measurements and studies focused on refining the lunar chronology (e.g., Marchi et al., 2009; Le Feuvre and Wieczorek, 2011; Robbins, 2013). The ability to distinguish different aged units independent of spectral data has implications for application of this technique to Mercury, where smooth plains units do not have observable spectral variation (**Chapter 4**).

In **Chapter 4**, the comprehensive cratering history of the mercurian north polar region (NPR) is placed into context with other smooth plains and heavily cratered terrain (HCT). The NPR contains ~7% of the total area of smooth plains on Mercury, and measures of crater frequencies indicate that the northern smooth plains (NSP) are comparable in age to the other regions of smooth plains, including the Caloris smooth plains, the Rudaki plains, plains south of Rachmaninoff, and plains within Beethoven and Rembrandt basins (Denevi et al., 2013a). Within the NSP are two crater populations, those superposed on the NSP ("post-plains") and those partially to entirely embayed ("buried"). The presence of both populations provides evidence for volcanic resurfacing. The post-plains crater population reveals that the NSP do not exhibit statistically distinguishable crater SFD subunits, nor do measures of ACD reveal volcanically resurfaced regions within the NSP. These results suggest that either the most recent outpouring of volcanic material resurfaced the majority of the region and/or volcanic

flooding to form the NSP occurred over a short geologic time. A short timescale of emplacement is further supported by the absence of kinks in the crater SFDs (characteristic to volcanic resurfacing; e.g., Neukum and Horn, 1976) for both the post-plains and buried crater populations. The buried crater population indicates volcanic flooding of originally HCT to form the NSP. Stratigraphic embayment relationships within the buried crater population, including partial crater flooding and the presence of smaller embayed craters within the filled interiors of larger craters and basins, indicate that a minimum of two episodes of resurfacing occurred. From embayed crater rim height measurements, I estimate the NSP to be regionally 0.73–1.76 km thick, with a minimum volume of volcanic material of 4.08–9.84 × 10^6 km^3. AMAs for the NSP range from ~3.7–2.5 Ga old, a span of 1.2 Ga, depending on the chronology applied.

In **Chapter 5**, vertical and horizontal shaking experiments were conducted in a laboratory setting to simulate the effects of seismic shaking on a regolith mixture. Under vertical and horizontal perturbation, the denser materials sank into the less dense matrix material, even when the density differences were small and when the denser particles were smaller than those of the matrix. Completed under terrestrial conditions, the experimental results are nonetheless relevant for interpreting remotely sensed data of other planetary surfaces. The different densities of minerals may promote density- and size-driven mechanical sorting in planetary regoliths that may explain differences in TiO_2 abundances for some regions estimated by Clementine spectral reflectance (CSR) and Lunar Prospector Gamma Ray Spectrometer (LP GRS) measurements.

Returned lunar regolith samples have a variety of grain sizes, compositions, and densities (e.g., Papike et al., 1982). However, the lunar sample suite is compositionally

limited with respect to TiO_2, and the absence of samples with moderate titanium abundances (e.g., Blewett et al., 1997; Giguere et al., 2000; Gillis et al., 2003) may significantly influence the calibrations of CSR algorithms (Lucey et al., 1995; Blewett et al., 1997; Lucey et al., 1998; 2000) and the assumptions applied to calibrate a spectral mixing model used to analyze LP GRS data (e.g., Lawrence et al., 2004; Prettyman et al., 2006). Therefore, until additional samples encompassing the range of titanium abundances predicted by CSR and LP GRS are obtained, the accuracy of the abundance estimates may not be further evaluated. A collimated gamma ray spectrometer with a native spatial footprint of less than ~45 km selected as an instrument on a future lunar lander mission is another option to provide ground truth elemental abundance in lieu of samples (e.g., Lawrence et al., 2004; Prettyman et al., 2006). The primary shortcoming of LP GRS elemental abundances is the large spatial footprint (2° pixel scale or 60 km pixel scale at the equator) that allows for contamination in some regions from highland components and limits detection of spatially limited mare units (e.g., Mare Frigoris).

Future experimental investigations of seismic shaking investigations of density- and size-driven sorting would benefit from shaking tables with variable amplitudes, frequencies, and motion. Simulations of lunar-like seismic events would be improved by assigning the setup to approximate moonquakes and impact events, based on amplitudes and frequencies obtained from Apollo seismic experiments. Employing vertical and horizontal motion during a single experiment would more realistically simulate a planetary surface affected by seismic shaking. In addition to experimental modifications, incorporating numerical models is a logical next step toward scaling experimental results to a planetary scale (e.g., Asphaug et al., 1996; Richardson et al., 2005).

In **Chapter 6**, initial results of a comparative impact melt investigation for Mercury and the Moon are presented. Impact melt-generation models (e.g., Cintala and Grieve, 1998a; 1998b) predict that for similar sizes, craters on Mercury should produce greater volumes of impact melt due to the greater impact velocities than on the Moon (e.g., Gault et al., 1975). However, previous workers were unable to quantitatively test these predictions due to the available data, but LRO and MESSENGER facilitate acquisition of comprehensive measurements to test these theoretical models. Craters 8–200 km in diameter with ponded impact melt deposits were identified, the interior extents of melt deposits were mapped, and melt pond area was calculated as a proxy for volume. For craters ≥30 km in diameter, mercurian craters contain larger areal extents of interior ponded impact melt than their lunar counterparts, findings consistent with the theoretical models (e.g., Grieve and Cintala, 1992; 1997; Pierazzo et al., 1997; Cintala and Grieve, 1998a; 1998b). Further quantitative comparison to melt-generation models necessitates volume estimates, which will be derived from depth to diameter relationships (Pike, 1988; Barnouin et al., 2012) and topography from both DTMs and laser altimeter measurements from the Lunar Orbiter Laser Altimeter and Mercury Laser Altimeter (e.g., Barnouin et al., 2010; 2012). Crater scaling laws (e.g., Croft, 1985; Holsapple, 1993) must also be applied to account for planetary-specific variables (e.g., gravity, target and projectile strengths, target and projectile densities, impact velocity).

The focus of my postdoctoral research in the NASA Postdoctoral Program is continuing the work presented in **Chapter 6**. Over the course of two years I will (1) Compile a global catalog of craters 8 to 200 km in diameter with smooth infill deposits on the Moon and Mercury and then classify the deposits as “impact melt”,

"volcanic", or "other", (2) Compare the spatial extents of melt deposits and estimate volumes, and (3) Complete a quantitative morphologic analysis of impact melt deposits. This expanded investigation will facilitate the compilation of a global dataset to improve understanding of the effects of planetary variables during the impact process and will be instrumental in testing accepted melt-generation models (e.g., Grieve and Cintala, 1997; Pierazzo et al., 1997; Cintala and Grieve, 1998a; 1998b; Barr and Citron, 2011) using quantitative measurements.

REFERENCES

Arthur, D.W.G., Agnieray, A.P., Horvath, R.A., Wood, C.A., Chapman, C.R., 1963. No. 30. The System of Lunar Craters, Quadrant I. Communications of the Lunar and Planetary Laboratory 2, 71–78.

Asphaug, E., King, P.J., Swift, M.R., Merrifield, M.R., 2001. Brazil Nuts on Eros: Size-Sorting of Asteroid Regolith. Lunar Planet. Sci. Conf. 32, 1708.

Asphaug, E., Melosh, H.J., 1993. The Stickney Impact of Phobos: A Dynamical Model. Icarus 101, 144–164.

Asphaug, E., Moore, J.M., Morrison, D., Benz, W., Nolan, M.C., Sullivan, R.J., 1996. Mechanical and Geological Effects of Impact Cratering on Ida. Icarus 120, 158–184.

Baddeley, A., Turner, R., 2005. spatstat: An R Package for Analyzing Spatial Point Patterns. Journal of Statistical Software 12, 1–42.

Baker, D.M.H., Head, J.W., Schon, S.C., Ernst, C.M., Prockter, L.M., Murchie, S.L., Denevi, B.W., Solomon, S.C., Strom, R.G., 2011. The transition from complex crater to peak-ring basin on Mercury: New observations from MESSENGER flyby data and constraints on basin formation models. Planet. Space Sci. 59, 1932–1948.

Balcerski, J.A., Hauck, S.A., Sun, P., Klimczak, C., Byrne, P.K., Dombard, A.J., Barnouin, O.S., Zuber, M.T., Phillips, R.J., Solomon, S.C., 2012. Tilted Crater Floors: Recording the History of Mercury's Long-Wavelength Deformation. Lunar Planet. Sci. Conf. 43, abstract 1850.

Baldwin, R.B., 1964. Lunar Crater Counts. Astron. J. 69, 377–392.

Baldwin, R.B., 1969. Absolute Ages of Lunar Maria and Large Craters. Icarus 11, 320–331.

Baldwin, R.B., 1971. On the History of Lunar Impact Cratering: The Absolute Time Scale and the Origin of Planetesimals. Icarus 14, 36–52.

Baldwin, R.B., 1985. Relative and Absolute Ages of Individual Craters and the Rate of Infalls on the Moon in the Post-Imbrium Period. Icarus 61, 63–91.

Barnouin, O.S., Seelos, K.D., McGovern, A., Denevi, B.W., Zuber, M.T., Smith, D.E., Robinson, M.S., Neumann, G.A., Mazarico, E.M., Torrence, M.H., 2010. Impact melt volume estimates in small-to-medium sized craters on the Moon from the Lunar Orbiter Laser Altimeter (LOLA) and Lunar Reconnaissance Orbiter Camera (LROC). American Geophysical Union Fall Meeting 2010, abstract P53C-1540.

Barnouin, O.S., Zuber, M.T., Smith, D.E., Neumann, G.A., Herrick, R.R., Chappelow, J.E., Murchie, S.L., Prockter, L.M., 2012. The morphology of craters on Mercury: Results from MESSENGER flybys. Icarus 219, 414–427.

Barr, A.C., Citron, R.I., 2011. Scaling of melt production in hypervelocity impacts from high-resolution numerical simulations. Icarus 211, 913–916.

Basaltic Volcanism Study Project, 1981. Basaltic Volcanism on the Terrestrial Planets. Basaltic Volcanism on the Terrestrial Planets. Pergamon Press. 1286 p.

Basu, A., Griffiths, S.A., McKay, D.S., Nace, G., 1980. Petrography of lunar soil 15601. Proc. Lunar Plan. Sci. Conf. 11th, 1727–1741.

Belton, M.J.S., Head, J.W., Pieters, C.M., Greeley, R., McEwen, A.S., Neukum, G., Klaasen, K.P., Anger, C.D., Carr, M.H., Chapman, C.R., 1992. Lunar Impact Basins and Crustal Heterogeneity: New Western Limb and Far Side Data from Galileo. Science 255, 570–576.

Benoit, P.H., Hagedorn, N.L., Kracher, A., Sears, D.W.G., White, J., 2003. Grain Size and Density Separation on Asteroids: Comparison of Seismic Shaking and Fluidization. Lunar Planet. Sci. Conf. 34, abstract 1033.

Blewett, D.T., Lucey, P.G., Hawke, B.R., Jolliff, B.L., 1997. Clementine images of the lunar sample-return stations: Refinement of FeO and TiO_2 mapping techniques. J. Geophys. Res. 102, 16319–16325.

Boyce, J.M., 1976. Ages of flow units in the lunar nearside maria based on Lunar Orbiter IV photographs. Proc. Lunar Sci. Conf. 7th, 2717–2728.

Boyce, J.M., Dial, A.L., Jr., 1975. Relative ages of flow units in Mare Imbrium and Sinus Iridum. Proc. Lunar Sci. Conf. 6th, 2585–2595.

Boyce, J.M., Dial, A.L., Jr., Soderblom, L.A., 1974. Ages of the lunar nearside light plains and maria. Proc. Lunar Sci. Conf. 5th, 11–23.

Breu, A.P.J., Ensner, H.-M., Kruelle, C., Rehberg, I., 2003. Reversing the Brazil-Nut Effect: Competition between Percolation and Condensation. Phys. Rev. Lett. 90, 014302.

Bridgwater, J., 1976. Fundamental Powder Mixing Mechanisms. Powder Technol. 15, 215–236.

Bugiolacchi, R., Guest, J.E., 2008. Compositional and temporal investigation of exposed lunar basalts in the Mare Imbrium region. Icarus 197, 1–18.

Burtally, N., King, P.J., Swift, M.R., 2002. Spontaneous Air-Driven Separation in Vertically Vibrated Fine Granular Mixtures. Science 295, 1877–1880.

Burtally, N., King, P.J., Swift, M.R., Leaper, M., 2003. Dynamical behaviour of fine granular glass/bronze mixtures under vertical vibration. Granular Matter 5, 57–66.

Byrne, P.K., Klimczak, C., Williams, D.A., Hurwitz, D.M., Solomon, S.C., Head, J.W., Preusker, F., Oberst, J., 2013. An assemblage of lava flow features on Mercury. J. Geophys. Res. 118, 1–20.

Carr, M.H., 1965. Geologic map and section of the Timocharis region of the Moon. U.S. Geol. Surv. Map I–462 (LAC–40).

Carr, M.H., Kirk, R.L., McEwen, A.S., Veverka, J., Thomas, P., Head, J.W., Murchie, S., 1994. The Geology of Gaspra. Icarus 107, 61–71.

Carrier, W.D., Bromwell, L.G., Martin, R.T., 1972. Strength and compressibility of returned lunar soil. Proc. Lunar Sci. Conf. 3rd, 3223–3234.

Carrier, W.D., Mitchell, J.K., Mahmood, A., 1973. The relative density of lunar soil. Proc. Lunar Sci. Conf. 4th, 2403–2411.

Chapman, C.R., McKinnon, W., 1986. Cratering of planetary satellites, in: Burns, J.A., Matthews, M.S. (Eds.), Satellites. The University of Arizona Press, Tucson, pp. 492–580.

Charette, M.P., McCord, T.B., Pieters, C., Adams, J.B., 1974. Application of Remote Spectral Reflectance Measurements to Lunar Geology Classification and Determination of Titanium Content of Lunar Soils. J. Geophys. Res. 79, 1605–1613.

Cheng, A.F., Izenberg, N., Chapman, C.R., Zuber, M.T., 2002. Ponded deposits on asteroid 433 Eros. Meteorit. Planet. Sci. 37, 1095–1105.

Ciamarra, M., Vizia, M., Fierro, A., Tarzia, M., Coniglio, A., Nicodemi, M., 2006. Granular Species Segregation under Vertical Tapping: Effects of Size, Density, Friction, and Shaking Amplitude. Phys. Rev. Lett. 96, 058001.

Cintala, M.J., 1992. Impact-Induced Thermal Effects in the Lunar and Mercurian Regoliths. J. Geophys. Res. 97, 947–973.

Cintala, M.J., Grieve, R.A.F., 1998a. Scaling impact-melt and crater dimensions: Implications for the lunar cratering record. Meteorit. Planet. Sci. 33, 889–912.

Cintala, M.J., Grieve, R.A.F., 1998b. Erratum: Scaling impact melting and crater dimensions: Implications for the lunar cratering record. Meteorit. Planet. Sci. 33, 1343.

Cintala, M.J., Head, J.W., Veverka, J., 1978. Characteristics of the cratering process on small satellites and asteroids. Proc. Lunar Plan. Sci. Conf. 9th, 3803–3830.

Coffin, M.F., Eldholm, O., 1994. Large igneous provinces: crustal structure, dimensions, and external consequences. Rev. Geophys. 32, 1–36.

Committee on the Planetary Science Decadal Survey, 2011. Vision and Voyages for Planetary Science in the Decade 2013-2022. The National Academies Press. 382 p.

Committee on the Scientific Context for Exploration of the Moon National Research Council, 2007. The Scientific Context for Exploration of the Moon: Final Report. The National Academies Press. 107 p.

Crater Analysis Techniques Working Group, 1979. Standard Techniques for Presentation and Analysis of Crater Size-Frequency Data. Icarus 37, 467–474.

Croft, S.K., 1985. The Scaling of Complex Craters. J. Geophys. Res. 90, C828–C842.

Danielson, G.E., Klaasen, K.P., Anderson, J.L., 1975. Acquisition and Description of Mariner 10 Television Science Data at Mercury. J. Geophys. Res. 80, 2357–2393.

Davies, M.E., Colvin, T.R., 2000. Lunar coordinates in the regions of the Apollo landers. J. Geophys. Res. 105, 20277–20280.

Davis, J.C., 2002. Statistics and Data Analysis in Geology, 3rd ed. John Wiley & Sons, Inc., New York. 638 p.

Deer, W.A., Howie, R.A., Zussman, J., 1966. An introduction to rock-forming minerals, 1st ed. John Wiley & Sons, Inc. 525 p.

De Hon, R.A., 1974. Thickness of mare material in the Tranquillitatis and Nectaris basins. Proc. Lunar Sci. Conf. 5th, 53–59.

Denevi, B.W., Ernst, C.M., Meyer, H.M., Robinson, M.S., Murchie, S.L., Whitten, J.L., Head, J.W., Watters, T.R., Solomon, S.C., Ostrach, L.R., Chapman, C.R., Byrne, P.K., Klimczak, C., Peplowski, P.N., 2013a. The distribution and origin of smooth plains on Mercury. J. Geophys. Res. 118, 1–17.

Denevi, B.W., Ernst, C.M., Whitten, J.L., Head, J.W., Murchie, S.L., Watters, T.R., Byrne, P.K., Blewett, D.T., Solomon, S.C., Fassett, C.I., 2013b. The Volcanic Origin of a Region of Intercrater Plains on Mercury. Lunar Planet. Sci. Conf. 44, abstract 1218.

Denevi, B.W., Robinson, M.S., Solomon, S.C., Murchie, S.L., Blewett, D.T., Domingue, D.L., McCoy, T.J., Ernst, C.M., Head, J.W., Watters, T.R., Chabot, N.L., 2009. The Evolution of Mercury's Crust: A Global Perspective from MESSENGER. Science 324, 613–618.

Devillard, P., 1990. Scaling behaviour in size segregation (“Brazil Nuts”). J. Phys. France 51, 369–373.

Devine, J.M., McKay, D.S., Papike, J.J., 1982. Lunar Regolith: Petrology of the <10 μm Fraction. J. Geophys. Res. 87, A260–A268.

Domingue, D.L., Murchie, S.L., Denevi, B.W., Chabot, N.L., 2013. MESSENGER’s Mercury Global Color Mosaic: Photometric Update. Lunar Planet. Sci. Conf. 44, abstract 1324.

Dorman, J., Evans, S., Nakamura, Y., Latham, G., 1978. On the time-varying properties of the lunar seismic meteoroid population. Lunar Planet. Sci. Conf. 9th, 3615–3626.

Dundas, C.M., McEwen, A.S., 2007. Rays and secondary craters of Tycho. Icarus 186, 31–40.

Duran, J., Jullien, R., 1998. Attractive Forces in a Granular Cocktail. Phys. Rev. Lett. 80, 3547–3550.

El-Baz, F., 1972. King Crater and Its Environs. In: Apollo 16 Preliminary Science Report, NASA SP-315, 29–62 to 29–70.

Elphic, R.C., Lawrence, D.J., Feldman, W.C., Barraclough, B.L., Gasnault, O.M., Maurice, S., Lucey, P.G., Blewett, D.T., Binder, A.B., 2002. Lunar Prospector neutron spectrometer constraints on TiO_2. J. Geophys. Res. 107, 5024.

Elphic, R.C., Lawrence, D.J., Feldman, W.C., Barraclough, B.L., Maurice, S., Binder, A.B., Lucey, P.G., 1998. Lunar Fe and Ti Abundances: Comparison of Lunar Prospector and Clementine Data. Science 281, 1493–1496.

Elphic, R.C., Lawrence, D.J., Feldman, W.C., Barraclough, B.L., Maurice, S., Binder, A.B., Lucey, P.G., 2000. Lunar rare earth element distribution and ramifications for FeO and TiO_2: Lunar Prospector neutron spectrometer observations. J. Geophys. Res. 105, 20333–20346.

Ernst, C.M., Murchie, S.L., Barnouin, O.S., Robinson, M.S., Denevi, B.W., Blewett, D.T., Head, J.W., Izenberg, N.R., Solomon, S.C., Roberts, J.H., 2010. Exposure of spectrally distinct material by impact craters on Mercury: Implications for global stratigraphy. Icarus 209, 210–223.

Fassett, C.I., Head, J.W., Baker, D.M.H., Zuber, M.T., Smith, D.E., Neumann, G.A., Solomon, S.C., Klimczak, C., Strom, R.G., Chapman, C.R., Prockter, L.M., Phillips, R.J., Oberst, J., Preusker, F., 2012. Large impact basins on Mercury: Global distribution, characteristics, and modification history from MESSENGER orbital data. J. Geophys. Res. 117, E00L08.

Fassett, C.I., Head, J.W., Blewett, D.T., Chapman, C.R., Dickson, J.L., Murchie, S.L., Solomon, S.C., Watters, T.R., 2009. Caloris impact basin: Exterior geomorphology, stratigraphy, morphometry, radial sculpture, and smooth plains deposits. Earth Planet. Sci. Lett. 285, 297–308.

Fassett, C.I., Kadish, S.J., Head, J.W., Solomon, S.C., Strom, R.G., 2011. The global population of large craters on Mercury and comparison with the Moon. Geophys. Res. Lett. 38, L10202.

Feldman, W.C., Ahola, K., Barraclough, B.L., Belian, R.D., Black, R.K., Elphic, R.C., Everett, D.T., Fuller, K.R., Kroesche, J., Lawrence, D.J., Lawson, S.L., Longmire, J.L., Maurice, S., Miller, M.C., Prettyman, T.H., Storms, S.A., Thornton, G.W., 2004. Gamma-Ray, Neutron, and Alpha-Particle Spectrometers for the Lunar Prospector mission. J. Geophys. Res. 109.

Feldman, W.C., Barraclough, B.L., Fuller, K.R., Lawrence, D.J., Maurice, S., Miller, M.C., Prettyman, T.H., Binder, A.B., 1999. The Lunar Prospector gamma-ray and neutron spectrometers. Nucl. Instrum. Methods Phys. Res., Sect. A 422, 562–566.

Feldman, W.C., Binder, A.B., Hubbard, G.S., McMurry, R.E.J., Miller, M.C., Prettyman, T.H., 1996. The Lunar Prospector Gamma-Ray Spectrometer. Lunar Planet. Sci. Conf. 27, 355–356.

Freed, A.M., Blair, D.M., Watters, T.R., Klimczak, C., Byrne, P.K., Solomon, S.C., Zuber, M.T., Melosh, H.J., 2012. On the origin of graben and ridges within and near volcanically buried craters and basins in Mercury's northern plains. J. Geophys. Res. 117, E00L06.

French, B.M., 1998. Traces of catastrophe: A Handbook of Shock-Metamorphic Effects in Terrestrial Meteorite Impact Structures. Technical Report, LPI Contribution 954. 120 p.

Gallas, J.A.C., Herrmann, H.J., Sokołowski, S., 1992. Convection Cells in Vibrating Granular Media. Phys. Rev. Lett. 69, 1371–1374.

Gault, D.E., 1970. Saturation and equilibrium conditions for impact cratering on the lunar surface: Criteria and implications. Radio Sci. 5, 273–291.

Gault, D.E., Cassen, P., Burns, J.A., Strom, R.G., 1977. Mercury. Annu. Rev. Astron. Astrophys. 15, 97–126.

Gault, D.E., Guest, J.E., Murray, J.B., Dzurisin, D., Malin, M.C., 1975. Some Comparisons of Impact Craters on Mercury and the Moon. J. Geophys. Res. 80, 2444–2460.

Gault, D.E., Hörz, F., Brownlee, D.E., Hartung, J.B., 1974. Mixing of the lunar regolith. Proc. Lunar Sci. Conf. 5th, 2365–2386.

Giguere, T.A., Taylor, G.J., Hawke, B.R., Lucey, P.G., 2000. The titanium contents of lunar mare basalts. Meteorit. Planet. Sci. 35, 193–200.

Gillis, J.J., Jolliff, B.L., Elphic, R.C., 2003. A revised algorithm for calculating TiO_2 from Clementine UVVIS data: A synthesis of rock, soil, and remotely sensed TiO_2 concentrations. J. Geophys. Res. 108, 5009.

Goreaud, F., Pélissier, R., 1999. On explicit formulas of edge effect correction for Ripley's *K*–function. Journal of Vegetation Science 10, 433–438.

Goudge, T.A., Head, J.W., Kerber, L.A., Blewett, D.T., Denevi, B.W., Murchie, S.L., Izenberg, N.R., McClintock, W.E., Holsclaw, G.M., Domingue, D.L., Gillis-Davis, J.J., Xiao, Z., Strom, R.G., Helbert, J., Solomon, S.C., 2012. Global Inventory and Characterization of Pyroclastic Deposits on Mercury: New Insights into Pyroclastic Activity from MESSENGER Orbital Data. Lunar Planet. Sci. Conf. 43, abstract 1325.

Greeley, R., 1994. Planetary Landscapes, 2nd ed. Chapman and Hall, New York, NY. 288 p.

Greeley, R., Gault, D.E., 1970. Precision Size-Frequency Distributions of Craters for 12 Selected Areas of the Lunar Surface. The Moon 2, 10–77.

Greenberg, R., Bottke, W.F., Nolan, M., Geissler, P., Petit, J.-M., Durda, D.D., Asphaug, E., Head, J., 1996. Collisional and Dynamical History of Ida. Icarus 120, 106–118.

Grieve, R.A.F., Cintala, M.J., 1992. An analysis of differential impact melt-crater scaling and implications for the terrestrial impact record. Meteoritics 27, 526–538.

Grieve, R.A.F., Cintala, M.J., 1997. Planetary Differences in Impact Melting. Adv. Space Res. 20, 1551–1560.

Guest, J.E., Gault, D.E., 1976. Crater populations in the early history of Mercury. Geophys. Res. Lett. 3, 121–123.

Guest, J.E., O'Donnell, W.P., 1977. Surface history of Mercury: A review. Vistas Astron. 20, 273–300.

Haase, P., 1995. Spatial pattern analysis in ecology based on Ripley's *K*–function: Introduction and methods of edge correction. Journal of Vegetation Science 6, 575–582.

Hackman, R.J., 1966. Geologic map of the Montes Apenninus region of the Moon. U.S. Geol. Surv. Map I–463 (LAC–41).

Hale, W., Head, J.W., 1979. Central peaks in lunar craters: Morphology and morphometry. Proc. Lunar Plan. Sci. Conf. 10th, 2623–2633.

Hapke, B.W., 2001. Space weathering from Mercury to the asteroid belt. J. Geophys. Res. 106, 10039–10073.

Hartmann, W.K., 1984. Does Crater “Saturation Equilibrium” Occur in the Solar System? Icarus 60, 56–74.

Hartmann, W.K., Strom, R.G., Weidenschilling, S.J., Blasius, K.R., Woronow, A., Dence, M.R., Grieve, R.A.F., Diaz, J., Chapman, C.R., Shoemaker, E.M., Jones, K.L., 1981. Chronology of planetary volcanism by comparative studies of planetary cratering, in: Basaltic Volcanism on the Terrestrial Planets, Pergamon Press, New York, pp. 1049–1127.

Harwood, C.F., 1977. Powder Segregation Due to Vibration. Powder Technol. 16, 51–57.

Hawke, B.R., Cintala, M.J., 1977. Impact Melts on Mercury and the Moon. Bull. AAS 9, 531.

Hawke, B.R., Head, J.W., 1977a. Impact melt on lunar crater rims, in: Roddy, D.J., Pepin, R.O., Merrill, R.B. (Eds.), Impact and explosion cratering: Planetary and terrestrial implications; Proceedings of the Symposium on Planetary Cratering Mechanics, New York, pp. 815–841.

Hawke, B.R., Head, J.W., 1977b. Impact Melt in Lunar Crater Interiors. Lunar Sci. Conf. 8, 415–416.

Hawkins, S.E., Boldt, J.D., Darlington, E.H., Espiritu, R., Gold, R.E., Gotwols, B., Grey, M.P., Hash, C.D., Hayes, J.R., Jaskulek, S.E., Kardian, C.J., Keller, M.R., Malaret, E.R., Murchie, S.L., Murphy, P.K., Peacock, K., Prockter, L.M., Reiter, R.A., Robinson, M.S., Schaefer, E.D., Shelton, R.G., Sterner, R.E., Taylor, H.W., Watters, T.R., Williams, B.D., 2007. The Mercury Dual Imaging System on the MESSENGER Spacecraft. Space Sci. Rev. 131, 247–338.

Head, J.W., 1982. Lava flooding of ancient planetary crusts: Geometry, thickness, and volumes of flooded lunar impact basins. Moon Planets 26, 61–88.

Head, J.W., Chapman, C.R., Strom, R.G., Fassett, C.I., Denevi, B.W., Blewett, D.T., Ernst, C.M., Watters, T.R., Solomon, S.C., Murchie, S.L., Prockter, L.M., Chabot, N.L., Gillis-Davis, J.J., Whitten, J.L., Goudge, T.A., Baker, D.M.H., Hurwitz, D.M., Ostrach, L.R., Xiao, Z., Merline, W.J., Kerber, L.A., Dickson, J.L., Oberst, J., Byrne, P.K., Klimczak, C., Nittler, L.R., 2011. Flood Volcanism in the Northern High Latitudes of Mercury Revealed by MESSENGER. Science 333, 1853–1856.

Head, J.W., Fassett, C.I., Kadish, S.J., Smith, D.E., Zuber, M.T., Neumann, G.A., Mazarico, E.M., 2010. Global Distribution of Large Lunar Craters: Implications for Resurfacing and Impactor Populations. Science 329, 1504–1507.

Head, J.W., Kreslavsky, M.A., Pratt, S., 2002. Northern lowlands of Mars: Evidence for widespread volcanic flooding and tectonic deformation in the Hesperian Period. J. Geophys. Res. 107.

Head, J.W., Murchie, S.L., Prockter, L.M., Robinson, M.S., Solomon, S.C., Strom, R.G., Chapman, C.R., Watters, T.R., McClintock, W.E., Blewett, D.T., Gillis-Davis, J.J., 2008. Volcanism on Mercury: Evidence from the First MESSENGER Flyby. Science 321, 69–72.

Head, J.W., Murchie, S.L., Prockter, L.M., Solomon, S.C., Strom, R.G., Chapman, C.R., Watters, T.R., Blewett, D.T., Gillis-Davis, J.J., Fassett, C.I., Dickson, J.L., Hurwitz, D.M., Ostrach, L.R., 2009. Evidence for intrusive activity on Mercury from the first MESSENGER flyby. Earth Planet. Sci. Lett. 285, 251–262.

Head, J.W., Wilson, L., 1992. Lunar mare volcanism: Stratigraphy, eruption conditions, and the evolution of secondary crusts. Geological Society of America 56, 2155–2175.

Heiken, G., 1975. Petrology of Lunar Soils. Rev. Geophys. Space Phys. 13, 567–587.

Hiesinger, H., Head, J.W., Wolf, U., Jaumann, R., Neukum, G., 2002. Lunar mare basalt flow units: Thicknesses determined from crater size-frequency distributions. Geophys. Res. Lett. 29, 89–1.

Hiesinger, H., Head, J.W., Wolf, U., Jaumann, R., Neukum, G., 2003. Ages and stratigraphy of mare basalts in Oceanus Procellarum, Mare Nubium, Mare Cognitum, and Mare Insularum. J. Geophys. Res. 108, 5065.

Hiesinger, H., Head, J.W., Wolf, U., Jaumann, R., Neukum, G., 2010. Ages and stratigraphy of lunar mare basalts in Mare Frigoris and other nearside maria based on crater size-frequency distribution measurements. J. Geophys. Res. 115, 03003.

Hiesinger, H., Head, J.W., Wolf, U., Jaumann, R., Neukum, G., 2011. Ages and stratigraphy of lunar mare basalts: A synthesis. Spec. Pap. - Geol. Soc. Am. 477, 1–51.

Hiesinger, H., Jaumann, R., Neukum, G., Head, J.W., 2000. Ages of mare basalts on the lunar nearside. J. Geophys. Res. 105, 29239–29275.

Hiesinger, H., van der Bogert, C.H., Pasckert, J.H., Funcke, L., Giacomini, L., Ostrach, L.R., Robinson, M.S., 2012. How old are young lunar craters? J. Geophys. Res. 117.

Holsapple, K.A., 1993. The scaling of impact processes in planetary sciences. Annu. Rev. Earth Planet. Sci. 21, 333–373.

Holsapple, K.A., Schmidt, R.M., 1982. On the Scaling of Crater Dimensions 2. Impact Processes. J. Geophys. Res. 87, 1849–1870.

Holsapple, K.A., Schmidt, R.M., 1987. Point Source Solutions and Coupling Parameters in Cratering Mechanics. J. Geophys. Res. 92, 6350–6376.

Hong, D., Quinn, P., Luding, S., 2001. Reverse Brazil Nut Problem: Competition between Percolation and Condensation. Phys. Rev. Lett. 86, 3423–3426.

Hörz, F., Cintala, M.J., 1997. Impact experiments related to the evolution of planetary regoliths. Meteorit. Planet. Sci. 32, 179–209.

Hörz, F., Cintala, M.J., See, T.H., Cardenas, F., Thompson, T.D., 1984. Grain Size Evolution and Fractionation Trends in an Experimental Regolith. J. Geophys. Res. 89, C183–C196.

Housen, K.R., Schmidt, R.M., Holsapple, K.A., 1983. Crater ejecta scaling laws: Fundamental Forms Based on Dimensional Analysis. J. Geophys. Res. 88, 2485–2499.

Howard, K.A., 1972. Ejecta Blankets of Large Craters Exemplified by King Crater, in: Apollo 16 Preliminary Science Report, NASA SP-315, 29–70 to 29–77.

Howard, K.A., 1974. Fresh lunar impact craters: Review of variations with size. Proc. Lunar Sci. Conf. 5th, 61–69.

Howard, K.A., Wilshire, H.G., 1975. Flows of impact melt at lunar craters. J. Res. U.S. Geol. Surv. 3, 237–251.

Huerta, D.A., Ruiz-Suárez, J.C., 2004. Vibration-Induced Granular Segregation: A Phenomenon Driven by Three Mechanisms. Phys. Rev. Lett. 92, 114301.

Hurwitz, D.M., Head, J.W., Byrne, P.K., Xiao, Z., Solomon, S.C., Zuber, M.T., Smith, D.E., Neumann, G.A., 2013. Investigating the origin of candidate lava channels on Mercury with MESSENGER data: Theory and observations. J. Geophys. Res. 118, 1–16.

Izenberg, N.R., Barnouin-Jha, O.S., 2006a. Laboratory Simulation of Surface Seismic Effects on Low Gravity Bodies. Lunar Planet. Sci. Conf. 37, abstract 2017.

Izenberg, N.R., Barnouin-Jha, O.S., 2006b. Laboratory Simulations of Seismic Modifications on Small Bodies. Spacecraft Reconnaissance of Asteroid and Comet Interiors, abstract 3029.

Jaeger, H.M., Nagel, S.R., 1992. Physics of the Granular State. Science 255, 1523–1531.

Jaeger, H.M., Nagel, S.R., Behringer, R.P., 1996. Granular solids, liquids, and gases. Rev. Mod. Phys. 68, 1259–1273.

Johnson, J.R., Larson, S.M., Singer, R.B., 1991. Remote Sensing of Potential Lunar Resources 1. Near-Side Compositional Properties. J. Geophys. Res. 96, 18861–18882.

Johnson, T.V., Saunders, R.S., Matson, D.L., Mosher, J.A., 1977. A TiO_2 abundance map for the northern maria. Proc. Lunar Sci. Conf. 8th, 1029–1036.

Jolliff, B.L., Gillis, J.J., Haskin, L.A., Korotev, R.L., Wieczorek, M.A., 2000. Major lunar crustal terranes: Surface expressions and crust-mantle origins. J. Geophys. Res. 105, 4197–4216.

Jullien, R., Meakin, P., Pavlovitch, A., 1992. Three-Dimensional Model for Particle-Size Segregation by Shaking. Phys. Rev. Lett. 69, 640–643.

Jullien, R., Meakin, P., Pavlovitch, A., 1993. Jullien, Meakin, and Pavlovitch Reply to Barker et al. Comment on: Three-Dimensional Model for Particle-Size Segregation by Shaking. Phys. Rev. Lett. 70, 2195.

Keller, M.R., Ernst, C.M., Denevi, B.W., Murchie, S.L., Chabot, N.L., Becker, K.J., Hash, C.D., Domingue, D.L., Sterner, R.E., 2013. Time-Dependent Calibration of MESSENGER's Wide-Angle Camera Following a Contamination Event. Lunar Planet. Sci. Conf. 44, 2489.

Kerber, L.A., Head, J.W., Blewett, D.T., Solomon, S.C., Wilson, L., Murchie, S.L., Robinson, M.S., Denevi, B.W., Domingue, D.L., 2011. The global distribution of pyroclastic deposits on Mercury: The view from MESSENGER flybys 1–3. Planet. Space Sci. 59, 1895–1909.

Kerber, L.A., Head, J.W., Solomon, S.C., Murchie, S.L., Blewett, D.T., Wilson, L., 2009. Explosive volcanic eruptions on Mercury: Eruption conditions, magma volatile content, and implications for interior volatile abundances. Earth Planet. Sci. Lett. 285, 263–271.

Kiefer, W.S., Murray, B.C., 1987. The Formation of Mercury's Smooth Plains. Icarus 72, 477–491.

Klimczak, C., Watters, T.R., Ernst, C.M., Freed, A.M., Byrne, P.K., Solomon, S.C., Blair, D.M., Head, J.W., 2012. Deformation associated with ghost craters and basins in volcanic smooth plains on Mercury: Strain analysis and implications for plains evolution. J. Geophys. Res. 117, E00L03.

Kneissl, T., van Gasselt, S., Neukum, G., 2011. Map-projection-independent crater size-frequency determination in GIS environments—New software tool for ArcGIS. Planet. Space Sci. 59, 1243–1254.

Knight, J.B., Jaeger, H.M., Nagel, S.R., 1993. Vibration-Induced Size Separation in Granular Media: The Convection Connection. Phys. Rev. Lett. 70, 3728–3731.

König, B., 1977. Investigations of primary and secondary impact structures on the Moon and laboratory experiments to study the ejecta of secondary particles. PhD Thesis, Ruprecht Karl Univ Heidelberg, 88 p. (translated from German).

Korotev, R.L., 1976. Geochemistry of grain-size fractions of soils from the Taurus-Littrow valley floor. Proc. Lunar Sci. Conf. 7th, 695–726.

Korotev, R.L., 1999. A new estimate of the composition of the feldspathic upper crust of the Moon. Lunar Planet. Sci. Conf. 30, abstract 1303.

Korotev, R.L., Jolliff, B.L., Zeigler, R.A., Gillis, J.J., Haskin, L.A., 2003. Feldspathic lunar meteorites and their implications for compositional remote sensing of the lunar surface and the composition of the lunar crust. Geochim. Cosmochim. Acta 67, 4895–4923.

Labotka, T.C., Kempa, M.J., White, C., Papike, J.J., Laul, J.C., 1980. The lunar regolith: Comparative petrology of the Apollo sites. Proc. Lunar Plan. Sci. Conf. 11th, 1285–1305.

Latham, G.V., Ewing, M., Press, F., Sutton, G., Dorman, J., Nakamura, Y., Toksoz, N., Wiggins, R., Derr, J., Duennebier, F., 1970a. Apollo 11 passive seismic experiment. Proc. Lunar Sci. Conf. 11th, 2309–2320.

Latham, G.V., Ewing, M., Press, F., Sutton, G., Dorman, J., Nakamura, Y., Toksoz, N., Wiggins, R., Derr, J., Duennebier, F., 1970b. Passive Seismic Experiment. Science 167, 455–457.

Lauretta, D.S., OSIRIS-REx Team, 2012. An Overview of the OSIRIS-REx Asteroid Sample Return Mission. Lunar Planet. Sci. Conf. 43, abstract 2491.

Lawrence, D.J., Elphic, R.C., Feldman, W.C., Prettyman, T.H., Gasnault, O.M., Maurice, S., 2003. Small-area thorium features on the lunar surface. J. Geophys. Res. 108, 5102.

Lawrence, D.J., Feldman, W.C., Barraclough, B.L., Binder, A.B., Elphic, R.C., Maurice, S., Miller, M.C., Prettyman, T.H., 2000. Thorium abundances on the lunar surface. J. Geophys. Res. 105, 20307–20332.

Lawrence, D.J., Maurice, S., Feldman, W.C., 2004. Gamma-ray measurements from Lunar Prospector: Time series data reduction for the Gamma-Ray Spectrometer. J. Geophys. Res. 109.

Le Feuvre, M., Wieczorek, M.A., 2008. Nonuniform cratering of the terrestrial planets. Icarus 197, 291–306.

Le Feuvre, M., Wieczorek, M.A., 2011. Nonuniform cratering of the Moon and a revised crater chronology of the inner Solar System. Icarus 214, 1–20.

Leake, M.A., 1982. The intercrater plains of Mercury and the Moon: Their nature, origin, and role in terrestrial planet evolution, in: Advances in Planetary Geology, NASA Technical Memorandum 84894, 1–537.

Lide, D.R. (Ed.), 2007. CRC Handbook of Chemistry and Physics, 88 ed. CRC Press. 2640 p.

Lindstrom, M.M., Nava, D.F., Lindstrom, D.J., Winzer, S.R., Lum, R.K.L., Schuhmann, P.J., Schuhmann, S., Philpotts, J.A., 1977. Geochemical studies of the White Breccia Boulders at North Ray Crater, Descartes region of the lunar highlands. Proc. Lunar Sci. Conf. 8th, 2137–2151.

Lucey, P.G., Blewett, D.T., Hawke, B.R., 1998. Mapping the FeO and TiO_2 content of the lunar surface with multispectral imagery. J. Geophys. Res. 103, 3679–3699.

Lucey, P.G., Blewett, D.T., Jolliff, B.L., 2000. Lunar iron and titanium abundance algorithms based on final processing of Clementine ultraviolet-visible images. J. Geophys. Res. 105, 20297–20306.

Lucey, P.G., Taylor, G.J., Malaret, E.R., 1995. Abundance and Distribution of Iron on the Moon. Science 268, 1150–1153.

M'Gonigle, J.W., Schleicher, D., 1972. Geologic map of the Plato quadrangle of the Moon. U.S. Geol. Surv. Map I–701 (LAC–12).

Malin, M.C., 1976. Observations of intercrater plains on Mercury. Geophys. Res. Lett. 3, 581–584.

Malin, M.C., 1978. Surfaces of Mercury and the Moon: Effects of resolution and lighting conditions on the discrimination of volcanic features. Proc. Lunar Plan. Sci. Conf. 9th, 3395–3409.

Marchi, S., Massironi, M., Cremonese, G., Martellato, E., Giacomini, L., Prockter, L.M., 2011. The effects of the target material properties and layering on the crater chronology: The case of Raditladi and Rachmaninoff basins on Mercury. Planet. Space Sci. 59, 1968–1980.

Marchi, S., Morbidelli, A., Cremonese, G., 2005. Flux of meteoroid impacts on Mercury. Astron. Astrophys. 431, 1123–1127.

Marchi, S., Mottola, S., Cremonese, G., Massironi, M., Martellato, E., 2009. A New Chronology for the Moon and Mercury. Astron. J. 137, 4936–4948.

Marcus, A.H., 1970. Comparison of Equilibrium Size Distributions for Lunar Craters. J. Geophys. Res. 75, 4977–4984.

McEwen, A.S., Bierhaus, E.B., 2006. The Importance of Secondary Cratering to Age Constraints on Planetary Surfaces. Ann. Rev. Earth Planet. Sci. 34, 535–567.

McEwen, A.S., Preblich, B.S., Turtle, E.P., Artemieva, N.A., Golombek, M.P., Hurst, M., Kirk, R., Burr, D.M., Christensen, P.R., 2005. The rayed crater Zunil and interpretations of small impact craters on Mars. Icarus 176, 351–381.

McEwen, A.S., Robinson, M.S., 1997. Mapping of the Moon by Clementine. Adv. Space Res. 19, 1523–1533.

McGill, G.E., 1977. Craters as “fossils”: The remote dating of planetary surface materials. Geol. Soc. Am. Bull. 88, 1102–1110.

McKay, D.S., Fruland, R.M., Heiken, G.H., 1974. Grain size and the evolution of lunar soils. Proc. Lunar Sci. Conf. 5th, 887–906.

Melosh, H.J., 1979. Acoustic Fluidization: A New Geologic Process? J. Geophys. Res. 84, 7513–7520.

Melosh, H.J., 1983. Acoustic Fluidization: Can sound waves explain why dry rock debris appears to flow like a fluid in some energetic geologic events? American Scientist 71, 158–165.

Melosh, H.J., 1989. Impact Cratering: A Geologic Process. Oxford University Press, New York. 245 p.

Metzger, M.J., Remy, B., Glasser, B.J., 2011. All the Brazil nuts are not on top: Vibration induced granular size segregation of binary, ternary, and multi-sized mixtures. Powder Technol. 205, 42–51.

Michael, G.G., Neukum, G., 2010. Planetary surface dating from crater size-frequency distribution measurements: Partial resurfacing events and statistical age uncertainty. Earth Planet. Sci. Lett. 294, 223–229.

Milkovich, S.M., Head, J.W., Wilson, L., 2002. Identification of mercurian volcanism: Resolution effects and implications for MESSENGER. Meteorit. Planet. Sci. 37, 1209–1222.

Miyamoto, H., Yano, H., Scheeres, D.J., Abe, S., Barnouin-Jha, O., Cheng, A.F., Demura, H., Gaskell, R.W., Hirata, N., Ishiguro, M., Michikami, T., Nakamura, A.M., Nakamura, R., Saito, J., Sasaki, S., 2007. Regolith Migration and Sorting on Asteroid Itokawa. Science 316, 1011–1014.

Möbius, M.E., Lauderdale, B.E., Nagel, S.R., Jaeger, H.M., 2001. Brazil-nut effect: Size separation of granular particles. Nature 414, 270.

Moore, H.J., 1965. Geologic map of the Aristarchus region of the Moon. U.S. Geol. Surv. Map I–465 (LAC–39).

Moore, H.J., 1972. Crater Shadowing Effects at Low Sun Angles, in: Apollo 15 Preliminary Science Report, NASA SP-289, 25–92 to 25–94.

Morris, R.V., 1985. Determination of Optical Penetration Depths from Reflectance and Transmittance Measurements on Albite Powders. Lunar Planet. Sci. Conf. 16, 581–582.

Murchie, S.L., Watters, T.R., Robinson, M.S., Head, J.W., Strom, R.G., Chapman, C.R., Solomon, S.C., McClintock, W.E., Prockter, L.M., Domingue, D.L., Blewett, D.T., 2008. Geology of the Caloris Basin, Mercury: A View from MESSENGER. Science 321, 73–76.

Murray, B.C., 1975. The Mariner 10 Pictures of Mercury: An Overview. J. Geophys. Res. 80, 2342–2344.

Murray, B.C., Belton, M.J.S., Danielson, G.E., Davies, M.E., Gault, D.E., Hapke, B.W., O'Leary, B., Strom, R.G., Suomi, V., Trask, N.J., 1974a. Mariner 10 Pictures of Mercury: First Results. Science 184, 459–461.

Murray, B.C., Belton, M.J.S., Danielson, G.E., Davies, M.E., Gault, D.E., Hapke, B.W., O'Leary, B., Strom, R.G., Suomi, V., Trask, N.J., 1974b. Mercury's Surface: Preliminary Description and Interpretation from Mariner 10 Pictures. Science 185, 169–179.

Murray, B.C., Strom, R.G., Trask, N.J., Gault, D.E., 1975. Surface History of Mercury: Implications for Terrestrial Planets. J. Geophys. Res. 80, 2508–2514.

Nakamura, Y., Dorman, J., Duennebier, F., Ewing, M., Lammlein, D., Latham, G., 1974. High-frequency lunar teleseismic events. Proc. Lunar Sci. Conf. 5th, 2883–2890.

Nakamura, Y., Latham, G.V., Dorman, H.J., 1982. Apollo Lunar Seismic Experiment–Final Summary. J. Geophys. Res., A117–A123.

Nakamura, Y., Latham, G.V., Dorman, H.J., Ibrahim, A.B.K., Koyama, J., Horvath, P., 1979. Shallow moonquakes: Depth, distribution and implications as to the present state of the lunar interior. Proc. Lunar Plan. Sci. Conf. 10th, 2299–2309.

National Aeronautics and Space Administration (NASA), 2004. The Vision for Space Exploration. NP-2004-01-334-HQ, NASA, Washington, D.C., 20546.

Neukum, G., 1983. Meteoritenbombardement and Datierung planetarer Oberflächen. Habilitationsschrift, Univ. München, Munich, Germany. 186 p. (translated from German).

Neukum, G., Basilevsky, A.T., Kneissl, T., Chapman, M.G., van Gasselt, S., Michael, G., Jaumann, R., Hoffmann, H., Lanz, J.K., 2010. The geologic evolution of Mars: Episodicity of resurfacing events and ages from cratering analysis of image data and correlation with radiometric ages of Martian meteorites. Earth Planet. Sci. Lett. 294, 204–222.

Neukum, G., Horn, P., 1976. Effects of lava flows on lunar crater populations. The Moon 15, 205–222.

Neukum, G., Ivanov, B.A., 1994. Crater Size Distributions and Impact Probabilities on Earth from Lunar, Terrestrial-Planet, and Asteroid Cratering Data, in: Gehrels, T. (Ed.), Hazards Due to Comets and Asteroids, The University of Arizona Press, Tucson. pp. 359–416.

Neukum, G., Ivanov, B.A., Hartmann, W.K., 2001a. Cratering Records in the Inner Solar System in Relation to the Lunar Reference System. Space Sci. Rev. 96, 55–86.

Neukum, G., König, B., 1976. Dating of individual lunar craters. Proc. Lunar Sci. Conf. 7th, 2867–2881.

Neukum, G., König, B., Arkani-Hamed, J., 1975a. A study of lunar impact crater size-distributions. The Moon 12, 201–229.

Neukum, G., König, B., Fechtig, H., Storzer, D., 1975b. Cratering in the Earth-Moon system: Consequences for age determination by crater counting. Proc. Lunar Sci. Conf. 6th, 2597–2620.

Neukum, G., Oberst, J., Hoffmann, H., Wagner, R.J., Ivanov, B.A., 2001b. Geologic evolution and cratering history of Mercury. Planet. Space Sci. 49, 1507–1521.

Nittler, L.R., Starr, R.D., Weider, S.Z., McCoy, T.J., Boynton, W.V., Ebel, D.S., Ernst, C.M., Evans, L.G., Goldsten, J.O., Hamara, D.K., Lawrence, D.J., McNutt, R.L., Schlemm, C.E., Solomon, S.C., Sprague, A.L., 2011. The Major-Element Composition of Mercury's Surface from MESSENGER X-ray Spectrometry. Science 333, 1847–1850.

Nozette, S., Rustan, P., Pleasance, L. P., Horan, D.M., Regeon, P., Shoemaker, E.M., Spudis, P.D., Acton, C.H., Baker, D.N., Blamont, J.E., Buratti, B.J., Corson, M.P., Davies, M.E., Duxbury, T.C., Eliason, E.M., Jakosky, B.M., Kordas, J.F., Lewis, I.T., Lichtenberg, C.L., Lucey, P.G., Malaret, E., Massie, M.A., Resnick, J.H., Rollins, C.J., Park, H.S., McEwen, A.S., Priest, R.E., Pieters, C.M., Reisse, R.A., Robinson, M.S., Simpson, R.A., Smith, D.E., Sorenson, T.C., Vorder Breugge, R.W., Zuber, M.T., 1994. The Clementine Mission to the Moon: Scientific Overview. Science 266, 1835–1839.

O'Keefe, J.D., Ahrens, T.J., 1977. Impact-induced energy partitioning, melting, and vaporization on terrestrial planets. Proc. Lunar Sci. Conf. 8th, 3357–3374.

O'Keefe, J.D., Ahrens, T.J., 1993. Planetary Cratering Mechanics. J. Geophys. Res. 98, 17011–17028.

Oberbeck, V.R., 1975. The Role of Ballistic Erosion and Sedimentation in Lunar Stratigraphy. Rev. Geophys. Space Phys. 13, 337–362.

Oberbeck, V.R., 2008. Comment on: Constraints on the depth and variability of the lunar regolith, by B.B. Wilcox, .M.S Robinson, P.C. Thomas, and B.R. Hawke. Meteorit. Planet. Sci. 43, 815–817.

Oberbeck, V.R., Morrison, R.H., 1973. On the formation of the lunar herringbone pattern. Proc. Lunar Sci. Conf. 4th, 107–123.

Oberbeck, V.R., Quaide, W.L., Arvidson, R.E., Aggarwal, H.R., 1977. Comparative Studies of Lunar, Martian, and Mercurian Craters and Plains. J. Geophys. Res. 82, 1681–1698.

Oberbeck, V.R., Quaide, W.L., Mahan, M., Paulson, J., 1973. Monte Carlo Calculations of Lunar Regolith Thickness Distributions. Icarus 19, 87–107.

Ostrach, L.R., Robinson, M.S., 2013. Using Crater Size-Frequency Measurements to Distinguish Age Units Within Volcanic Smooth Plains – A New Approach. Lunar Planet. Sci. Conf. 44, abstract 1086.

Ostrach, L.R., Robinson, M.S., Whitten, J.L., Fassett, C.I., Strom, R.G., Head, J.W., Solomon, S.C. Constraining the Timescale of Northern Smooth Plains Emplacement on Mercury. Icarus. In preparation.

Page, N.J., 1970. Geologic map of the Cassini quadrangle of the Moon. U.S. Geol. Surv. Map I–666 (LAC–25).

Papike, J.J., Ryder, G., Shearer, C.K., 1998. Lunar Samples. Rev. Mineral. Geochem. 36, 5.1–5.234.

Papike, J.J., Simon, S.B., Laul, J.C., 1982. The Lunar Regolith: Chemistry, Mineralogy, and Petrology. Rev. Geophys. Space Phys. 20, 761–826.

Papike, J.J., Vaniman, D.T., 1978a. Luna 24 ferrobasalts and the mare basalt suite: Comparative chemistry, mineralogy, and petrology, in: Mare Crisium: The View from Luna 24, Pergamon Press, New York. pp. 371–401.

Papike, J.J., Vaniman, D.T., 1978b. The lunar mare basalt suite. Geophys. Res. Lett. 5, 433–436.

Parsons, D.S., 1976. Particle Segregation in Fine Powders by Tapping as Simulation of Jostling During Transportation. Powder Technol. 13, 269–277.

Pierazzo, E., Vickery, A.M., Melosh, H.J., 1997. A Reevaluation of Impact Melt Production. Icarus 127, 408–423.

Pieters, C.M., 1978. Mare basalt types on the front side of the Moon: A summary of spectral reflectance data. Proc. Lunar Plan. Sci. Conf. 9th, 2825–2849.

Pike, R.J., 1974. Depth/diameter relations of fresh lunar craters: Revision from spacecraft data. Geophys. Res. Lett. 1, 291–294.

Pike, R.J., 1976. Crater dimensions from Apollo data and supplemental sources. The Moon 15, 463–477.

Pike, R.J., 1977. Size-dependence in the shape of fresh impact craters on the Moon, in: Roddy, D.J., Pepin, R.O., Merrill, R.B. (Eds.), Impact and explosion cratering: Planetary and terrestrial implications; Proceedings of the Symposium on Planetary Cratering Mechanics, New York, pp. 489–509.

Pike, R.J., 1988. Geomorphology of impact craters on Mercury, in: Vilas, F., Chapman, C.R., Matthews, M.S. (Eds.), Mercury. The University of Arizona Press, Tucson, pp. 165–273.

Pike, R.J., Wilhelms, D.E., 1978. Secondary-Impact Craters on the Moon: Topographic Form and Geologic Process. Lunar Planet. Sci. Conf. 9, 907–909.

Pommerening, A., Stoyan, D., 2006. Edge-correction needs in estimating indices of spatial forest structure. Can. J. For. Res. 36, 1723–1739.

Press, F., Buwalda, P., Neugebauer, M., 1960. A Lunar Seismic Experiment. J. Geophys. Res. 65, 3097–3105.

Prettyman, T.H., Hagerty, J.J., Elphic, R.C., Feldman, W.C., Lawrence, D.J., McKinney, G.W., Vaniman, D.T., 2006. Elemental composition of the lunar surface: Analysis of gamma ray spectroscopy data from Lunar Prospector. J. Geophys. Res. 111, 1–41.

Prockter, L.M., Ernst, C.M., Denevi, B.W., Chapman, C.R., Head, J.W., Fassett, C.I., Merline, W.J., Solomon, S.C., Watters, T.R., Strom, R.G., Cremonese, G., Marchi, S., Massironi, M., 2010. Evidence for Young Volcanism on Mercury from the Third MESSENGER Flyby. Science 329, 668–671.

Quaide, W.L., Oberbeck, V.R., 1968. Thickness Determinations of the Lunar Surface Layer from Lunar Impact Craters. J. Geophys. Res. 73, 5247–5270.

Richardson, J.E., 2009. Cratering saturation and equilibrium: A new model looks at an old problem. Icarus 204, 697–715.

Richardson, J.E., Melosh, H.J., Greenberg, R., O'Brien, D.P., 2005. The global effects of impact-induced seismic activity on fractured asteroid surface morphology. Icarus 179, 325–349.

Riner, M.A., Robinson, M.S., Eckart, J.M., Desch, S.J., 2008. Global survey of color variations on 433 Eros: Implications for regolith processes and asteroid environments. Icarus 198, 67–76.

Rippie, E.G., Olsen, J.L., Faiman, M.D., 1964. Segregation Kinetics of Particulate Solids Systems II. Particle Density—Size Interactions and Wall Effects. Journal of Pharmaceutical Sciences 53, 1360–1363.

Robbins, S.J., 2013. Revised lunar cratering chronology for planetary geological histories. Lunar Planet. Sci. Conf. 44, abstract 1619.

Robbins, S.J., Antonenko, I., Kirchoff, M.R., Chapman, C.R., Fassett, C.I., Herrick, R.R., Singer, K.N., Zanetti, M., Lehan, C., 2013a. The variability of crater indentification among expert crater analysts. Lunar Science Forum.

Robbins, S.J., Antonenko, I., Kirchoff, M.R., Chapman, C.R., Fassett, C.I., Herrick, R.R., Singer, K.N., Zanetti, M., Lehan, C., Huang, D., Gay, P.L., 2013b. The variability of crater indentification among expert and community crater analysts. Planetary Cratering Consortium 4.

Robinson, M.S., Brylow, S.M., Tschimmel, M., Humm, D., Lawrence, S.J., Thomas, P.C., Denevi, B.W., Bowman-Cisneros, E., Zerr, J., Ravine, M.A., Caplinger, M.A., Ghaemi, F.T., Schaffner, J.A., Malin, M.C., Mahanti, P., Bartels, A., Anderson, J., Tran, T.N., Eliason, E.M., McEwen, A.S., Turtle, E.P., Jolliff, B.L., Hiesinger, H., 2010. Lunar Reconnaissance Orbiter Camera (LROC) Instrument Overview. Space Sci. Rev. 150, 81–124.

Robinson, M.S., Davies, M.E., Colvin, T.R., Edwards, K., 1999. A revised control network for Mercury. J. Geophys. Res. 104, 30847–30852.

Robinson, M.S., Lucey, P.G., 1997. Recalibrated Mariner 10 Color Mosaics: Implications for Mercurian Volcanism. Science 275, 197–200.

Robinson, M.S., Murchie, S.L., Blewett, D.T., Domingue, D.L., Hawkins, S.E., Head, J.W., Holsclaw, G.M., McClintock, W.E., McCoy, T.J., McNutt, R.L., Prockter, L.M., Solomon, S.C., Watters, T.R., 2008. Reflectance and Color Variations on Mercury: Regolith Processes and Compositional Heterogeneity. Science 321, 66–69.

Robinson, M.S., Plescia, J.B., Jolliff, B.L., Lawrence, S.J., 2012. Planetary and Space Science. Planet. Space Sci. 69, 76–88.

Robinson, M.S., Taylor, G.J., 2001. Ferrous oxide in Mercury's crust and mantle. Meteorit. Planet. Sci. 36, 841–847.

Robinson, M.S., Thomas, P.C., Tran, T.N., Denevi, B.W., Bowman-Cisneros, E., Plescia, J.B., van der Bogert, C.H., Hiesinger, H., 2011. Highland Smooth Plains, an Exceptional Grouping. Lunar Planet. Sci. Conf. 42, abstract 2511.

Robinson, M.S., Thomas, P.C., Veverka, J., Murchie, S., Carcich, B., 2001. The nature of ponded deposits on Eros. Nature 413, 396–400.

Robinson, M.S., Thomas, P.C., Veverka, J., Murchie, S.L., Wilcox, B.B., 2002. The geology of 433 Eros. Meteorit. Planet. Sci. 37, 1651–1684.

Rosato, A., Strandburg, K.J., Prinz, F., Swendsen, R.H., 1987. Why the Brazil Nuts Are on Top: Size Segregation of Particulate Matter by Shaking. Phys. Rev. Lett. 58, 1038–1040.

Rosato, A.D., Blackmore, D.L., Zhang, N., Lan, Y., 2002. A perspective on vibration-induced size segregation of granular materials. Chem. Eng. Sci. 57, 265–275.

Schaber, G.G., 1969. Geologic map of the Sinus Iridum quadrangle of the Moon. U.S. Geol. Surv. Map I–602 (LAC–24).

Schaber, G.G., 1973. Eratosthenian Volcanism in Mare Imbrium: Source of Youngest Lava Flows. In: Apollo 17 Preliminary Science Report, NASA SP-330 30–17 to 30–25.

Schaber, G.G., Thompson, T.W., Zisk, S.H., 1975. Lava flows in Mare Imbrium: An evaluation of anomalously low Earth-based radar reflectivity. The Moon 13, 395–423.

Schröter, M., Ulrich, S., Kreft, J., Swift, J., Swinney, H., 2006. Mechanisms in the size segregation of a binary granular mixture. Phys. Rev. E 74, 011307.

Schultz, P.H., 1977. Endogenic modification of impact craters on Mercury. Phys. Earth Planet. Inter. 15, 202–219.

Schultz, P.H., Gault, D.E., 1975. Seismically induced modification of lunar surface features. Proc. Lunar Plan. Sci. Conf. 6th, 2845–2862.

Schultz, P.H., Greeley, R., Gault, D., 1977. Interpreting statistics of small lunar craters. Proc. Lunar Sci. Conf. 8th, 3539–3564.

Shinbrot, T., 2004. The brazil nut effect – in reverse. Nature 429, 352–353.

Shinbrot, T., Muzzio, F.J., 1998. Reverse Buoyancy in Shaken Granular Beds. Phys. Rev. Lett. 81, 4365–4368.

Shoemaker, E.M., 1962. Interpretation of Lunar Craters. In: Kopal, Z. (Ed.), Physics and Astronomy of the Moon. Academic Press Inc., New York, pp. 283–359.

Shoemaker, E.M., 1971. Origin of fragmental debris on the lunar surface and the history of bombardment on the Moon. Publicaciones Instituto Investigaciones Geologicas, Vol. 24. Universidad Barcelona.

Shoemaker, E.M., Batson, R.M., Bean, A.L., Conrad, C., Dahlem, D.H., Goddard, E.N., Hait, M.H., Larson, K.B., Schaber, G.G., Schleicher, D.L., Sutton, R.L., Swann, G.A., Waters, A.C., 1970. Preliminary Geologic Investigation of the Apollo 12 Landing Site, in: Apollo 12 Preliminary Science Report, NASA SP-235, 113–235.

Shoemaker, E.M., Batson, R.M., Holt, H.E., Morris, E.C., Rennilson, J.J., Whitaker, E.A., 1968. Television Observations from Surveyor VII, in: Surveyor VII A Preliminary Report, NASA SP-173, 13–81.

Shoemaker, E.M., Batson, R.M., Holt, H.E., Morris, E.C., Rennilson, J.J., Whitaker, E.A., 1969. Observations of the Lunar Regolith and the Earth from the Television Camera on Surveyor 7. J. Geophys. Res. 74, 6081–6119.

Shoemaker, E.M., Hackman, R.J., 1962. Stratigraphic Basis for a Lunar Time Scale, in: The Moon–IAU Symposium 14, 289–300.

Silverman, B.W., 1986. Density Estimation for Statistics and Data Analysis. Chapman and Hall, New York. 176 p.

Smith, D.E., Zuber, M.T., Phillips, R.J., Solomon, S.C., Hauck, S.A., Lemoine, F.G., Mazarico, E.M., Neumann, G.A., Peale, S.J., Margot, J.-L., Johnson, C.L., Torrence, M.H., Perry, M.E., Goossens, S., Head, J.W., Taylor, A.H., 2012. Gravity Field and Internal Structure of Mercury from MESSENGER. Science 336, 214–217.

Soderblom, L.A., 1970. A Model for Small-Impact Erosion Applied to the Lunar Surface. J. Geophys. Res. 75, 2655–2661.

Soderblom, L.A., 1972. The Process of Crater Removal in the Lunar Maria, in: Apollo 15 Preliminary Science Report, NASA SP-289, 25–87 to 25–91.

Soderblom, L.A., Lebofsky, L.A., 1972. Technique for Rapid Determination of Relative Ages of Lunar Areas from Orbital Photography. J. Geophys. Res. 77, 279–296.

Solomon, S.C., Klimczak, C., Byrne, P.K., Hauck, S.A., Balcerski, J.A., Dombard, A.J., Zuber, M.T., Smith, D.E., Phillips, R.J., Head, J.W., Watters, T.R., 2012. Long-Wavelength Topographic Change on Mercury: Evidence and Mechanisms. Lunar Planet. Sci. Conf. 43, abstract 1578.

Solomon, S.C., McNutt, R.L., Gold, R.E., Acuña, M.H., Baker, D.N., Boynton, W.V., Chapman, C.R., Cheng, A.F., Gloeckler, G., Head, J.W., Krimigis, S.M., McClintock, W.E., Murchie, S.L., Peale, S.J., Phillips, R.J., Robinson, M.S., Slavin, J.A., Smith, D.E., Strom, R.G., Trombka, J.I., Zuber, M.T., 2001. The MESSENGER mission to Mercury: scientific objectives and implementation. Planet. Space Sci. 49, 1445–1465.

Solomon, S.C., McNutt, R.L., Watters, T.R., Lawrence, D.J., Feldman, W.C., Head, J.W., Krimigis, S.M., Murchie, S.L., Phillips, R.J., Slavin, J.A., Zuber, M.T., 2008. Return to Mercury: A Global Perspective on MESSENGER's First Mercury Flyby. Science 321, 59–62.

Speyerer, E.J., Robinson, M.S., Denevi, B.W., Team, L.S., 2011. Lunar Reconnaissance Orbiter Camera Global Morphological Map of the Moon. Lunar Planet. Sci. Conf. 42, abstract 2387.

Spudis, P.D., Guest, J.E., 1988. Stratigraphy and geologic history of Mercury, in: Vilas, F., Chapman, C.R., Matthews, M.S. (Eds.), Mercury. The University of Arizona Press, Tucson, pp. 118–164.

Staid, M.I., Pieters, C.M., 2001. Mineralogy of the last lunar basalts: Results from Clementine. J. Geophys. Res. 106, 27887–27900.

Staid, M.I., Pieters, C.M., Besse, S., Boardman, J., Dhingra, D., Green, R., Head, J.W., Isaacson, P., Klima, R., Kramer, G., Mustard, J.M., Runyon, C., Sunshine, J., Taylor, L.A., 2011. The mineralogy of late stage lunar volcanism as observed by the Moon Mineralogy Mapper on Chandrayaan-1. J. Geophys. Res. 116, E00G10.

Stockstill-Cahill, K.R., McCoy, T.J., Nittler, L.R., Weider, S.Z., Hauck, S.A., 2012. Magnesium-rich crustal compositions on Mercury: Implications for magmatism from petrologic modeling. J. Geophys. Res. 117, E00L15.

Stöffler, D., Ryder, G., 2001. Stratigraphy and Isotope Ages of Lunar Geologic Units: Chronological Standard for the Inner Solar System. Space Sci. Rev. 96, 9–54.

Stöffler, D., Ryder, G., Ivanov, B.A., Artemieva, N.A., Cintala, M.J., Grieve, R.A.F., 2006. Cratering History and Lunar Chronology. Rev. Mineral. Geochem. 60, 519–596.

Strom, R.G., 1977. Origin and Relative Age of Lunar and Mercurian Intercrater Plains. Phys. Earth Planet. Inter. 15, 156–172.

Strom, R.G., 1979. Mercury: A Post-Mariner 10 Assessment. Space Sci. Rev. 24, 3–70.

Strom, R.G., Banks, M.E., Chapman, C.R., Fassett, C.I., Forde, J.A., Head, J.W., Merline, W.J., Prockter, L.M., Solomon, S.C., 2011. Mercury crater statistics from MESSENGER flybys: Implications for stratigraphy and resurfacing history. Planet. Space Sci. 59, 1960–1967.

Strom, R.G., Chapman, C.R., Merline, W.J., Solomon, S.C., Head, J.W., 2008. Mercury Cratering Record Viewed from MESSENGER's First Flyby. Science 321, 79–81.

Strom, R.G., Malhotra, R., Ito, T., Yoshida, F., Kring, D.A., 2005. The Origin of Planetary Impactors in the Inner Solar System. Science 309, 1847–1850.

Strom, R.G., Murray, B.C., Belton, M.J.S., Danielson, G.E., Davies, M.E., Gault, D.E., Hapke, B.W., O'Leary, B., Trask, N.J., Guest, J.E., 1975a. Preliminary Imaging Results From the Second Mercury Encounter. J. Geophys. Res. 80, 2345–2356.

Strom, R.G., Neukum, G., 1988. The cratering record on Mercury and the origin of impacting objects, in: Vilas, F., Chapman, C.R., Matthews, M.S. (Eds.), Mercury. The University of Arizona Press, Tucson, pp. 336–373.

Strom, R.G., Trask, N.J., Guest, J.E., 1975b. Tectonism and Volcanism on Mercury. J. Geophys. Res. 80, 2478–2507.

Taylor, L.A., Morris, R.V., Pieters, C.M., Patchen, A., Taylor, D.S., Wentworth, S., McKay, D.S., 2000. Chemical Characterization of Lunar Mare Soils. Lunar Planet. Sci. Conf. 31, 1697.

Thomas, P.C., Joseph, J., Carcich, B., Veverka, J., Clark, B.E., Bell, J.F., III, Byrd, A.W., Chomko, R., Robinson, M., Murchie, S., Prockter, L.M., Cheng, A., Izenberg, N., Malin, M., Chapman, C.R., McFadden, L.A., Kirk, R., Gaffey, M., Lucey, P.G., 2002. Eros: Shape, Topography, and Slope Processes. Icarus 155, 18–37.

Trask, N.J., 1966. Size and Spatial Distribution of Craters Estimated from the *Ranger* Photographs, in: Ranger VIII and IX, Part 2, Experimenters' Analyses and Interpretations, Jet Propul. Lab. Tech. Rep. 32-800 252–263.

Trask, N.J., 1975. Cratering History of the Heavily Cratered Terrain on Mercury. Proc. Intern. Coll. Planet. Geol.: Geol. Rom. 15, 471–476.

Trask, N.J., Guest, J.E., 1975. Preliminary Geologic Terrain Map of Mercury. J. Geophys. Res. 80, 2461–2477.

Trask, N.J., Strom, R.G., 1976. Additional Evidence of Mercurian Volcanism. Icarus 28, 559–563.

van der Bogert, C.H., Hiesinger, H., McEwen, A.S., Dundas, C., Bray, V.J., Robinson, M.S., Plescia, J.B., Reiss, D., Klemm, K., LROC Team, 2010. Discrepancies Between Crater Size-Frequency Distributions on Ejecta and Impact Melt Pools at Lunar Craters: An Effect of Differing Target Properties? Lunar Planet. Sci. Conf. 41, abstract 2165.

Vanel, L., Rosato, A.D., Dave, R.N., 1997. Rise-Time Regimes of a Large Sphere in Vibrated Bulk Solids. Phys. Rev. Lett. 78, 1255–1258.

Vaniman, D.T., Labotka, T.C., Papike, J.J., Simon, S.B., Laul, J.C., 1979. The Apollo 17 drill core: Petrologic systematics and the identification of a possible Tycho component. Proc. Lunar Plan. Sci. Conf. 10th, 1185–1227.

Veverka, J., Thomas, P.C., Robinson, M., Murchie, S., Chapman, C.R., Bell, M., Harch, A., Merline, W.J., Bell, J.F., III, Bussey, B., Carcich, B., Cheng, A., Clark, B., Domingue, D., Dunham, D., Farquhar, R., Gaffey, M.J., Hawkins, E., Izenberg, N., Joseph, J., Kirk, R., Li, H., Lucey, P., Malin, M., McFadden, L., Miller, J.K., Owen, W.M., Peterson, C., Prockter, L.M., Warren, J., Wellnitz, D., Williams, B.G., Yeomans, D.K., 2001. Imaging of Small-Scale Features on 433 Eros from NEAR: Evidence for a Complex Regolith. Science 292, 484–488.

Watters, T.R., 1993. Compressional Tectonism on Mars. J. Geophys. Res. 98, 17049–17060.

Watters, T.R., Murchie, S.L., Robinson, M.S., Solomon, S.C., Denevi, B.W., André, S.L., Head, J.W., 2009. Emplacement and tectonic deformation of smooth plains in the Caloris basin, Mercury. Earth Planet. Sci. Lett. 285, 309–319.

Watters, T.R., Solomon, S.C., Klimczak, C., Freed, A.M., Head, J.W., Ernst, C.M., Blair, D.M., Goudge, T.A., Byrne, P.K., 2012. Extension and contraction within volcanically buried impact craters and basins on Mercury. Geology 40, 1123–1126.

Weider, S.Z., Nittler, L.R., Starr, R.D., McCoy, T.J., Stockstill-Cahill, K.R., Byrne, P.K., Denevi, B.W., Head, J.W., Solomon, S.C., 2012. Chemical heterogeneity on Mercury's surface revealed by the MESSENGER X-Ray Spectrometer. J. Geophys. Res. 117, E00L05.

Werner, S.C., Ivanov, B.A., Neukum, G., 2009. Theoretical analysis of secondary cratering on Mars and an image-based study on the Cerberus Plains. Icarus 200, 406–417.

Wetherill, G.W., 1974. Pre-mare cratering and early solar system history. Proc. Sov.–Am. Conf. Cosmo. Moon & Plan. 1–35.

Whitten, J.L., Head, J.W., Murchie, S.L., Blewett, D.T., Denevi, B.W., Neumann, G.A., Zuber, M.T., Smith, D.E., Solomon, S.C., 2012. Intercrater Plains on Mercury: Topographic Assessment with MESSENGER Data. Lunar Planet. Sci. Conf. 43, abstract 1479.

Wilcox, B.B., Robinson, M.S., Thomas, P.C., Hawke, B.R., 2005. Constraints on the depth and variability of the lunar regolith. Meteorit. Planet. Sci. 40, 695–710.

Wilhelms, D.E., 1976a. Secondary impact craters of lunar basins. Proc. Lunar Sci. Conf. 7th, 2883–2901.

Wilhelms, D.E., 1976b. Mercurian volcanism questioned. Icarus 28, 551–558.

Wilhelms, D.E., 1987. The Geologic History of the Moon. U.S. Geol. Surv. Prof. Paper No. 1348.

Wilhelms, D.E., McCauley, J.F., 1971. Geologic Map of the Near Side of the Moon. U.S. Geol. Surv. Map I-703.

Wilhelms, D.E., Oberbeck, V.R., Aggarwal, H.R., 1978. Size-frequency distributions of primary and secondary lunar impact craters. Proc. Lunar Plan. Sci. Conf. 9th, 3735–3762.

Williams, J.C., 1976. The Segregation of Particulate Materials. A Review. Powder Technol. 15, 245–251.

Williams, K.K., Zuber, M.T., 1998. Measurement and Analysis of Lunar Basin Depths from Clementine Altimetry. Icarus 131, 107–122.

Wood, J.A., Dickey, J.S., Jr., Marvin, U.B., Powell, B.N., 1970. Lunar anorthosites and a geophysical model of the Moon. Proc. Apollo 11 Lunar Sci. Conf. 1, 965–988.

Woronow, A., 1977. Crater Saturation and Equilibrium: A Monte Carlo Simulation. J. Geophys. Res. 82, 2447–2456.

Xiao, Z., Strom, R.G., Chapman, C.R., Head, J.W., Klimczak, C., Ostrach, L.R., Helbert, J., D'Incecco, P., Controlling factors in impact excavation processes: Insights from comparisons of fresh complex impact craters on Mercury and the Moon. Icarus, accepted.

Young, R.A., 1975. Mare crater size-frequency distributions: Implications for relative surface ages and regolith development. Proc. Lunar Sci. Conf. 6th, 2645–2662.

Zuber, M.T., Smith, D.E., Phillips, R.J., Solomon, S.C., Neumann, G.A., Hauck, S.A., Peale, S.J., Barnouin, O.S., Head, J.W., Johnson, C.L., Lemoine, F.G., Mazarico, E.M., Torrence, M.H., Freed, A.M., Klimczak, C., Margot, J.-L., Oberst, J., Perry, M.E., McNutt, R.L., Balcerski, J.A., Michel, N., Talpe, M.J., Yang, D., 2012. Topography of the Northern Hemisphere of Mercury from MESSENGER Laser Altimetry. Science 336, 217–220.

APPENDIX A

FEATURED IMAGES

Table A1. LROC Featured Images[a]

Date	Featured Image Name	Website Link
06/20/2013	Oval Crater	http://lroc.sese.asu.edu/news/index.php?/archives/705-Oval-Crater.html
06/19/2013	Complicated Crater	http://lroc.sese.asu.edu/news/index.php?/archives/704-Complicated-Crater.html
06/18/2013	Ka-Pow!	http://lroc.sese.asu.edu/news/index.php?/archives/703-Ka-Pow!.html
05/09/2013	Messy Crater	http://lroc.sese.asu.edu/news/index.php?/archives/702-Messy-Crater.html
05/08/2013	Boulder Origin?	http://lroc.sese.asu.edu/news/index.php?/archives/701-Boulder-Origin.html
05/07/2013	Boulder Tales	http://lroc.sese.asu.edu/news/index.php?/archives/700-Boulder-Tales.html
04/12/2013	Crater Debris	http://lroc.sese.asu.edu/news/index.php?/archives/699-Crater-Debris.html
04/11/2013	Squished Crater	http://lroc.sese.asu.edu/news/index.php?/archives/698-Squished-Crater.html
04/10/2013	Rim Slumping	http://lroc.sese.asu.edu/news/index.php?/archives/696-Rim-Slumping.html
01/31/2013	Messy Melt	http://lroc.sese.asu.edu/news/index.php?/archives/695-Messy-Melt.html
01/30/2013	Boulder Fields	http://lroc.sese.asu.edu/news/index.php?/archives/694-Boulder-Fields.html
01/29/2013	Clam Shell	http://lroc.sese.asu.edu/news/index.php?/archives/693-Clam-Shell.html
01/17/2013	Channels and Fractures	http://lroc.sese.asu.edu/news/index.php?/archives/614-Channels-And-Fractures.html
01/16/2013	Melt Overlap	http://lroc.sese.asu.edu/news/index.php?/archives/613-Melt-Overlap.html
01/15/2013	Really Wrinkled	http://lroc.sese.asu.edu/news/index.php?/archives/612-Really-Wrinkled.html
10/18/2012	How Recent?	http://lroc.sese.asu.edu/news/index.php?/archives/611-How-Recent.html
10/17/2012	Bench Crater	http://lroc.sese.asu.edu/news/index.php?/archives/609-Bench-Crater.html
10/16/2012	Winding Channel of Melt	http://lroc.sese.asu.edu/news/index.php?/archives/608-Winding-Channel-of-Melt.html
09/13/2012	Rippled Pond	http://lroc.sese.asu.edu/news/index.php?/archives/610-Rippled-Pond.html
09/12/2012	Anaxagoras Exterior Melt	http://lroc.sese.asu.edu/news/index.php?/archives/607-Anaxagoras-Exterior-Melt.html
09/11/2012	Breached Levee	http://lroc.sese.asu.edu/news/index.php?/archives/603-Breached-Levee.html
08/09/2012	Sampling a Central Peak	http://lroc.sese.asu.edu/news/index.php?/archives/589-Sampling-a-Central-Peak.html
08/08/2012	Debris Channels	http://lroc.sese.asu.edu/news/index.php?/archives/588-Debris-Channels.html
08/07/2012	Mounded Floor	http://lroc.sese.asu.edu/news/index.php?/archives/575-Mounded-Floor.html
06/07/2012	Pyroclastic Excavation	http://lroc.sese.asu.edu/news/index.php?/archives/563-Pyroclastic-Excavation.html
06/06/2012	Rim Impact	http://lroc.sese.asu.edu/news/index.php?/archives/573-Rim-Impact.html
06/05/2012	Melt Boundary	http://lroc.sese.asu.edu/news/index.php?/archives/571-Melt-Boundary.html

[a]Complete online list of Featured Images written by the author: http://lroc.sese.asu.edu/news/index.php?/authors/30-Lillian-Ostrach.

Table A1., continued LROC Featured Images[a]

Date	Featured Image Name	Website Link
05/03/2012	Melt on a Rim	http://lroc.sese.asu.edu/news/index.php?/archives/557-Melt-on-a-Rim.html
05/02/2012	Crater in 3D!	http://lroc.sese.asu.edu/news/index.php?/archives/558-Crater-in-3D!.html
05/01/2012	Rolling Rolling Rolling	http://lroc.sese.asu.edu/news/index.php?/archives/556-Rolling-Rolling-Rolling.html
03/30/2012	Splish Splash	http://lroc.sese.asu.edu/news/index.php?/archives/530-Splish-Splash.html
03/29/2012	Not Your Average Scarp	http://lroc.sese.asu.edu/news/index.php?/archives/528-Not-Your-Average-Scarp.html
03/28/2012	Ejecta Starburst	http://lroc.sese.asu.edu/news/index.php?/archives/529-Ejecta-Starburst.html
02/02/2012	Shield Volcanoes in Lacus Veris!	http://lroc.sese.asu.edu/news/index.php?/archives/510-Shield-Volcanoes-in-Lacus-Veris!.html
02/01/2012	Fractures in Ohm's Melt	http://lroc.sese.asu.edu/news/index.php?/archives/511-Fractures-in-Ohms-Melt.html
01/31/2012	On the Floor of Thales	http://lroc.sese.asu.edu/news/index.php?/archives/512-On-the-Floor-of-Thales.html
12/08/2011	Ejecta blanket geology	http://lroc.sese.asu.edu/news/index.php?/archives/487-Ejecta-blanket-geology.html
12/07/2011	On the floor of Green M	http://lroc.sese.asu.edu/news/index.php?/archives/486-On-the-floor-of-Green-M.html
12/06/2011	Oblong Roche V	http://lroc.sese.asu.edu/news/index.php?/archives/485-Oblong-Roche-V.html
10/13/2011	Lunar landslides!	http://lroc.sese.asu.edu/news/index.php?/archives/466-Lunar-landslides!.html
10/11/2011	Perched boulders	http://lroc.sese.asu.edu/news/index.php?/archives/465-Perched-boulders.html
09/29/2011	Farside impact!	http://lroc.sese.asu.edu/news/index.php?/archives/464-Farside-impact!.html
09/28/2011	Follow the highlands-mare boundary in Tsiolkovskiy!	http://lroc.sese.asu.edu/news/index.php?/archives/461-Follow-the-highlands-mare-boundary-in-Tsiolkovskiy!.html
09/27/2011	Scarps in Schrödinger	http://lroc.sese.asu.edu/news/index.php?/archives/460-Scarps-in-Schroedinger.html
08/18/2011	Ray of boulders	http://lroc.sese.asu.edu/news/index.php?/archives/439-Ray-of-boulders.html
08/17/2011	Sampling Schrödinger	http://lroc.sese.asu.edu/news/index.php?/archives/438-Sampling-Schroedinger.html
08/16/2011	Lunar overhang?	http://lroc.sese.asu.edu/news/index.php?/archives/437-Lunar-overhang.html
07/14/2011	Splash and flow	http://lroc.sese.asu.edu/news/index.php?/archives/418-Splash-and-flow.html
07/13/2011	Stress and pull	http://lroc.sese.asu.edu/news/index.php?/archives/417-Stress-and-pull.html
07/12/2011	Relative age relationships	http://lroc.sese.asu.edu/news/index.php?/archives/416-Relative-age-relationships.html
06/02/2011	Dry debris or liquid flow?	http://lroc.sese.asu.edu/news/index.php?/archives/386-Dry-debris-or-liquid-flow.html

[a]Complete online list of Featured Images written by the author: http://lroc.sese.asu.edu/news/index.php?/authors/30-Lillian-Ostrach.

Table A1., continued LROC Featured Images[a]

Date	Featured Image Name	Website Link
06/01/2011	Look at that flow!	http://lroc.sese.asu.edu/news/index.php?/archives/384-Look-at-that-flow!.html
05/31/2011	Impact melt in Anaxagoras crater	http://lroc.sese.asu.edu/news/index.php?/archives/383-Impact-melt-in-Anaxagoras-crater.html
04/28/2011	Slumping rim of Darwin C	http://lroc.sese.asu.edu/news/index.php?/archives/377-Slumping-rim-of-Darwin-C.html
04/27/2011	Another small volcano?	http://lroc.sese.asu.edu/news/index.php?/archives/376-Another-small-volcano.html
04/26/2011	Forked wrinkle ridge	http://lroc.sese.asu.edu/news/index.php?/archives/374-Forked-wrinkle-ridge.html
03/24/2011	Boulder clusters on a ridge crest	http://lroc.sese.asu.edu/news/index.php?/archives/365-Boulder-clusters-on-a-ridge-crest.html
03/23/2011	Scouring secondary ejecta	http://lroc.sese.asu.edu/news/index.php?/archives/364-Scouring-secondary-ejecta.html
03/22/2011	Small crater in Oceanus Procellarum	http://lroc.sese.asu.edu/news/index.php?/archives/265-Small-crater-in-Oceanus-Procellarum.html
02/15/2011	Farside northern highlands	http://lroc.sese.asu.edu/news/index.php?/archives/110-Farside-northern-highlands.html
02/11/2011	Rimae Bürg	http://lroc.sese.asu.edu/news/index.php?/archives/330-Rimae-Buerg.html
02/10/2011	Rima Bradley	http://lroc.sese.asu.edu/news/index.php?/archives/329-Rima-Bradley.html
02/09/2011	Rupes Recta	http://lroc.sese.asu.edu/news/index.php?/archives/328-Rupes-Recta.html
12/03/2010	Rilles as far as the eye can see in Prinz!	http://lroc.sese.asu.edu/news/index.php?/archives/316-Rilles-as-far-as-the-eye-can-see-in-Prinz!.html
12/02/2010	Secrets of Schröteri	http://lroc.sese.asu.edu/news/index.php?/archives/314-Secrets-of-Schroeteri.html
12/01/2010	Rimae Posidonius	http://lroc.sese.asu.edu/news/index.php?/archives/313-Rimae-Posidonius.html
10/29/2010	Boulder trails in Menelaus crater	http://lroc.sese.asu.edu/news/index.php?/archives/307-Boulder-trails-in-Menelaus-crater.html
10/28/2010	Southern rim of Menelaus crater	http://lroc.sese.asu.edu/news/index.php?/archives/306-Southern-rim-of-Menelaus-crater.html

[a]Complete online list of Featured Images written by the author: http://lroc.sese.asu.edu/news/index.php?/authors/30-Lillian-Ostrach.

Table A2. Apollo Image Archive Featured Images

Date	Featured Image Name	Website Link
02/24/2009	Mysterious Gaudibert Crater	http://apollo.sese.asu.edu/LIW/20090224.html
01/13/2009	Menelaus' Distinctive Rays	http://apollo.sese.asu.edu/LIW/20090224.html

APPENDIX B

TABULATED CRATER STATISTICS AND PRODUCTION FUNCTION/EQUILIBRIUM FUNCTION LEAST SQUARES FITS FOR SELECTED REGIONS IN MARE IMBRIUM, MARE SERENITATIS, AND MARE TRANQUILLITATIS

All tabulated cumulative size-frequency data is provided for pseudo-log bins (**Chapter 2**, Section 2.3.2) equal to or greater than the 7 pixel threshold.

Table B1. Cumulative SFD Data: AS15-M-1010, 87° Incidence Angle, Analyst A.

D (km)[a]	n[b]	Ncum[c]	Area (km^2)	Frequency	Uncertainty[d]
0.07	1072	4217	1.00E+02	4.22E+01	6.49E-01
0.08	766	3145	1.00E+02	3.15E+01	5.61E-01
0.09	543	2379	1.00E+02	2.38E+01	4.88E-01
0.1	406	1836	1.00E+02	1.84E+01	4.29E-01
0.11	319	1430	1.00E+02	1.43E+01	3.78E-01
0.12	190	1111	1.00E+02	1.11E+01	3.33E-01
0.13	187	921	1.00E+02	9.21E+00	3.04E-01
0.14	133	734	1.00E+02	7.34E+00	2.71E-01
0.15	199	601	1.00E+02	6.01E+00	2.45E-01
0.17	185	402	1.00E+02	4.02E+00	2.01E-01
0.2	130	217	1.00E+02	2.17E+00	1.47E-01
0.25	46	87	1.00E+02	8.70E-01	9.33E-02
0.3	18	41	1.00E+02	4.10E-01	6.40E-02
0.35	6	23	1.00E+02	2.30E-01	4.80E-02
0.4	10	17	1.00E+02	1.70E-01	4.12E-02
0.45	3	7	1.00E+02	7.00E-02	2.65E-02
0.5	2	4	1.00E+02	4.00E-02	2.00E-02
0.6	1	2	1.00E+02	2.00E-02	1.41E-02
1.2	1	1	1.00E+02	1.00E-02	1.00E-02

[a]Diameter (km) for lower bin limit.
[b]Number of craters per diameter bin.
[c]Cumulative number of craters per diameter bin.
[d]Uncertainty estimates are calculated from the square root of the number of craters for a given bin.

Table B2. Cumulative SFD Data: AS15-M-1010, 87° Incidence Angle, Analyst L.

D (km)[a]	n[b]	Ncum[c]	Area (km^2)	Frequency	Uncertainty[d]
0.07	921	3499	1.00E+02	3.50E+01	5.92E-01
0.08	629	2578	1.00E+02	2.58E+01	5.08E-01
0.09	484	1949	1.00E+02	1.95E+01	4.42E-01
0.1	326	1465	1.00E+02	1.47E+01	3.83E-01
0.11	232	1139	1.00E+02	1.14E+01	3.38E-01
0.12	162	907	1.00E+02	9.07E+00	3.01E-01
0.13	153	745	1.00E+02	7.45E+00	2.73E-01
0.14	107	592	1.00E+02	5.92E+00	2.43E-01
0.15	169	485	1.00E+02	4.85E+00	2.20E-01
0.17	119	316	1.00E+02	3.16E+00	1.78E-01
0.2	117	197	1.00E+02	1.97E+00	1.40E-01
0.25	39	80	1.00E+02	8.00E-01	8.94E-02
0.3	21	41	1.00E+02	4.10E-01	6.40E-02
0.35	6	20	1.00E+02	2.00E-01	4.47E-02
0.4	5	14	1.00E+02	1.40E-01	3.74E-02
0.45	4	9	1.00E+02	9.00E-02	3.00E-02
0.5	2	5	1.00E+02	5.00E-02	2.24E-02
0.6	2	3	1.00E+02	3.00E-02	1.73E-02
1.2	1	1	1.00E+02	1.00E-02	1.00E-02

[a]Diameter (km) for lower bin limit.
[b]Number of craters per diameter bin.
[c]Cumulative number of craters per diameter bin.
[d]Uncertainty estimates are calculated from the square root of the number of craters for a given bin.

Table B3. Cumulative SFD Data: AS15-M-1152, 82° Incidence Angle, Analyst A.

D (km)[a]	n[b]	Ncum[c]	Area (km^2)	Frequency	Uncertainty[d]
0.07	512	2132	1.00E+02	2.13E+01	4.62E-01
0.08	300	1620	1.00E+02	1.62E+01	4.03E-01
0.09	232	1320	1.00E+02	1.32E+01	3.63E-01
0.1	216	1088	1.00E+02	1.09E+01	3.30E-01
0.11	161	872	1.00E+02	8.72E+00	2.95E-01
0.12	104	711	1.00E+02	7.11E+00	2.67E-01
0.13	96	607	1.00E+02	6.07E+00	2.46E-01
0.14	65	511	1.00E+02	5.11E+00	2.26E-01
0.15	124	446	1.00E+02	4.46E+00	2.11E-01
0.17	127	322	1.00E+02	3.22E+00	1.79E-01
0.2	115	195	1.00E+02	1.95E+00	1.40E-01
0.25	45	80	1.00E+02	8.00E-01	8.94E-02
0.3	12	35	1.00E+02	3.50E-01	5.92E-02
0.35	9	23	1.00E+02	2.30E-01	4.80E-02
0.4	7	14	1.00E+02	1.40E-01	3.74E-02
0.45	3	7	1.00E+02	7.00E-02	2.65E-02
0.5	3	4	1.00E+02	4.00E-02	2.00E-02
1.2	1	1	1.00E+02	1.00E-02	1.00E-02

[a]Diameter (km) for lower bin limit.
[b]Number of craters per diameter bin.
[c]Cumulative number of craters per diameter bin.
[d]Uncertainty estimates are calculated from the square root of the number of craters for a given bin.

Table B4. Cumulative SFD Data: AS15-M-1152, 82° Incidence Angle, Analyst L.

D (km)[a]	n[b]	Ncum[c]	Area (km^2)	Frequency	Uncertainty[d]
0.07	751	2993	1.00E+02	2.99E+01	5.47E-01
0.08	503	2242	1.00E+02	2.24E+01	4.74E-01
0.09	339	1739	1.00E+02	1.74E+01	4.17E-01
0.1	272	1400	1.00E+02	1.40E+01	3.74E-01
0.11	237	1128	1.00E+02	1.13E+01	3.36E-01
0.12	136	891	1.00E+02	8.91E+00	2.99E-01
0.13	132	755	1.00E+02	7.55E+00	2.75E-01
0.14	119	623	1.00E+02	6.23E+00	2.50E-01
0.15	165	504	1.00E+02	5.04E+00	2.25E-01
0.17	132	339	1.00E+02	3.39E+00	1.84E-01
0.2	117	207	1.00E+02	2.07E+00	1.44E-01
0.25	46	90	1.00E+02	9.00E-01	9.49E-02
0.3	19	44	1.00E+02	4.40E-01	6.63E-02
0.35	9	25	1.00E+02	2.50E-01	5.00E-02
0.4	8	16	1.00E+02	1.60E-01	4.00E-02
0.45	2	8	1.00E+02	8.00E-02	2.83E-02
0.5	3	6	1.00E+02	6.00E-02	2.45E-02
0.6	1	3	1.00E+02	3.00E-02	1.73E-02
0.7	1	2	1.00E+02	2.00E-02	1.41E-02
1.2	1	1	1.00E+02	1.00E-02	1.00E-02

[a]Diameter (km) for lower bin limit.
[b]Number of craters per diameter bin.
[c]Cumulative number of craters per diameter bin.
[d]Uncertainty estimates are calculated from the square root of the number of craters for a given bin.

Table B5. Cumulative SFD Data: AS15-M-1835, 71° Incidence Angle, Analyst A.

D (km)[a]	n[b]	Ncum[c]	Area (km^2)	Frequency	Uncertainty[d]
0.07	326	1380	1.00E+02	1.38E+01	3.72E-01
0.08	199	1054	1.00E+02	1.05E+01	3.25E-01
0.09	146	855	1.00E+02	8.55E+00	2.92E-01
0.1	120	709	1.00E+02	7.09E+00	2.66E-01
0.11	89	589	1.00E+02	5.89E+00	2.43E-01
0.12	80	500	1.00E+02	5.00E+00	2.24E-01
0.13	67	420	1.00E+02	4.20E+00	2.05E-01
0.14	43	353	1.00E+02	3.53E+00	1.88E-01
0.15	87	310	1.00E+02	3.10E+00	1.76E-01
0.17	65	223	1.00E+02	2.23E+00	1.49E-01
0.2	84	158	1.00E+02	1.58E+00	1.26E-01
0.25	31	74	1.00E+02	7.40E-01	8.60E-02
0.3	22	43	1.00E+02	4.30E-01	6.56E-02
0.35	8	21	1.00E+02	2.10E-01	4.58E-02
0.4	6	13	1.00E+02	1.30E-01	3.61E-02
0.45	3	7	1.00E+02	7.00E-02	2.65E-02
0.5	3	4	1.00E+02	4.00E-02	2.00E-02
1.1	1	1	1.00E+02	1.00E-02	1.00E-02

[a]Diameter (km) for lower bin limit.
[b]Number of craters per diameter bin.
[c]Cumulative number of craters per diameter bin.
[d]Uncertainty estimates are calculated from the square root of the number of craters for a given bin.

Table B6. Cumulative SFD Data: AS15-M-1835, 71° Incidence Angle, Analyst L.

D (km)[a]	n[b]	Ncum[c]	Area (km^2)	Frequency	Uncertainty[d]
0.07	407	1929	1.00E+02	1.93E+01	4.39E-01
0.08	298	1522	1.00E+02	1.52E+01	3.90E-01
0.09	223	1224	1.00E+02	1.22E+01	3.50E-01
0.1	171	1001	1.00E+02	1.00E+01	3.16E-01
0.11	140	830	1.00E+02	8.30E+00	2.88E-01
0.12	109	690	1.00E+02	6.90E+00	2.63E-01
0.13	103	581	1.00E+02	5.81E+00	2.41E-01
0.14	84	478	1.00E+02	4.78E+00	2.19E-01
0.15	104	394	1.00E+02	3.94E+00	1.99E-01
0.17	88	290	1.00E+02	2.90E+00	1.70E-01
0.2	122	202	1.00E+02	2.02E+00	1.42E-01
0.25	38	80	1.00E+02	8.00E-01	8.94E-02
0.3	9	42	1.00E+02	4.20E-01	6.48E-02
0.35	18	33	1.00E+02	3.30E-01	5.75E-02
0.4	7	15	1.00E+02	1.50E-01	3.87E-02
0.45	3	8	1.00E+02	8.00E-02	2.83E-02
0.5	2	5	1.00E+02	5.00E-02	2.24E-02
0.6	2	3	1.00E+02	3.00E-02	1.73E-02
1.2	1	1	1.00E+02	1.00E-02	1.00E-02

[a]Diameter (km) for lower bin limit.
[b]Number of craters per diameter bin.
[c]Cumulative number of craters per diameter bin.
[d]Uncertainty estimates are calculated from the square root of the number of craters for a given bin.

Table B7. Cumulative SFD Data: AS15-M-1835, 71° Incidence Angle, Analyst S.

D (km)[a]	n[b]	Ncum[c]	Area (km^2)	Frequency	Uncertainty[d]
0.07	65	682	1.00E+02	6.82E+00	2.61E-01
0.08	82	617	1.00E+02	6.17E+00	2.48E-01
0.09	55	535	1.00E+02	5.35E+00	2.31E-01
0.1	50	480	1.00E+02	4.80E+00	2.19E-01
0.11	43	430	1.00E+02	4.30E+00	2.07E-01
0.12	48	387	1.00E+02	3.87E+00	1.97E-01
0.13	35	339	1.00E+02	3.39E+00	1.84E-01
0.14	46	304	1.00E+02	3.04E+00	1.74E-01
0.15	58	258	1.00E+02	2.58E+00	1.61E-01
0.17	65	200	1.00E+02	2.00E+00	1.41E-01
0.2	66	135	1.00E+02	1.35E+00	1.16E-01
0.25	35	69	1.00E+02	6.90E-01	8.31E-02
0.3	16	34	1.00E+02	3.40E-01	5.83E-02
0.35	9	18	1.00E+02	1.80E-01	4.24E-02
0.4	3	9	1.00E+02	9.00E-02	3.00E-02
0.45	3	6	1.00E+02	6.00E-02	2.45E-02
0.5	1	3	1.00E+02	3.00E-02	1.73E-02
0.6	2	2	1.00E+02	2.00E-02	1.41E-02

[a]Diameter (km) for lower bin limit.
[b]Number of craters per diameter bin.
[c]Cumulative number of craters per diameter bin.
[d]Uncertainty estimates are calculated from the square root of the number of craters for a given bin.

Table B8. Cumulative SFD Data: AS15-M-2461, 50° Incidence Angle, Analyst L.

D (km)[a]	n[b]	Ncum[c]	Area (km^2)	Frequency	Uncertainty[d]
0.07	111	682	1.00E+02	6.82E+00	2.61E-01
0.08	80	571	1.00E+02	5.71E+00	2.39E-01
0.09	49	491	1.00E+02	4.91E+00	2.22E-01
0.1	48	442	1.00E+02	4.42E+00	2.10E-01
0.11	41	394	1.00E+02	3.94E+00	1.99E-01
0.12	38	353	1.00E+02	3.53E+00	1.88E-01
0.13	45	315	1.00E+02	3.15E+00	1.78E-01
0.14	39	270	1.00E+02	2.70E+00	1.64E-01
0.15	43	231	1.00E+02	2.31E+00	1.52E-01
0.17	61	188	1.00E+02	1.88E+00	1.37E-01
0.2	52	127	1.00E+02	1.27E+00	1.13E-01
0.25	33	75	1.00E+02	7.50E-01	8.66E-02
0.3	18	42	1.00E+02	4.20E-01	6.48E-02
0.35	8	24	1.00E+02	2.40E-01	4.90E-02
0.4	5	16	1.00E+02	1.60E-01	4.00E-02
0.45	7	11	1.00E+02	1.10E-01	3.32E-02
0.6	3	4	1.00E+02	4.00E-02	2.00E-02
1.2	1	1	1.00E+02	1.00E-02	1.00E-02

[a]Diameter (km) for lower bin limit.
[b]Number of craters per diameter bin.
[c]Cumulative number of craters per diameter bin.
[d]Uncertainty estimates are calculated from the square root of the number of craters for a given bin.

Table B9. Cumulative SFD Data: AS15-M-2461, 50° Incidence Angle, Analyst L.

D (km)[a]	n[b]	Ncum[c]	Area (km^2)	Frequency	Uncertainty[d]
0.07	5	306	1.00E+02	3.06E+00	1.75E-01
0.08	9	301	1.00E+02	3.01E+00	1.74E-01
0.09	15	292	1.00E+02	2.92E+00	1.71E-01
0.1	15	277	1.00E+02	2.77E+00	1.66E-01
0.11	18	262	1.00E+02	2.62E+00	1.62E-01
0.12	19	244	1.00E+02	2.44E+00	1.56E-01
0.13	14	225	1.00E+02	2.25E+00	1.50E-01
0.14	17	211	1.00E+02	2.11E+00	1.45E-01
0.15	44	194	1.00E+02	1.94E+00	1.39E-01
0.17	38	150	1.00E+02	1.50E+00	1.23E-01
0.2	53	112	1.00E+02	1.12E+00	1.06E-01
0.25	23	59	1.00E+02	5.90E-01	7.68E-02
0.3	19	36	1.00E+02	3.60E-01	6.00E-02
0.35	6	17	1.00E+02	1.70E-01	4.12E-02
0.4	4	11	1.00E+02	1.10E-01	3.32E-02
0.45	4	7	1.00E+02	7.00E-02	2.65E-02
0.5	1	3	1.00E+02	3.00E-02	1.73E-02
0.6	1	2	1.00E+02	2.00E-02	1.41E-02
0.7	1	1	1.00E+02	1.00E-02	1.00E-02

[a]Diameter (km) for lower bin limit.
[b]Number of craters per diameter bin.
[c]Cumulative number of craters per diameter bin.
[d]Uncertainty estimates are calculated from the square root of the number of craters for a given bin.

Table B10. Cumulative SFD Data: LROC NAC M104633604L, 56° Incidence Angle.[*]

D (km)[a]	n[b]	Ncum[c]	Area (km^2)	Frequency	Uncertainty[d]
0.014	92	624	4.00E+00	1.56E+02	6.25E+00
0.015	113	532	4.00E+00	1.33E+02	5.77E+00
0.017	118	419	4.00E+00	1.05E+02	5.12E+00
0.02	107	301	4.00E+00	7.53E+01	4.34E+00
0.025	44	194	4.00E+00	4.85E+01	3.48E+00
0.03	38	150	4.00E+00	3.75E+01	3.06E+00
0.035	26	112	4.00E+00	2.80E+01	2.65E+00
0.04	27	86	4.00E+00	2.15E+01	2.32E+00
0.045	11	59	4.00E+00	1.48E+01	1.92E+00
0.05	16	48	4.00E+00	1.20E+01	1.73E+00
0.06	13	32	4.00E+00	8.00E+00	1.41E+00
0.07	4	19	4.00E+00	4.75E+00	1.09E+00
0.08	1	15	4.00E+00	3.75E+00	9.68E-01
0.09	3	14	4.00E+00	3.50E+00	9.35E-01
0.1	1	11	4.00E+00	2.75E+00	8.29E-01
0.11	1	10	4.00E+00	2.50E+00	7.91E-01
0.12	3	9	4.00E+00	2.25E+00	7.50E-01
0.13	1	6	4.00E+00	1.50E+00	6.12E-01
0.14	3	5	4.00E+00	1.25E+00	5.59E-01
0.2	2	2	4.00E+00	5.00E-01	3.54E-01

[*]Measurements by analyst L.
[a]Diameter (km) for lower bin limit.
[b]Number of craters per diameter bin.
[c]Cumulative number of craters per diameter bin.
[d]Uncertainty estimates are calculated from the square root of the number of craters for a given bin.

Table B11. Cumulative SFD Data: Apollo 11 Landing Site, 82° Incidence Angle.[*]

D (km)[a]	n[b]	Ncum[c]	Area (km^2)	Frequency	Uncertainty[d]
0.005	1800	4661	2.09E+00	2.23E+03	3.26E+01
0.006	979	2861	2.09E+00	1.37E+03	2.55E+01
0.007	580	1882	2.09E+00	8.99E+02	2.07E+01
0.008	373	1302	2.09E+00	6.22E+02	1.72E+01
0.009	217	929	2.09E+00	4.44E+02	1.46E+01
0.01	131	712	2.09E+00	3.40E+02	1.27E+01
0.011	112	581	2.09E+00	2.78E+02	1.15E+01
0.012	65	469	2.09E+00	2.24E+02	1.03E+01
0.013	53	404	2.09E+00	1.93E+02	9.60E+00
0.014	60	351	2.09E+00	1.68E+02	8.95E+00
0.015	61	291	2.09E+00	1.39E+02	8.15E+00
0.017	69	230	2.09E+00	1.10E+02	7.24E+00
0.02	56	161	2.09E+00	7.69E+01	6.06E+00
0.025	24	105	2.09E+00	5.01E+01	4.89E+00
0.03	11	81	2.09E+00	3.87E+01	4.30E+00
0.035	17	70	2.09E+00	3.34E+01	4.00E+00
0.04	7	53	2.09E+00	2.53E+01	3.48E+00
0.045	10	46	2.09E+00	2.20E+01	3.24E+00
0.05	4	36	2.09E+00	1.72E+01	2.87E+00
0.06	4	32	2.09E+00	1.53E+01	2.70E+00
0.07	7	28	2.09E+00	1.34E+01	2.53E+00
0.08	1	21	2.09E+00	1.00E+01	2.19E+00
0.09	5	20	2.09E+00	9.55E+00	2.14E+00
0.1	1	15	2.09E+00	7.16E+00	1.85E+00
0.11	2	14	2.09E+00	6.69E+00	1.79E+00
0.12	1	12	2.09E+00	5.73E+00	1.65E+00
0.13	1	11	2.09E+00	5.25E+00	1.58E+00
0.15	2	10	2.09E+00	4.78E+00	1.51E+00
0.17	2	8	2.09E+00	3.82E+00	1.35E+00
0.2	4	6	2.09E+00	2.87E+00	1.17E+00
0.25	1	2	2.09E+00	9.55E-01	6.75E-01
0.3	1	1	2.09E+00	4.78E-01	4.78E-01

[*]Measurements by analyst L.

[a]Diameter (km) for lower bin limit.

[b]Number of craters per diameter bin.

[c]Cumulative number of craters per diameter bin.

[d]Uncertainty estimates are calculated from the square root of the number of craters for a given bin.

Table B12. Cumulative SFD Data: Apollo 11 Landing Site, 64° Incidence Angle.[*]

D (km)[a]	n[b]	Ncum[c]	Area (km^2)	Frequency	Uncertainty[d]
0.005	1494	4002	2.17E+00	1.85E+03	2.92E+01
0.006	869	2508	2.17E+00	1.16E+03	2.31E+01
0.007	507	1639	2.17E+00	7.57E+02	1.87E+01
0.008	316	1132	2.17E+00	5.23E+02	1.55E+01
0.009	196	816	2.17E+00	3.77E+02	1.32E+01
0.01	136	620	2.17E+00	2.86E+02	1.15E+01
0.011	69	484	2.17E+00	2.24E+02	1.02E+01
0.012	70	415	2.17E+00	1.92E+02	9.41E+00
0.013	58	345	2.17E+00	1.59E+02	8.58E+00
0.014	35	287	2.17E+00	1.33E+02	7.82E+00
0.015	48	252	2.17E+00	1.16E+02	7.33E+00
0.017	65	204	2.17E+00	9.42E+01	6.60E+00
0.02	49	139	2.17E+00	6.42E+01	5.45E+00
0.025	23	90	2.17E+00	4.16E+01	4.38E+00
0.03	8	67	2.17E+00	3.09E+01	3.78E+00
0.035	12	59	2.17E+00	2.73E+01	3.55E+00
0.04	9	47	2.17E+00	2.17E+01	3.17E+00
0.045	6	38	2.17E+00	1.76E+01	2.85E+00
0.05	8	32	2.17E+00	1.48E+01	2.61E+00
0.06	3	24	2.17E+00	1.11E+01	2.26E+00
0.07	5	21	2.17E+00	9.70E+00	2.12E+00
0.08	3	16	2.17E+00	7.39E+00	1.85E+00
0.1	1	13	2.17E+00	6.00E+00	1.67E+00
0.11	2	12	2.17E+00	5.54E+00	1.60E+00
0.12	2	10	2.17E+00	4.62E+00	1.46E+00
0.15	2	8	2.17E+00	3.69E+00	1.31E+00
0.17	2	6	2.17E+00	2.77E+00	1.13E+00
0.2	3	4	2.17E+00	1.85E+00	9.24E-01
0.25	1	1	2.17E+00	4.62E-01	4.62E-01

[*]Measurements by analyst L.

[a]Diameter (km) for lower bin limit.

[b]Number of craters per diameter bin.

[c]Cumulative number of craters per diameter bin.

[d]Uncertainty estimates are calculated from the square root of the number of craters for a given bin.

Table B13. Cumulative SFD Data: LROC WAC, 66° Incidence Angle, Box 1.*

D (km)[a]	n[b]	Ncum[c]	Area (km^2)	Frequency	Uncertainty[d]
0.7	4	7	4.00E+02	1.75E-02	6.61E-03
0.8	1	3	4.00E+02	7.50E-03	4.33E-03
0.9	1	2	4.00E+02	5.00E-03	3.54E-03
1.1	1	1	4.00E+02	2.50E-03	2.50E-03

*Measurements by analyst L.
[a]Diameter (km) for lower bin limit.
[b]Number of craters per diameter bin.
[c]Cumulative number of craters per diameter bin.
[d]Uncertainty estimates are calculated from the square root of the number of craters for a given bin.

Table B14. Cumulative SFD Data: LROC WAC, 66° Incidence Angle, Box 2.*

D (km)[a]	n[b]	Ncum[c]	Area (km^2)	Frequency	Uncertainty[d]
0.7	4	10	4.00E+02	2.50E-02	7.91E-03
0.8	5	6	4.00E+02	1.50E-02	6.12E-03
0.9	1	1	4.00E+02	2.50E-03	2.50E-03

*Measurements by analyst L.
[a]Diameter (km) for lower bin limit.
[b]Number of craters per diameter bin.
[c]Cumulative number of craters per diameter bin.
[d]Uncertainty estimates are calculated from the square root of the number of craters for a given bin.

Table B15. Cumulative SFD Data: LROC WAC, 66° Incidence Angle, Box 3.*

D (km)[a]	n[b]	Ncum[c]	Area (km^2)	Frequency	Uncertainty[d]
0.7	3	5	4.00E+02	1.25E-02	5.59E-03
0.9	2	2	4.00E+02	5.00E-03	3.54E-03

*Measurements by analyst L.
[a]Diameter (km) for lower bin limit.
[b]Number of craters per diameter bin.
[c]Cumulative number of craters per diameter bin.
[d]Uncertainty estimates are calculated from the square root of the number of craters for a given bin.

Table B16. Cumulative SFD Data: LROC WAC, 46° Incidence Angle, Box 1.*

D (km)[a]	n[b]	Ncum[c]	Area (km^2)	Frequency	Uncertainty[d]
0.7	4	8	4.00E+02	2.00E-02	7.07E-03
0.8	2	4	4.00E+02	1.00E-02	5.00E-03
0.9	1	2	4.00E+02	5.00E-03	3.54E-03
1.2	1	1	4.00E+02	2.50E-03	2.50E-03

*Measurements by analyst L.
[a]Diameter (km) for lower bin limit.
[b]Number of craters per diameter bin.
[c]Cumulative number of craters per diameter bin.
[d]Uncertainty estimates are calculated from the square root of the number of craters for a given bin.

Table B17. Cumulative SFD Data: LROC WAC, 46° Incidence Angle, Box 2.*

D (km)[a]	n[b]	Ncum[c]	Area (km^2)	Frequency	Uncertainty[d]
0.7	3	6	4.00E+02	1.50E-02	6.12E-03
0.8	3	3	4.00E+02	7.50E-03	4.33E-03

*Measurements by analyst L.
[a]Diameter (km) for lower bin limit.
[b]Number of craters per diameter bin.
[c]Cumulative number of craters per diameter bin.
[d]Uncertainty estimates are calculated from the square root of the number of craters for a given bin.

Table B18. Cumulative SFD Data: LROC WAC, 46° Incidence Angle, Box 3.*

D (km)[a]	n[b]	Ncum[c]	Area (km^2)	Frequency	Uncertainty[d]
0.7	1	3	4.00E+02	7.50E-03	4.33E-03
0.8	1	2	4.00E+02	5.00E-03	3.54E-03
0.9	1	1	4.00E+02	2.50E-03	2.50E-03

*Measurements by analyst L.
[a]Diameter (km) for lower bin limit.
[b]Number of craters per diameter bin.
[c]Cumulative number of craters per diameter bin.
[d]Uncertainty estimates are calculated from the square root of the number of craters for a given bin.

Table B19. Cumulative SFD Data: Mare Serenitatis, LROC WAC, 66° Incidence Angle.*

D (km)[a]	n[b]	Ncum[c]	Area (km^2)	Frequency	Uncertainty[d]
0.7	269	680	3.90E+04	1.74E-02	6.69E-04
0.8	145	411	3.90E+04	1.05E-02	5.20E-04
0.9	98	266	3.90E+04	6.82E-03	4.18E-04
1	54	168	3.90E+04	4.31E-03	3.32E-04
1.1	35	114	3.90E+04	2.92E-03	2.74E-04
1.2	23	79	3.90E+04	2.03E-03	2.28E-04
1.3	15	56	3.90E+04	1.44E-03	1.92E-04
1.4	9	41	3.90E+04	1.05E-03	1.64E-04
1.5	15	32	3.90E+04	8.21E-04	1.45E-04
1.7	9	17	3.90E+04	4.36E-04	1.06E-04
2	3	8	3.90E+04	2.05E-04	7.25E-05
4	2	5	3.90E+04	1.28E-04	5.74E-05
5	3	3	3.90E+04	7.69E-05	4.44E-05

*Measurements by analyst L.
[a]Diameter (km) for lower bin limit.
[b]Number of craters per diameter bin.
[c]Cumulative number of craters per diameter bin.
[d]Uncertainty estimates are calculated from the square root of the number of craters for a given bin.

Table B20. Cumulative SFD Data: Mare Serenitatis, LROC WAC, 46° Incidence Angle.*

D (km)[a]	n[b]	Ncum[c]	Area (km^2)	Frequency	Uncertainty[d]
0.7	252	613	3.90E+04	1.57E-02	6.35E-04
0.8	144	361	3.90E+04	9.26E-03	4.87E-04
0.9	78	217	3.90E+04	5.57E-03	3.78E-04
1	48	139	3.90E+04	3.57E-03	3.02E-04
1.1	27	91	3.90E+04	2.33E-03	2.45E-04
1.2	18	64	3.90E+04	1.64E-03	2.05E-04
1.3	9	46	3.90E+04	1.18E-03	1.74E-04
1.4	13	37	3.90E+04	9.49E-04	1.56E-04
1.5	12	24	3.90E+04	6.16E-04	1.26E-04
1.7	5	12	3.90E+04	3.08E-04	8.88E-05
2	2	7	3.90E+04	1.80E-04	6.79E-05
4	2	5	3.90E+04	1.28E-04	5.74E-05
5	3	3	3.90E+04	7.69E-05	4.44E-05

*Measurements by analyst L.
[a]Diameter (km) for lower bin limit.
[b]Number of craters per diameter bin.
[c]Cumulative number of craters per diameter bin.
[d]Uncertainty estimates are calculated from the square root of the number of craters for a given bin.

Cumulative SFDs below are displayed with calculated least squares fits to production and equilibrium. Crater data shown without calculated uncertainties or 7 pixel threshold grayed out.

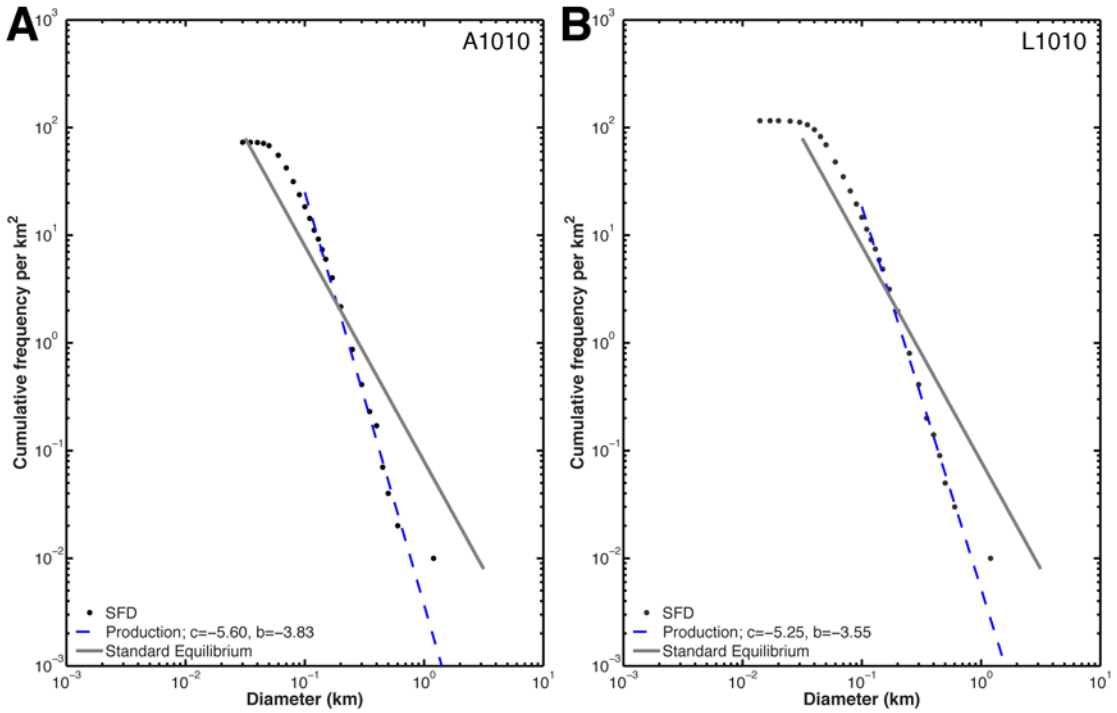

Figure B1. Crater SFDs for AS15-M-1010 (87° incidence angle) with production function fit and standard equilibrium. (A) SFD measured by analyst A, (B) SFD measured by analyst L.

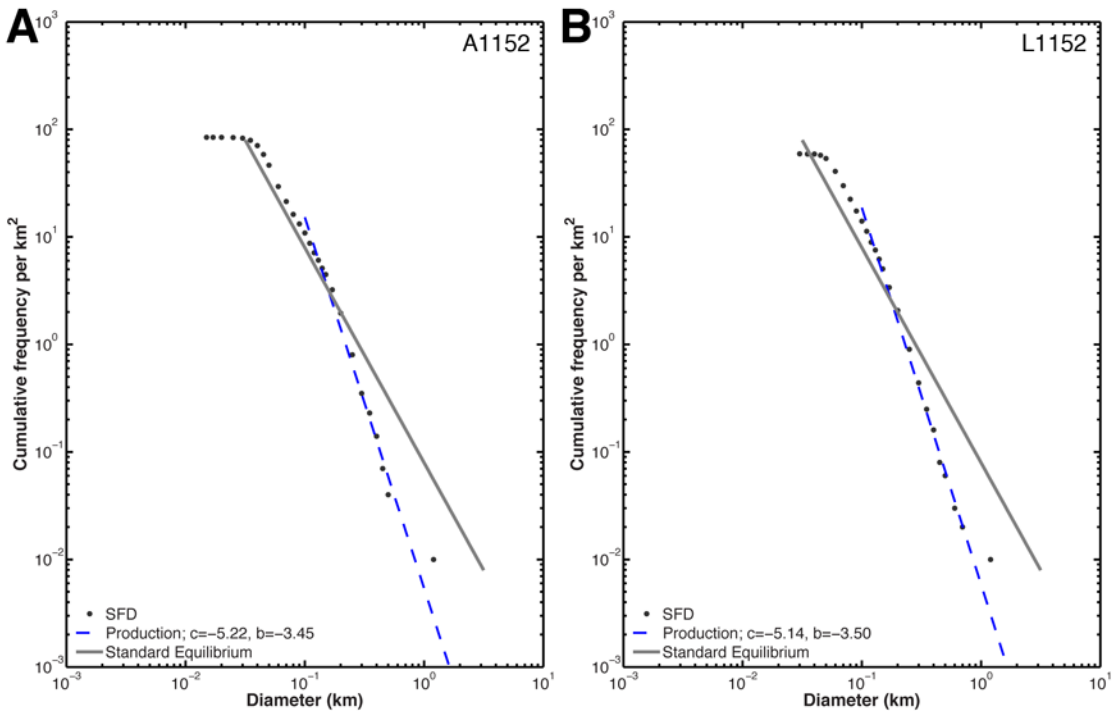

Figure B2. Crater SFDs for AS15-M-1152 (82° incidence angle) with production function fit and standard equilibrium. (A) SFD measured by analyst A, (B) SFD measured by analyst L.

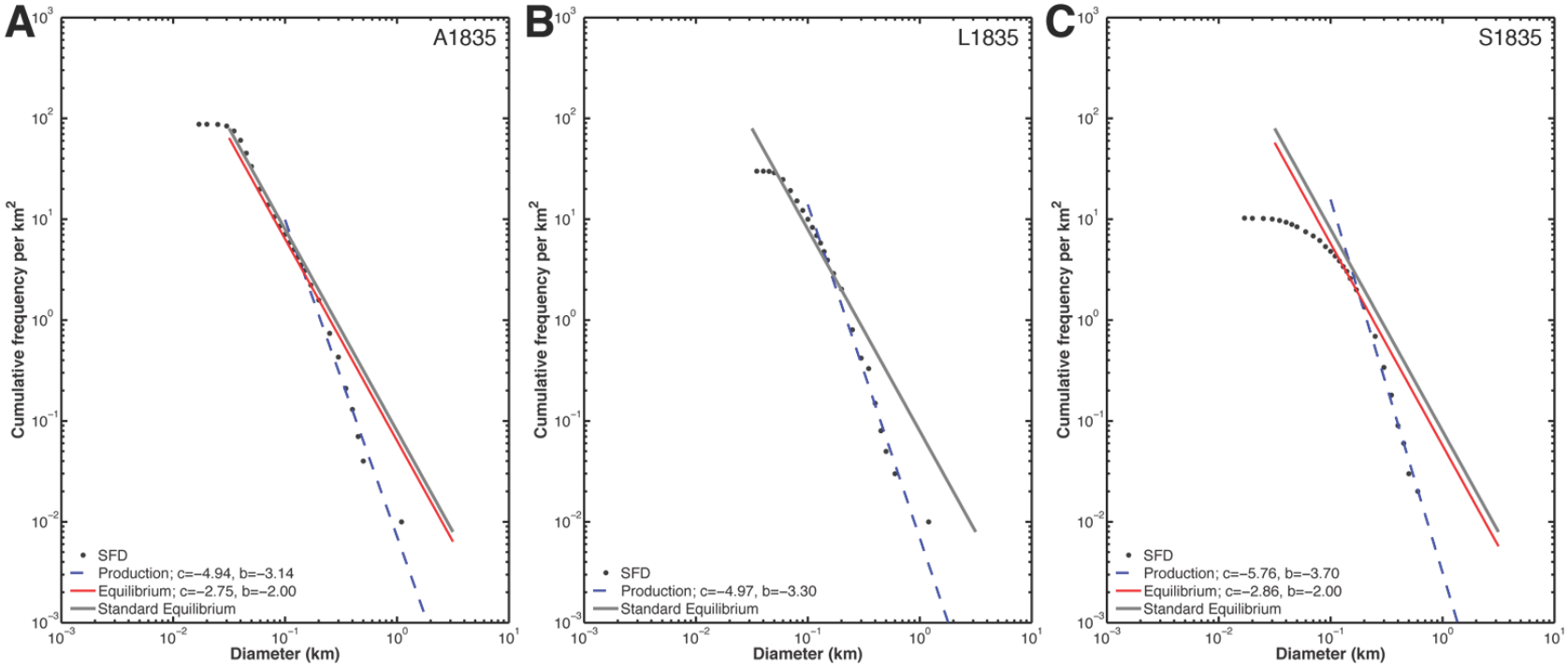

Figure B3. Crater SFDs for AS15-M-1835 (71° incidence angle) with production function fit, equilibrium fit to a -2 slope, and standard equilibrium. (A) SFD measured by analyst A, (B) SFD measured by analyst L, (C) SFD measured by analyst S.

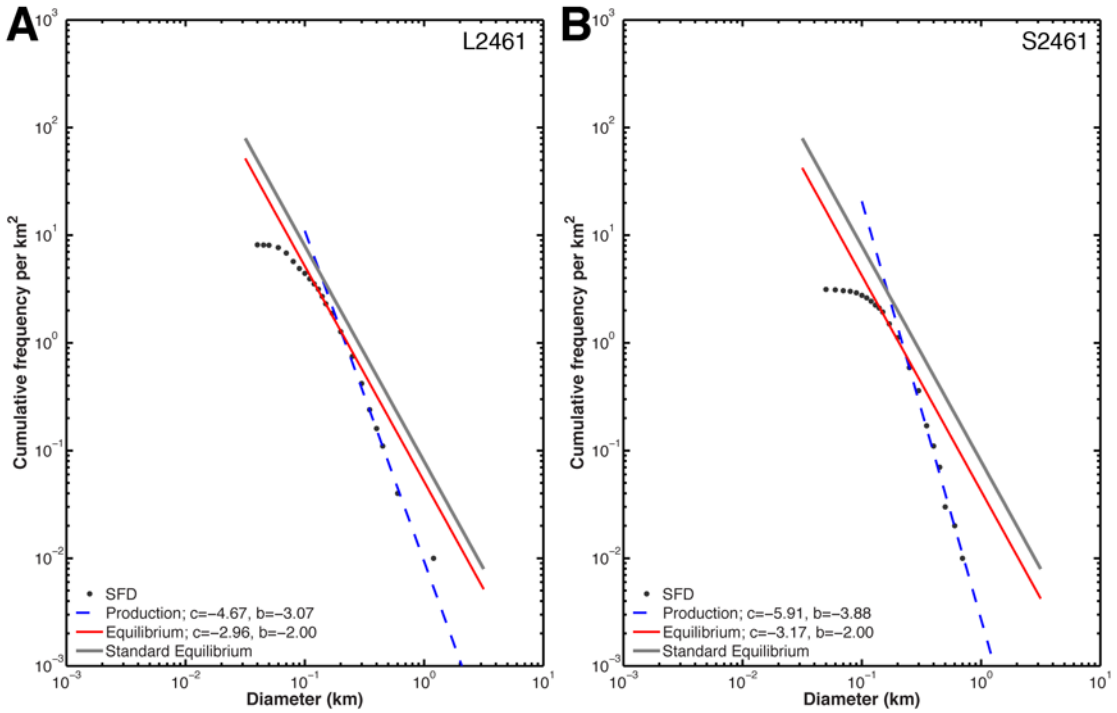

Figure B4. Crater SFDs for AS15-M-2461 (50° incidence angle) with production function fit, equilibrium fit to a -2 slope, and standard equilibrium. (A) SFD measured by analyst L, (B) SFD measured by analyst S.

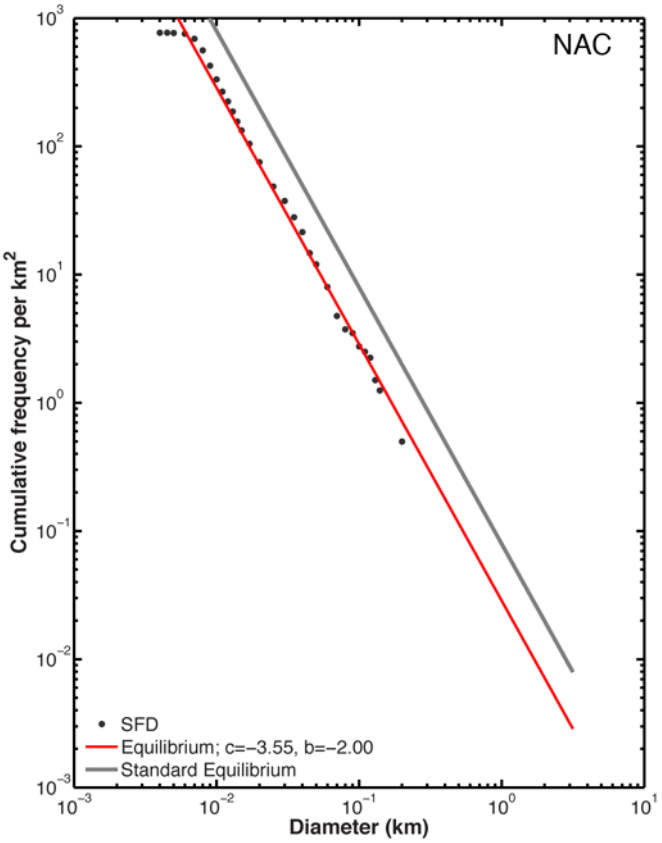

Figure B5. Crater SFD for LROC NAC M104633604L (56° incidence angle) equilibrium fit to a -2 slope and standard equilibrium; the production function is not observed.

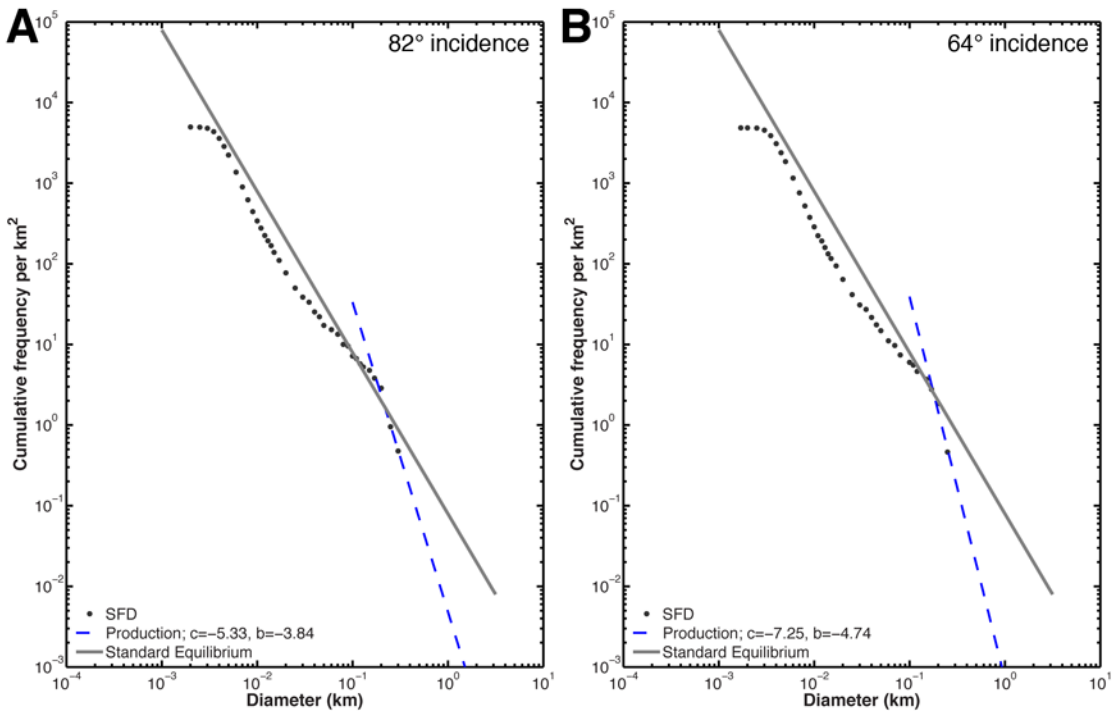

Figure B6. Crater SFDs for LROC NAC (A) M116161085R (82° incidence angle) and (B) M150368601R (64° incidence angle) with production function fit and standard equilibrium.

APPENDIX C

EDGE CORRECTION: POINT CORRECTION TECHNIQUE

A grid of evenly spaced points was created for the study area using a modification to the Repeating Shapes extension for ArcMap 10 (J. Jenness, http://www.jennesant.com). Point grid spacing was determined from the LROC WAC basemap (100 meter pixel scale) resolution for simplicity and ease of application. Increasing the spacing of the point grid will decrease the correction effectiveness because fewer points will be included in each neighborhood. For example, when 400 m spacing is used for the point correction, neighborhoods within 25 km of the boundary contain between 7 fewer to 11 more points than the 100 m spacing point correction (Figure C1). Decreasing the spacing will slightly increase the correction effectiveness because more points will be included in each neighborhood; 50 m point grid spacing corresponds to 2 fewer to 1 more points contained in neighborhoods within 25 km of the boundary compared to the 100 m spacing point correction (Figure C2). The differences between point correction values near the edges for 50 m and 100 m spacing do not substantially alter the resulting corrected ACD map, indicating that a 100 m point grid spacing for studies using LROC WAC basemaps is sufficient.

The corrected ACD map reflects the proportion of the study area contained within each neighborhood at each output cell location (Figure 3.4, 3.5, 3.8). When a neighborhood is fully contained within the study area, the point grid density will be at a maximum. As a sampling boundary is approached, the resulting point grid density magnitude will reflect the proportion of the study area contained within the neighborhood. For example, an output cell at a square corner will have a point correction of 0.25 (e.g., Figure 3.4), because 25% of the neighborhood area is contained within the valid study area. Once the point correction is determined for the study region (e.g., Figure 3.4, 3.5, 3.8), the ACD magnitudes are divided by the point correction to derive a "corrected" ACD map with minimized edge effects and then extracted to the study region boundary extent (e.g., Figure 3.3, 3.6A,B, 3.7B,C).

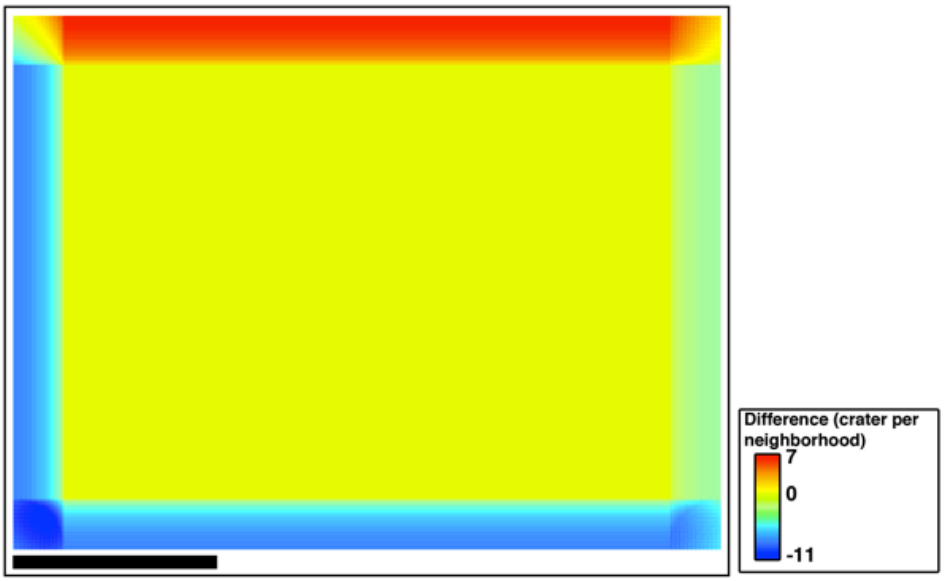

Figure C1: Point correction validation; difference between point correction of 100 m grid spacing and 400 m grid spacing and differences observed are within one neighborhood radius (25 km) of the measured edge. Scalebar is 100 km.

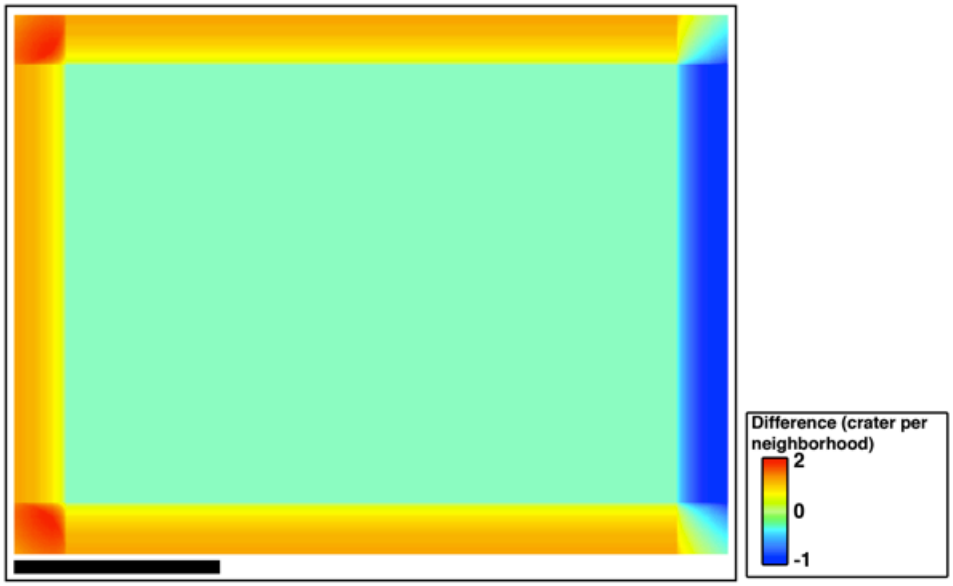

Figure C2: Point correction validation; difference between point correction of 100 m grid spacing and 50 m grid spacing. Differences are observed within one neighborhood radius (25 km) of the measured edge. Scalebar is 100 km.

APPENDIX D

TABULATED CRATER STATISTICS FOR THE NORTH POLAR REGION OF MERCURY

Table D1. N(20) Values for NHCT Subareas

Subarea Name	Measurement Area (km^2)	N(20)
He1a1*	1.45E+06	122 ± 9
He1a2	1.31E+06	111 ± 9
He1a3	9.11E+05	74 ± 9
He2a1	1.19E+06	111 ± 10
He2a2	1.46E+06	101 ± 8
He2a3	1.02E+06	108 ± 10
He3a1	1.03E+06	120 ± 11
He3a2	1.19E+06	119 ± 10
He3a3	1.45E+06	86 ± 8

*He1a1 = NHCT, example 1, area 1, etc.

Table D2. N(10) Values for NSP *SP1* Subareas

Subarea Name	Measurement Area (km^2)	N(10)[a]
Se1a1*	1.06E+06	81 ± 9
Se1a2	8.85E+05	64 ± 9
Se1a3	1.08E+06	69 ± 8
Se1a4	1.06E+06	57 ± 7
Se2a1	1.38E+06	70 ± 7
Se2a2	1.14E+06	78 ± 8
Se2a3	7.89E+05	68 ± 9
Se2a4	7.51E+05	51 ± 8
Se3a1	9.61E+05	69 ± 8
Se3a2	1.09E+06	60 ± 7
Se3a3	1.27E+06	75 ± 8
Se3a4	7.58E+05	69 ± 10

[a]*sp1* N(10) = 67 ± 4

*Se1a1 = NSP, example 1, area 1, etc.

Table D3. North Polar Heavily Cratered Terrain Crater Population Data – Cumulative.

Diameter[a]	Ncum[b]	Area (km^2)	Frequency	Uncertainty[c]
8	1056	3.67E+06	2.88E-04	1.64E-05
11.31	750	3.67E+06	2.04E-04	1.27E-05
16	492	3.67E+06	1.34E-04	1.07E-05
22.63	336	3.67E+06	9.16E-05	8.89E-06
32	230	3.67E+06	6.27E-05	6.21E-06
45.25	128	3.67E+06	3.49E-05	4.54E-06
64	69	3.67E+06	1.88E-05	2.90E-06
90.51	27	3.67E+06	7.36E-06	1.97E-06
128	13	3.67E+06	3.54E-06	1.18E-06
181	4	3.67E+06	1.09E-06	6.29E-07
256	1	3.67E+06	2.72E-07	2.72E-07

[a]Diameter in km for lower bin limit.
[b]Cumulative number of craters per diameter bin.
[c]Uncertainty estimates are calculated from the square root of the number of craters for a given bin.

Table D4. North Polar Heavily Cratered Terrain Crater Population Data – R-Plot.

Diameter[a]	n[b]	Area (km^2)	Relative Value	Uncertainty[c]
8	306	3.67E+06	0.021666	1.24E-03
11.31	258	3.67E+06	0.036535	2.27E-03
16	156	3.67E+06	0.044182	3.54E-03
22.63	106	3.67E+06	0.060042	5.83E-03
32	102	3.67E+06	0.115553	1.14E-02
45.25	59	3.67E+06	0.133679	1.74E-02
64	42	3.67E+06	0.190323	2.94E-02
90.51	14	3.67E+06	0.126882	3.39E-02
128	9	3.67E+06	0.163134	5.44E-02
181	3	3.67E+06	0.108756	6.28E-02
256	1	3.67E+06	0.072504	7.25E-02

[a]Diameter in km for lower bin limit.
[b]Number of craters per diameter bin.
[c]Uncertainty estimates are calculated from the square root of the number of craters for a given bin.

Table D5. Northern Smooth Plains Post-Plains Crater Population Data – Cumulative.

Diameter[a]	Ncum[b]	Area (km^2)	Frequency	Uncertainty[c]
8	501	5.59E+06	8.96E-05	6.17E-06
11.31	290	5.59E+06	5.19E-05	4.95E-06
16	180	5.59E+06	3.22E-05	3.49E-06
22.63	95	5.59E+06	1.70E-05	2.43E-06
32	46	5.59E+06	8.23E-06	1.68E-06
45.25	22	5.59E+06	3.94E-06	1.24E-06
64	12	5.59E+06	2.15E-06	8.76E-07
90.51	6	5.59E+06	1.07E-06	4.80E-07
128	1	5.59E+06	1.79E-07	1.79E-07
181	1	5.59E+06	1.79E-07	1.79E-07

[a]Diameter in km for lower bin limit.
[b]Cumulative number of craters per diameter bin.
[c]Uncertainty estimates are calculated from the square root of the number of craters for a given bin.

Table D6. Northern Smooth Plains Post-Plains Crater Population Data – R-Plot.

Diameter[a]	n[b]	Area (km^2)	Relative Value	Uncertainty[c]
8	211	5.59E+06	0.009808	6.75E-04
11.31	110	5.59E+06	0.010227	9.75E-04
16	85	5.59E+06	0.015805	1.71E-03
22.63	49	5.59E+06	0.018222	2.60E-03
32	24	5.59E+06	0.017850	3.64E-03
45.25	10	5.59E+06	0.014875	4.70E-03
64	6	5.59E+06	0.017850	7.29E-03
90.51	5	5.59E+06	0.029751	1.33E-02
128	0	5.59E+06	0	0
181	1	5.59E+06	0.023801	2.38E-02

[a]Diameter in km for lower bin limit.
[b]Number of craters per diameter bin.
[c]Uncertainty estimates are calculated from the square root of the number of craters for a given bin.

Table D7. Northern Smooth Plains Buried Crater Population Data – Cumulative.

Diameter[a]	Ncum[b]	Area (km^2)	Frequency	Uncertainty[c]
8	355	3.79E+06	9.37E-05	9.66E-06
11.31	261	3.79E+06	6.89E-05	8.41E-06
16	194	3.79E+06	5.12E-05	7.17E-06
22.63	143	3.79E+06	3.77E-05	5.97E-06
32	103	3.79E+06	2.72E-05	5.05E-06
45.25	74	3.79E+06	1.95E-05	3.40E-06
64	41	3.79E+06	1.08E-05	2.36E-06
90.51	20	3.79E+06	5.28E-06	2.64E-06
128	16	3.79E+06	4.22E-06	1.60E-06
181.02	9	3.79E+06	2.37E-06	1.19E-06
256	5	3.79E+06	1.32E-06	9.33E-07
362.04	3	3.79E+06	7.92E-07	5.60E-07

[a]Diameter in km for lower bin limit.
[b]Cumulative number of craters per diameter bin.
[c]Uncertainty estimates are calculated from the square root of the number of craters for a given bin.

Table D8. Northern Smooth Plains Buried Crater Population Data – R-Plot.

Diameter[a]	n[b]	Area (km^2)	Relative Value	Uncertainty[c]
8	94	3.79E+06	0.007110	6.65E-04
11.31	67	3.79E+06	0.010310	1.12E-03
16	51	3.79E+06	0.015945	1.96E-03
22.63	40	3.79E+06	0.025409	3.47E-03
32	59	3.79E+06	0.073150	8.43E-03
45.25	33	3.79E+06	0.085006	1.26E-02
64	21	3.79E+06	0.112257	2.01E-02
90.51	4	3.79E+06	0.052656	1.76E-02
128	7	3.79E+06	0.169303	4.64E-02
181.02	4	3.79E+06	0.210625	7.02E-02
256	2	3.79E+06	0.239706	9.93E-02
362.04	2	3.79E+06	0.479413	1.99E-01

[a]Diameter in km for lower bin limit.
[b]Number of craters per diameter bin.
[c]Uncertainty estimates are calculated from the square root of the number of craters for a given bin.

APPENDIX E

AUTHOR PERMISSION FOR USE OF CO-AUTHORED MATERIALS

Mark S. Robinson, Brett W. Denevi, and Peter C. Thomas have granted permission for the use of co-authored materials in Chapter 2.

Mark S. Robinson, Brett W. Denevi, Caleb I. Fassett, James W. Head, Sean C. Solomon, Robert G. Strom, and Jennifer L. Whitten have granted permission for the use of co-authored materials in Chapter 4.

Mark S. Robinson and Brett W. Denevi have granted permission for the use of co-authored materials in Chapter 6.

BIOGRAPHICAL SKETCH

Lillian Rose Ostrach became interested in planetary science at an early age. She received her Sc.B. in Geology-Biology from Brown University in 2007 and completed her Sc.M. in Geological Sciences at Brown University in 2008. Admitted to the School of Earth and Space Exploration Doctoral Program at Arizona State University in 2008, Lillian was a Ph.D. Candidate until October 2013. After defending her Ph.D. in October 2013, she will begin a NASA Postdoctoral Program Fellowship at the NASA Goddard Spaceflight Facility in Greenbelt, MD, where she will continue comparative investigations of the impact cratering process and impact crater products. During her Ph.D. program, Ostrach collaborated extensively with the Lunar Reconnaissance Orbiter Camera (LROC) and MErcury Surface, Space ENvironment, GEochemistry, and Ranging (MESSENGER) science teams.